

STUDY OF REACTION PATHWAYS AND KINETICS
IN Cu(In_xGa_{1-x})Se₂ THIN FILM GROWTH

By

WOO KYOUNG KIM

A DISSERTATION PRESENTED TO THE GRADUATE SCHOOL
OF THE UNIVERSITY OF FLORIDA IN PARTIAL FULFILLMENT
OF THE REQUIREMENTS FOR THE DEGREE OF
DOCTOR OF PHILOSOPHY

UNIVERSITY OF FLORIDA

2006

Copyright 2006

by

Woo Kyoung Kim

To my wife Eun Mi, lovely son Jin Woo and my parents.

ACKNOWLEDGMENTS

First of all, I would like to express my sincere appreciation to my research advisor, Dr. Timothy J. Anderson. His academic encouragement and considerate support have inspired me to establish the capability to perform independent research, which will be an invaluable asset to my future career. I also want to show my gratitude to my supervisory committee, Dr. Sheng S. Li, Dr. Oscar D. Crisalle and Dr. Valentin Craciun, for kind advice and helpful discussion. I also want to give my special thanks to Dr. E. Andrew Payzant in Oak Ridge National Laboratory for his generous assistance in high temperature X-ray diffraction experiments, and Dr. Jianyun Shen for her help in thermodynamic calculation.

Many thanks should be returned to former members of the UF solar cell research team, Dr. Suku Kim, Dr. Serkan Kincal and Dr. Seokhyun Yoon, who instructed me how to operate the MEE system and how to conduct my research. It was also a great pleasure to work with Jiyon Song, Ryan Kaczynski, Ryan Acher, Xuege Wang, Andre Baran, Wei Liu and Matt Monroe in the UF solar cell research team, and many other graduate students in electronic material processing group. Finally, I would like to thank Gerald R. Bourne for teaching me how to use FIB, and Kerry Siebein for TEM-EDS analysis at Major Analytical Instrumentation Center.

TABLE OF CONTENTS

	<u>page</u>
ACKNOWLEDGMENTS	iv
LIST OF TABLES	ix
LIST OF FIGURES	xi
ABSTRACT.....	xviii
CHAPTER	
1 INTRODUCTION	1
1.1 Photovoltaic Devices	1
1.2 Fundamental Physics of Solar Cells	2
1.3 Why CIGS ?	5
1.4 CIGS Deposition Processes	8
1.5 MEE System Description	13
1.6 Statement of Thesis Work	16
2 BINARY AND TERNARY PHASE DIAGRAM ASSESSMENT	19
2.1 Cu-Se Binary Phase Diagram Assessment	19
2.1.1 Introduction	19
2.1.2 Experimental Information	20
2.1.3 Thermodynamic Optimization.....	22
2.1.4 Results and Discussion	26
2.1.5 Summary.....	28
2.2 Thermodynamic Description of Ternary Compounds in Cu-In-Se System	40
2.2.1 Introduction	40
2.2.2 Extrapolation of Binary Gibbs Energy to Ternary	41
2.2.3 Experimental Information	44
2.2.3.1 Ternary compounds.....	44
2.2.3.2 Thermodynamic properties	44
2.2.3.3 Phase diagrams.....	45
2.2.4 <i>Ab initio</i> Calculation on the Ternary Cu-In-Se Compounds	46
2.2.5 Establishment of Thermodynamic Descriptions	47
2.2.5.1 Sub-lattice model for different ternary compounds	47

2.2.5.2 Evaluation of Gibbs energies of end-members in the sub-lattice model	48
2.2.6 Summary.....	52
2.3 Cu-Ga-In Ternary Phase Diagram Calculation.....	58
2.3.1 Introduction	58
2.3.2 Review of Sub-binary Phase Diagrams.....	58
2.3.3 Prediction of Cu-Ga-In Ternary Phase Diagrams	61
2.3.4 Modification of Cu-Ga-In Ternary Phase Diagrams	65
2.3.5 Summary and Future Work	67
3 METAL (CU, IN, GA)-SE REACTION PATHWAYS	69
3.1 Introduction.....	69
3.2 Experimental.....	71
3.2.1 Precursor Preparation	71
3.2.2 <i>In situ</i> high-temperature X-ray diffraction	73
3.3 Cu-Se Binary Formation.....	74
3.3.1 Glass/Cu/Se Precursor	74
3.3.2 Glass/Cu-Se Precursor	75
3.4. In-Se Binary Formation	78
3.4.1 Glass/In/Se precursor.....	78
3.4.2 Glass/In-Se Precursor	80
3.5 Ga-Se Binary Formation.....	82
3.5.1 Glass/Ga/Se Precursor	82
3.5.2 Glass/Ga-Se Precursor	83
3.6 Summary.....	85
4 CUINSE2 FORMATION PATHWAYS AND KINETICS	86
4.1 Introduction.....	86
4.2 Glass/In ₂ Se ₃ /CuSe Precursor	88
4.2.1 Precursor Preparation	88
4.2.2 Temperature Ramp Annealing	90
4.2.3 Isothermal Annealing	91
4.3 Glass/InSe/Cu-Se Precursor.....	96
4.3.1 Precursor Preparation	96
4.3.2 Temperature Ramp Annealing	97
4.4 Glass/CuSe/In-Se Precursor.....	99
4.4.1 Precursor Preparation	99
4.4.2 Temperature Ramp Annealing	100
4.5 Glass/Mo/Cu-In-Se Precursor.....	101
4.5.1 Precursor Preparation	101
4.5.2 Temperature Ramp Annealing	102
4.5.3 Isothermal Annealing	102
4.6 Selenization of Glass/Mo/Cu-In Precursor.....	105
4.6.1 Precursor Preparation	105
4.6.2 Selenization Chamber Design	107

4.6.3 Temperature Ramp Selenization	108
4.6.4 Isothermal Selenization	110
4.7 Summary.....	115
5 CUGASE2 FORMATION PATHWAYS AND KINETICS	120
5.1 Introduction.....	120
5.2 Glass/GaSe/CuSe Precursor.....	121
5.2.1 Precursor Preparation	121
5.2.2 Temperature Ramp Annealing	122
5.2.3 Isothermal Annealing	122
5.2.4 TEM-EDS Analysis.....	133
5.3 Glass/Mo/Cu-Ga-Se Precursor	135
5.3.1 Precursor Preparation	135
5.3.2 Temperature Ramp Annealing	136
5.3.3 Isothermal Annealing	138
5.4 Selenization of Glass/Mo/Cu-Ga Precursor.....	143
5.4.1 Precursor Preparation	143
5.4.2 Selenization Chamber Design	143
5.4.3 Temperature Ramp Selenization	145
5.4.4 Isothermal Selenization	147
5.5 Summary.....	152
6 CU(IN,GA)SE2 FORMATION FROM SELENIZATION OF METALLIC CU-GA-IN	155
6.1 Introduction.....	155
6.2 Experimental.....	156
6.3 Results and Discussion	157
6.3.1 Precursor Characterization	157
6.3.2 Temperature Ramp Annealing	158
6.3.3 Isothermal Annealing	163
6.3.4 Comparison Between CIS, CGS, and CIGS Formation	167
6.4 Summary.....	169
7 DIFFUSION MODELING OF Cu-In SELENIZATION	170
7.1 Introduction.....	170
7.2 Multi-component Diffusion Theory	171
7.3 Thermodynamic and Kinetic Basis for DICTRA	174
7.4 Diffusion Modeling of Selenization of Cu-In Precursor	176
7.4.1 Kinetic Experiments	176
7.4.2 Diffusion Modeling Using DICTRA	178
7.5 Summary.....	181

8 DEFECT CHARACTERIZATION BY DEEP LEVEL TRANSIENT SPECTROSCOPY (DLTS) TECHNIQUE	182
8.1 Introduction.....	182
8.2 Operation Principle of DLTS Technique.....	183
8.3 Equipment Description of UF-DLTS System.....	185
8.4 DLTS Measurement of CIGS Cells.....	189
8.4.1 DLTS Scan	189
8.4.2 Estimation of Trap Activation Energy and Capture Cross-section	191
8.4.3 Estimation of Trap Density	192
8.5 Summary.....	195
9 CONCLUSIONS AND FUTURE WORK.....	198
APPENDIX EXPLORATION OF MEDICI SIMULATION OF CIGS SOLAR CELLS	201
A.1 Overview of Medici	201
A.2 Non-uniformity of Doping Concentration	202
A.3 Medici Simulation of C-V Profile	203
A.4 Medici Simulation on Grading Band Gap CIGS Cell.....	206
LIST OF REFERENCES	209
BIOGRAPHICAL SKETCH	218

LIST OF TABLES

<u>Table</u>	<u>page</u>
1-1 Structural and electrical properties of CuInSe ₂ and CuGaSe ₂ with chalcopyrite structure.....	8
2-1 Thermodynamic parameters in Cu-Se system.....	29
2-2 Parameters for functions used in Table 2-1 in the form of equation (2-1).....	30
2-3 Phase equilibria in the Cu-Se system	31
2-4 Experimental and calculated standard formation enthalpies ($\Delta H_f^\circ_{298.15K}$) and entropies ($^{\circ}S_{298}$) of Cu-Se compounds.....	32
2-5 The experimental values of the standard formation enthalpy ($\Delta H_{f,298K}^0$) and energy ($\Delta E_{f,0}^0$) of α -CuInSe ₂	45
2-6 Parameters used to calculate ΔE^f of CuIn ₃ Se ₅ and CuIn ₅ Se ₈	50
2-7. Experimental results of phase relationships of Cu-Ga-In ternary system	66
4-1 The composition of the as-deposited glass/Mo/Cu-In precursor films as determined by EPMA scans along the surface	107
5-1 Estimated kinetic parameters for the CuGaSe ₂ formation from glass/GaSe/CuSe bilayer precursor films	130
5-2 Estimated kinetic parameters for the CuGaSe ₂ formation from glass/Mo/Cu-Ga-Se precursor films.....	141
5-3 Estimated kinetic parameters for the CuGaSe ₂ formation from selenization of glass/Mo/Cu-Ga precursor films.....	148
6-1 Estimated kinetic parameters for the CIGS formation from selenization of glass/Mo/Cu-Ga-In precursor films	166
6-2 Comparison of reaction pathways and kinetics for CIS, CGS and CIGS formation from selenization of metallic precursors.....	167
8-1 Equipment specification of UF-DLTS system.....	189

8-2	DLTS scan results of EPV-CIGS cells at a reverse bias (V_R) of 0.4 V, a trap-filling pulse of 0.8 V, and a saturation pulse width of 10 ms.....	191
8-3	Trap density calculation from DLTS analysis of EPV-CIGS cell.	194
8-4	Summary of DLTS analysis for EPV-CIGS cell.....	196
8-5	Summary of DLTS analysis for EPV-CIGS cell.....	197
9-1	Summary of reaction kinetics of $\text{Cu}(\text{In}_x\text{Ga}_{1-x})\text{Se}_2$ formation from different precursor structures	199
A-1	Design parameters of solar cell for Medici simulation.	203
A-2	Basic design parameters of solar cell for Medici simulation	206
A-3	Deep defect parameters of solar cells for Medici simulation.....	207
A-4	Comparison of performance parameters of CIGS cells simulated by Medici.....	208

LIST OF FIGURES

<u>Figure</u>	<u>page</u>
1-1 Solar spectrum of AM0 and AM1.5 based on ASTM G173.....	3
1-2 Schematic diagram of light-induced electron-hole creation in a p-n junction photodiode.....	4
1-3 I-V characteristic of a solar cell under illumination.....	4
1-4 Efficiency trend of thin film solar cells (CuInSe ₂ , CdTe and a-Si). Taken from Zweibel	6
1-5 The schematic structure of a conventional CIGS solar cell.	7
1-6 Tetragonal unit cell of a Cu(In,Ga)Se ₂ chalcopyrite lattice.	8
1-7 Schematic diagram of NREL three-stage process for CIGS fabrication.....	9
1-8 Schematic diagram of the two-step process for CIGS fabrication.....	10
1-9 Schematic diagram of ISET non-vacuum process for CIGS fabrication.	12
1-10 Schematic diagram of MEE reactor system.	13
1-11 Schematic top view of MEE reactor.	14
1-12 The LabVIEW-based HMI system of MEE reactor.....	16
2-1 Calculated Cu-Se phase diagram.....	33
2-2 Comparison between the calculated Cu-Se phase diagram and experimental data .	34
2-3 Comparison between the calculated chemical potential of Cu and experimental data in $\beta\text{-Cu}_{2-x}\text{Se}$ phase	35
2-4 Comparison between the calculated chemical potential of Se and experimental data at 1373 and 1473K.....	36
2-5 Comparison between the calculated Se ₂ partial pressure and experimental data in Cu-Se system.....	37

2-6	Comparison between the calculated heat capacity of each phase and experimental data for Cu ₂ Se	38
2-7	Comparison between calculated heat capacity of each phase and experimental data for CuSe	39
2-8	Geometrical construction of (a) Kohler and (b) Muggianu model.....	42
2-9	Geometrical construction of Toop model.....	43
2-10	Pseudo-binary In ₂ Se ₃ -Cu ₂ Se phase diagram	53
2-11	Optimized Gibbs energy α-CuInSe ₂ , β-CuIn ₃ Se ₅ and γ-CuIn ₅ Se ₈ compared with that estimated from EMF experiments and ab initio calculation	54
2-12.	Optimized Gibbs energy of formation of α-CuInSe ₂ , β-CuIn ₃ Se ₅ and γ-CuIn ₅ Se ₈ compared with that estimated from EMF experiments and ab initio calculation.....	55
2-13	Isothermal sections of Cu-In-Se at 500 °C. (a) Calculation, (b) Experimental evaluation	56
2-14	Isothermal sections of Cu-In-Se at 800 °C. (a) Calculation, (b) Experimental evaluation	56
2-15	Isothermal sections of Cu-In-Se at 900 °C. (a) Calculation, (b) Experimental evaluation	57
2-16	Calculated phase diagram of Cu-In binary system.....	59
2-17	Calculated phase diagram of Cu-Ga binary system	60
2-18	Calculated phase diagram of Ga-In binary system.....	60
2-19	Isothermal section (500 °C, 1atm) of the Cu-Ga-In ternary phase piagram based on the Muggianu's equation	62
2-20	Isothermal section (500 °C, 1atm) of the Cu-Ga-In ternary phase piagram based on the Muggianu's equation for the range of 0 < x(In) < 0.2 and 0.2 < x(Ga) < 0.4	63
2-21	Isothermal section (350 °C, 1atm) of the Cu-Ga-In ternary phase piagram based on the Muggianu's equation	63
2-22	Isothermal section (800 °C, 1atm) of Cu-Ga-In ternary Phase Diagram based on the Muggianu's equation	64
2-23	Vapor pressure as a function of temperature in the Cu-Ga-In mixture (Cu:Ga:In = 1:1:1 mole ratio).....	64

2-24	Vapor pressure as a function of temperature in the Cu-Ga-In mixture (Cu:Ga:In = 2:1:1 mole ratio).....	65
2-25	Modified isothermal section (350 °C, 1atm) of the Cu-Ga-In ternary phase diagram with experimental data (symbol).....	67
2-26	Modified isothermal section (500 °C, 1atm) of the Cu-Ga-In ternary phase diagram.....	67
3-1	Phase diagram of In-Se binary system	70
3-2	Phase diagram of Ga-Se binary system.....	71
3-3	As-grown precursor structure along with overall atomic composition	72
3-4	Phase evolution of glass/Cu/Se precursor observed by <i>in situ</i> X-ray diffraction....	74
3-5	Phase evolution of glass/Cu-Se precursor observed by <i>in situ</i> X-ray diffraction.	77
3-6	Phase evolution of glass/In/Se precursor observed by <i>in situ</i> X-ray diffraction	79
3-7	Phase evolution of glass/In-Se precursor observed by <i>in situ</i> X-ray diffraction.....	81
3-8	Phase evolution of glass/Ga/Se precursor observed by <i>in situ</i> X-ray diffraction.....	82
3-9	Phase evolution of glass/Ga-Se precursor observed by <i>in situ</i> X-ray diffraction.. ..	84
4-1	TEM micrographs of as-grown glass/In ₂ Se ₃ /CuSe bilayer precursor films	89
4-2	Room temperature XRD scans and TEM micrographs of as-grown precursor films.....	89
4-3	<i>In situ</i> XRD scans during temperature ramp annealing (10 °C/min) of the glass/In ₂ Se ₃ /CuSe sample.....	90
4-4	<i>In situ</i> time-resolved XRD scans during isothermal annealing of the glass/ In ₂ Se ₃ /CuSe precursor structure at 250 °C	92
4-5	Avrami model plot for glass/In ₂ Se ₃ /CuSe precursor structure.....	94
4-6	Parabolic model plot for glass/In ₂ Se ₃ /CuSe precursor structure	95
4-7	Arrhenius plot of the parabolic rate constant for glass/In ₂ Se ₃ /CuSe precursor structure	96
4-8	Room temperature XRD scans of as-grown precursor films	97
4-9	<i>In situ</i> XRD scans during temperature ramp annealing (30 °C/min) of the glass/InSe/Cu-Se sample.	98

4-10	Room temperature XRD scans of as-grown glass/CuSe/In-Se precursor	99
4-11	<i>In situ</i> XRD scans during temperature ramp annealing (30 °C/min) of the glass/CuSe/In-Se sample.....	100
4-12	Temperature ramp annealing of glass/Mo/Cu-In-Se precursor	102
4-13	Isothermal annealing of glass/Mo/Cu-In-Se precursor at selected temperatures in the range 140 to 350 °C.....	103
4-14	CuInSe ₂ grain sizes estimated by X-ray diffraction vs. isothermal annealing temperature of glass/Mo/Cu-In-Se precursor.....	104
4-15	θ-2θ and grazing incident X-ray diffraction (at $\omega = 1.0$ and 0.5°) patterns of an as-deposited glass/Mo/Cu-In precursor film	105
4-16	Surface and cross-sectional SEM images of an as-deposited glass/Mo/Cu-In precursor film and selenized film.....	106
4-17	Selenium chamber design using PANalytical X’Pert system	107
4-18	<i>In situ</i> X-ray diffraction pattern evolution during the selenization of a glass/Mo/Cu-In precursor films in the 2θ range.....	109
4-19	<i>In situ</i> X-ray diffraction pattern evolution during the isothermal selenization of a glass/Mo/Cu-In precursor film at 280 °C	110
4-20	The Avrami model plot for α-CuInSe ₂ formation by selenization of glass/Mo/Cu-In precursor films	112
4-21	Arrhenius plot for Avrami kinetic constant for α-CuInSe ₂ formation by selenization of glass/Mo/Cu-In precursor films	112
4-22	The parabolic rate model for α-CuInSe ₂ formation by selenization of glass/Mo/Cu-In precursor films	114
4-23	The parabolic rate model for α-CuInSe ₂ formation by selenization of glass/Mo/Cu-In precursor films	114
4-24	Reaction pathway of CIS formation from In ₂ Se ₃ /CuSe precursor projected in ternary Cu-In-Se isothermal phase diagram at 500 °C.....	116
4-25	Reaction pathway of CIS formation from intimately mixed Cu-In-Se precursor projected in ternary Cu-In-Se isothermal phase diagram at 500 °C.....	117
4-26	Comparison of reaction rates for CIS formation from different precursors estimated by the parabolic and Avrami model.....	119

5-1	Room temperature XRD scans and TEM micrograph of as-grown precursor films.....	121
5-2	In situ XRD scans during temperature ramp annealing (30 °C/min) of the glass/GaSe/CuSe sample.....	123
5-3	In situ time-resolved XRD scans during isothermal annealing of the glass/GaSe/CuSe precursor structure at selected temperatures	125
5-4	Fractional reaction (α) with respect to time (t) at selected isothermal temperatures	126
5-5	Parabolic rate model plot for glass/GaSe/CuSe precursor structure	127
5-6	Arrhenius plot of the Parabolic rate constant for glass/GaSe/CuSe precursor structure	127
5-7	Fractional reaction (α) with respect to time ($t+t^*$) and Avrami model plot at selected isothermal temperatures	130
5-8	Modified Avrami model plot for glass/GaSe/CuSe precursor structure	131
5-9	Arrhenius plot of the Avrami model rate constant for glass/GaSe/CuSe precursor structure	132
5-10	TEM-EDS analysis on (a) as-grown glass/GaSe/CuSe precursor, (b) sample annealed at 300 °C, for 30 min.....	134
5-11	Room temperature X-ray diffraction of (a) as-grown glass/Mo/Cu-Ga-Se precursor, and (b) thermally annealed CuGaSe ₂	135
5-12	In situ XRD scans during temperature ramp annealing (30 °C/min) of the glass/Mo/Cu-Ga-Se sample	137
5-13	<i>In situ</i> time-resolved XRD scans during isothermal annealing of the glass/Mo/Cu-Ga-Se precursor structure at selected temperatures.....	139
5-14	Comparison of fractional reaction for isothermal experiments and modified Avrami model prediction	140
5-15	Modified Avrami model plot for glass/Mo/Cu-Ga-Se precursor structure	141
5-16	Arrhenius plot of the Avrami model rate constant for glass/Mo/Cu-Ga-Se precursor structure	142
5-17	Room-temperature XRD scans of Cu-Ga as-grown precursor and selenized CuGaSe ₂ film.....	144

5-18	X-ray sample holder with a graphite dome for selenization of Cu-Ga precursor films.....	144
5-19	In situ XRD scans during temperature ramp selenization of Cu-Ga/Mo/glass precursor.....	146
5-20	In situ XRD scans during isothermal selenization of Cu-Ga/Mo/glass precursor at four different temperatures	147
5-21	Comparison of fractional reaction for isothermal experiments and modified Avrami model prediction	149
5-22	Modified Avrami model for the CuGaSe ₂ formation by selenization of glass/Mo/Cu-Ga precursor	150
5-23	Arrhenius plot of the Avrami model rate constant for the CuGaSe ₂ formation by selenization of glass/Mo/Cu-Ga precursor	150
5-24	Comparison of reaction rates for CIS and CGS formation from different precursors estimated by the parabolic model	154
5-25	Comparison of reaction rates for CIS and CGS formation from different precursors estimated by the Avrami model.....	154
6-1	Room-temperature XRD scans of glass/Mo/Cu-Ga-In as-grown precursor	157
6-2	Surface (top) and cross-sectional (bottom) SEM images of (a) an as-deposited glass/Mo/Cu-Ga-In precursor film and (b) selenized film	158
6-3	Temperature ramp HT-XRD scans with a bare glass substrate.	159
6-4	In situ XRD scans during temperature ramp selenization of Cu-Ga-In/Mo/glass precursor.....	160
6-5	Cell refinement for room temperature X-ray diffraction data of a selenized CIGS sample using the tetragonal, I-42d (122) cell type	162
6-6	Lattice constants (a, c) vs. Ga composition of CIGS	162
6-7	In situ XRD scans during isothermal selenization of glass/Mo/Cu-Ga-In precursor at four different temperatures	164
6-8	Avrami model and corresponding Arrhenius plot (inset) for CIGS formation by selenization of glass/Mo/Cu-Ga-In precursor	165
6-9	Arrhenius plot for Avrami rate constant for CIGS formation by selenization of glass/Mo/Cu-Ga-In precursor.....	165

6-10	Comparison of fractional reaction for isothermal experiments and Avrami model prediction.....	166
6-11	Comparison of reaction rates for selenization of different metallic precursors estimated by the Avrami model.	168
7-1	The CIS thickness vs. time obtained from kinetic experiment.	176
7-2	The schematic diagram of the simplified reaction of CuInSe ₂ formation from selenization of Cu-In precursor.....	177
7-3	The modified Cu-In phase diagram including metastable CuIn phase	179
7-4	The comparison of CIS growth rates between the DICTRA prediction and experiments	180
8-1	Schematic diagram of UF-DLTS system.	186
8-2	Schematic top view of LN2 cryostat in the DLTS system.	186
8-3	Simplified wiring diagram of UF-DLTS system.....	187
8-4	UF-DLTS system.	188
8-5	DLTS scans for the EPV-CIGS cell at different delay times (0.02 to 1.0 ms).	190
8-6	Arrhenius plot of DLTS scans for EPV-CIGS cells.....	192
8-7	Capacitance-temperature scan for a EPV-CIGS cell at a reverse bias of 0.4 V....	193
8-8	Capacitance-voltage (C-V) measurement for EPV-CIGS at different temperatures.	194
A-1.	A band- gap and doping profile for CIS-graded solar cell.	204
A-2	Absorption coefficient profiles for the materials used in Medici simulation.....	205
A-3	Medici simulation results on C-V profile for the uniform doping and graded doping CIS cells.	205
A-4	Current- Voltage (C-V) plots for CIGS cells predicted by Medici simulation.	208

Abstract of Dissertation Presented to the Graduate School
of the University of Florida in Partial Fulfillment of the
Requirements for the Degree of Doctor of Philosophy

STUDY OF REACTION PATHWAYS AND KINETICS IN Cu<sub>(In_xGa_{1-x})Se₂} THIN
FILM GROWTH</sub>

By

Woo Kyoung Kim

August 2006

Chair: Timothy James Anderson

Major Department: Chemical Engineering

Assessment of the thermochemistry and phase equilibrium data of the Cu-Se binary and Cu-In-Se ternary systems was performed to suggest the phase diagrams. Sub-lattice models were used to describe the Gibbs energy of the condensed solutions. Coupled with previously reported assessments, the Cu-Ga-In phase diagram was predicted by extrapolation of the Cu-Ga, Cu-In and Ga-In binary systems. Ternary interaction parameters were and subsequently added to achieve consistency with recent ternary experimental data.

In situ high-temperature X-ray diffraction technique was used to investigate the reaction pathways and phase evolution of binary Cu-Se, In-Se and Ga-Se compounds prepared as an intimate mixture or bi-layer. The results revealed that the overall phase transformation of binary metal (Cu, In and Ga)-Se compounds qualitatively follows the sequence predicted by the phase diagram, but the detailed reaction path of each binary

compound depends on the as-deposited precursor structure and phases produced during the deposition process.

Reaction pathways and kinetics of polycrystalline α -CuInSe₂ (CIS), CuGaSe₂ (CGS), and Cu(In,Ga)Se₂ (CIGS) formation were also systematically investigated using *in situ* high-temperature X-ray diffraction during thermal annealing of stacked bilayer and intimately mixed monolayer precursors, and selenization of elementally mixed metal precursors. The lowest temperature to form CIS was identified as \sim 140 °C, which was achieved by thermal annealing of intimately mixed Cu-In-Se precursor. Formation temperatures of CGS (i.e. 260 to 300 °C) were relatively higher than those of CIS (i.e. 140 to 250 °C) and CIGS (i.e. 260 °C). MoSe₂ formation was always clearly observed during selenization and for CIS, only after complete formation of CIS. Quantitative analysis of time-resolved X-ray diffraction data by adopting the Avrami and parabolic rate models provided reaction order, rate constant, and activation energy.

DICTRA simulation of CIS formation by selenization of a Cu-In precursor was performed using the kinetic results obtained by time-resolved, *in situ* HTXRD experiments along with the thermodynamic description of the CIS system. The target reaction system was simplified as a pseudo-binary reaction, CuIn + 2Se \rightarrow CuInSe₂, for which the reliable mobility parameters for Se transport in CIS were obtained.

CHAPTER 1 INTRODUCTION

1.1 Photovoltaic Devices

Semiconductor photonic devices generally fall into one of three functional categories. One group of photonic devices converts electrical energy into photo-energy such as light emitting diodes (LEDs) and laser diodes, while the other two groups of photonic devices convert photo-energy into electrical energy. If the purpose of photo-to-electrical energy conversion is to detect or determine information about the photon energy, the device is called a photodetector. If the purpose of energy conversion is to produce electrical power, the device is called a photovoltaic device or solar cell [Pie96].

A solar cell converts sunlight into electricity through the photovoltaic effect which was first observed by nineteen-year-old Edmund Becquerel, a French experimental physicist, in 1839 while experimenting with an electrolytic cell composed of two metal electrodes. He found that certain materials would produce small amounts of electric current when exposed to light [Bec39, M  l93].

Solar cell technology and its application have been enormously developed during the last four decades. Silicon was the first commercial solar cell material and is still most widely used in solar cell application. The potential compound semiconductors such as GaAs, CdTe, InP, CdS and Cu(In,Ga)Se₂ cell have been actively developed [M  l93].

Photovoltaics as one of the renewable energy technologies is a lot friendlier to the environment than conventional energy technologies, which mainly rely on fossil fuels. Fossil fuels contribute significantly to many environmental problems, e.g., greenhouse

gases, air pollution, and water and soil contamination. The performance of a solar cell is measured in terms of its efficiency converting sunlight into electricity. Only sunlight with certain energies (or wavelengths) will work efficiently to create electricity, and much of it is reflected or absorbed by the materials that make up the cell. Because of this, a typical commercial solar cell has an efficiency of 15%—about only one-sixth of the sunlight striking the cell generates electricity. Low efficiencies mean that larger arrays are needed and thus high manufacturing costs are required. Therefore, improving solar cell efficiencies while holding down the manufacturing cost is an important goal of the solar cell industry and university research support [Nre06].

1.2 Fundamental Physics of Solar Cells

For the photovoltaic conversion, it is necessary to separate the light-induced electrons and holes, and collect them at external contacts. This requires an internal electric field, which can be generated by homojunctions and heterojunctions of semiconductors, e.g., p-n junction, Schottky barrier, and MIS (metal-insulator-semiconductor) structure. Currently, p-n junction solar cells are the most widely used devices for photovoltaic energy conversion.

The solar radiation reaching the earth has a spectral distribution due to partial reflection by atmosphere and partial transmittance to surface of the earth. The radiation distribution outside the atmosphere is similar to that of a “black body” radiation at ~5800K, while the atmosphere at the surface of the earth selectively absorbs the radiation at certain wavelengths. As shown in Figure 1-1, the standard solar spectra (e.g., AM0 and AM1.5) defined by air mass (AM) are important in photovoltaic application. The AM0 represents solar spectrum outside of the atmosphere and AM1.5 corresponds the spectrum at sea level. More generally, the AM_x is expressed by $x = 1/\cos(\theta_z)$, where θ_z is

the zenith angle of the sun. When the sun is located at the zenith of the receiving area (i.e., $\theta_z=0$ and thus $x=1$), AM1 would be spectrum received at sea level on a clear day with the sun at its zenith. Generally, the AM1.5 spectrum, which is equivalent to a zenith angle of 48.19° , is accepted as a reference spectrum in PV application.

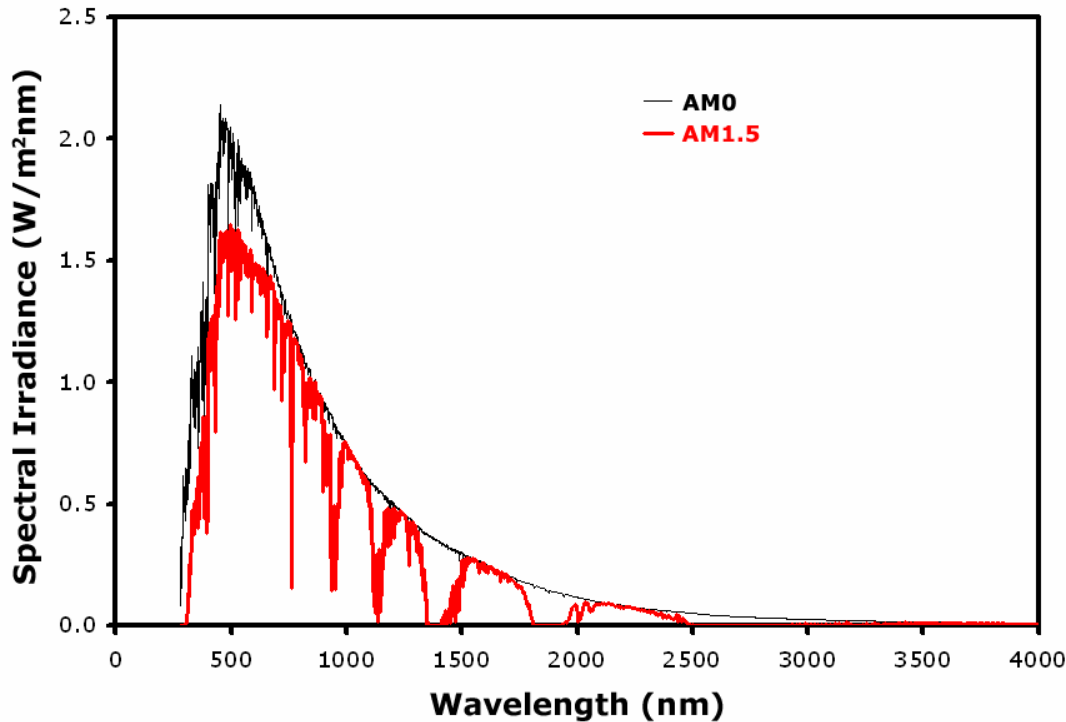


Figure 1-1. Solar spectrum of AM0 and AM1.5 based on ASTM G173.

Electron-hole pairs in a p-n junction diode are created by absorption of light and then minority carriers of each side move to a junction, as shown in Figure 1-2. At thermodynamic equilibrium with no current flows, minority carriers reaching the edges of the depletion region are immediately swept out by the electric field (i.e., built-in bias) to the opposite side of the junction, which consequently yields a current flow in the reverse direction of built-in bias.

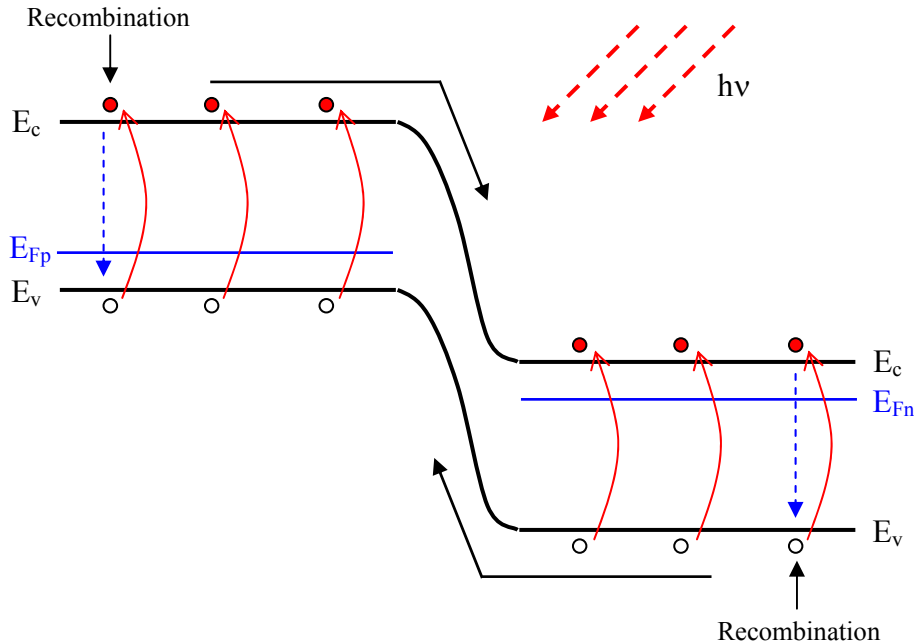


Figure 1-2. Schematic diagram of light-induced electron-hole creation in a p-n junction photodiode.

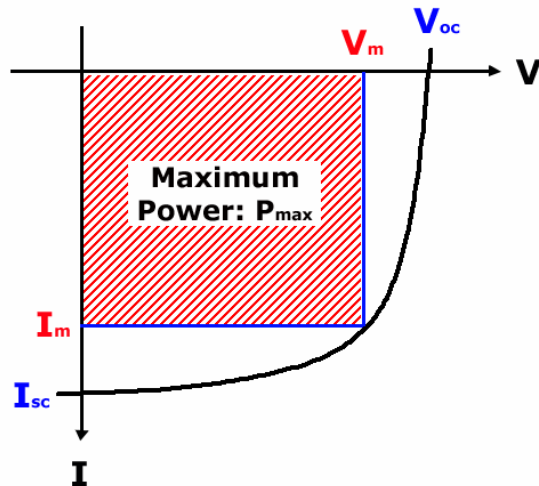


Figure 1-3. I-V characteristic of a solar cell under illumination.

Several solar cell parameters under illumination are graphically defined in I-V characteristics, as shown in Figure 1-3. First, V_{oc} (open circuit voltage) and I_{sc} (short circuit current) are the maximum voltage and current that can be supplied or derived by the cell for applied illumination conditions, respectively. Next, the I_m and V_m are the

current and voltage to yield the maximum power rectangle, i.e., $P_{max} = I_m V_m < I_{sc} V_{oc}$.

Finally, the fill factor (*F.F.*) and power conversion efficiency (η) are often used to represent the solar cell performance and are determined by

$$FF \equiv \frac{P_{max}}{I_{sc}V_{oc}} = \frac{I_m V_m}{I_{sc}V_{oc}} \quad (1-1)$$

$$\eta \equiv \frac{P_{max}}{P_{in}} = \frac{I_m V_m}{P_{in}} = \frac{FF \cdot I_{sc}V_{oc}}{P_{in}} \quad (1-2)$$

where P_{in} is the incident photon energy per second. The above relationships, equation (1-1) and (1-2), demonstrate that solar cell efficiency (η) is proportional to I_{sc} , V_{oc} and fill factor. However, considering the general expressions for V_{oc} and I_{sc} , the fundamental material parameters that determine the efficiency of the solar cell are the lifetime and mobility of the minority carriers, and the interface recombination velocities. These parameters are not independent from each other, and are controlled by the structural and electrical properties of the solar cell.

1.3 Why CIGS ?

Silicon was the first commercial solar cell material and is still most generally used in solar cell applications. However, silicon is not the ideal material for solar cells because it has low light absorption efficiency as well as an indirect band gap. A large number of binary, ternary, and quaternary compound semiconductors have been investigated for their potential as high performance and inexpensive solar cells that can serve as an alternative to silicon-based solar cells such as single-crystalline, polycrystalline, and amorphous silicon. One of the most promising strategies to lower solar cell manufacturing costs will be the thin-film photovoltaic technology in which thin absorber films (typically $< 5 \mu\text{m}$) are deposited on inexpensive substrates such as

polymer. Chalcopyrite α -CuInSe₂ (CIS) and its alloys with Ga or S are the most promising candidates as an absorber for high efficiency thin film solar cells. Recently, the development of CIGS has made rapid progress, and conversion efficiency of 19.5% (AM 1.5G) has been achieved on a laboratory scale [Con05]. The efficiencies of three conventional thin film solar cells (i.e., CuInSe₂, CdTe and a-Si) are compared in Figure 1-4, which suggests that CIS-based cell is the most suitable for high performance thin film solar cells. Furthermore, CuInSe₂ compound has many advantages as a solar cell absorber, for instance, a high absorption coefficient ($\sim 10^5$ cm⁻¹), excellent radiation resistance, direct band gap and wide range of stoichiometry.

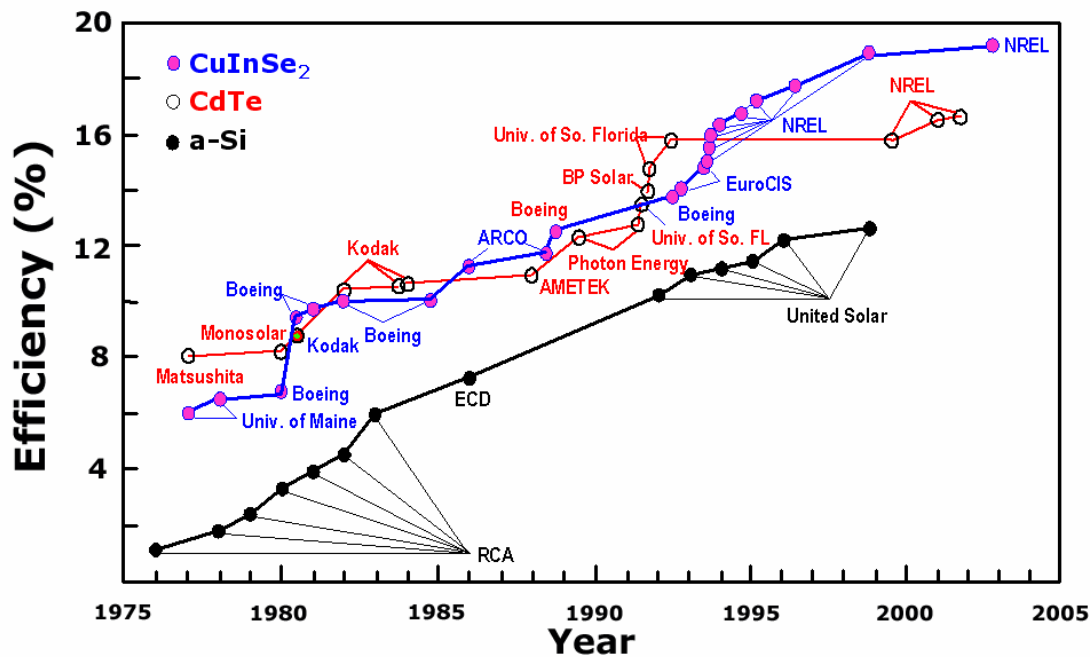


Figure 1-4. Efficiency trend of thin film solar cells (CuInSe₂, CdTe and a-Si). Taken from Zweibel [Zwe05].

The schematic structure of a typical CIGS-based thin film solar cell is shown in Figure 1-5. In this structure, a soda-lime glass (SLG) is widely used as a substrate. In a soda-lime glass, the out-diffused Na ion is believed to increase the electrical conductivity and to reduce the grain boundary energy barrier by either forming Na_{In} defects or

removing mid-gap traps [Wei99]. However, Na₂Se is believed to cause a poor adhesion between CIGS and Mo [Hua03]. The recent trend includes flexible substrates such as polymer and metal foils because the flexibility of substrates allows a potential application to portable solar cells, and a roll-to-roll manufacturing, which promises substantial cost reduction. The Mo is a back contact electrode, which is generally deposited by sputtering. Polycrystalline CIGS acts as a p-type light absorber, and more importantly forms a p-n junction with an n-type CdS buffer layer. The ZnO (or ZnO:Al) transparent conducting film serves as a window layer, and anti-reflection (AR) coating (e.g., MgF₂) improves the light absorption efficiency. As a front contact material, a bilayer Ni/Al grid is used.

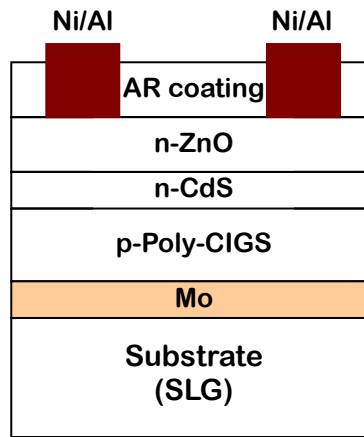


Figure 1-5. The schematic structure of a conventional CIGS solar cell.

CuInSe₂ crystallizes in a diamond-like lattice structure with a face-centered tetragonal unit cell that is referred to a chalcopyrite structure as pictured in Figure 1-6. Each selenium atom serves as the center of a tetrahedron of two Cu and two In atoms, and each metallic atom is surrounded by a tetrahedron of selenium atoms. In this structure, each anion (selenium) has two Cu and two In (or Ga) cations as nearest neighbors, whereas each anion has four cations nearly randomly as nearest neighbors in zinc-blende structure. While the two lattice constants of the chalcopyrite structure (i.e., x-

and y-direction) are the same as the lattice constant of the zinc blende structure, the lattice constant of z-direction is a double of that of zinc blende structure.

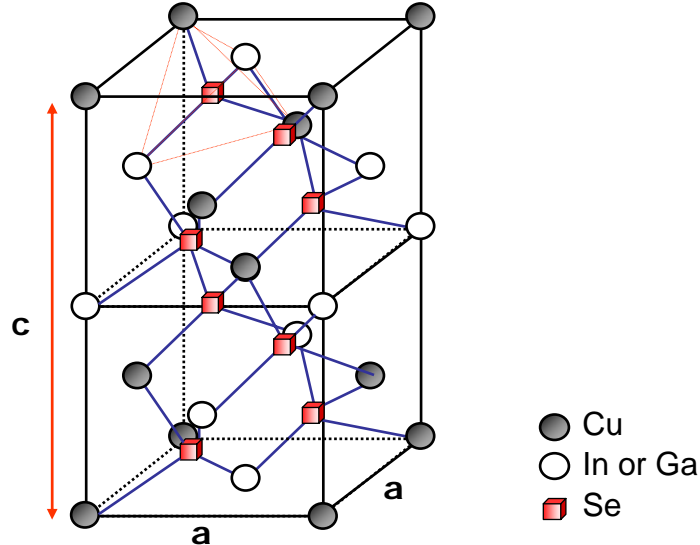


Figure 1-6. Tetragonal unit cell of a Cu(In,Ga)Se₂ chalcopyrite lattice.

Typical lattice constants and electrical properties for CuInSe₂ and CuGaSe₂ with a chalcopyrite structure are summarized in Table 1-1.

Table 1-1. Structural and electrical properties of CuInSe₂ and CuGaSe₂ with chalcopyrite structure.

	Lattice constants		Bandgap energy Eg (eV)	Absorption coefficient α (cm ⁻¹)
	a (nm)	c (nm)		
CuInSe ₂	0.5784	1.1614	1.04	$\sim 1 \times 10^5$
CuGaSe ₂	0.5596	1.1002	1.68	$> 3 \times 10^4$

1.4 CIGS Deposition Processes

Almost every method of semiconductor processing has been tried to synthesize CIGS compound, but only a few of them were successful in producing a high quality CIGS absorber for thin film photovoltaic cell. In this chapter, the widely employed techniques to fabricate high quality CIGS films and the recent efforts to develop low-cost non-vacuum processes are summarized.

A sophisticated vacuum co-evaporation process is characterized by simultaneous exposure of high-temperature substrate to Cu, Ga, In and Se vapor fluxes, and known to provide the best control of composition through precise control of the temperature and thus each elemental flux. Even though several co-evaporation methods including simple single-layer and bilayer processes are available, an NREL 3-stage process using physical vapor deposition (PVD) system currently holds the best CIGS cell efficiency of 19.5 % [Con05].

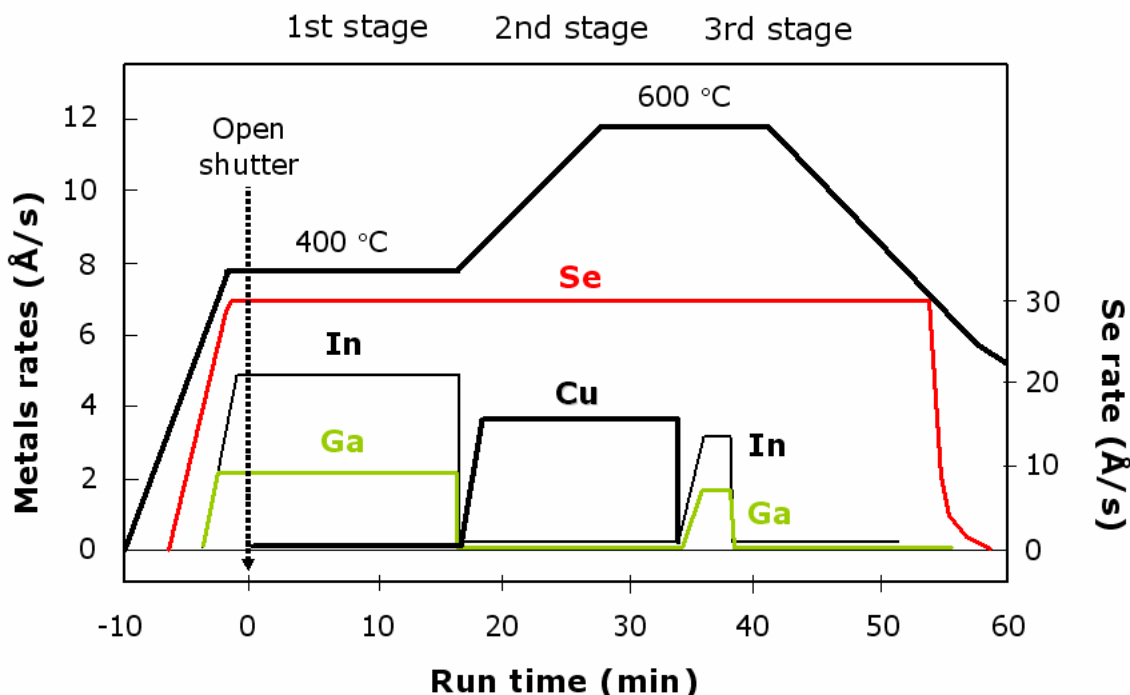


Figure 1-7. Schematic diagram of NREL three-stage process for CIGS fabrication.
(Provided by Dr. Noufi in NREL)

The schematic diagram of the NREL three-stage process is illustrated in Figure 1-7. During the first stage, the In, Ga and Se are deposited to form the sesquiselenide, $(In,Ga)_2Se_3$. After the second stage of only Cu+Se flux, a Cu-rich CIGS is produced along with a secondary Cu-Se binary compound (e.g., conducting Cu_2Se), which is known to facilitate the CIGS grain growth. Finally, a slightly Cu-poor CIGS forms by

adding more indium and gallium at third stage. The three-stage PVD process, however, has not been successfully implemented in industrial large-area module production mainly due to high production cost caused by high-vacuum and high-temperature operation conditions. Furthermore, co-deposition technique has a limitation in achieving uniformity in large scale deposition.

Another conventional process to produce a device-quality CIGS absorber is called the two-step method, which has been successfully employed in a commercial line of Shell Solar and Showa Shell. The commercialized two-step process consists of the deposition of a metallic precursor (e.g., Cu/In/Ga) followed by subsequent selenization, as shown in Figure 1-8. Traditionally, the metal precursors are prepared by sputtering and then selenized at high temperature ($\sim 600^\circ\text{C}$) in a reactive H_2Se or Se vapor ambient. However, since H_2Se gas and Se vapor are extremely toxic, a safer selenization method is required.

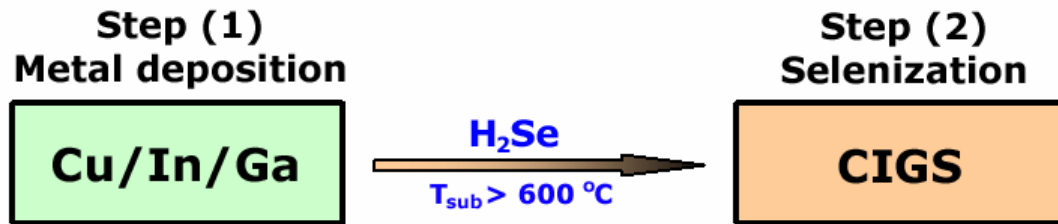


Figure 1-8. Schematic diagram of the two-step process for CIGS fabrication.

Palm *et al.* suggested the deposition of a selenium layer on metal precursor by evaporation followed by a rapid thermal annealing [Pal03]. As a novel CIS process, Bindu *et al.* deposited selenium films on glass substrate using chemical bath deposition (CBD) at room temperature, totally avoiding use of H_2Se or Se vapor [Bin03]. Indium and copper were then deposited on the selenium layer to yield glass/Se/In/Cu or glass/Se/Cu/In precursor by sequential vacuum evaporation. Finally, the stacked layer

precursors were thermally annealed in high vacuum (10^{-5} mbar) at the temperature range 423 to 673K.

As stated in the previous section, CIGS is similar in its performance and stability to currently dominant crystalline silicon devices, but their market share is still quite low (<1%) mainly due to high production cost. Therefore, the development of more cost effective process, preferably based on low temperature and non-vacuum technique, is essential to successful commercialization of CIGS-based thin film solar cells. Example approaches include electrodeposition and screen printing. Precursor layers obtained by these techniques, however, have not exhibited electronic properties suitable for commercial solar cells, and also require additional thermal treatments to optimize cell performance parameters [Gan06].

Electrodeposition has been considered as a suitable process for large-scale industrial processes, requiring low energy consumption and low capital investment [Zwe99, Bha00]. Two basic methods of electrodeposition to form CIS or CIGS have been explored with appreciable results. One method represents the co-deposition all elements, i.e., Cu, In, Ga and Se [Cal98, Bha98, Tau05] and the other includes the deposition of metallic precursors followed by subsequent selenization [Pro96, Gan06]. Basically, electrodeposition of Cu-In-Ga-Se alloys is carried out potentiostatically on Mo-coated substrates from aqueous solutions containing complex agents, e.g., CuCl, InCl_3 , $\text{Ga}(\text{NO}_3)_3 \cdot 7\text{H}_2\text{O}$, H_2SeO_3 and KSCN [Tau05, Gan06]. A small area efficiency of over 10% was obtained by electrodeposition of quaternary CIGS followed by subsequent thermal annealing [Gui03]. By adding additional indium and gallium, and applying high-temperature annealing in vacuum, an efficiency of 15.4% was reported [Bha00]. The

stability of the chemical solution, large area non-uniformity and high deposition rate remain a significant challenge [Kae04].

International Solar Electric Technology, Inc. (ISET) employed an interesting non-vacuum process for low cost mass production for CIGS solar cells. ISET uses a coating technology of water based precursor inks made of nano-particles of mixed oxides of Cu, In and Ga that are converted to yield CIGS absorber layers of desired electronic properties. The schematic process diagram is shown in Figure 1-9.

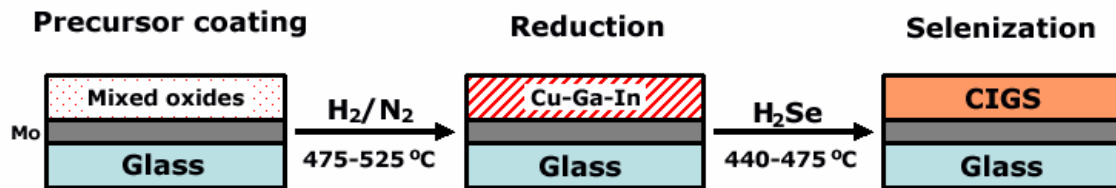


Figure 1-9. Schematic diagram of ISET non-vacuum process for CIGS fabrication.

A water based precursor ink is coated on Mo-coated glass substrate using a ‘knife blade’ coating technique [Kap01, Kap03]. After drying, a layer of mixed oxides with a typical thickness of around 2.5~3.0 μm is left on the glass/Mo substrate. This oxide layer is then reduced under a forming gas mixture of H_2 and N_2 at temperatures in the range 475 to 525 °C to obtain a compact coating of metal alloys of Cu-Ga-In. Finally, this alloy coating is selenized in H_2Se gas ambient at a temperature in the range 440 to 475 °C to yield CIGS layer. They reported that small area solar cells with efficiency of ~ 13% have been fabricated by this process. The main advantages of this non-vacuum process include high compositional control of the absorber layer, high material utilization and low cost.

Spray deposition has also been taken into account as a possible non-vacuum technique that is amenable to the manufacture of large area films with low processing costs. Schulz *et al.* has employed nanoparticle-based precursors for spray deposition of CIGS materials [Sch98]. In their approach, nanoparticle colloids were prepared by reacting a mixture of CuI and/or $[\text{Cu}(\text{CH}_3\text{CN})_4](\text{BF}_4)_2$ and/or InI_3 and/or GaI_3 in pyridine with Na_2Se in methanol at reduced temperature under inert atmosphere. Colloids with the compositions $\text{CuInSe}_{2.5}$, CuSe , In_2Se_3 and $\text{Cu}_{1.10}\text{In}_{0.68}\text{Ga}_{0.23}\text{Se}_x$ were prepared by each corresponding reaction.

1.5 MEE System Description

The solar cell research group in the University of Florida has been using a Plasma Migration Enhanced Epitaxy (PMEE) reactor system to produce $\text{Cu}(\text{In},\text{Ga})\text{Se}_2$ -based absorber layers.

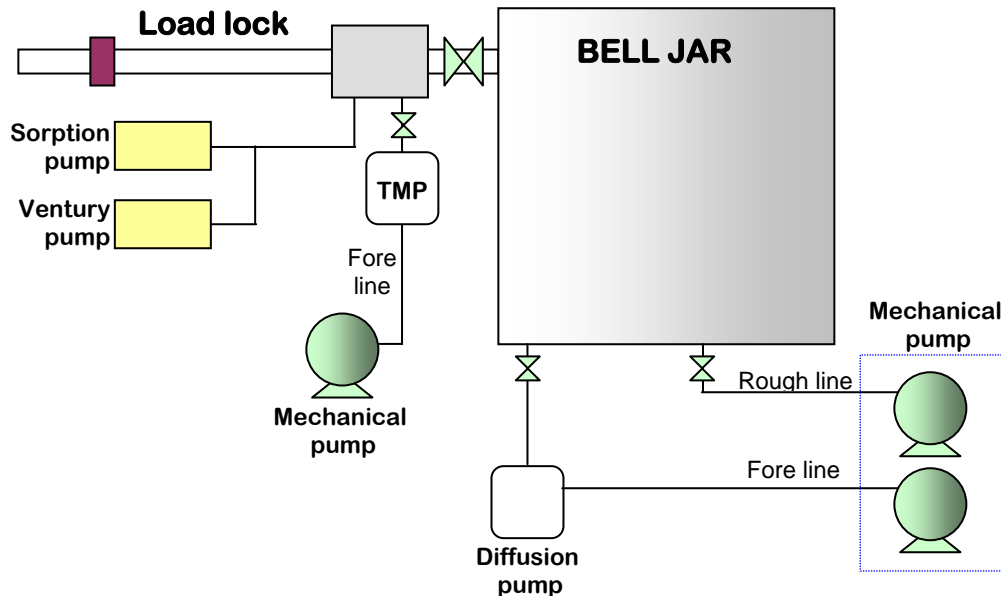


Figure 1-10. Schematic diagram of MEE reactor system.

The MEE system is essentially a modified Molecular Beam Epitaxy (MBE) system under an ultra high vacuum environment, as schematically shown in Figure 1-10. The

pumping unit is composed of three mechanical pumps, a large capacity diffusion pump, a turbo molecular pump (TMP), and a liquid-nitrogen cryogenic pump inside the system. To obtain sufficiently low pressure for opening the TMP gate valve in the load lock, the combination of a Venturi pump and a sorption pump are employed. Using the ultra high vacuum pumping system, the normal operation pressure during deposition is in the range 10^{-8} to 10^{-7} Torr, depending on the source fluxes and the temperature of the substrates.

In comparison with a traditional MBE system, which typically has a drawback of low productivity, one of outstanding advantages of the PMEE system is that it is able to process nine substrates simultaneously by employing a large rotating platen. The various types of substrates, such as 2" x 2", 1cmx1cm square substrates, or 2" diameter round wafers of Si or GaAs, can be loaded on the rotating platen.

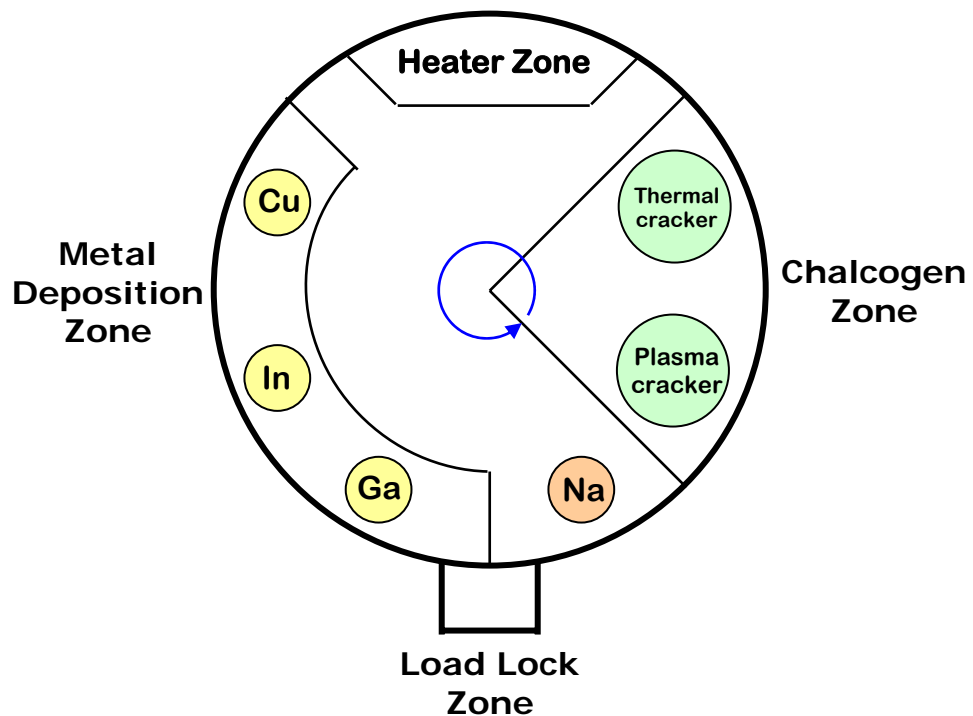


Figure 1-11. Schematic top view of MEE reactor.

The inside of the system consists of four different zones, as shown in Figure 1-11, a heater zone, a metal deposition zone, a load lock zone, and a chalcogen zone. The system

uses a rotating platen so that every substrate experiences four zones sequentially and also periodically.

In the heater zone there is a radiation heater to heat the substrates that pass through this zone. The substrates continuously cool while they pass through the other zones because they do not encounter any other heat sources in these zones.

In the metal deposition zone three different of metals, such as copper (Cu), indium (In) and gallium (Ga), can be deposited. Each metal source is evaporated from an effusion cell fitted with a single or dual filament heater. The fluxes produced by the Cu and In source are monitored on a real time basis by Electron Impact Emission Spectroscopy (EIES) sensors, which are calibrated using Quartz Crystal Monitors (QCM). In the case of Ga, the flux is monitored by QCM.

The loadlock zone is connected to a load-lock system, which is used to load and unload substrates. Therefore, during the deposition, it acts as a cooling zone where neither deposition nor heating occurs.

Finally, selenium (Se) is deposited in the chalcogen zone. Selenium vapor is known to be a mixture of low molecular weight polymers Se through Se_8 . Among them, high molecular weight species may not easily react with other species, even in high temperature conditions, so they are traditionally cracked thermally or exposed to a plasma. Unfortunately, there is no flow sensor instrumented in the system to measure a Se flux and thus the flux is estimated by measuring the film thickness after deposition. In the case of counter-clock wise rotational deposition, each substrate experiences the four steps of heating → metal deposition → cooling → selenium deposition repeatedly and each atomic layer ($\sim 0.5 \text{ nm CIGS/cycle}$) is deposited sequentially on the substrate.

To achieve the real time control of the PMEE reactor, a LabVIEW based human machine interface (HMI) system is configured as shown in Figure 1-12 [Kin02]. By using this system, one can monitor and control the important operation parameters such as the substrate heater temperature, and each source temperature, the flux of each source and even the sequence of film deposition in a central computer.

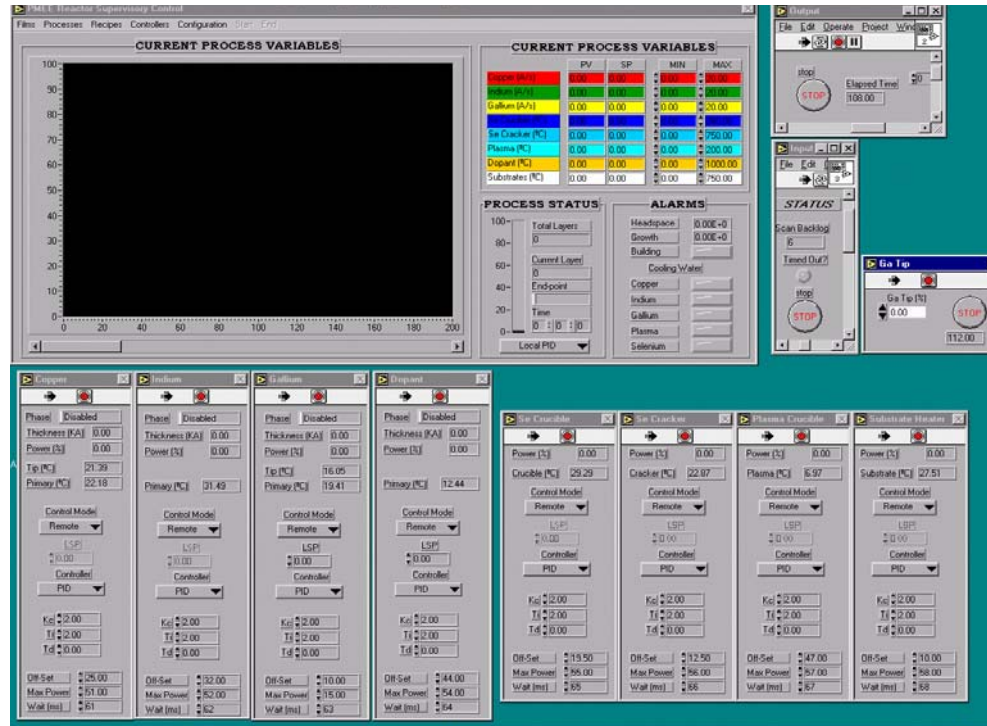


Figure 1-12. The LabVIEW-based HMI system of MEE reactor.

1.6 Statement of Thesis Work

Chalcopyrite Cu(In,Ga)Se₂ based cells have clearly demonstrated their potential as high efficiency thin film solar cells. In addition to their high cell efficiency, CIGS thin-film solar cells exhibit outstanding long-term outdoor stability, excellent radiation hardness, and the potential for use in a high performance CIGS/CGS tandem arrangement. The route used to synthesize the CIGS absorber material is critical to achieving high cell efficiency as well as high processing throughput. As summarized in Chapter 1.4, a variety of processing sequences lead to the formation of CIGS. This flexibility is partly

due to an inherent stability of α -CIGS and a rich phase diagram (α -CuInSe₂ is in equilibrium with 8 different solid phases and a Se-rich liquid) [Göd00a-c]. The complex chemistry of the quaternary CIGS system, however, has forced absorber synthesis optimization to primarily traverse an empirical path and discouraged exploration of substantially different approaches. In particular, very little is known about the fundamental thermochemistry and reaction pathways in the system.

Therefore, in this thesis, the equilibrium pathways and reaction kinetics for the formation of Cu(In_xGa_{1-x})Se₂ (CIGS), its sub-ternaries (i.e., CuInSe₂ and CuGaSe₂) and sub-binaries are systematically investigated to assist the development of a cost-effective and high performance CIGS growth process.

First, the thermodynamic description of Cu-Se binary, Cu-In-Se and Cu-Ga-In ternary systems are evaluated using the software package ThermoCalc along with available experimental information, as described in Chapter 2. This thermodynamic description is essential to the reliable calculation of chemical potentials and identification of equilibrium phases, which are combined with species diffusivities to estimate the diffusion controlled reaction rate.

Before digging into the reaction of complicated ternary (e.g., CIS and CGS) and quaternary (CIGS) compounds, the phase evolution of binary metal-selenides (e.g., Cu-Se, In-Se and Ga-Se) is qualitatively investigated using *in situ* high temperature X-ray diffraction (HTXRD) and compared with the prediction by equilibrium phase diagrams in Chapter 3. Understanding the phase transformation of metal-selenide binaries is very important in designing binary bi- or multi-layer precursors for rapid thermal processing, which is a promising low-cost approach of CIGS film fabrication.

In Chapter 4, the reaction pathways and kinetics of α -CIS formation from different precursors (e.g., glass/In₂Se₃/CuSe, glass/InSe/Cu-Se, glass/CuSe/In-Se and glass/Mo/Cu-In-Se) and selenization of metallic glass/Mo/Cu-In precursor are systematically investigated using a time-resolved, *in situ* HTXRD equipped with a customized selenium chamber. Quantitative kinetic analysis using selected solid-state growth models provides kinetic parameters including reaction order, rate constant, and activation energy as well.

In Chapter 5, the successful implementation of *in situ* HTXRD technique in α -CIS system (Chapter 4) is extended to exploring the CGS formation from thermal annealing of stacked precursors (e.g., glass/GaSe/CuSe and glass/Mo/Cu-Ga-Se) and selenization of glass/Mo/Cu-Ga precursor. Subsequently, the reaction pathways and kinetics for quaternary CIGS formation by the selenization of metallic glass/Mo/Cu-Ga-In precursors are investigated in Chapter 6.

Since most solid-state reactions follow a diffusion limited process, it is expected that the diffusion-limited reaction rate would be predicted by thermodynamic chemical potentials and diffusivities (or mobilities) of species. Therefore, for a given set of thermodynamic descriptions, (e.g., results obtained in Chapter 2), the reaction rates experimentally obtained in Chapter 4 through 6 can be used to establish the mobility database of each element (e.g., Cu, In, Ga and Se) in various compounds by employing the companion software to ThermoCalc, DICTRA (DIffusion-Controlled TRAnsformation) program. In Chapter 7, kinetic data for α -CIS formation by selenization of glass/Mo/Cu-In precursor are used to obtain a mobility expression of selenium.

CHAPTER 2

BINARY AND TERNARY PHASE DIAGRAM ASSESSMENT

2.1 Cu-Se Binary Phase Diagram Assessment

2.1.1 Introduction

The Cu-Se system is an important constitutional binary of the chalcopyrite $\text{Cu}(\text{In}_x\text{Ga}_{1-x})\text{Se}_2$, which is one of the most promising absorber materials for high-efficiency thin film solar cells. Phase equilibria and thermodynamic properties of the Cu-Se system have been studied by many research groups using differential thermal analysis (DTA), X-ray diffraction, microscopy, calorimetry, electromotive force (EMF), and vapor pressure measurement. More recently, an excellent review paper on the phase equilibria of the Cu-In system based on the evaluation of the abundant experimental data was published by Glazov *et al.* [Gla00], who have been studying this system for many years and have carried out precise measurements.

A thermodynamic description, established with the computer-based CALculation of PHAse Diagram (CALPHAD) method [Sau98], is represented as a set of models to express the Gibbs energy of each phase as a function of temperature, pressure and composition. The parameters used in the models of different phases are optimized using the available phase equilibrium and thermo-chemical data. This optimization is expected to make the thermodynamic description self-consistent and able to provide complete information about phase equilibria, thermo-chemical properties as well as driving forces of phase transformation and mass transport.

The reliable description for binary Cu-Se system is also a crucial part of the thermodynamic databases for the higher order systems such as the ternary Cu-In-Se and Cu-Ga-Se, and quaternary Cu-In-Ga-Se systems. Thermodynamic optimization for the Cu-Se system was first performed by Chang [Cha99] using the previously reported experimental data and ThermoCalc program, which is one of most popular CALPHAD software. In his work, an association model and a three-sub-lattice model were employed for liquid and Cu_{2-x}Se phases, respectively. The other intermediate phases, Cu_3Se_2 , CuSe and CuSe_2 , were modeled as line compounds.

In this work, the efforts to improve the previous optimization results by Chang were incorporated to make the models for different phases in the Cu-Se system more compatible with higher order systems, and the calculated phase diagram and thermodynamic properties more coincident with the recently evaluated results, especially the values suggested by Glazov [Gla00].

2.1.2 Experimental Information

The liquid phase of this system exhibits two miscibility gaps. One in the Cu-rich region was reported by several research groups [Gla91, Göd00b, Ber72, Hey66, Bab75, Bur74, Mur75], and the other in Se-rich region was tentatively mapped by Glazov [Gla00] and Gödecke [Göd00b] based on very few experimental data. As to the terminal phases, a small solubility of Se in Cu was measured by Smart [Sma46] and Taylor [Tay76], while negligible solubility of Cu in Se was proposed by Chakrabarti [Cha81]. Four intermediate compounds were experimentally identified including Cu_{2-x}Se , Cu_3Se_2 , CuSe and CuSe_2 . Among them, only Cu_{2-x}Se melts congruently. The Cu_{2-x}Se has two polymorphs of α - Cu_{2-x}Se (low temperature phase) and β - Cu_{2-x}Se (high temperature

phase). The CuSe has three polymorphs including α -CuSe, β -CuSe and γ -CuSe. Their crystal structures were summarized by Glazov [Gla00] and Chang [Cha99]. The equilibrium reactions of the Cu-Se system were reported in many papers [Göd00b, Hey66, Ber68, Ogo69, Ogo72, Ber72, Aza76, Abr84]. The key equilibrium points have been more recently evaluated and presented with the different accuracy according to the experimental conditions by Glazov [Gla00]. Some phase transformation temperatures were confirmed to an accuracy of one tenth degree of Kelvin.

The standard enthalpies of formation and entropies of the intermediate compounds have been determined by various techniques [Hey66, Gat56, Val68, Rau70, Ask76, Mil74] and summarized by Chang [Cha99]. The heat capacities of two polymorphs of Cu₂Se were measured using an adiabatic calorimetry in the range 193 to 773 K [Kub73] and in the range 300 to 1390 K [Bla78]. As pointed out by Kubaschewski [Kub73], the measured heat capacities of the α -Cu_{2-x}Se phase are not reliable above 325 K on account of the α - β transformation. The heat capacities of three polymorphs of CuSe were measured in the range 5.7 to 652.7 K [Sto96] using the same method as used by Kubaschewski [Kub73].

The chemical potential of Cu in Cu_{2-x}Se, as a function of temperature, was measured using coulometric titrations with a solid state galvanic cell, Pt/Cu/CuBr/Cu_{2-x}Se/graphite [Mos89]. The activities of Se in molten mixture of Cu and Se were measured by a modified dew-point method at 1373 K [Bla78], and by the transportation method at 1437 K [Aza76]. Several gaseous species have been detected including Se_n (n = 1 to 8), Cu, Cu₂, CuSe, and Cu₂Se. The vapor pressure of Se₂ over different condensed phases in the Cu-Se system was reported by Rau [Rau70].

2.1.3 Thermodynamic Optimization

The CALPHAD method was applied to obtain a consistent thermodynamic description of the entire Cu-Se system by employing the PARROT module of the ThermoCalc program package [Din91]. The CALPHAD method is based on two basic principles: the total Gibbs energy of a system will be at a minimum at thermodynamic equilibrium and the chemical potential of every element in different equilibrium phases is the same. Thermodynamic optimization by CALPHAD method can provide the following advantages;

- Predicts phase diagrams and thermodynamic properties of a system under conditions where no experimental information is available.
- Calculates phase diagrams and thermodynamic properties for a higher order system based on the models of its lower order sub-systems.
- Calculates meta-stable phase diagram.
- Determine the driving force of phase transformation.

The standard Gibbs energy function ${}^0G_i^\varphi(T)$ for the element i in phase φ is described by an equation suggested by SGTE [Din91]:

$${}^0G_i^\varphi(T) = G_i^\varphi(T) - H_i^{SER} = a + b \cdot T + c \cdot T \cdot \ln T + d \cdot T^2 + e \cdot T^3 + f \cdot T^{-1} \quad (2-1)$$

where H_i^{SER} is the molar enthalpy of element i at 298.15 K and 1 bar in its standard element reference (SER) state, and φ represents any possible phase. The parameters for ${}^0G_{Cu}^\varphi(T)$ and ${}^0G_{Se}^\varphi(T)$ functions were taken from the SGTE compilation [Din91] and the evaluation results by Chang [Cha99], respectively.

To allow the established database to be easily extended to higher order systems and to be compatible with the general CALPHAD database, the sub-lattice models with the

different constitutions according to their structures as presented by Saunders [Sau98] were employed for all the stable phases of the Cu-Se system.

The liquid phase is described by an ionic two-sub-lattice model that can be schematically represented as $(\text{Cu}^{+1})_p(\text{Se}^{-2}, \text{Va}^{-q}, \text{Se})_q$. This model is able to describe the short range ordering effectively and is straightforwardly extended to higher order systems as compared to the associated solution model used by Chang [Cha99]. The Cu^{+1} state is considered as the only species in the cationic sub-lattice. Another oxidation state Cu^{+2} is neglected due to its very small amount. Neutral selenium and hypothetically charged vacancy are introduced in an anion sub-lattice to maintain the charge neutrality by adjusting the values of p and q .

The Cu-rich solid solution phase is described by a two-sub-lattice model in terms of $(\text{Cu}, \text{Se})(\text{Va})$, which is generally used for the alloy fcc phase in CALPHAD solution database such as SSOL [Din91]. The line compounds Cu_3Se_2 , CuSe , and CuSe_2 are described by a two-sub-lattice model in terms of $(\text{Cu})_p(\text{Se})_q$ where p and q are the stoichiometric coefficients of the compounds.

The two polymorphs of the non-stoichiometric Cu_{2-x}Se compound are described by a three-sub-lattice model based on the structural study [Cha99]. In this work, the sub-lattice constitutions $(\text{Cu}, \text{Va})_1(\text{Se}, \text{Va})_1(\text{Cu})_1$ used by Chang [Cha99] is simplified to $(\text{Cu}, \text{Va})_1(\text{Se})_1(\text{Cu})_1$ since the measured compositions of Cu_{2-x}Se always show a deficit of Cu. The simplification is intended to keep the number of parameters to be optimized as low as possible while still permitting the results to be matched with the apparent data. It does not mean no vacancy exists in the other two sub-lattices.

For any phase φ in the Cu-Se system, the Gibbs energy is represented by

$$G^\varphi = {}^{ref}G^\varphi + {}^{id}G^\varphi + {}^{xs}G^\varphi \quad (2-2)$$

The Gibbs energies, ${}^{ref}G^\varphi$, ${}^{id}G^\varphi$ and ${}^{xs}G^\varphi$ for different phases are described by the following equations:

for the liquid phase,

$${}^{ref}G^{liq} = y_{Cu^{+1}} \cdot y_{Se^{-2}} \cdot {}^0G_{Cu^{+1}:Se^{-2}}^{liq} + y_{Cu^{+1}} \cdot y_{V_a^{-q}} \cdot {}^0G_{Cu^{+1}:V_a^{-q}}^{liq} + q \cdot y_{Se} \cdot {}^0G_{Se}^{liq} \quad (2-3)$$

$${}^{id}G^{liq} = RT \cdot q(y_{Se^{-2}} \cdot \ln y_{Se^{-2}} + y_{V_a^{-q}} \cdot \ln y_{V_a^{-q}} + y_{Se} \cdot \ln y_{Se}) \quad (2-4)$$

$${}^{xs}G^{liq} = y_{Se^{-2}} \cdot y_{V_a^{-q}} \cdot L_{Cu^{+1}:Se^{-2}, V_a^{-q}}^{liq} + y_{Se^{-2}} \cdot y_{Se} \cdot L_{Cu^{+1}:Se^{-2}, Se}^{liq} \quad (2-5)$$

for the Cu-rich solid solution phase,

$${}^{ref}G^{Cu_fcc} = y_{Cu} \cdot {}^0G_{Cu:V_a}^{Cu_fcc} + y_{Se} \cdot {}^0G_{Se:V_a}^{Cu_fcc} \quad (2-6)$$

$${}^{id}G^{Cu_fcc} = RT(y_{Cu} \cdot \ln y_{Cu} + y_{Se} \cdot \ln y_{Se}) \quad (2-7)$$

$${}^{xs}G^{Cu_fcc} = y_{Cu} \cdot y_{Se} \cdot L_{Cu, Se: V_a}^{Cu_fcc} \quad (2-8)$$

for the line compound phases in terms of Cu_pSe_q

$${}^{ref}G^{Cu_pSe_q} = {}^0G_{Cu:Se}^{Cu_pSe_q} \quad (2-9)$$

$${}^{id}G^{Cu_pSe_q} = 0 \quad (2-10)$$

$${}^{xs}G^{Cu_pSe_q} = 0 \quad (2-11)$$

and for the non-stoichiometric compound phases such as $\alpha\text{-Cu}_{2-x}\text{Se}$ and $\beta\text{-Cu}_{2-x}\text{Se}$ represented as phase φ ,

$${}^{ref}G^\varphi = y_{Cu} \cdot {}^0G_{Cu:Se:Cu}^\varphi + y_{V_a} \cdot {}^0G_{V_a:Se:V_a}^\varphi \quad (2-12)$$

$${}^{id}G^\varphi = RT(y_{Cu} \cdot \ln y_{Cu} + y_{V_a} \cdot \ln y_{V_a}) \quad (2-13)$$

$${}^{xs}G^\varphi = y_{Cu} \cdot y_{V_a} \cdot {}^0L_{Cu, V_a:Se:Cu}^\varphi \quad (2-14)$$

In equation (2-3)-(2-14), ${}^0G_{A:B}^\varphi$ and ${}^0G_{A:B:C}^\varphi$ represent the Gibbs energy of the so-called end-member compounds AB and ABC, respectively, where A, B, and C is a species such as Cu, In, Se, Va, Cu^{+1} , Se^{-2} and Va^{-q} ; ${}^0L_{A,B:B:C}^\varphi$ is the interaction parameter for the species A and B in the first sub-lattice, while the second and third sub-lattices are occupied by B and C, respectively; y'_A and y''_A represent the site fraction of A in the first and second sub-lattice, respectively. An end-member compound could be a real or a hypothetical compound. The Gibbs energy for the end-member is represented by the same expression as that for the elements:

$${}^0G_{A:B:C}^\varphi(T) = a + b \cdot T + c \cdot T \cdot \ln T + d \cdot T^2 + e \cdot T^3 + f \cdot T^{-1} \quad (2-15)$$

Each interaction parameter can be expressed by the expansion of site fraction and the temperature dependence as the following:

$$L = \sum_{y=0}^n {}^v L(y_i - y_j)^v \quad (2-16)$$

$${}^v L = {}^v L_A + {}^v L_B \cdot T \quad (2-17)$$

For the compounds like $Cu_{2-x}Se$ and $CuSe$ for which the heat capacities have been measured at different temperatures [Mos89, Bla78, Aza76], the latter four terms (c, d, e and f) of equation (2-15) were obtained from the heat capacity data using the following expression:

$$C_p(T) = A + B \cdot T + C \cdot T^2 + D \cdot T^{-2} \quad (2-18)$$

In comparison of equations (15) and (18), the following relations can be derived by using the fundamental relationships of thermodynamics

$$c = -A; \quad d = -B/2; \quad e = -C/6; \quad f = -D/2 \quad (2-19)$$

Before the optimization, the evaluated heat capacity data are directly put into the Gibbs energy expressions in terms of c , d , e and f . It can reduce the arbitrary optimization due to too many unknown parameters. For the compound $\alpha\text{-Cu}_{2-x}\text{Se}$, only the experimental heat capacity data at low temperature were used in optimization for the reason that $\alpha\text{-}\beta$ transformation would raise the heat effect.

Thermodynamic optimization was then performed by using the selected experimental data presented in Figure 2-2 and Tables 2-3 and 2-4. A set of self-consistent model parameters were obtained as the optimization result, with which the calculated phase diagram and thermo-chemical properties of the system agree well with the evaluated experimental results.

2.1.4 Results and Discussion

The optimized parameters for describing the Gibbs energy of each phase in the Cu-Se system are listed in Tables 2-1 and 2-2. The calculated Cu-Se phase diagram is presented in Figure 2-1 and is compared with the literature data in Figure 2-2. Calculated key equilibrium points are compared with the evaluated values [Gla00] in Table 2-3. The comparison of the calculated standard enthalpy of formation and entropy of the compounds is shown in Table 2-4. The calculated chemical potential of Cu is compared with the experimental data in Figure 2-3. The calculated chemical potential of Se is compared with the values converted from the experimental activity data [Mos89] in Figure 2-4. The comparison of the calculated vapor pressures of Se over different condensed phases with the experiments is shown in Figure 2-5. The comparison of calculated heat capacities of the Cu_{2-x}Se and CuSe compounds with those of different polymorphs is presented in Figure 2-6 and 2-7.

It can be seen that the overall calculated phase diagram and most of the key phase equilibrium points agree well with the experimentally evaluated results [Gla00]. The calculated standard enthalpy of formation, absolute entropy, heat capacity of the compounds, and the vapor pressure of Se_2 also agree well with the experimental data. The calculated chemical potentials of Cu and Se agree with most of the experimental data.

The calculated eutectoid temperature of $\alpha\text{-Cu}_{2-x}\text{Se}/\beta\text{-Cu}_{2-x}\text{Se}/\text{Cu}_3\text{Se}_2$ (334.9K), however, is much higher than that (≤ 253 K) suggested by Glazov [Gla00] based on the experiments [Ogo69, Ogo72]. If the lower value of the eutectoid temperature is used as constant and other model parameters are adjusted, the vapor pressure of Se_2 will not agree with the experimental data [Rau70]. The inconsistency can not be solved by adjusting any model parameters of the three phases. Since it is believed that achieving equilibrium between the gas-solid is more likely than between the solid-solid at low temperature, a large weight factor was used for Se vapor pressure data during optimization.

The calculated Cu chemical potential of the Cu_{2-x}Se compound agrees well with EMF measurements [Mos89] for $x < 0.04$, while it decreases more steeply than experimental values for $x > 0.04$. The difference may be caused by the fact that the rate of Cu diffusion is not sufficiently high to maintain the sample homogeneous during coulometric titration. Another possibility is the presence of electric current that when combined with the ionic component causes the apparent Cu titration amount to be greater than the actual value. The calculated Se chemical potentials are compared with experimental values for liquid phases measured by two different methods, a modified

dew point method at 1373K [Bla78] and a transportation method at 1473K [Aza76]. The results reveal that the calculated values lie well between the two experimental results.

2.1.5 Summary

A thermodynamic description for the Cu-Se system has been established based on the abundant experimental data, the recent evaluation [Gla00], and the previous optimization work [Cha99]. Sub-lattice models with various constitutions were applied for different phases of the system. The models used in this work allow easy extension of the database to higher order systems. The calculated phase diagram and thermo-chemical properties agree well with experimental results and thus demonstrate the self-consistency of the established thermodynamic description.

Table 2-1. Thermodynamic parameters in Cu-Se system

Phase/model	Function	Reference
Liquid / $(\text{Cu}^{+1})_p(\text{Se}^{-2}, \text{Va}^{-q}, \text{Se})_q$	$G(\text{LIQ}, \text{CU}+1:\text{SE}-2;0) = G_{\text{CU}2\text{SE}} \text{B} + 17762.5 - 12.5*T$	This work
	$G(\text{LIQ}, \text{CU}+1:\text{VA};0) = G_{\text{CU}} \text{S} + 13263.3 - 9.76894748*T$	This work
	$G(\text{LIQ}, \text{SE};0) = G_{\text{SE}} \text{L}$	[Din91]
	$G(\text{LIQ}, \text{CU}+1:\text{SE}-2, \text{VA};0) = 159272.8 - 87.93*T$	This work
	$G(\text{LIQ}, \text{CU}+1:\text{SE}-2, \text{VA};1) = 63335 - 48.1634*T$	This work
	$G(\text{LIQ}, \text{CU}+1:\text{SE}-2, \text{SE};0) = -1235 - 5*T$	This work
	$G(\text{LIQ}, \text{CU}+1:\text{SE}-2, \text{SE};1) = -22612.66$	This work
α-Cu₂Se / $(\text{Cu}, \text{Va})(\text{Se})(\text{Cu})$	$G(\text{CU}2\text{SE} \text{A}, \text{CU}:\text{SE}:\text{CU};0) = G_{\text{CU}2\text{SE}} \text{A}$	This work
	$G(\text{CU}2\text{SE} \text{A}, \text{VA}:\text{SE}:\text{CU};0) = 50000 + G_{\text{CU}} \text{S} + G_{\text{SE}} \text{S}$	This work
	$G(\text{CU}2\text{SE} \text{A}, \text{CU}, \text{VA}:\text{*}:\text{CU};0) = 50000$	This work
	$G(\text{CU}2\text{SE} \text{A}, \text{CU}, \text{VA}:\text{*}:\text{CU};1) = -43000$	This work
β-Cu₂Se / $(\text{Cu}, \text{Va})(\text{Se})(\text{Cu})$	$G(\text{CU}2\text{SE} \text{B}, \text{CU}:\text{SE}:\text{CU};0) = G_{\text{CU}2\text{SE}} \text{B}$	This work
	$G(\text{CU}2\text{SE} \text{B}, \text{VA}:\text{SE}:\text{CU};0) = 46000 + 18.7*T + G_{\text{CU}2\text{SE}} \text{B} - G_{\text{CU}} \text{S}$	This work
	$G(\text{CU}2\text{SE} \text{B}, \text{CU}, \text{VA}:\text{*}:\text{CU};0) = -28998 + 14.002*T$	This work
	$G(\text{CU}2\text{SE} \text{B}, \text{CU}, \text{VA}:\text{*}:\text{CU};1) = -8.803*T$	This work
Cu₃Se₂ / $(\text{Cu})_{0.6}(\text{Se})_{0.4}$	$G(\text{CU}3\text{SE}2, \text{CU}:\text{SE};0) = G_{\text{CU}3\text{SE}} 2$	This work
α-CuSe / $(\text{Cu})_{0.5}(\text{Se})_{0.5}$	$G(\text{CUSE} \text{A}, \text{CU}:\text{SE};0) = G_{\text{CUSE}} \text{A}$	This work
β-CuSe / $(\text{Cu})_{0.5}(\text{Se})_{0.5}$	$G(\text{CUSE} \text{B}, \text{CU}:\text{SE};0) = G_{\text{CUSE}} \text{B}$	This work
γ-CuSe / $(\text{Cu})_{0.5}(\text{Se})_{0.5}$	$G(\text{CUSE} \text{G}, \text{CU}:\text{SE};0) = G_{\text{CUSE}} \text{G}$	This work
CuSe₂ / $(\text{Cu})_{0.33}(\text{Se})_{0.67}$	$G(\text{CUSE}2, \text{CU}:\text{SE};0) = G_{\text{CUSE}} 2$	This work
α-Cu / $(\text{Cu}, \text{Se})(\text{Va})$	$G(\text{CU} \text{FCC}, \text{CU}:\text{VA};0) = G_{\text{CU}} \text{S}$	[Din91]
	$G(\text{CU} \text{FCC}, \text{SE}:\text{VA};0) = G_{\text{SE}} \text{S} + 5000$	This work
	$G(\text{CU} \text{FCC}, \text{CU}, \text{SE}:\text{VA};0) = -14500$	This work
γ-Se	$G(\text{SE} \text{S}, \text{SE};0) = G_{\text{SE}} \text{S}$	[Din91]

Table 2-2. Parameters for functions used in Table 2-1 in the form of equation (2-1)

	a	b	c	d×10²	e×10⁶	f×10⁻²	T(K) range
GCU_S	-7770.4580	130.4852	-24.1124	-0.2657	0.1292	524.7780	298-1358
	-13309.7200	183.6498	-31.3800	0	0	0	1358-3200
GSE_S	-6657.6530	92.5397	-19.1400	-1.2295	2.6767	0	298-760
	-9059.1660	150.3342	-28.5520	0	0	0	760-1500
GSE_L	-9809.1960	288.8134	-52.4000	2.4925	-5.4550	0	298-1000
	8433.1372	-78.4769	5.3990	-3.5945	5.2017	0	1000-1150
	-7460.6200	192.6463	-36.0000	0	0	0	1150-1500
GCU2SE_A	-86772.3609	285.8666	-58.6000	-3.8700	0	0	298-6000
GCU2SE_B	-85571.9722	454.3173	-90.4176	0.8600	-1.5000	516.6747	298-6000
GCU3SE2	-31329.6700	172.9600	-32.0000	0.0319	0	0	298-6000
GCUSE_A	-28151.0213	110.6613	-21.5224	-0.9115	2.0400	281.4303	298-6000
GCUSE_B	-27103.8019	111.0630	-22.3684	-0.3715	-2.1800	251.0000	298-6000
GCUSE_G	-31321.3585	284.3542	-53.3380	6.2458	-24.0000	0	298-6000
GCUSE2	-28485.6977	265.0188	-45.3806	0.4484	0	0	298-6000

Table 2-3. Phase equilibria in the Cu-Se system

Equilibrium	Phase composition(at.% Se)			T (K)	Type	Ref.
$L_2 \leftrightarrow L_1 + \beta\text{-Cu}_{2-x}\text{Se}$	31.5 32.6	$\cong 4$ 3	33.3 33.5	1380 1380.0	Monotectic	[Gla00] This work
$L_1 \leftrightarrow \text{Cu} + \beta\text{-Cu}_{2-x}\text{Se}$	$\cong 1.8$ 2.16	0.021 8×10^{-5}	33.3 33.5	1336±5 1334.2	Eutectic	[Gla00] This work
$L_2 \leftrightarrow L_3 + \beta\text{-Cu}_{2-x}\text{Se}$	52.5 50.4	36.5 36.3	$\cong 99.6$ 96.7	796±1 795.8	Monotectic	[Gla00] This work
$\beta\text{-Cu}_{2-x}\text{Se} + L_3 \leftrightarrow \gamma\text{-CuSe}$	36.5 36.4	$\cong 100$ 99.2	50.0 50.0	652.7 652.7	Peritectic	[Gla00] This work
$\gamma\text{-CuSe} + L_3 \leftrightarrow \text{CuSe}_2$	50.0 50.0	$\cong 100$ 99.7	66.7 66.7	605 604.9	Peritectic	[Gla00] This work
$L_3 \leftrightarrow \text{CuSe}_2 + \text{Se}$	$\cong 100$ 100	66.7 66.7	100 100	494±1 494.0	Eutectic	[Gla00] This work
$\beta\text{-Cu}_{2-x}\text{Se}; \gamma\text{-CuSe}; \beta\text{-CuSe}$	36.5 35.5	50.0 50.0	50.0 50.0	410 410.1	Peritectoid or Eutectoid	[Gla00] This work
$\gamma\text{-CuSe}; \beta\text{-CuSe}; \text{CuSe}_2$	50.0 50.0	50.0 50.0	66.7 66.7	410 410.1	Peritectoid or Eutectoid	[Gla00] This work
$\text{Cu} + \beta\text{-Cu}_{2-x}\text{Se} \leftrightarrow \alpha\text{-Cu}_{2-x}\text{Se}$	$\cong 4 \times 10^{-8}$ 5.24×10^{-9}	$\cong 33.3$ 33.3	$\cong 33.3$ 33.3	396±15 395.8	Peritectoid	[Gla00] This work
$\beta\text{-Cu}_{2-x}\text{Se} + \beta\text{-CuSe} \leftrightarrow \text{Cu}_3\text{Se}_2$	$\cong 36.3$ 35.4	50.0 50.0	40.0 40.0	386 385.6	Peritectoid	[Gla00] This work
$\text{Cu}_3\text{Se}_2; \beta\text{-CuSe}; \alpha\text{-CuSe}$	40.0 40.0	50.0 50.0	50.0 50.0	326.8 326.4	Peritectoid or Eutectoid	[Gla00] This work
$\beta\text{-CuSe}; \alpha\text{-CuSe}; \text{CuSe}_2$	50.0 50.0	50.0 50.0	66.7 66.7	326.8 326.4	Peritectoid or Eutectoid	[Gla00] This work
$\beta\text{-Cu}_{2-x}\text{Se} \leftrightarrow \alpha\text{-Cu}_{2-x}\text{Se} + \text{Cu}_3\text{Se}_2$	$\cong 35.4$ 35.0	$\cong 34$ 33.3	40.0 40.0	≤ 253 334.9	Eutectoid	[Gla00] This work
$L \leftrightarrow L_1 + L_2$	18 16.3			1699 1698.7	Critical point	[Gla00] This work
$L_1 \leftrightarrow \beta\text{-Cu}_{2-x}\text{Se}$	33.4 33.8			1421 1421.2	Congruent melting point	[Gla00] This work

Table 2-4. Experimental and calculated standard formation enthalpies ($\Delta H_f^\circ_{298.15K}$) and entropies (S°_{298}) of Cu-Se compounds.

Compound	$-\Delta H_f^\circ_{298.15K}$ (kJ/mole)	S°_{298} (J/mole.K)	Method	Reference
$\alpha\text{-Cu}_2\text{Se}$	59.3	-	Calorimetry	[Gat56]
	69.9	-	EMF	[Val68]
	62.8	157.4	Vapor pressure	[Rau70]
	65.7	113.9	EMF	[Ask76]
	65.3	129.7	Evaluation	[Mil74]
	59.3	129.7	Assessment	[Cha99]
	65.86 (± 0.53)	129.7 (± 4.2)	Evaluation	[Gla00]
	65.9	129.7	Assessment	This work
Cu_3Se_2	98.9	-	Calorimetry	[Gat56]
	124.5	-	DTA	[Hey66]
	94.6	185	EMF	[Ask76]
	104.6	207.2	Evaluation	[Mil74]
	104.6	210.7	Assessment	[Cha99]
	98.91 (± 0.54)	207.11 (± 21)	Evaluation	[Gla00]
	108.8	207.8	Assessment	This work
$\alpha\text{-CuSe}$	39.6	-	Calorimetry	[Gat56]
	46.0	-	EMF	[Val68]
	44.0	86.2	Vapor pressure	[Rau70]
	32.6	74.1	EMF	[Ask76]
	41.8	78.2	Evaluation	[Mil74]
	40.8	78.2	Assessment	[Cha99]
	39.54 (± 0.42)	79.36 (± 0.06)	Evaluation	[Gla00]
CuSe_2	41.7	79.4	Assessment	This work
	43.1	-	Calorimetry	[Gat56]
	49.0	120.6	Vapor pressure	[rau70]
	39.3	98.8	EMF	[Ask76]
	48.1	107.4	Evaluation	[Mil74]
	48.1	115.4	Assessment	[Cha99]
	43.10 (± 7.1)	107.5 (± 10.5)	Evaluation	[Gla00]
	46.0	108.7	Assessment	This work

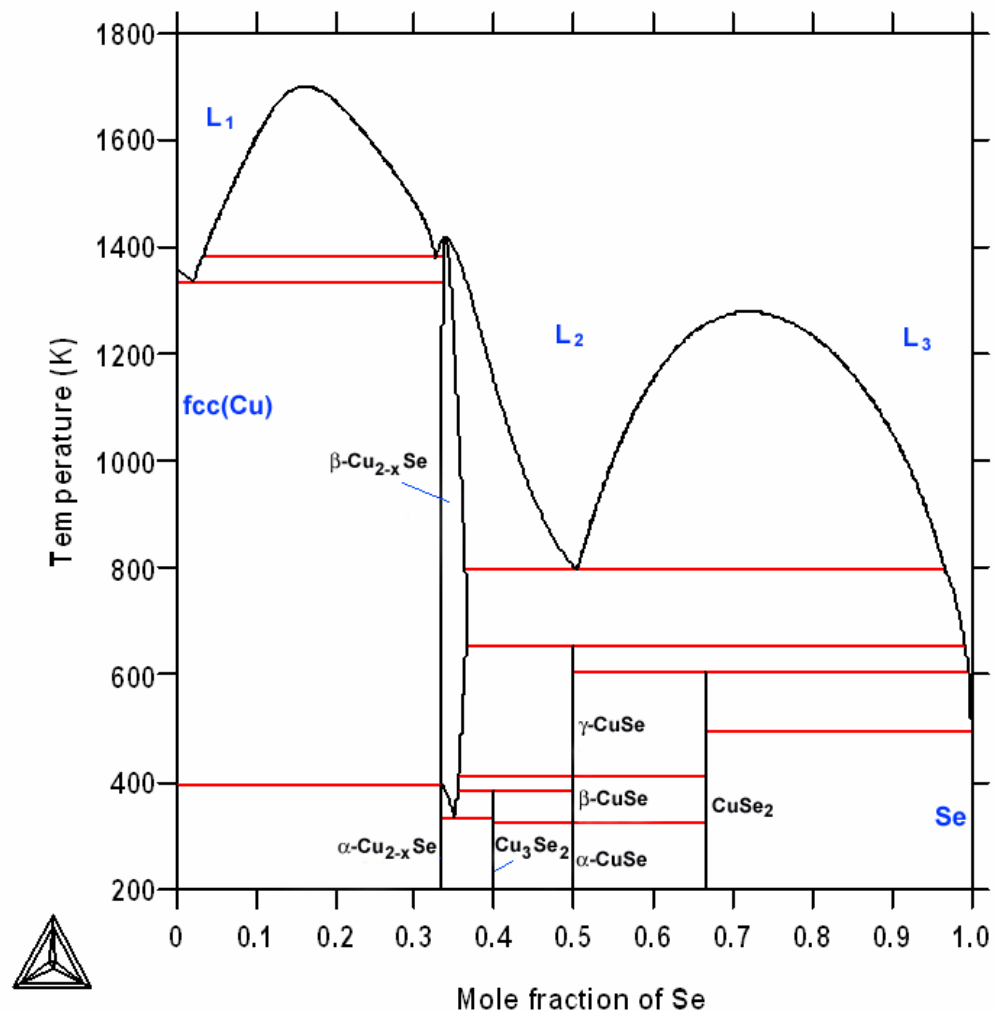


Figure 2-1. Calculated Cu-Se phase diagram

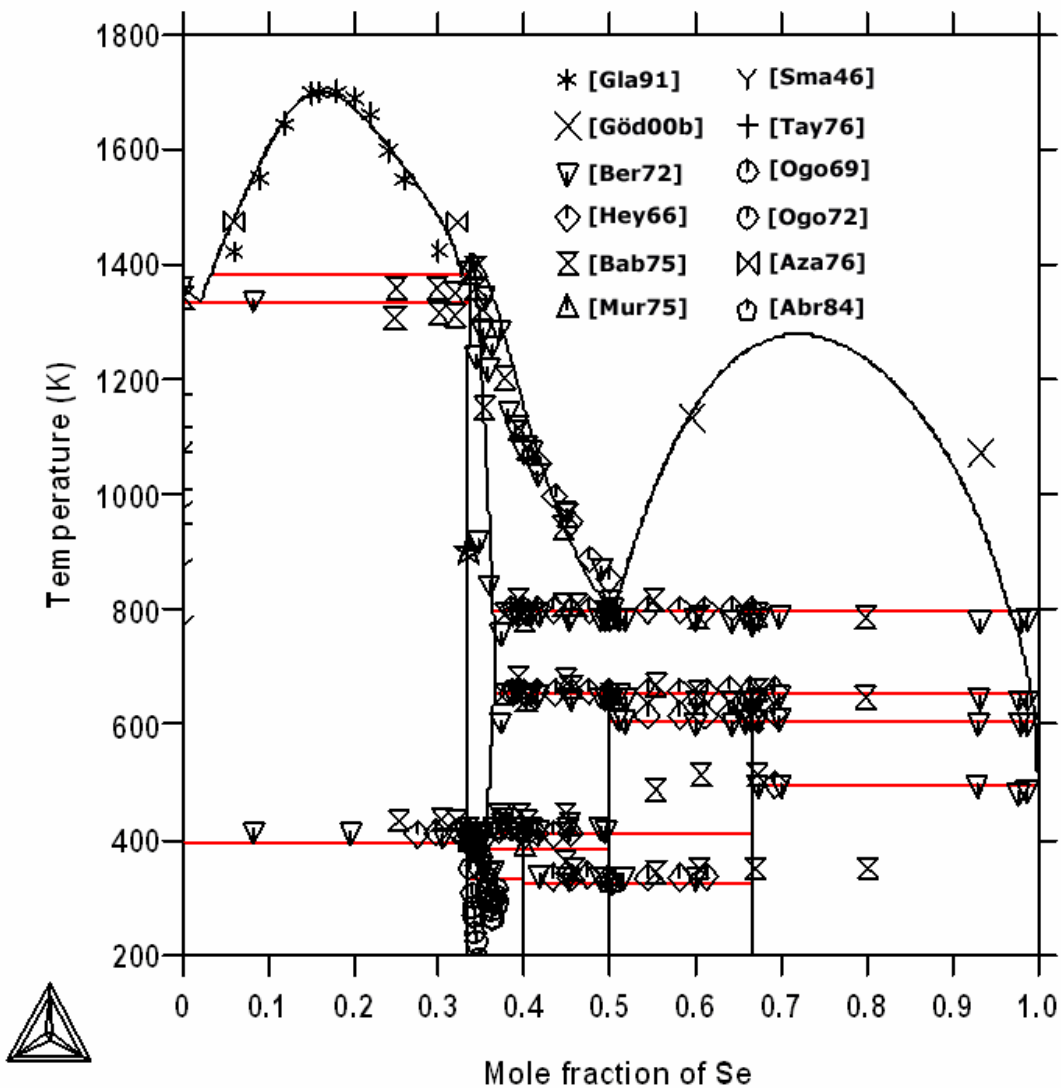


Figure 2-2. Comparison between the calculated Cu-Se phase diagram and experimental data

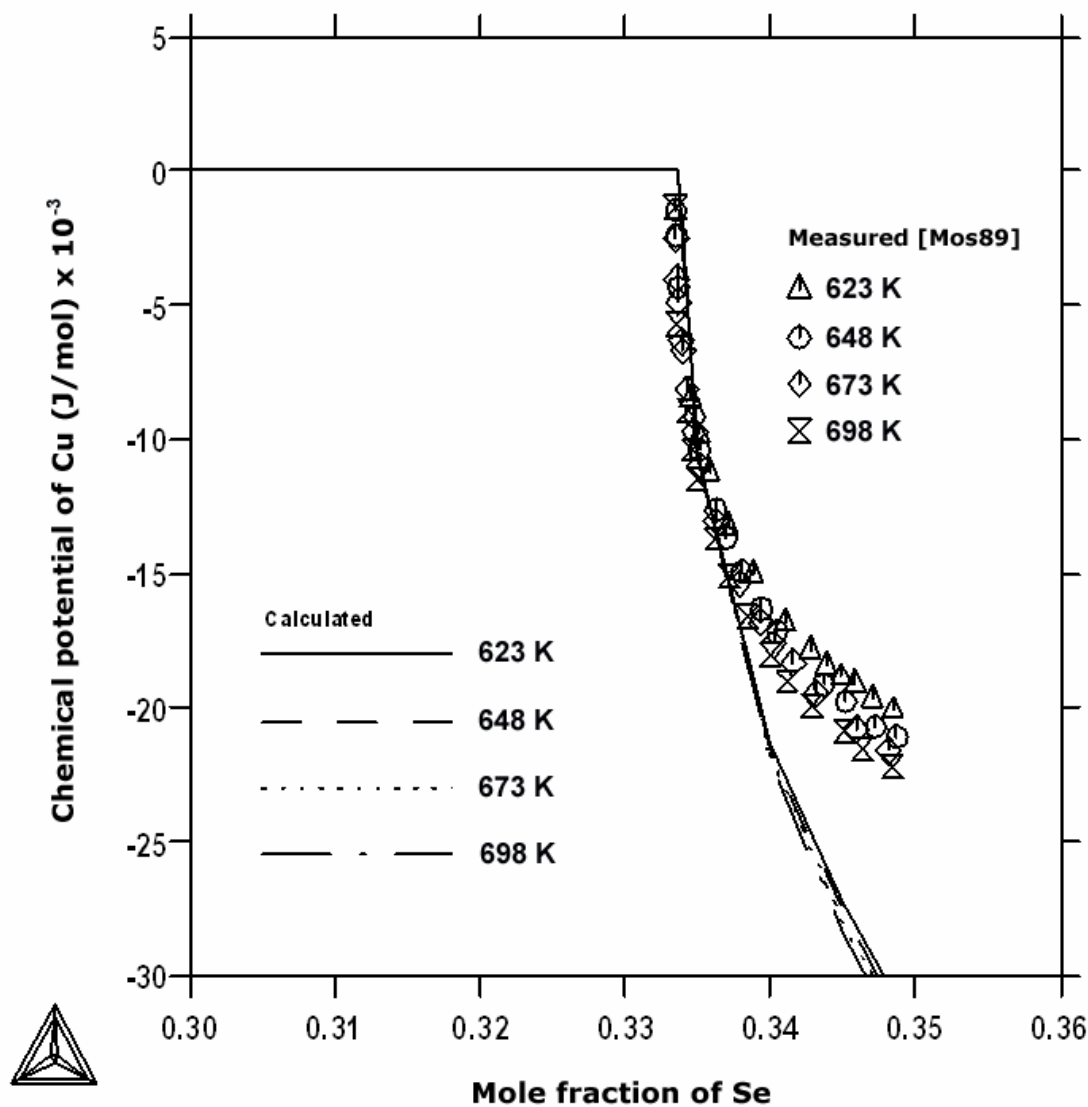


Figure 2-3. Comparison between the calculated chemical potential of Cu and experimental data in $\beta\text{-Cu}_{2-x}\text{Se}$ phase

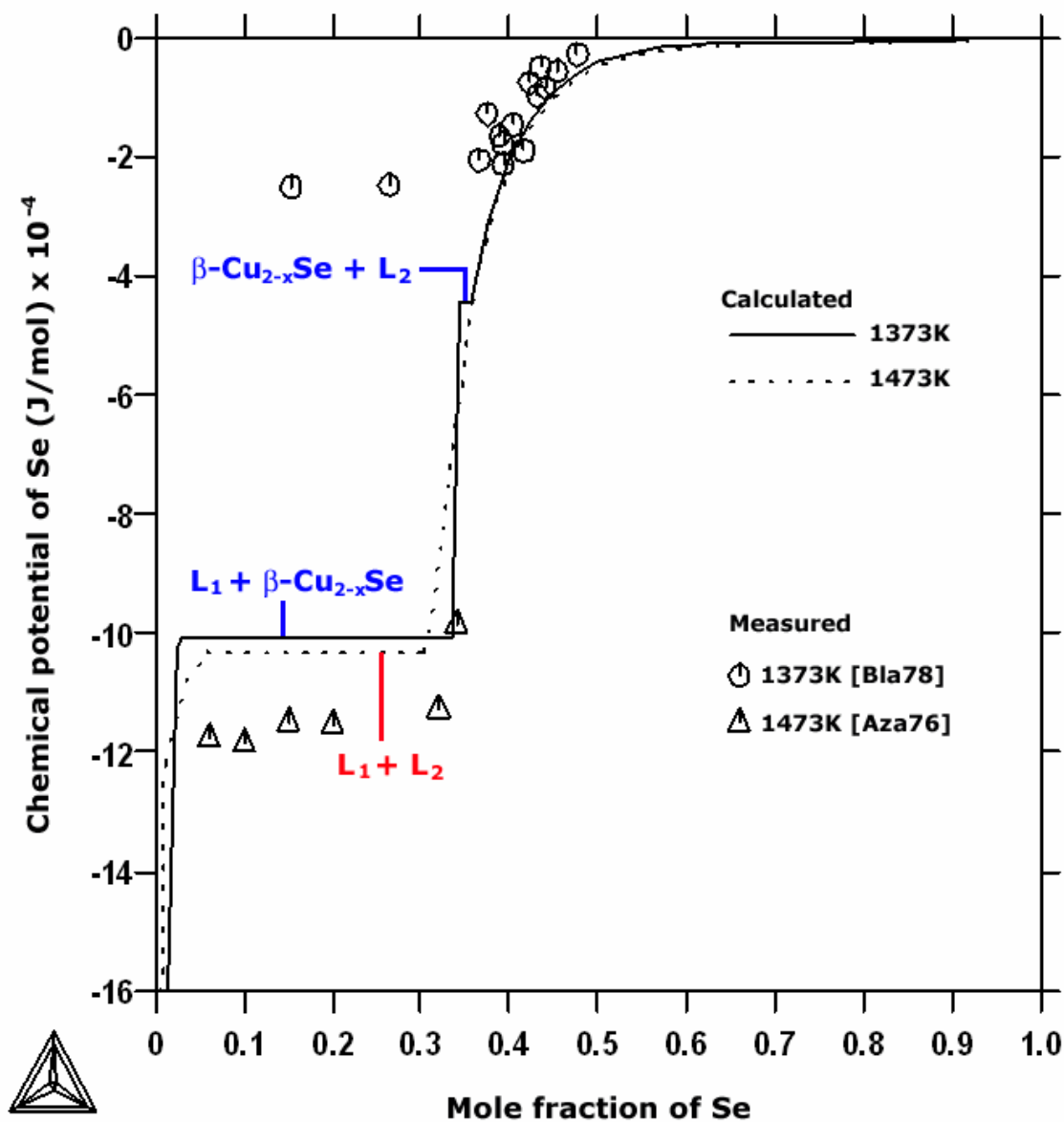


Figure 2-4. Comparison between the calculated chemical potential of Se and experimental data at 1373 and 1473K

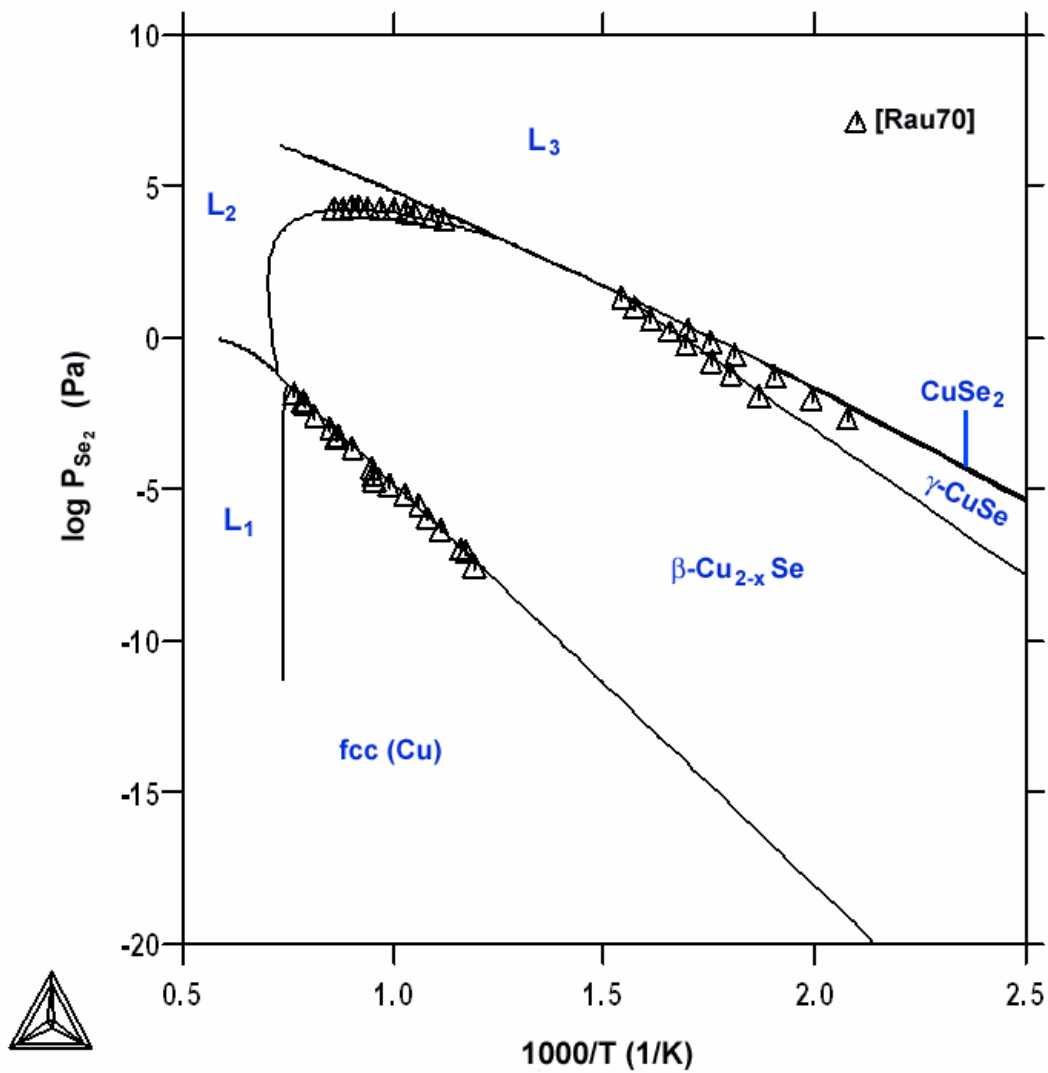


Figure 2-5. Comparison between the calculated Se_2 partial pressure and experimental data in Cu-Se system

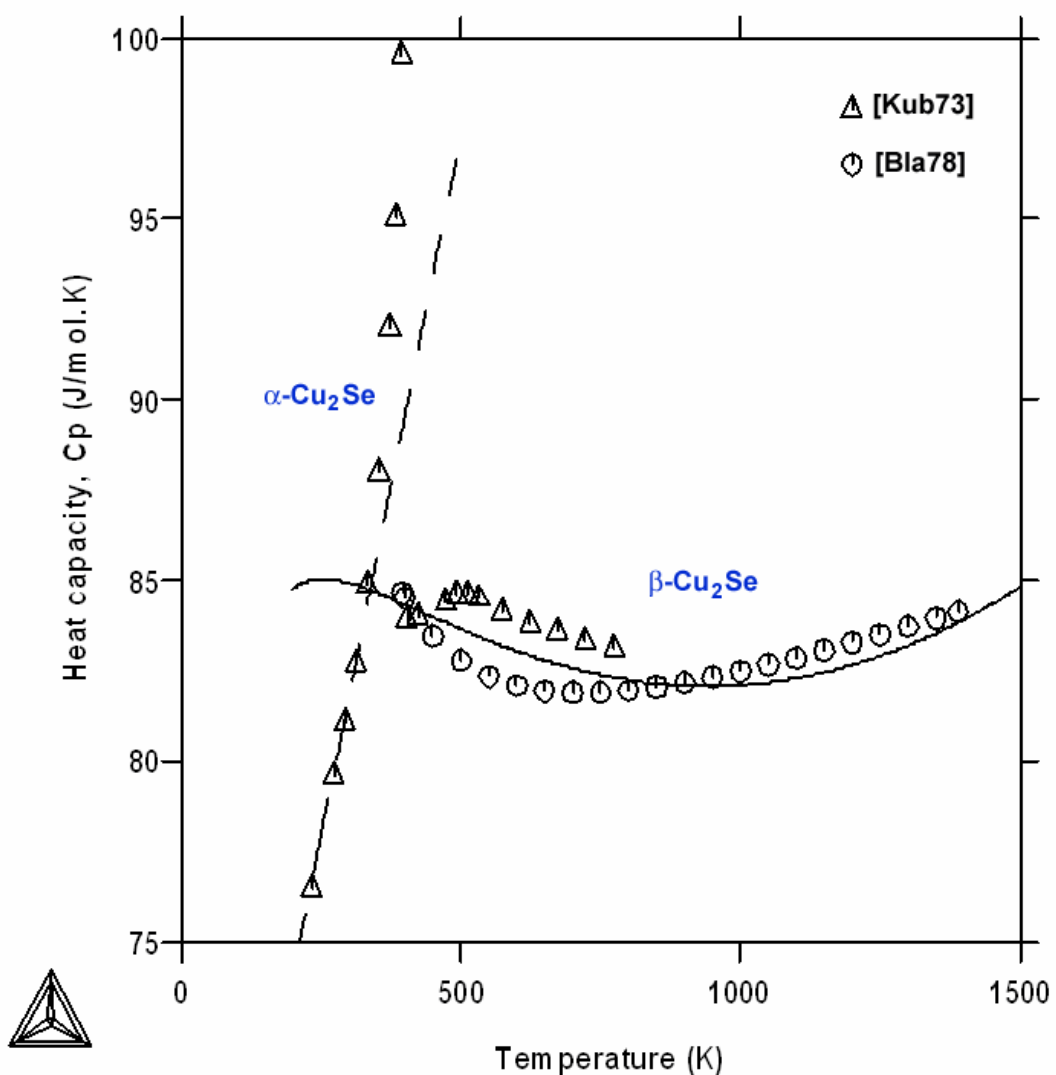


Figure 2-6. Comparison between the calculated heat capacity of each phase and experimental data for Cu_2Se

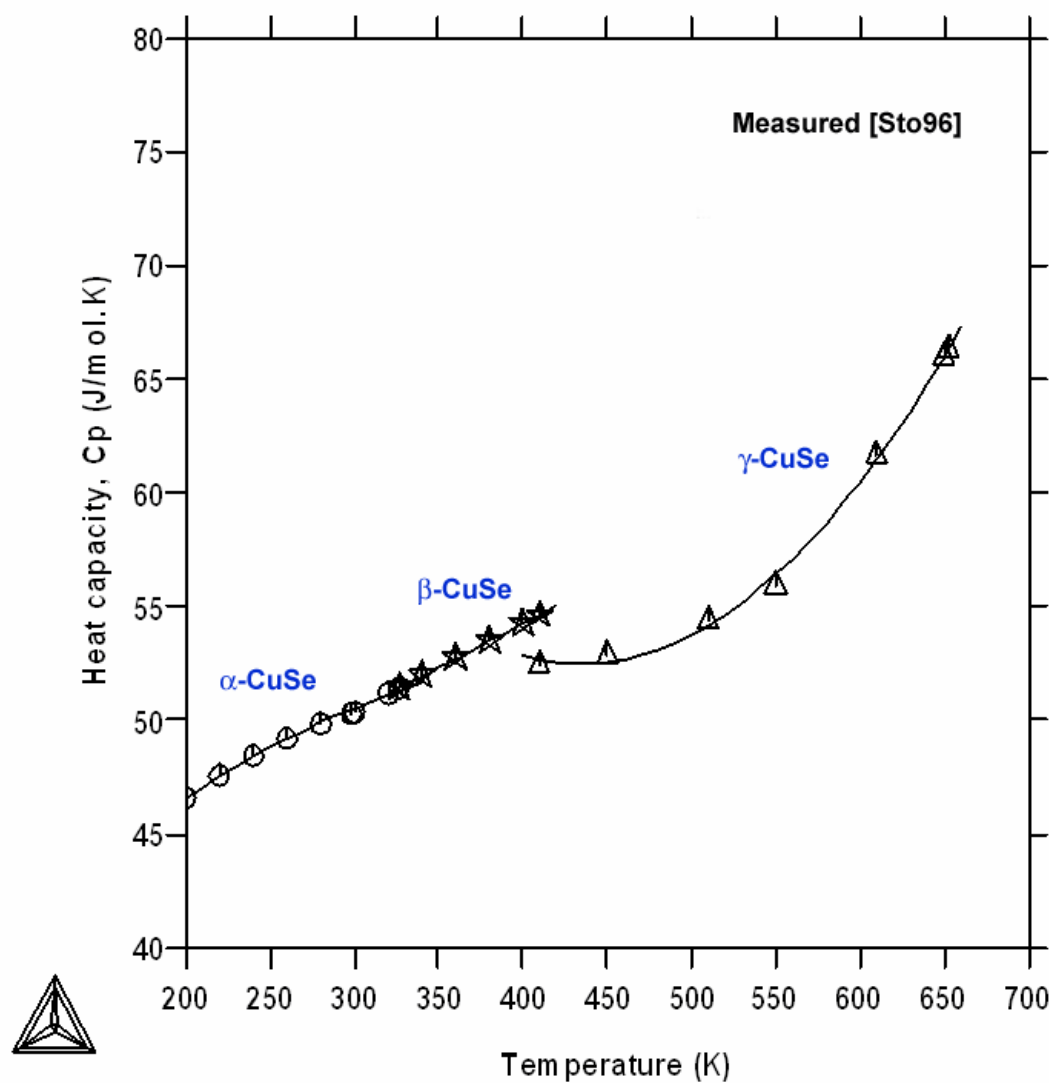


Figure 2-7. Comparison between calculated heat capacity of each phase and experimental data for CuSe

2.2 Thermodynamic Description of Ternary Compounds in Cu-In-Se System

2.2.1 Introduction

Since the chalcopyrite CuInSe₂ (CIS) was first synthesized in 1953, the Cu-In-Se ternary system has attracted considerable attention due to its application as an absorber material in solar cells. CIS-based cells currently hold the world-record energy conversion efficiency (19.5%, AM1.5G, 100mW/cm²) for thin film technologies [Con05]. This compound has a large homogeneity range of composition and complicated phase relationships with the other phases. A small deviation in composition about the stoichiometry (Cu:In:Se = 1:1:2) or the existence of secondary phases produces large changes in CIS material properties and thus its device characteristics. There is a lack of reliable thermodynamic data for the ternary compounds in the Cu-In-Se system. Unfortunately these properties are essential to understanding reaction pathways to synthesize CIS and development of novel processes to fabricate cost-effective high-quality CIS films.

Common experimental techniques to measure thermodynamic properties can not be directly used to estimate the Gibbs energy of these ternary compounds as it is not easy to know their exact corresponding compositions due to large homogeneity range of the ternary compounds, e.g., α -CuInSe₂ and β -CuIn₃Se₅ in pseudo-binary In₂Se₃-Cu₂Se phase diagram shown in Figure 2-10. In this work [She06], a set of thermodynamic descriptions for the dominant ternary compounds in the Cu-In-Se system is established by integrating the relevant information, which includes:

- Experimental measurements of the thermodynamic properties of the Cu-In-Se ternary compounds.
- Experimental measurements of phase equilibria including Cu-In-Se ternary compounds.

- Established thermodynamic model of the three sub-binaries, i.e., Cu-Se, Cu-In and In-Se.
- Ab initio calculation on the defect formation energy in the Cu-In-Se ternary compounds.

2.2.2 Extrapolation of Binary Gibbs Energy to Ternary

In the CALPHAD method, the excess Gibbs energy expression of a higher-order system is usually predicted from that of the lower-order systems if insufficient experimental data are available for the higher-order system. The basic formulae for doing this are based on various geometrical weightings of the mole fractions [Hil80] and expressed for ternary system by the general expression:

$$G_{mix}^{xs} = \sum_{i=1}^3 \sum_{j=1}^3 x_i x_j \frac{G_{ij}^{xs}}{X_{i(j)} X_{j(i)}} + x_1 x_2 x_3 L_{123} \quad (2-20)$$

$$\text{and } X_{i(j)} = x_i + w_{ij} x_3; \quad X_{1(12)} = x_1 + w_{12} x_3 \quad (2-21)$$

$$X_{i(j)} + X_{j(i)} = 1 \quad (2-22)$$

where G_{mix}^{xs} is the contribution of non-ideal interactions between the components of ternary system, also known as the excess Gibbs energy of mixing, x_i is a mole fraction of i component in ternary compound, $X_{i(j)}$ is a mole fraction of i component in binary i-j compound, G_{ij}^{xs} is the excess Gibbs energy of mixing for binary i-j compound, L_{123} is an excess ternary interaction parameter, and w_{ij} is a weighting factor. By adopting different weighting factors, the three commonly used methods such as Kohler, Muggianu and Toop models are easily generated.

In the Kohler model, a weighting factor is defined as

$$w_{12} = \frac{x_1}{x_1 + x_2} \quad (2-23)$$

$$X_{1(12)} = x_1 + \frac{x_1}{x_1 + x_2} x_3 = \frac{x_1}{x_1 + x_2}; X_{2(12)} = \frac{x_2}{x_1 + x_2} \quad (2-24)$$

and can be described geometrically as Figure 2-8 (a). The Muggianu model adopts a simple weighting factor defined as

$$w_{12} = w_{21} = 0.5 \quad (2-25)$$

$$X_{1(12)} = x_1 + 0.5x_3 = \frac{1}{2}(1 + x_1 - x_2); X_{2(12)} = \frac{1}{2}(1 + x_2 - x_1) \quad (2-26)$$

and is geometrically represented by Figure 2-8 (b). In the Maggianu extrapolation it can be seen that the line from the ternary alloy composition to the edge binaries forms a right-angle to the binary. This leads to the consequence that, when the alloy composition is dilute in two of the components, the interaction parameter of these two components will approach regular behavior because the term $(x_i - x_j)$ becomes small.

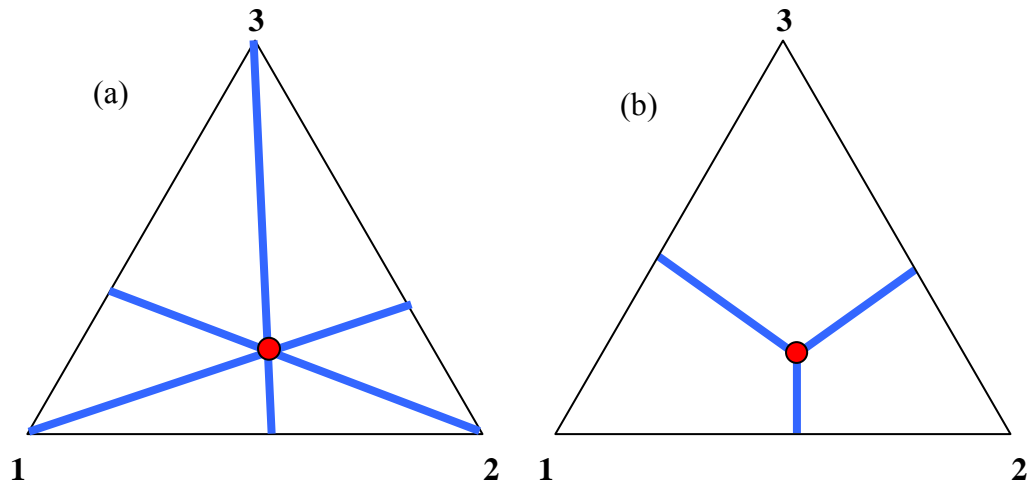


Figure 2-8. Geometrical construction of (a) Kohler and (b) Muggianu model

Both the Kohler and Muggianu models can be considered symmetrical as they treat all three components in the same way. Another method called the Toop model is different in that it considers one of the binary systems does not behave in the same as the others, and thus its weighting factor is defined as

$$w_{12} = 0; \quad w_{21} = 1 \quad (2-27)$$

$$X_{1(12)} = x_1; \quad X_{2(12)} = 1 - x_1 = x_2 + x_3 \quad (2-28)$$

and geometrically described as Figure 2-9.

Practically, the phase boundaries calculated by either the Muggianu and Kohler extrapolations seem to provide similar results [Ans78], but it was also noted that the choice of extrapolation method should receive more attention when exact knowledge of partial quantities such as activity coefficients is more critical. It is known that the Toop model is not suitable for metallic systems but may be appropriate for some ionic liquid systems. It should, however, be used carefully in all cases as the extrapolation is dependent on which binary is chosen to behave differently, and it is possible to obtain three different answers depending on this choice [Sau98].

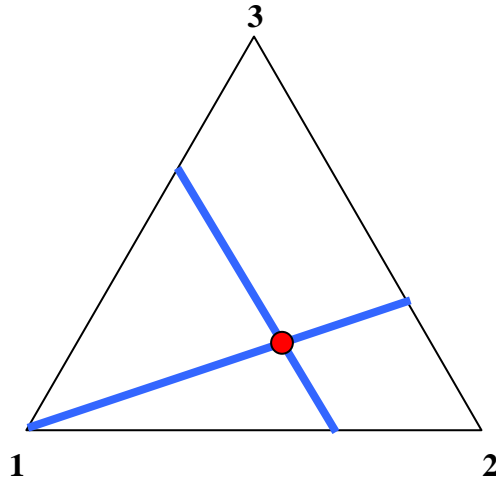


Figure 2-9. Geometrical construction of Toop model

The ThermoCalc program used for optimization of the Cu-In-Se ternary system is adopting a Muggianu model. By plugging equations (2-25) and (2-26) into equation (2-20) with Redlich-Kister equation for the binary excess Gibbs energy, G_{ij}^{xs} , as expressed by

$$G_{mix}^{xs} = x_1x_2 \left\{ L_{12}^0 + L_{12}^1(x_1 - x_2) + \dots \right\} + x_2x_3 \left\{ L_{23}^0 + L_{23}^1(x_2 - x_3) + \dots \right\} + x_1x_3 \left\{ L_{13}^0 + L_{13}^1(x_1 - x_3) + \dots \right\} \quad (2-29)$$

where L^0 is the binary interaction parameter of regular solution model and L^1 is the binary interaction parameter of sub-regular solution model. It is generally called the Redlich-Kister-Muggianu equation.

2.2.3 Experimental Information

2.2.3.1 Ternary compounds

Four ternary compounds $\text{Cu}_{13}\text{In}_3\text{Se}_{11}$, CuInSe_2 , CuIn_3Se_5 , and CuIn_5Se_8 , located on the $\text{Cu}_2\text{Se}-\text{In}_2\text{Se}_3$ pseudo-binary section (Figure 2-10), were identified as stable phases, though several other compounds have been reported [Göd00a-c]. The CuInSe_2 , CuIn_3Se_5 and CuIn_5Se_8 phases have large homogeneity ranges. Under atmospheric pressure, CuInSe_2 has two polymorphs separated by a first order transition between chalcopyrite (α) and sphalerite (δ) structures. The CuIn_3Se_5 has a tetragonal chalcopyrite-like structure and the CuIn_5Se_8 has a hexagonal structure. Interestingly, it was found that another phase often co-exists with a hexagonal CuIn_5Se_8 . This co-existing phase could be a trigonal [Mer00] or tetragonal [Koh00] structure. The $\text{Cu}_{13}\text{In}_3\text{Se}_{11}$ is reported as a line compound [Göd00b], which is stable within the narrow temperature range 923 to 947 °C.

2.2.3.2 Thermodynamic properties

Only few thermodynamic data are available for CuInSe_2 compounds. The heat capacity of CuInSe_2 was measured by Boehnke *et al.* using both pulsed and semi-adiabatic calorimetric techniques, but only at low temperature (<300K) [Boe87]. The experimental values of the enthalpy of formation of CuInSe_2 at 298K are summarized in

Table 2-5. No thermodynamic information, however, has been reported concerning the CuIn₃Se₅ and CuIn₅Se₈ compounds.

Table 2-5. The experimental values of the standard formation enthalpy ($\Delta H_{f,298K}^0$) and energy ($\Delta E_{f,0}^0$) of α -CuInSe₂

$-\Delta H_{f,298K}^0$ (kJ/mol)	Method	Reference
267.4	Mass Spectrometry	[Ber73]
260.2	Calculation	[Gla79]
280.0	Calculation	[Gom84]
189.8	Calculation	[Red48]
204.4	Calculation	[Moo99]
<hr/>		
$\Delta E_{f,0}^0$ (kJ/mol)		
190.30	<i>ab initio</i>	[Zha98]

Electro-motive force (EMF) measurements were performed by Ider [Ide03], to extract Gibbs energy information of ternary compounds (e.g., CuInSe₂, CuIn₃Se₅, CuIn₅Se₈) from the appropriate galvanic cell reactions. It is noted that since the exact composition of the participating ternary compounds is generally unknown or may be far from the stoichiometry, the resulting thermodynamic properties directly calculated from cell reactions may not be quite reliable.

2.2.3.3 Phase diagrams

The Cu₂Se-In₂Se₃ pseudo-binary section [Kon82, Fea86, Haa98] and projection of liquidus surface [Mer00, Kon82, Fea86, Boe87, Bac88] have been reported by several authors. These phase diagrams, however, are quite divergent and thus very difficult to assess. Gödecke *et al.* reported a series of phase diagrams of the Cu-In-Se system based on thorough experiments using more than 240 alloys [Göd00a-c], where the phase diagrams, including a projection of liquidus surfaces, a projection of four-phase plane, three isothermal sections and ten isopleths, are self-consistent.

2.2.4 *Ab initio* Calculation on the Ternary Cu-In-Se Compounds

The formation energies of different point defects in various Cu-In-Se ternary compounds were calculated by Zhang using an *ab initio* method. The existence of a series of unusual ordered defect compounds (ODC) along the CuSe₂-In₂Se₃ section and their large off-stoichiometry are explained by the particularly low formation energy of the (2V_{Cu}+In_{Cu}) defect pair in these compounds [Zha98].

The CuIn₃Se₅ and CuIn₅Se₈ are considered as ODC's of CuInSe₂ and form by the reaction of



where n=2.5, m=0.5 for CuIn₃Se₅ and n=4 m=1 for CuIn₅Se₈. The energy change of the reaction is calculated by

$$\Delta E_r = \Delta E_{neu} + \Delta E_{int} + \Delta E_{ord} \quad (2-31)$$

where ΔE_{neu} is the formation energy of non-interacting neutral defects, ΔE_{int} is the intra-pair interaction energy, and ΔE_{ord} is the pair-pair ordering energy. The formation energies of CuIn₃Se₅ and CuIn₅Se₈ compounds can then be calculated by

$$\Delta E_{\text{CuIn}_3\text{Se}_5}^f = 2.5\Delta E_{\text{CuInSe}_2}^f + 0.5E_{In} - 1.5E_{Cu} + \Delta E_r(\text{CuIn}_3\text{Se}_5) \quad (2-32)$$

$$\Delta E_{\text{CuIn}_5\text{Se}_8}^f = 4\Delta E_{\text{CuInSe}_2}^f + E_{In} - 3E_{Cu} + \Delta E_r(\text{CuIn}_5\text{Se}_8) \quad (2-33)$$

As the defect compounds are related to the end-members in the sub-lattice model, their formation energies are used to estimate the Gibbs energy of the end-members. It can largely reduce the arbitrary aspects of the model parameters. For example, the formation energy of V_{Cu} is defined as the energy change of the reaction



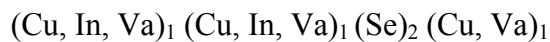
InInSe₂(α) is regarded as a end-member in the sub-lattice model of CuInSe₂(α) and its Gibbs energy can be estimated from the formation energy of V_{Cu}.

2.2.5 Establishment of Thermodynamic Descriptions

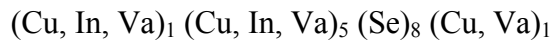
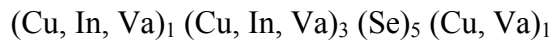
In this work, sub-lattice models [Sau98] are used to describe thermodynamic properties of the ternary compounds. Unlike conventional thermodynamic optimization evaluating model parameters from abundant sources of phase diagrams and thermodynamic experiments, only one set of data were selected for this work to avoid the possible confusion caused by randomly mixing the divergent data for such a complicated system.

2.2.5.1 Sub-lattice model for different ternary compounds

The α -CuInSe₂ belongs to the family of I-III-VI₂ chalcopyrite semiconductors whose structure is similar to the zinc-blende structure where each of the two cations (Cu and In) are coordinated by four anions (Se), but the Se is coordinated by (2Cu + 2In) with different nearest-neighbors. The Se deficiency is mainly caused by Cu occupying an interstitial position [Zha98], the sub-lattice structure of α -CuInSe₂ is thus considered as



Formula (5.37) in [Sau98] is used to calculate Gibbs energy of this phase where the Gibbs energy of the 18 end-members including Cu₁In₁Se₂Va₁, Cu₁Cu₁Se₂Va₁, and Va₁Cu₁Se₂Va₁, needs to be estimated. In the same manner, the sub-lattice structures of CuIn₃Se₅ and CuIn₅Se₈ are expressed by



The δ -CuInSe₂ is a disordered phase of α -CuInSe₂ with a sphalerite structure where the two metals (Cu and In) can be replaced by each other much more easily than in α -

CuInSe₂ to achieve almost random mixing. The sub-lattice structure of the δ-CuInSe₂ is considered as (Cu,In,Va)₂(Se)₁(Se,Va)₂ to keep its composition close to the section of Cu₂Se-In₂Se₃, as observed experimentally.

2.2.5.2 Evaluation of Gibbs energies of end-members in the sub-lattice model

Gibbs energy of formation of CuInSe₂(α)

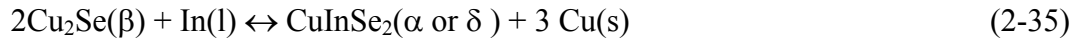
To estimate the Gibbs energy of formation of CuInSe₂(α), the EMF results reported by Ider [Ide03] were utilized. Three different kinds of galvanic cells were designed:

Cell I: W, In(l), In₂O₃(s) // YSZ // In₂O₃(s), Cu₂Se(β), Cu(s), CuInSe₂(α or δ), C, W

Cell II: W, In(l), In₂O₃(s) // YSZ // In₂O₃(s), Cu₁In₃Se₅(s), CuInSe₂(α or δ), C, W

Cell III: W, In(l), In₂O₃(s) // YSZ // In₂O₃(s), Cu₁In₅Se₈(s), Cu₁In₃Se₅(s), C, W

The overall reaction of cell I is expressed as



In this work, the composition of CuInSe₂ is assumed to be in stoichiometry because the CuInSe₂ phase has a relatively narrow composition range when it is in equilibrium with Cu₂Se(β). Thus if the solubility of In in Cu₂Se(β) phase is negligible, the Gibbs energy of formation of CuInSe₂(α) can be directly calculated by

$$\Delta G_{\text{CuInSe}_2(\alpha)}^f = \Delta G_R (\text{cell I}) + 2\Delta G_{\text{Cu}_2\text{Se}(\beta)}^f \quad (2-36)$$

and ΔG_R was reported by Ider [Ide03] as

$$\Delta G_R = -99520 + 54.50 \times T \quad [\text{J/mol}] \quad (949 \text{ to } 1044 \text{ K}) \quad (2-37)$$

From assessment of the Cu-Se system, the $\Delta G_{\text{Cu}_2\text{Se}(\beta)}^f$ is expressed by

$$\begin{aligned} \Delta G_{\text{Cu}_2\text{Se}(\beta)}^f = & - 60221.86 - 95.47 \times T + 10.21 \times T \ln(T) - 0.01 \times T^2 + 3.70 \times 10^{-6} \times T^3 \\ & - 53288.13/T \quad [\text{J/mol}] \end{aligned} \quad (2-38)$$

Plugging equations (2-37) and (2-38) into equation (2-36) yields

$$\Delta G_{CuInSe_2(\alpha)}^f = -209963.72 - 36.43 \times T + 20.41 \times T \ln(T) - 0.02 \times T^2 + 7.40 \times 10^{-6} \times T^3 - 106576.26/T \quad [J/mol] \quad (2-39)$$

The standard enthalpy of formation of CuInSe₂(α) at 298.15K calculated from $\Delta G_{CuInSe_2(\alpha)}^f$ obtained by equation (2-39) is around 218.50 kJ/mol, which is similar to the literature values listed in Table 2-5.

Estimation of Gibbs energy of CuInSe₂(δ), CuIn₃Se₅ and CuIn₅Se₈

As mentioned before, EMF experimental results can provide only a rough estimation of the Gibbs energy of formation of CuInSe₂(δ), CuIn₃Se₅ and CuIn₅Se₈ mainly because of their non-stoichiometric composition during cell reaction. Ider [Ide03] reported the Gibbs energy change of reaction for cell I through III such as

$$\Delta G_R (Cell I) = -89520 + 45.10 \times T \quad [J/mol] \quad (1055 \text{ to } 1150K) \quad (2-40)$$

$$\Delta G_R (Cell II) = 90160 - 110.77 \times T \quad [J/mol] \quad (868 \text{ to } 1045K) \quad (2-41)$$

$$\Delta G_R (Cell III) = 109180 - 125.90 \times T \quad [J/mol] \quad (1054 \text{ to } 1179K) \quad (2-42)$$

In the exactly same manner as for CuInSe₂(α), the Gibbs energies of formation of other ternary compounds (i.e., CuInSe₂(δ), CuIn₃Se₅ and CuIn₅Se₈) were estimated as

$$\Delta G_{CuInSe_2(\delta)}^f = -209963.72 - 145.83 \times T + 20.41 \times T \ln(T) - 0.02 \times T^2 + 7.40 \times 10^{-6} \times T^3 - 106576.26/T \quad [J/mol] \quad (2-43)$$

$$\Delta G_{CuIn_3Se_5}^f = -438646.71 - 1794.61 \times T + 259.98 \times T \ln(T) - 9.84 \times 10^{-2} \times T^2 + 2.40 \times 10^{-5} \times T^3 - 528546.24/T \quad [J/mol] \quad (2-44)$$

$$\Delta G_{CuIn_5Se_8}^f = -717569.69 - 3404.57 \times T + 499.55 \times T \ln(T) - 1.48 \times 10^{-1} \times T^2 + 4.07 \times 10^{-5} \times T^3 - 1163668.00/T \quad [J/mol] \quad (2-45)$$

On the other hand, the Gibbs energy of formation of CuIn₃Se₅ and CuIn₅Se₈ at their stoichiometric composition can also be estimated by *ab initio* calculation where they are considered as ordered defect compounds of CuInSe₂. In the same pattern as equations (2-32) and (2-33), the Gibbs energy of formation of CuIn₃Se₅ and CuIn₅Se₈ are expressed by

$$\Delta G_{CuIn_3Se_5}^f = 2.5\Delta G_{CuInSe_2}^f + 0.5G_{In} - 1.5G_{Cu} + \Delta G_r(CuIn_3Se_5) \quad (2-46)$$

$$\Delta G_{CuIn_5Se_8}^f = 4\Delta G_{CuInSe_2}^f + G_{In} - 3G_{Cu} + \Delta G_r(CuIn_5Se_8) \quad (2-47)$$

In this work, the volume and entropy change for the defect formation reaction is assumed to be negligible and thus the values of $\Delta G_r(CuIn_3Se_5)$ and $\Delta G_r(CuIn_5Se_8)$ are identical to $\Delta E_r(CuIn_3Se_5)$ and $\Delta E_r(CuIn_5Se_8)$ calculated by equation (2-31) where the values of ΔE_{neu} , ΔE_{int} , and ΔE_{ord} are taken from [Zha98] as shown in Table 2-6. The value of $\Delta G_{CuInSe_2(\alpha)}^f$ is directly calculated from equation (2-39).

In summary, the estimated Gibbs energies of formation from the *ab initio* study are

$$\begin{aligned} \Delta G_{CuIn_3Se_5}^f = & -557341.00 - 337.26 \times T + 51.04 \times T \ln(T) - 5.51 \times 10^{-2} \times T^2 \\ & + 1.85 \times 10^{-5} \times T^3 - 266441.00/T \quad [\text{J/mol}] \end{aligned} \quad (2-48)$$

$$\begin{aligned} \Delta G_{CuIn_5Se_8}^f = & -892788.00 - 538.09 \times T + 81.66 \times T \ln(T) - 8.81 \times 10^{-2} \times T^2 \\ & + 2.96 \times 10^{-5} \times T^3 - 426305.00/T \quad [\text{J/mol}] \end{aligned} \quad (2-49)$$

Table 2-6. Parameters used to calculate ΔE^f of CuIn₃Se₅ and CuIn₅Se₈ [Zha98].

	$\Delta E_{neu}(\text{eV})$	$\Delta E_{int}(\text{eV})$	$\Delta E_{ord}(\text{eV})$	$\Delta E_r(\text{eV})$
CuIn ₃ Se ₅	2.27	-2.105	-0.225	-0.06
CuIn ₅ Se ₈	4.54	-4.21	-0.43	-0.10

Estimation of the Gibbs energy of other end-members

The Gibbs energy of the other end-members in the α -CuInSe₂, β -CuIn₃Se₅, γ -CuIn₅Se₈ compounds is estimated using the defect formation energies calculated by Zhang [Zha98] according the defect formation reactions such as equation (2-34).

For example,

$$G_{\text{Va}_1\text{Cu}_1\text{Se}_2\text{Va}_1}^0 = G_{\text{CuInSe}_2(\alpha)}^0 + E_{\text{Va}(Cu)} - G_{\text{Cu}}^0 \quad (2-50)$$

$$G_{\text{Cu}_1\text{In}_1\text{Se}_2\text{Cu}_1}^0 = G_{\text{CuInSe}_2(\alpha)}^0 + E_{\text{Cu}(i)} + G_{\text{Cu}}^0 \quad (2-51)$$

Optimization of parameters in the Gibbs energy expressions

The Gibbs energy expressions of the ternary compounds are adjusted to satisfy the relevant experimental phase relationships [Göd00a-c]. The results are compared with the available data. It is believed that the complicated phase relationships may play an important role in controlling the chemical potentials of these compounds within a reasonable range. Finally, the Gibbs energy parameters are optimized as

$$\begin{aligned} G_{\text{CuInSe}_2(\alpha)}^0 &= -251102.38 - 688.51 \times T - 135.95 \times T \ln(T) + 0.03 \times T^2 \\ &\quad - 3.47 \times 10^{-6} \times T^3 - 265806.00/T \quad [\text{J/mol}] \end{aligned} \quad (2-52)$$

$$G_{\text{CuInSe}_2(\delta)}^0 = -186607.34 + 505.39 \times T - 114.87 \times T \ln(T) \quad [\text{J/mol}] \quad (2-53)$$

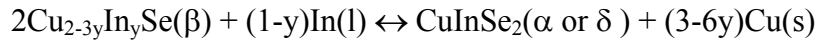
$$\begin{aligned} G_{\text{CuIn}_3\text{Se}_5}^0 &= -550466.88 + 1175.69 \times T - 249.24 \times T \ln(T) - 1.02 \times 10^{-3} \times T^2 \\ &\quad - 1.22 \times 10^{-7} \times T^3 - 582645.00/T \quad [\text{J/mol}] \end{aligned} \quad (2-54)$$

$$\begin{aligned} G_{\text{CuIn}_5\text{Se}_8}^0 &= -940623.58 + 1916.46 \times T - 389.81 \times T \ln(T) + 7.32 \times 10^{-6} \times T^2 \\ &\quad - 2.90 \times 10^{-7} \times T^3 - 1006060.00/T \quad [\text{J/mol}] \end{aligned} \quad (2-55)$$

The optimized Gibbs energy (G^0) and Gibbs energy of formation (ΔG^f) are compared with the results of EMF experiment and Ab initio calculation, as represented in Figures 2-11 and 12.

2.2.6 Summary

The EMF experimental results, *ab initio* calculation, and phase equilibrium data were successfully combined to establish reliable descriptions of Gibbs energy for ternary compounds in the Cu-In-Se system. The EMF result was directly adopted only for the Gibbs energy of $\text{CuInSe}_2(\alpha)$ by assuming the stoichiometric composition. The influence of the solubility of indium in $\text{Cu}_2\text{Se}(\beta)$ on the electronic transfer and thus the Gibbs energy of formation was also considered. The reaction was considered as



The number of electrons to be transferred is (3-6y) to form one mole of $\text{CuInSe}_2(\alpha)$. The difference of Gibbs energy of formation between $\text{Cu}_{2-3y}\text{In}_y\text{Se}(\beta)$ and Cu_2Se is calculated using the formation energy of the defect pair ($2V_{\text{Cu}} + \text{In}_{\text{Cu}}$) [Zha98]. This approach, however, yields an unreasonable value of enthalpy of formation for CuInSe_2 at 298.15K, whereas the calculation using $\Delta G_{\text{Cu}_2\text{Se}(\beta)}^f$ expression in equation (2-38) shows reasonable results, which is in a good agreement with most of literature values.

The comparison of the optimized Gibbs energy of the $\text{CuInSe}_2(\delta)$, CuIn_3Se_5 and CuIn_5Se_8 with that estimated by EMF experiment and *ab initio* calculation demonstrates reasonable agreement. The phase relationships concerning these ternary compounds follow the experimental isothermal section of the Cu-In-Se system at 500, 800 and 900 °C shown in Figures 2-13 to 15, respectively. It can be concluded that a set of reliable

Gibbs energy expression was obtained, although its precision would be further improved with additional experimental and theoretical study.

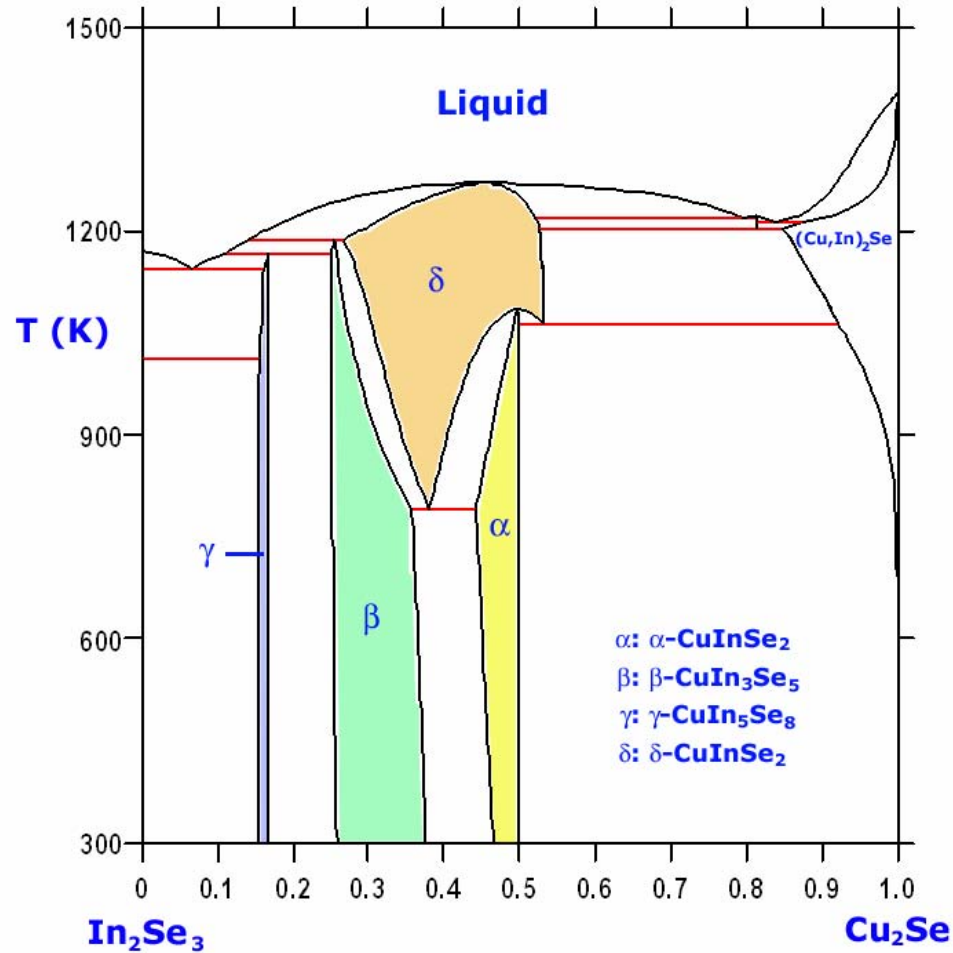


Figure 2-10. Pseudo-binary In_2Se_3 - Cu_2Se phase diagram [Göd00a]

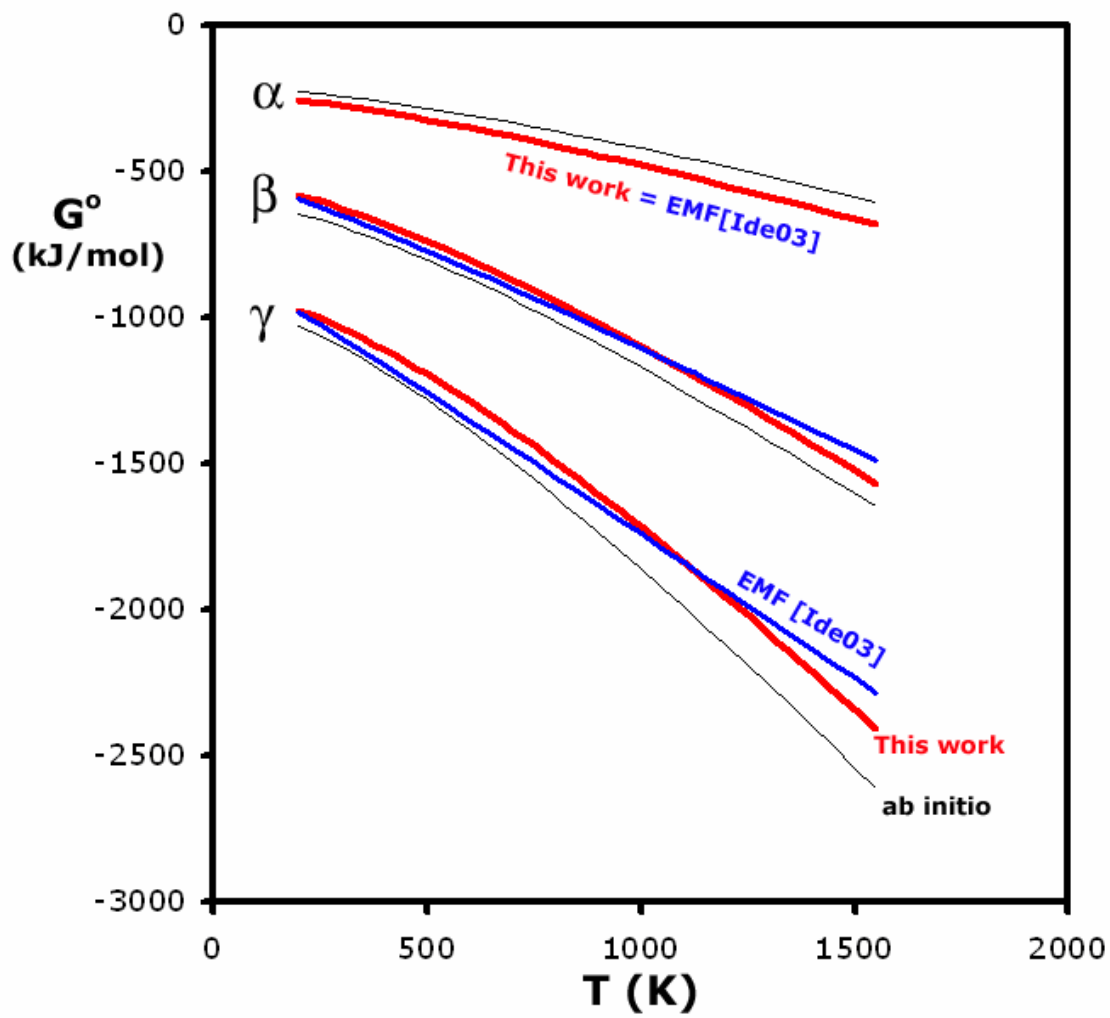


Figure 2-11. Optimized Gibbs energy α -CuInSe₂, β -CuIn₃Se₅ and γ -CuIn₅Se₈ compared with that estimated from EMF experiments and ab initio calculation

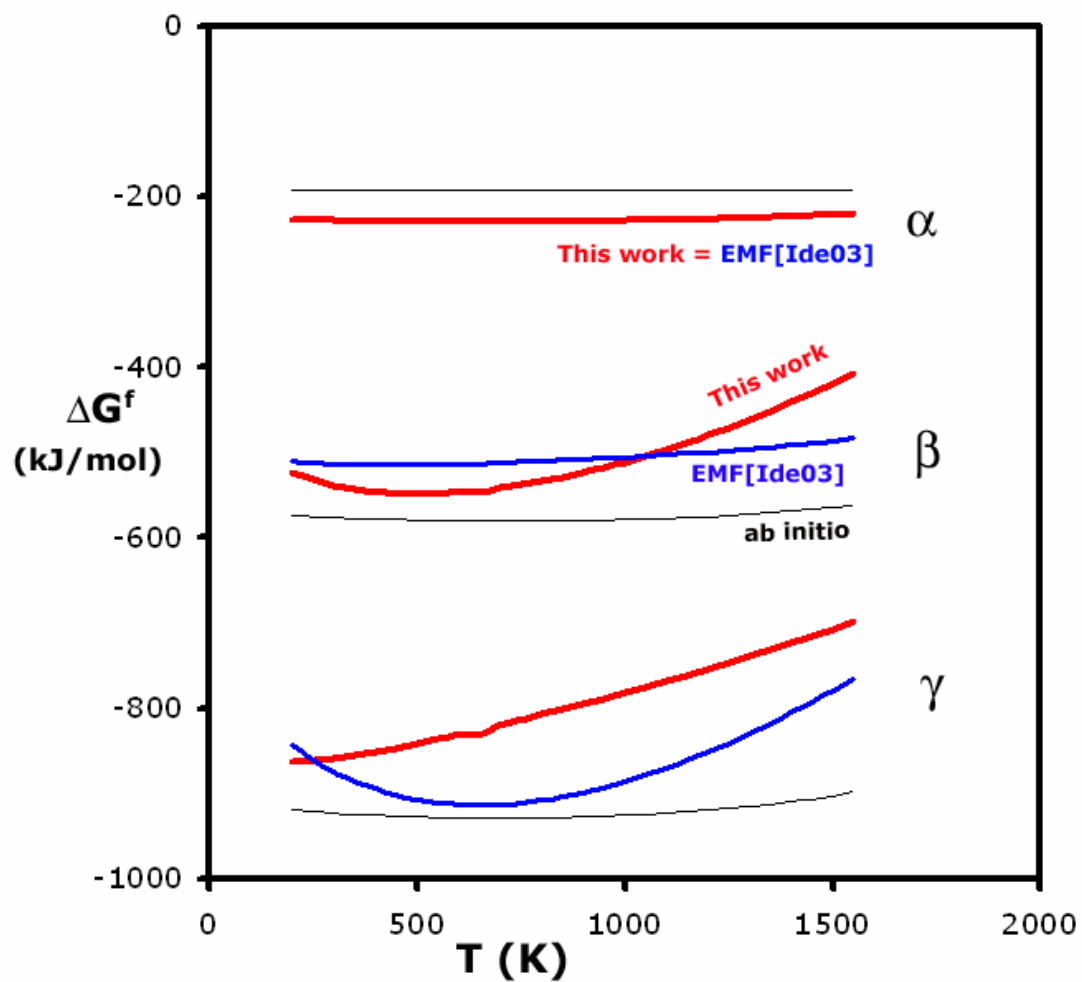


Figure 2-12. Optimized Gibbs energy of formation of α -CuInSe₂, β -CuIn₃Se₅ and γ -CuIn₅Se₈ compared with that estimated from EMF experiments and ab initio calculation

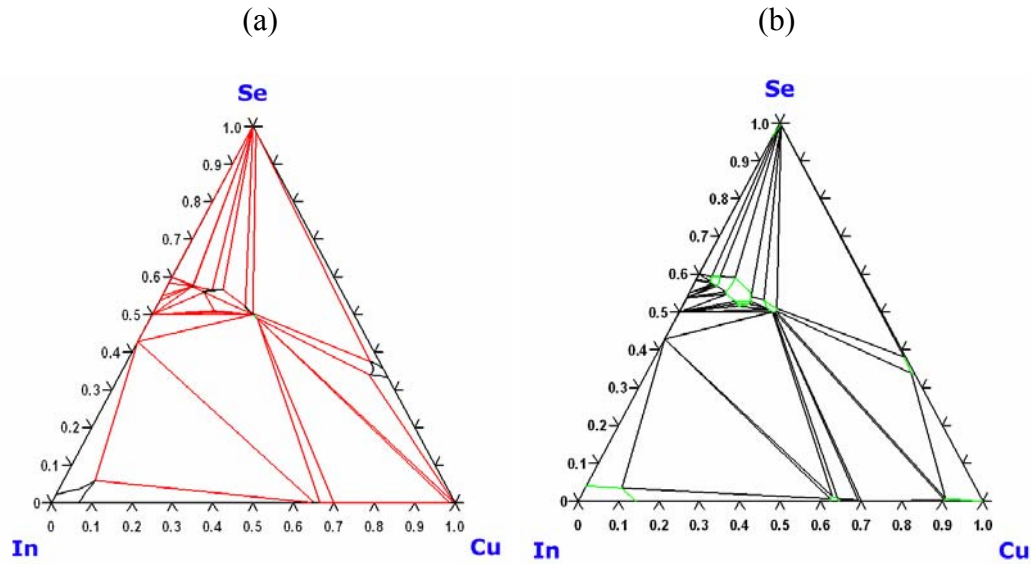


Figure 2-13. Isothermal sections of Cu-In-Se at 500 °C. (a) Calculation [She06], (b) Experimental evaluation [Göd00c]

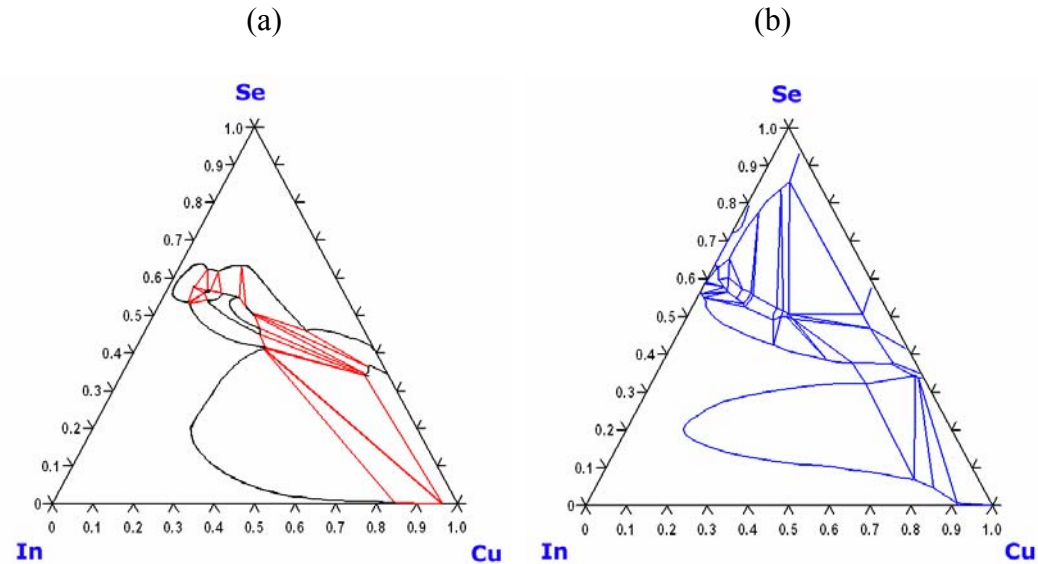


Figure 2-14. Isothermal sections of Cu-In-Se at 800 °C. (a) Calculation [She06], (b) Experimental evaluation [Göd00c]

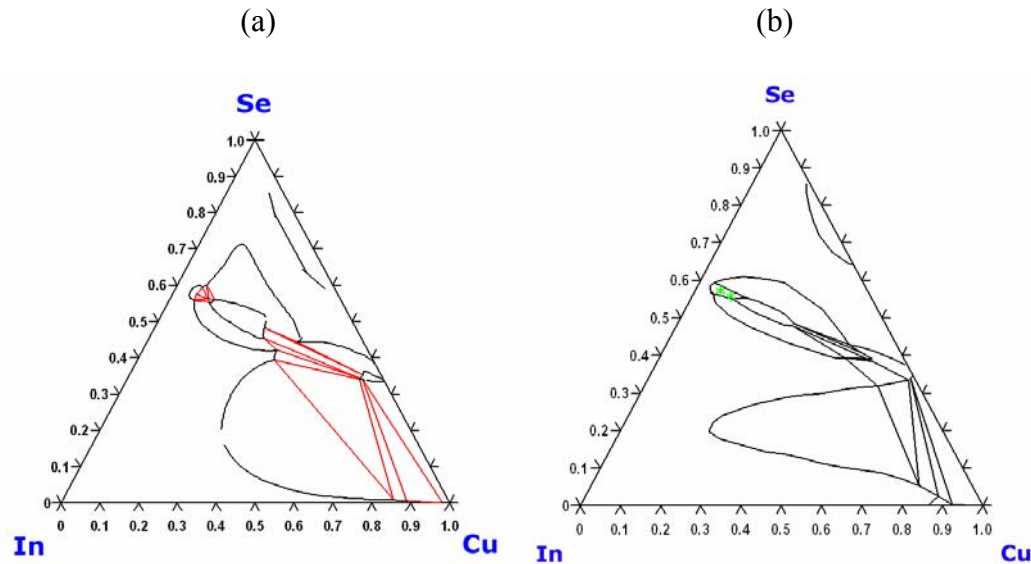


Figure 2-15. Isothermal sections of Cu-In-Se at 900 °C. (a) Calculation [She06], (b) Experimental evaluation [Göd00c]

2.3 Cu-Ga-In Ternary Phase Diagram Calculation

2.3.1 Introduction

The selenization of metallic Cu/Ga/In precursors is one of the most promising industrial processes for CIGS cell fabrication, which is generally called the “two-step process” and has been commercially employed by Shell Solar and Showa Shell. The commercialized two-step process consists of the deposition of metallic precursors (i.e., Cu/Ga/In) followed by subsequent selenization, as shown in Figure 1-8. Traditionally, the metal precursors are prepared by sputter deposition and then selenized at high temperature (~600 °C) in a reactive H₂Se or Se vapor ambient. Therefore, understanding the equilibrium phase relationships in the Cu-Ga-In ternary system is essential to the optimization of the two-step process.

2.3.2 Review of Sub-binary Phase Diagrams

The phase diagrams of the three sub-binary systems, e.g., Cu-In, Cu-Ga and Ga-In, were well assessed by Liu [Liu02], Subramanian [Sub88], and Anderson and Ansara [And91], respectively. Thermodynamic assessment of the Cu-In binary phase diagram was first performed by Kao *et al.* [Kao93], based on the review [Bol93] of thermodynamic and phase equilibrium data available in the literature. In their assessment, a Redlich-Kister expression was used to represent the Gibbs energies of the liquid and Cu phase, and a Wagner-Schottky model was employed for the Gibbs energy of η -Cu₂In phase. All other intermetallic phases were then approximated as line compounds. Recently, Liu *et al.* [Liu02] reassessed the Cu-In binary phase diagram by including additional experimental data [Bah99, Dic00] and adopting a three-sublattice models for γ and η' phases, while assuming stoichiometric compounds for other intermetallic phases,

as shown in Figure 2-16. Most recently, Bahari *et al.* reported new experimental data using DSC, XRD, and EPMA analysis [Bah03]. The results indicate the existence of a solubility region of indium in copper with the limit of the solid solution at 5.20 at.% In at 400 °C and of six intermediate phases, i.e., the three low-temperature phases δ , η and θ , $\text{Cu}_{11}\text{In}_9(\theta)$, and the three high-temperature phases γ , η' and β . The boundaries of each phase were defined with respect to temperature and composition.

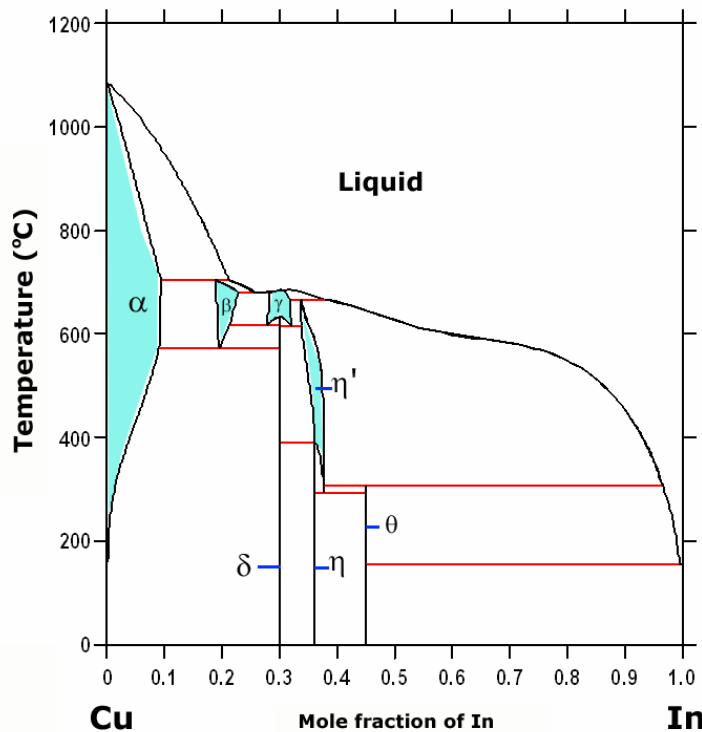


Figure 2-16. Calculated phase diagram of Cu-In binary system [Liu02]

The general features of the Cu-Ga phase relationships have been well established by Hansen [Han58] and subsequently revised by Kittl [Kit64]. Subramanian *et al.* [Sub88] used these accurately established phase boundaries and some additional thermodynamic data to optimize the thermodynamic parameters for the various intermediate phases. The calculated phase diagram containing three binary phases β , γ and ξ is shown in Figure 2-17.

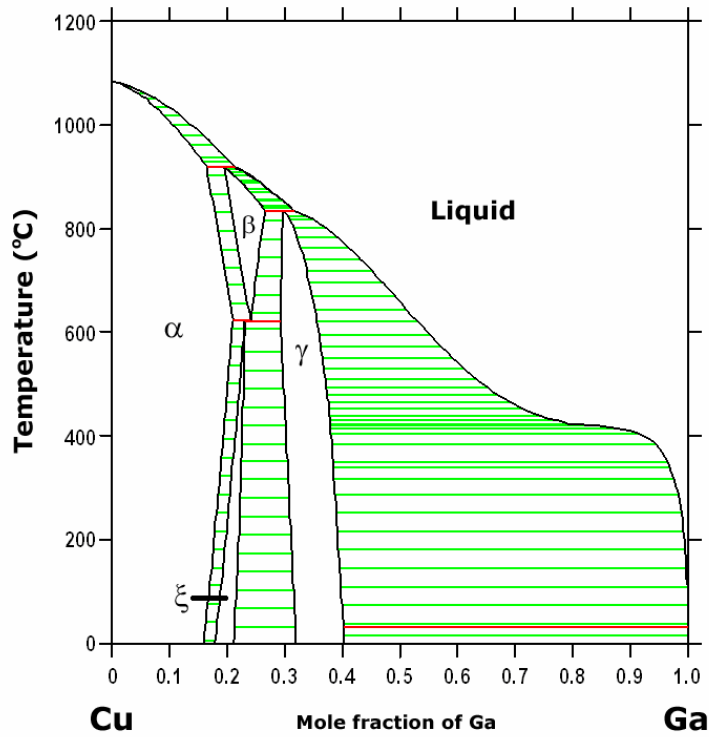


Figure 2-17. Calculated phase diagram of Cu-Ga binary system [Ide03]

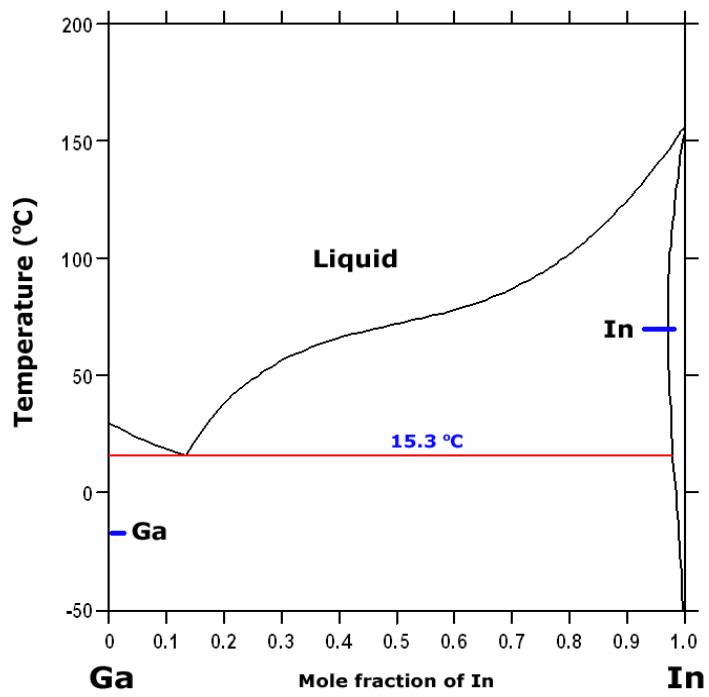


Figure 2-18. Calculated phase diagram of Ga-In binary system [And91]

The Ga-In binary system is known to be a simple eutectic type with negligible solubility of indium in solid α -Ga. The Ga-In binary phase diagram assessed by Anderson and Ansara [And91] showed a retrograde tetragonal indium solidus with solubilities of 2.3 at.% gallium in indium at the eutectic temperature of 15.3 °C and of 14.2 at.% indium in the liquid, as evidenced by Figure 2-18.

2.3.3 Prediction of Cu-Ga-In Ternary Phase Diagrams

Unfortunately, there are no experimental data available about the interaction between ternary Cu-Ga-In components. Therefore, Muggianu's equation based on the summation of the binary interaction parameters was employed to extrapolate the excess Gibbs energy of mixing into ternary system [Sau98], as described in section 2.2.2.

To use the ThermoCalc program to estimate the CGI ternary phase diagram, it is necessary to prepare the TDB (Thermodynamic DataBase) module containing the Gibbs energy information of pure Cu, Ga and In elements as well as the interaction parameters of three sub-binary Cu-Ga, Cu-In and Ga-In systems. The TDB module of ternary Cu-Ga-In system was composed by combining three binary data described in the previous section 2.3.1. For the simplification, the Cu-Ga binary compounds (i.e., β , γ and ξ) were modeled by solid-solution models, while the Cu-In binary compounds (i.e., δ , γ , η and θ) except β phase modeled by solid-solution model were modeled by sub-lattice models. The Cu-Ga-In ternary phase diagram was then predicted using ThermoCalc program, as shown in Figures 2-19 to 22. Five different solid solution phases (i.e., Cu-fcc, δ -Cu₇In₃, η -Cu₂In, ξ -Cu₇Ga₂ and γ -Cu₉Ga₄) and a liquid phase region were included in the 500 °C isothermal section of Cu-Ga-In ternary phase diagram shown in Figure 2-19. It is noted that the ternary phase diagrams presented in Figures 2-19 to 22 were estimated on the

basis of binary information only and thus the models do not contain any ternary interaction parameters. To obtain a more reliable ternary phase diagram, one needs to investigate the existence of any new ternary phases and the solubility of the third element in binary compounds, and optimize the ternary interaction parameters in a form of $G_{123} = x_1x_2x_3(L_1x_1 + L_2x_2 + L_3x_3)$.

Furthermore, the vapor pressures for Cu-Ga-In mixtures at several compositions were calculated using the ThermoCalc program in combination with the Cu-Ga-In ternary TDB module. Selected results shown in Figures 2-23 and 2-24 revealed that six vapor phase species (i.e., Cu, Cu₂, Ga, Ga₂, In and In₂) dominate the gas phase and the atomic indium is the most volatile among them.

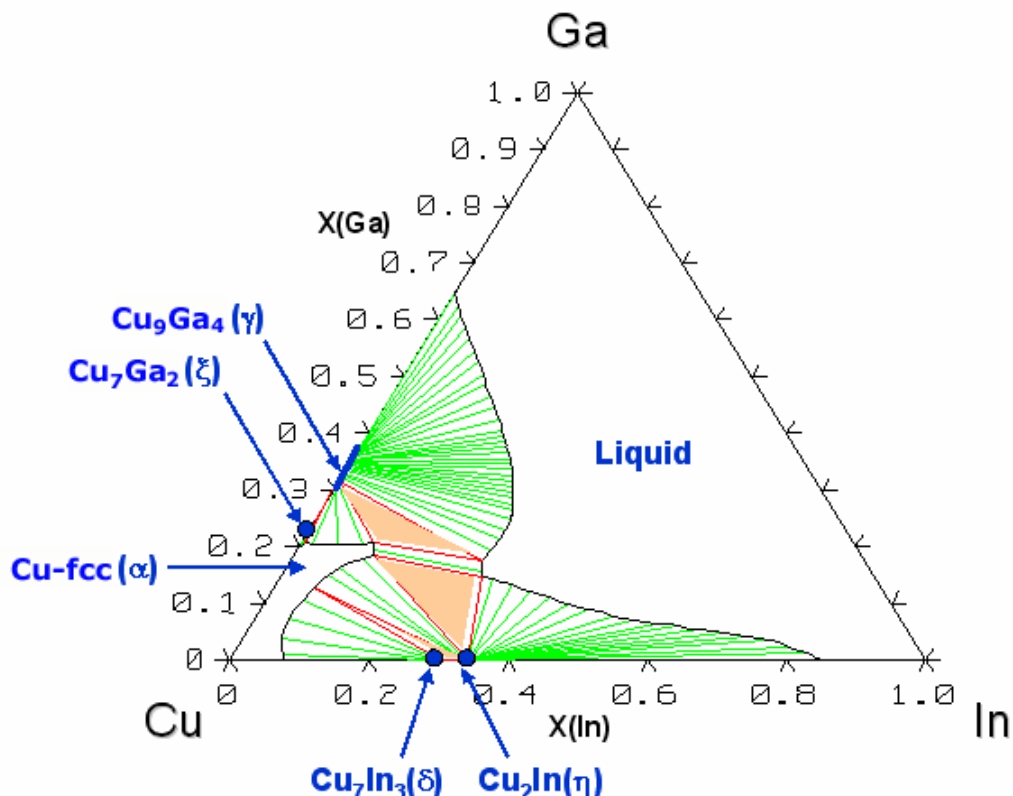


Figure 2-19. Isothermal section (500 °C, 1atm) of the Cu-Ga-In ternary phase diagram based on the Muggianu's equation

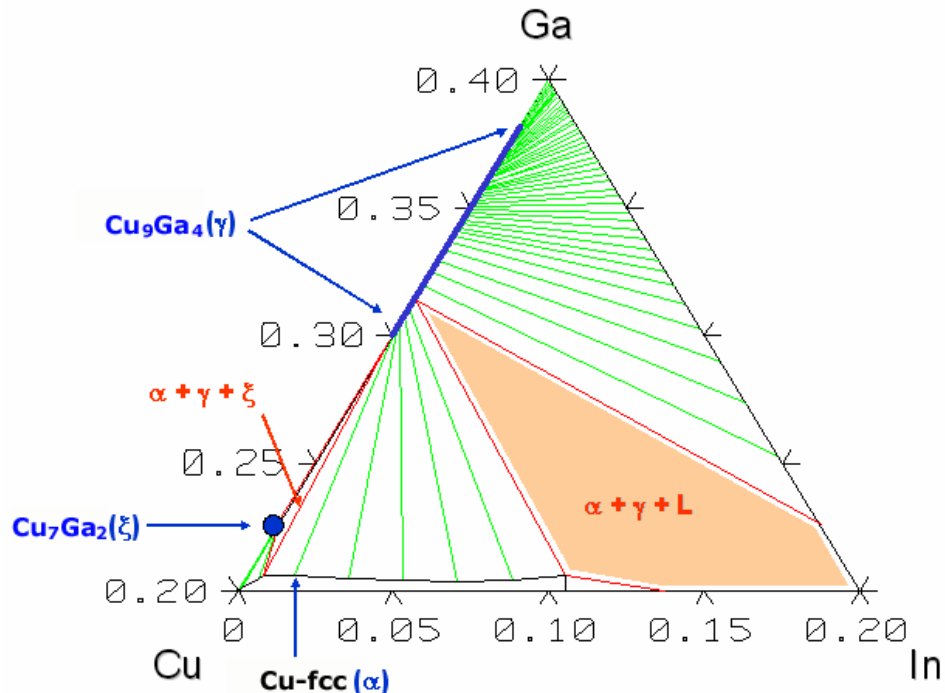


Figure 2-20. Isothermal section (500 °C, 1atm) of the Cu-Ga-In ternary phase piagram based on the Muggianu's equation for the range of $0 < x(\text{In}) < 0.2$ and $0.2 < x(\text{Ga}) < 0.4$

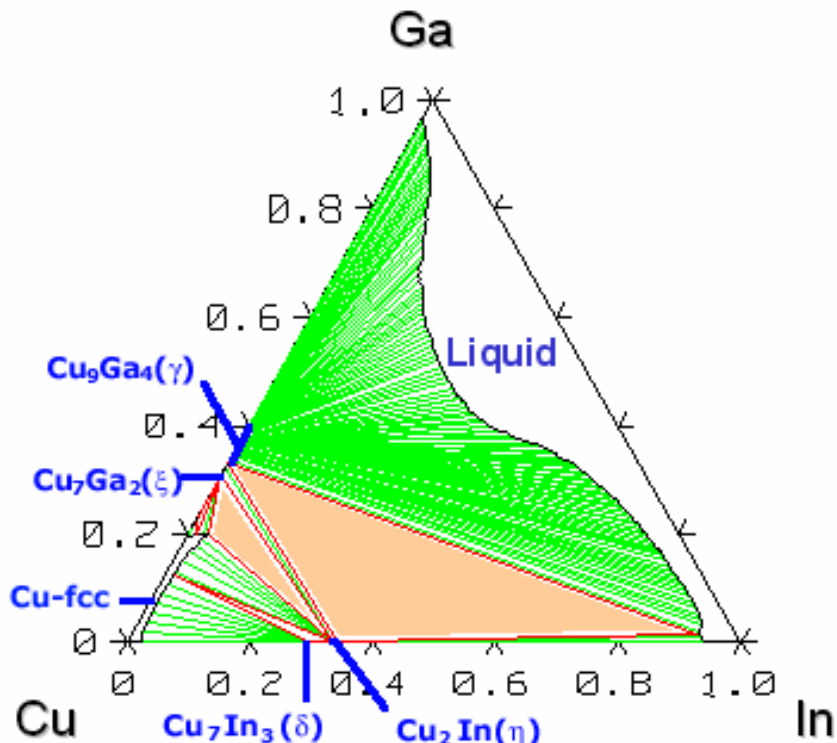


Figure 2-21. Isothermal section (350 °C, 1atm) of the Cu-Ga-In ternary phase piagram based on the Muggianu's equation

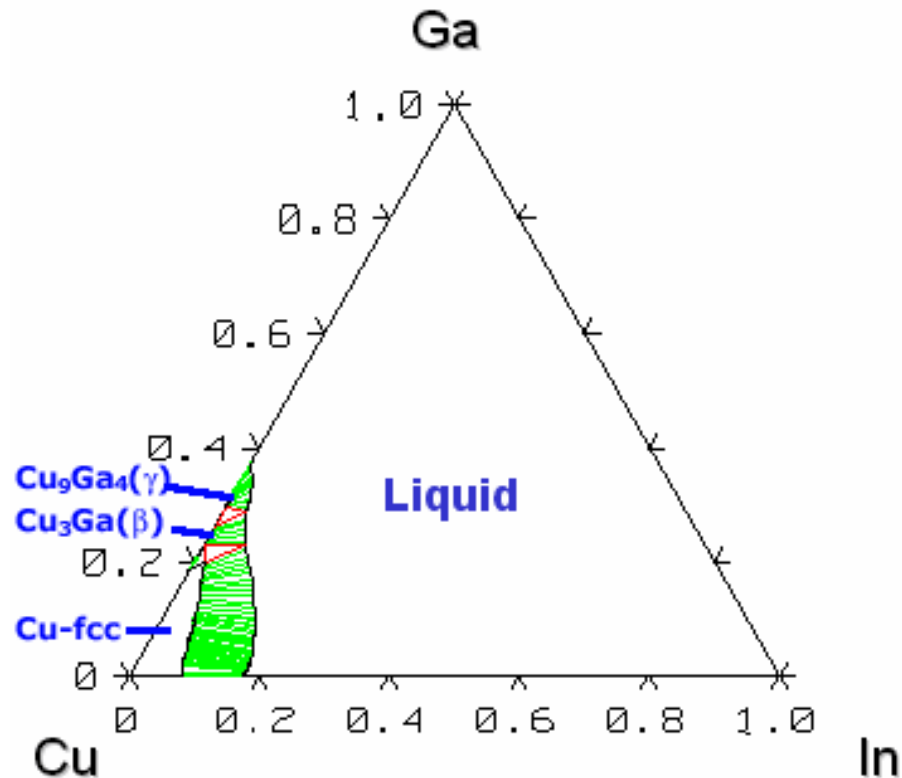


Figure 2-22. Isothermal section ($800\text{ }^{\circ}\text{C}$, 1atm) of Cu-Ga-In ternary Phase Diagram based on the Muggianu's equation

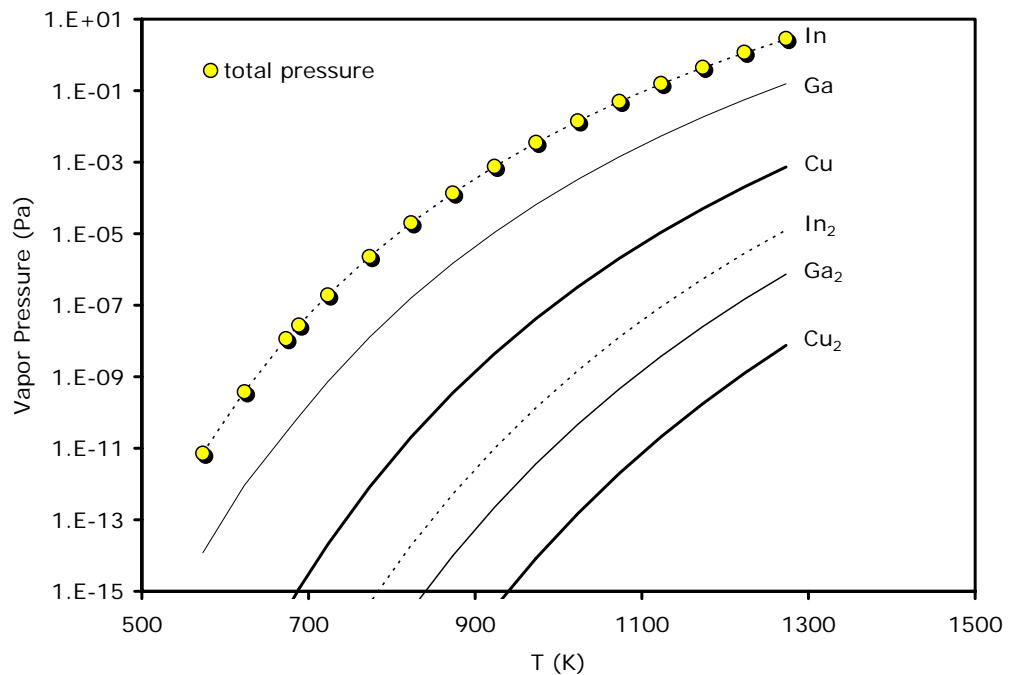


Figure 2-23. Vapor pressure as a function of temperature in the Cu-Ga-In mixture (Cu:Ga:In = 1:1:1 mole ratio)

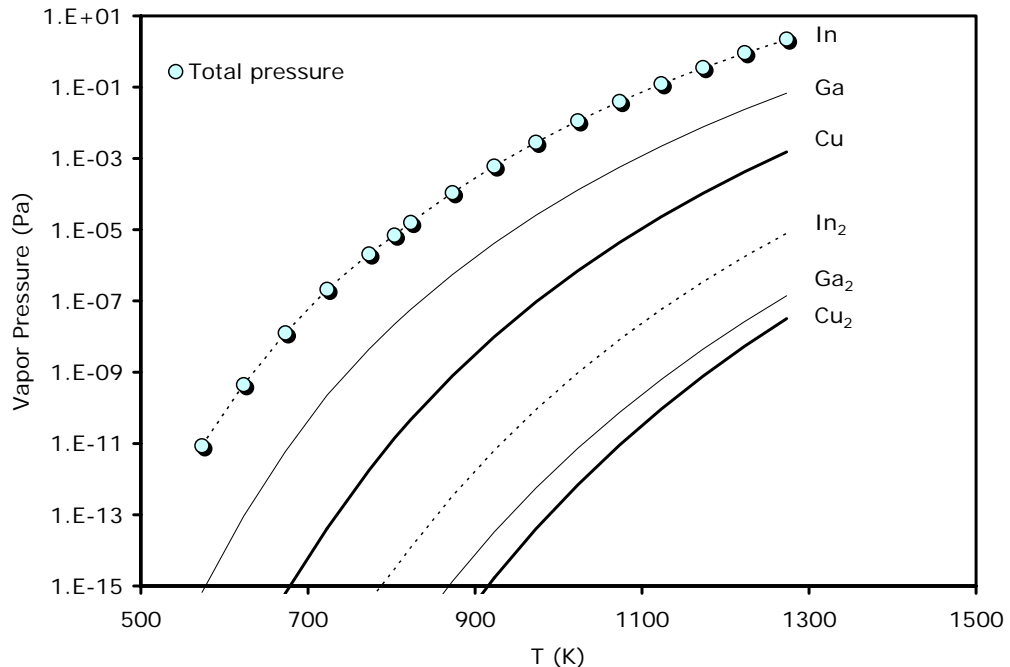


Figure 2-24. Vapor pressure as a function of temperature in the Cu-Ga-In mixture (Cu:Ga:In = 2:1:1 mole ratio)

2.3.4 Modification of Cu-Ga-In Ternary Phase Diagrams

Recently, an experimental result concerning the ternary phase relationship of the Cu-Ga-In system was reported [Pur06b]. In their study, samples were prepared by sequential DC-magnetron sputtering of 8 triple layers of the sequence Cu/CuGa₂/In on Mo-coated glass substrates to ensure a good mixing of the components. The samples were annealed in H₂ ambient to reduce any oxides at 350 °C for 2 min and then cooled to room temperature for subsequent X-ray diffraction analysis. Cu₁₆(In,Ga)₉, Cu₉(Ga,In)₄ alloys, and elemental indium were identified as the equilibrium phases in the Cu-Ga-In composition studied. This was arrived at by assuming that the shifts of Cu₁₆In₉ and Cu₉Ga₄ reflection peaks resulted from the substitution of indium by gallium and gallium by indium, respectively. Considering their results as summarized in Table 2-7, the Cu-Ga-In ternary phase diagram predicted by the Muggianu's equation was modified.

Table 2-7. Experimental results of phase relationships of Cu-Ga-In ternary system

No.	Atomic fraction			Equilibrium phases at 350 °C
	Cu	In	Ga	
1	0.479	0.458	0.063	$\text{Cu}_{16}(\text{In},\text{Ga})_9$, In
2	0.550	0.365	0.086	$\text{Cu}_{16}(\text{In},\text{Ga})_9$, In
3	0.479	0.417	0.104	$\text{Cu}_{16}(\text{In},\text{Ga})_9$, $\text{Cu}_9(\text{Ga},\text{In})_4$, In
4	0.479	0.391	0.130	$\text{Cu}_{16}(\text{In},\text{Ga})_9$, $\text{Cu}_9(\text{Ga},\text{In})_4$, In
5	0.479	0.359	0.161	$\text{Cu}_{16}(\text{In},\text{Ga})_9$, $\text{Cu}_9(\text{Ga},\text{In})_4$, In
6	0.479	0.328	0.193	$\text{Cu}_9(\text{Ga},\text{In})_4$, In
7	0.640	0.230	0.129	$\text{Cu}_{16}(\text{In},\text{Ga})_9$, $\text{Cu}_9(\text{Ga},\text{In})_4$
8	0.659	0.123	0.218	$\text{Cu}_9(\text{Ga},\text{In})_4$

Based on experimental data at 350 °C, the thermodynamic parameters were manually adjusted to account for the extended solid solutions as reported. To describe the solubility of indium into Cu_9Ga_4 , which is expressed as $\text{Cu}_9(\text{Ga},\text{In})_4$, the two-sublattice model described by (Cu,Va) (Ga,In) was employed. The resulting isothermal section of Cu-Ga-In ternary phase diagram at 350 °C and 1 atm along with experimental data is shown in Figure 2-25.

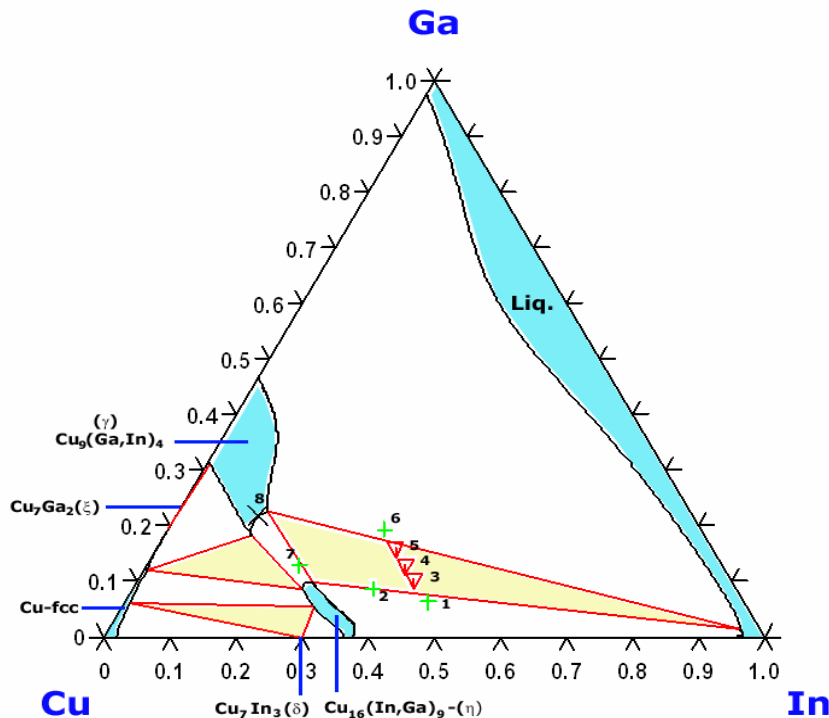


Figure 2-25. Modified isothermal section ($350\text{ }^{\circ}\text{C}$, 1atm) of the Cu-Ga-In ternary phase diagram with experimental data (symbol)

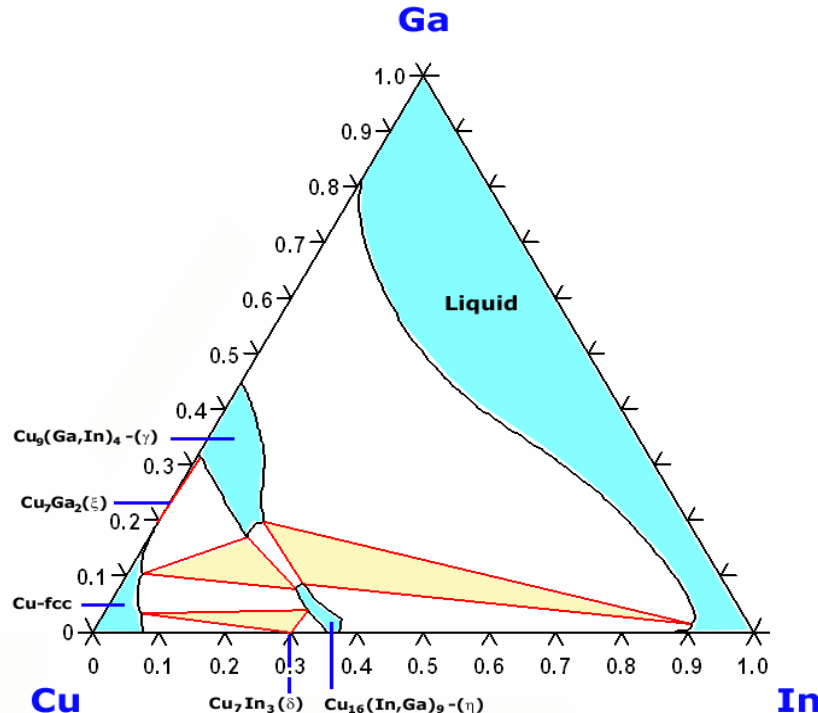


Figure 2-26. Modified isothermal section ($500\text{ }^{\circ}\text{C}$, 1atm) of the Cu-Ga-In ternary phase diagram

Furthermore, the optimized thermodynamic parameters are used to predict the isothermal section of Cu-Ga-In phase diagram at $500\text{ }^{\circ}\text{C}$ and 1 atm, as displayed in Figure 2-26. It should be noted, however, that the experimental data used here were based on thin film Cu-Ga-In samples which may have a different equilibrium from bulk material.

2.3.5 Summary and Future Work

The Cu-Ga-In ternary phase diagram was predicted by ThermoCalc program employing a Maggianu's equation based on the sub-binary phase diagrams. Subsequently, the predicted ternary phase diagrams were modified using recent

experimental data. In the future, the further optimization can be achieved by the followings:

- Modify the thermodynamic descriptions for the sub-binary systems to make the models extendable to higher-order systems (sub-lattice model is preferred).
- Perform the thermal analysis along with X-ray measurements to identify the phase transformation temperatures.
- Measure the solubility of the third elements in binary phases (e.g., Ga in $\delta\text{-Cu}_7\text{In}_3$) to estimate the interaction parameters between elements in a sub-lattice.
- Perform the EMF experiments to obtain the ternary interaction parameters for the liquid and Cu-fcc phases.

CHAPTER 3

METAL (CU, IN, GA)-SE REACTION PATHWAYS

3.1 Introduction

The phase equilibria of the binary Cu-Se system have been reviewed by Glazov *et al.* [Gla00] and a thermodynamic assessment using the ThermoCalc software was discussed in chapter 2. Four intermediate binary compounds Cu_{2-x}Se , Cu_3Se_2 , CuSe , and CuSe_2 were experimentally identified. The Cu_{2-x}Se compound is known to melt congruently and have two polymorphs: the low-temperature stable α - Cu_{2-x}Se phase and the high-temperature modification (i.e., β - Cu_{2-x}Se) having a transition temperature of around 396K. Three CuSe polymorphs α - CuSe , β - CuSe , and γ - CuSe were also reported. A thermodynamic assessment of the binary In-Se system was performed based on the evaluation of literature by Li *et al.* [Li04]. Multiple intermediate compounds (In_4Se_3 , InSe , In_6Se_7 , $\text{In}_9\text{Se}_{11}$, In_5Se_7 and polymorphic In_2Se_3 (α , β , γ and δ)) were identified as shown in the phase diagram in Figure 3-1. Phase diagram evaluation and thermodynamic assessment of the binary Ga-Se system have been reported by Dieleman *et al.* [Die82] and by Ider [Ide03], respectively. According to their reports, only two binary compounds (i.e., GaSe and Ga_2Se_3) are stable in the Ga-Se system, as shown in Figure 3-2. Furthermore, Ga_2Se_3 has two polymorphisms: a low-temperature stable β - Ga_2Se_3 phase and its high-temperature modification (i.e., α - Ga_2Se_3) with a transition temperature of around 967K.

In this thesis (Chapter 4), a systematic study of the reaction pathways and kinetics of formation of CuInSe₂ using *in situ* high-temperature XRD is presented. In these studies, the reaction pathway and kinetics of α -CuInSe₂ formation from different precursors (*e.g.*, InSe/CuSe [Kim05a] and In₂Se₃/CuSe [Kim05b, Chapter4]) and selenization of metallic Cu-In precursor have been presented [Kim06a, Chapter4]. In this chapter, the reaction pathways for binary metal (*i.e.*, Cu, In and Ga)-Se formation from various precursor structures were investigated by *in situ* high-temperature X-ray diffraction.

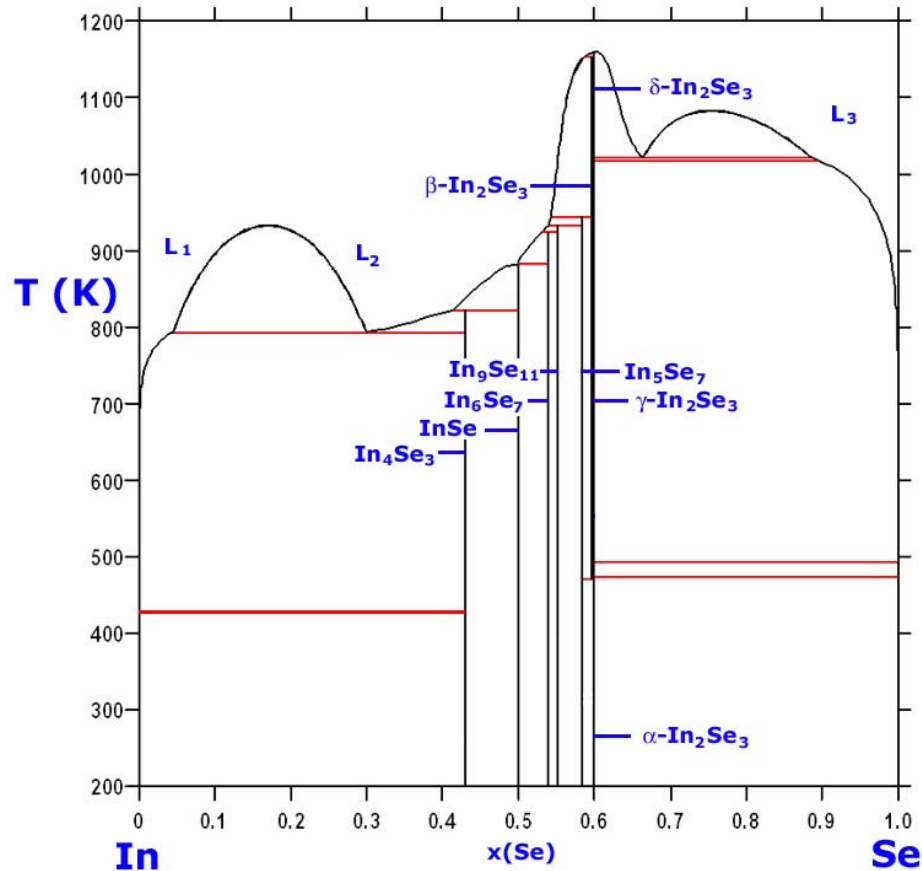


Figure 3-1. Phase diagram of In-Se binary system [Li04]

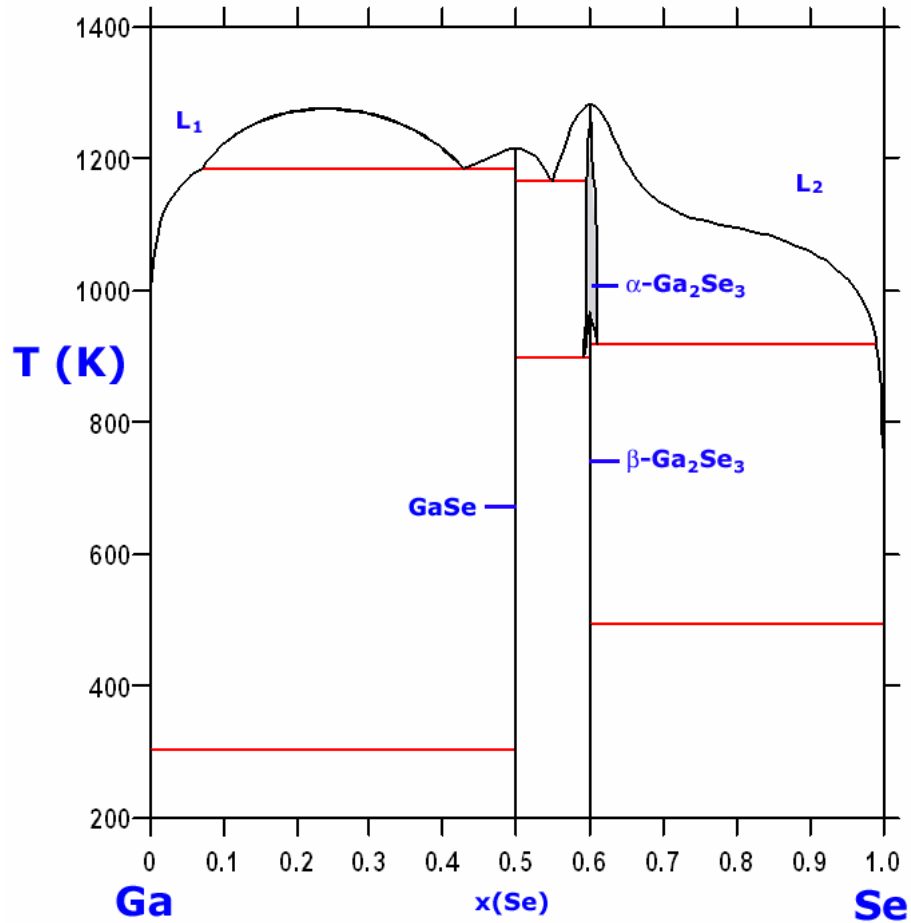


Figure 3-2. Phase diagram of Ga-Se binary system [Ide03]

3.2 Experimental

3.2.1 Precursor Preparation

Precursor films used in this study were grown using a migration enhanced epitaxy (MEE) system described in Chapter 1.5. As in traditional molecular beam epitaxy, an ultra high vacuum environment and effusion cells are employed to generate molecular beam fluxes of elemental sources. In MEE, however, the substrate is sequentially exposed to each source through revolution of a platen containing the substrate, rather than a simultaneous co-deposition from all the sources. The fluxes of Cu and In sources are controlled by electron impact emission spectroscopy (EIES) sensors while those of Ga and Se sources are controlled by the source temperature. The base pressure of the system

was established at 8×10^{-9} Torr, and the pressure during deposition was maintained in the range of 10^{-7} to 10^{-8} Torr depending on the operating conditions. Further details of the deposition technique and experimental apparatus are given elsewhere [Kim05b].

As shown in Figure 3-3, single-layer and bilayer metal(i.e., Cu, In and Ga)-Se precursor films were deposited on extremely smooth and sodium-free (alkali level < 0.3%) thin glass substrates (Corning #7059). Glass substrates with a thickness of 0.4 (± 0.127) mm were employed to minimize the temperature difference and response time between the Pt/Rh heater strip (width $\sim 0.5''$) and the precursor film ($0.5'' \times 0.5''$) in the HTXRD furnace used for subsequent characterization.

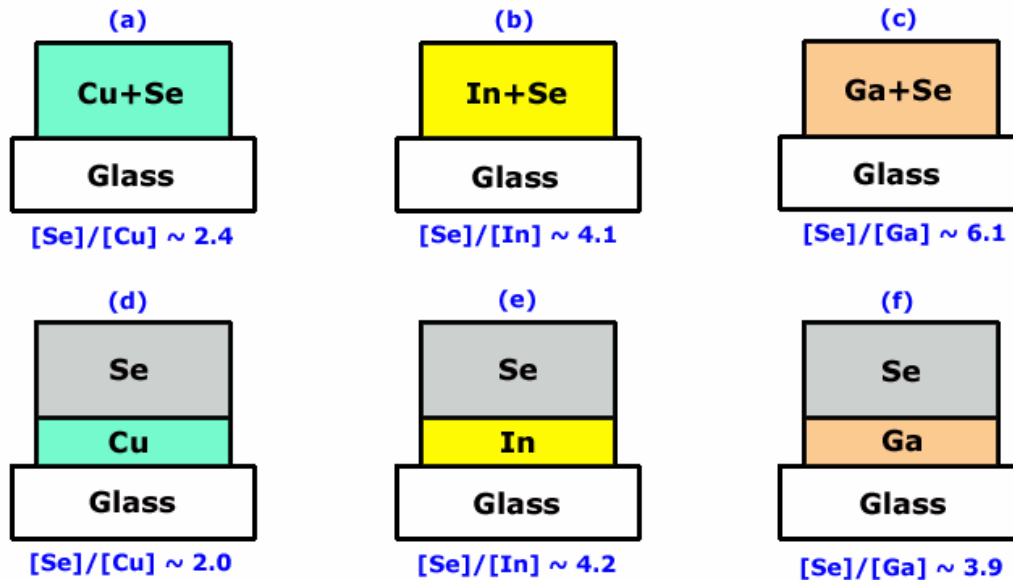


Figure 3-3. As-grown precursor structure along with overall atomic composition

The elementally mixed single-layer precursors (i.e., Figure 3-3(a)-(c)) were fabricated by co-depositing metal and Se without heating the substrate to minimize the potential reaction between metal and Se. Bilayer precursors (i.e., Figure 3-3(d)-(f)) were prepared by depositing a metal film followed by subsequent deposition of a Se film without heating the substrate. Selenium deposition was controlled to maintain a Se-

excess atomic composition, i.e., $[Se]/[Metal] > 2.0$, to compensate for the selenium volatilization losses during thermal annealing in the HTXRD furnace. The atomic composition of as-grown precursors was measured by inductively coupled plasma optical emission spectroscopy (ICP-OES), as inserted in Figure 3-3.

3.2.2 *In situ* high-temperature X-ray diffraction

Two types of high-temperature X-ray diffractometers (HTXRD), i.e., Scintag-HTXRD and PANalytical-HTXRD, were used in this study. The Scintag-HTXRD consists of a Scintag PAD X vertical θ/θ goniometer, a Buehler HDK 2.3 furnace, and an mBraun linear position sensitive detector (LPSD). In contrast to conventional X-ray point scanning detectors that perform the scanning step-by-step from lower to higher angles, the LPSD collects the XRD data simultaneously over the $10^\circ 2\theta$ window, dramatically shortening the data collection time. This permits *in situ* time-resolved studies of phase transformations, crystallization, and grain growth. A type-S thermocouple is welded onto the bottom of a Pt/Rh strip heater to measure the heater temperature directly and gives feedback to the temperature controller. Precursors are mounted on the heater strip using carbon or silver paints to improve the thermal contact between the precursor and heater strip. The PANalytical-HTXRD system is composed of a PANalytical X’Pert Pro MPD θ/θ X-ray diffractometer equipped with an Anton Paar XRK-900 furnace and an X’Celerator solid state detector. A surrounding heater is used in a PANalytical-HTXRD, while a strip heater is used in the Scintag-HTXRD. Both HTXRD furnaces were purged by flowing He and the precursor surface temperature in the furnace was calibrated from measurement of the lattice expansion of silver powder dispersed on an identical substrate and comparing the results to the equation suggested by

Touloukian [Tou77]. Since a PANalytical-HTXRD provides better resolution than a Scintag-HTXRD, it was used for the samples having a poor signal to noise ratio.

3.3 Cu-Se Binary Formation

3.3.1 Glass/Cu/Se Precursor

Phase evolution in the glass/Cu/Se precursor with an atomic composition of $[Se]/[Cu] \sim 2.0$ was investigated during temperature ramp annealing using a PANalytical-HTXRD purged by flowing He. The as-grown precursor was first scanned at 25 °C for 10 min and then heated to 60 °C at a rate of 20 °C/min. The X-ray diffraction data were collected for 10 min at every 10 °C during subsequent ramp heating to 470 °C at a rate of 20 °C/min, as shown in Figure 3-4.

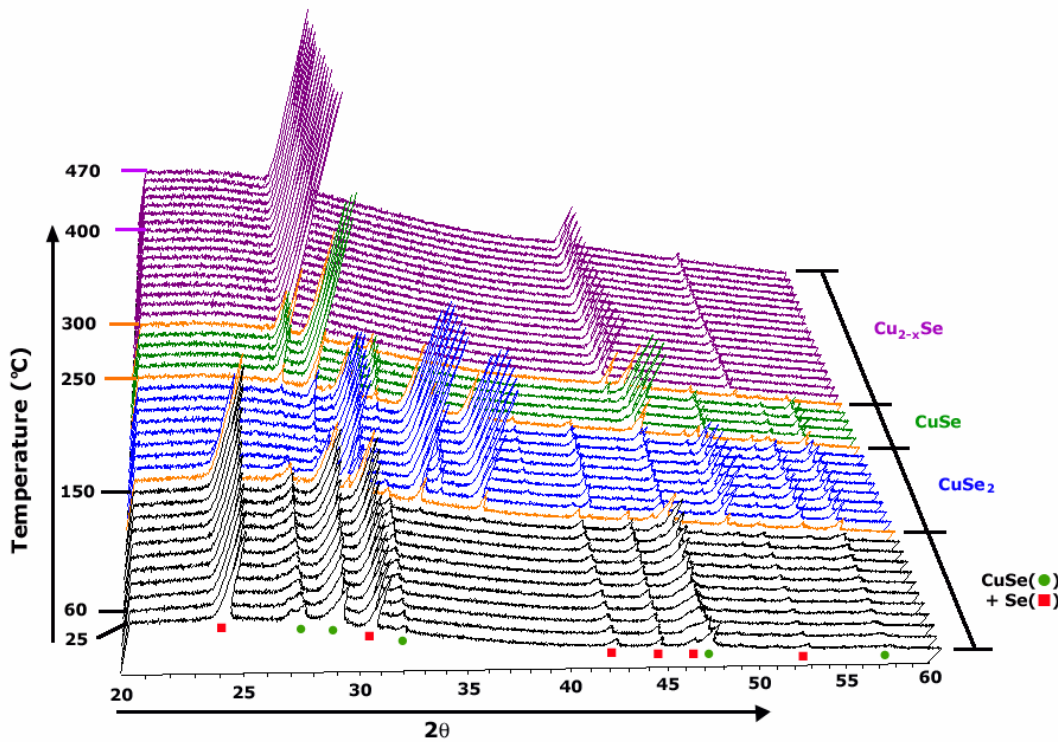


Figure 3-4. Phase evolution of glass/Cu/Se precursor observed by *in situ* X-ray diffraction. (JCPDF) Se: 06-0362, CuSe: 20-1020, CuSe₂: 26-1115, Cu_{2-x}Se: 06-0680.

The diffraction data at 25 °C show the scattering by elemental Se and CuSe, which demonstrates the crystalline CuSe forms during the precursor preparation even without heating substrate ($T_{\text{substrate}} = 40 \sim 60$ °C). The transformation of CuSe into CuSe_2 was initiated at approximately 160 °C, at which temperature the crystalline Se phase suddenly disappeared, presumably by rapid formation of CuSe_2 through reaction of CuSe with the excess Se. It is noted that rapid disappearance of Se-related peaks occurs well below the Se melting temperature (~221 °C). The Se is likely to be released from CuSe_2 as evidenced by the decrease of reflection intensities of CuSe_2 , which is then followed by the subsequent transformation of CuSe_2 into γ -CuSe at around 250 °C. Further heating above 300 °C leads to the release of more Se to yield β - Cu_{2-x}Se , which is the most stable compound of the Cu-Se binary system at high temperature (Figure 2-1). A series of temperature-dependent phase evolutions of glass/Cu/Se precursor qualitatively follow the same sequence (i.e., $\text{CuSe}_2 \rightarrow \text{CuSe} \rightarrow \text{Cu}_{2-x}\text{Se}$) as predicted equilibrium phase diagram [Gla00, She06], even though the actual phase transition temperatures are different from the equilibrium values. The temperature-dependent phase transformation of this precursor can be summarized as



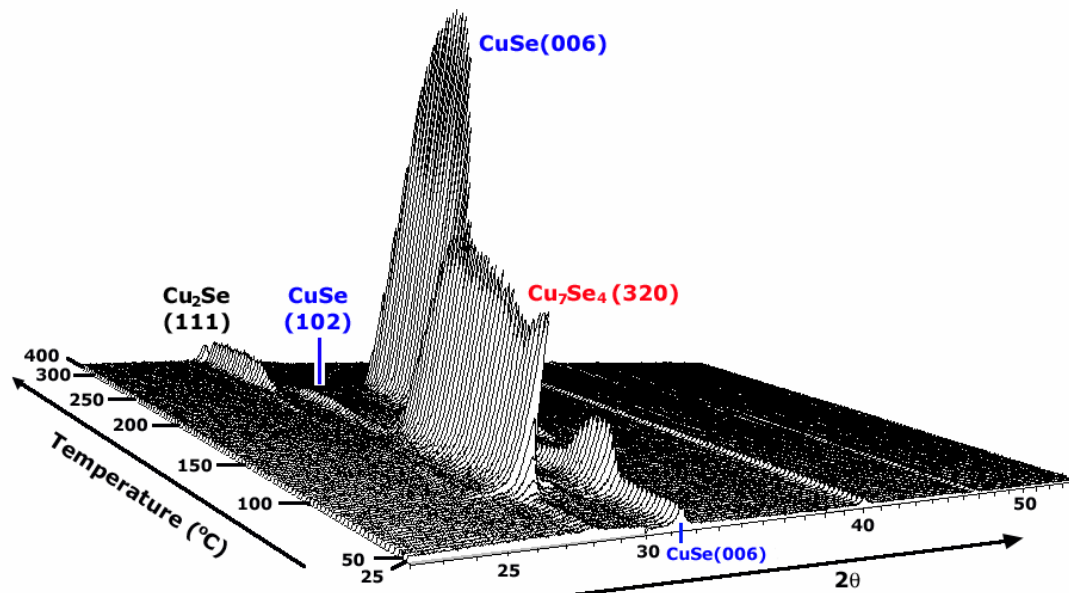
$$T \cong 160 \text{ } ^\circ\text{C}$$



3.3.2 Glass/Cu-Se Precursor

Temperature-dependent phase evolution of glass/Cu-Se precursor with an atomic composition of $[\text{Se}]/[\text{Cu}] \sim 2.4$ was investigated using the Scintag-HTXRD system. The glass/Cu-Se precursor was first scanned at 25 °C and then heated to 50 °C at a rate of 20

°C/min. Four sequential scans (1min acquisition/scan) over the range 22 to 54° (2θ) were taken at 10 °C increments while the sample was heated from 50 to 300 °C at a rate of 30 °C/min in a flowing He atmosphere. After scans at 300 °C, the samples were heated to 400 °C at a rate of 60 °C/min and then scanned twice. As shown in Figure 3-5, only a weak CuSe (006) peak is detected at 25 °C and unlike Figure 3-4, there are no broad background peaks. Since this peak is so weak, it is not detected in every part of sample. The metastable Cu₇Se₄ phase begins to form at ~80 °C as evidenced by Cu₇Se₄(320, 321).



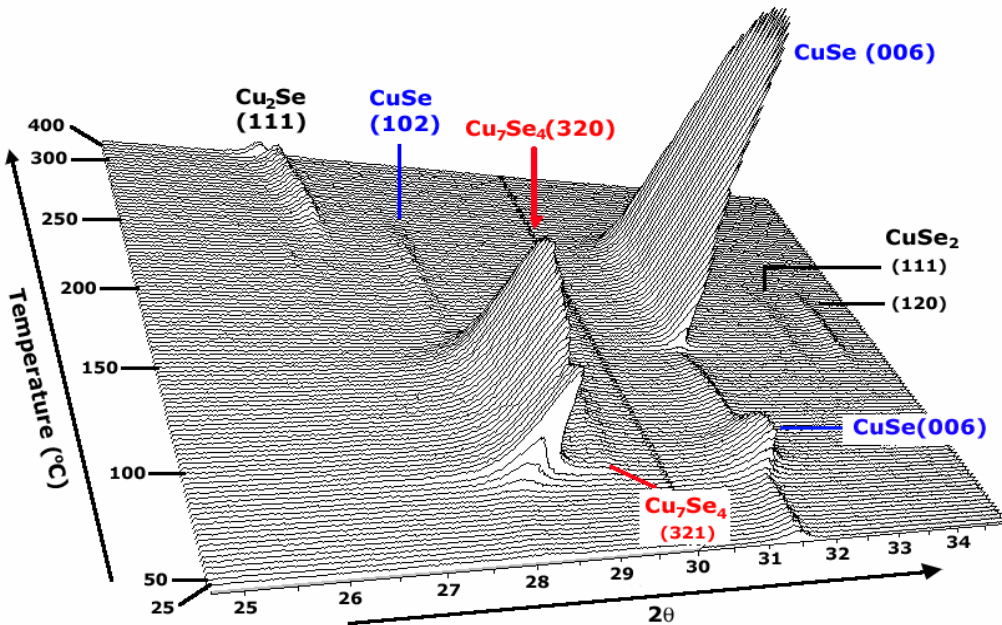
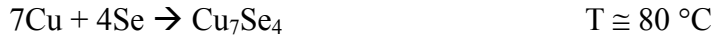


Figure 3-5. Phase evolution of glass/Cu-Se precursor observed by *in situ* X-ray diffraction.(Bottom: 25 to 34° 2θ magnified). (JCPDF) CuSe: 20-1020, Cu₇Se₄: 26-0557, Cu₂Se: 46-1129.

As this metastable phase forms, the CuSe (006) reflection begins to increase and then decrease as more Cu₇Se₃ forms to return to a weak peak. It is possible that CuSe formation begins to increase and serves as the seed for nucleating Cu₇Se₄, which grows encloses the CuSe seed to reduce the peak intensity. The subsequent CuSe peak intensity at higher temperature indicates that only a small portion of the Cu is now found in the CuSe phase.

The metastable Cu₇Se₄ phase reacts with amorphous Se (no evidence of Se recrystallization) to form the CuSe at ~170 °C, and the coexisting CuSe is partially further selenized to yield the CuSe₂ at ~160 °C, as evidenced by CuSe₂ (111, 120) peaks, which then disappear by decomposing to CuSe at ~210 °C. Interestingly, the phase evolution (i.e., CuSe → CuSe₂ → CuSe → Cu₂Se) of as-grown CuSe is very similar to that (i.e., CuSe → CuSe₂ → CuSe → Cu_{2-x}Se + Cu₂Se) of glass/Cu/Se described in the

previous section. Finally, the development of CuSe is maximized at ~220 °C followed by peritectic decomposition to the β -Cu₂Se by releasing Se at above 240 °C. Therefore, the dominant phase evolution of glass/Cu-Se precursor is summarized as



It is expected that the intermediate mixtures of Cu-Se phases reduce Se loss as compared to the bilayer structure exposing the surface of the Se top layer to the gas flow. Furthermore this sample had a larger atomic Se/Cu ratio (2.4 vs. 2.0) than the Se/Cu structure.

3.4. In-Se Binary Formation

3.4.1 Glass/In/Se precursor

The phase evolution of glass/In/Se bi-layer precursor with an overall atomic composition of [Se]/[In]~4.2 was investigated using the Scintag-HTXRD. The glass/In/Se precursor was first scanned at 25 °C and then heated to 60 °C at a rate of 20 °C/min. Then four sequential scans (1min acquisition/scan) over a range of 22 to 54° (2θ) were taken at 10 °C increments while the sample was heated from 60 to 400 °C at a rate of 30 °C/min in a flowing He atmosphere. As shown in Figure 3-6, the reflection peaks of pure In, Se and In₄Se₃ phase were detected at 25 °C. The most In-rich compound, In₄Se₃, is expected to form at the interface of indium and selenium during the deposition of selenium on pre-deposited In/glass (i.e., the second deposition stage), which provides selenium with an extremely indium-rich environment, thus favoring formation of In₄Se₃. The reflection intensity of pure In begins to decrease at ~120 °C and then

completely disappears at ~ 150 °C, which nearly coincides with its melting temperature ($T_m \sim 151$ °C). The peaks of selenium and In_4Se_3 suddenly disappear together at the same temperature of around 170 °C. Since the thermodynamic melting temperature of selenium is around 221 °C, the abrupt disappearance of selenium peak at 170 °C is likely explained by the reaction of selenium with In_4Se_3 and liquid indium rather than by melting of selenium. Furthermore, the simultaneous disappearance of In_4Se_3 and Se peaks strongly supports this explanation. No crystalline phases, however, were identified until the appearance of In_2Se_3 at around 330 °C, which is attributed to the formation of a glassy In_xSe_y phase.

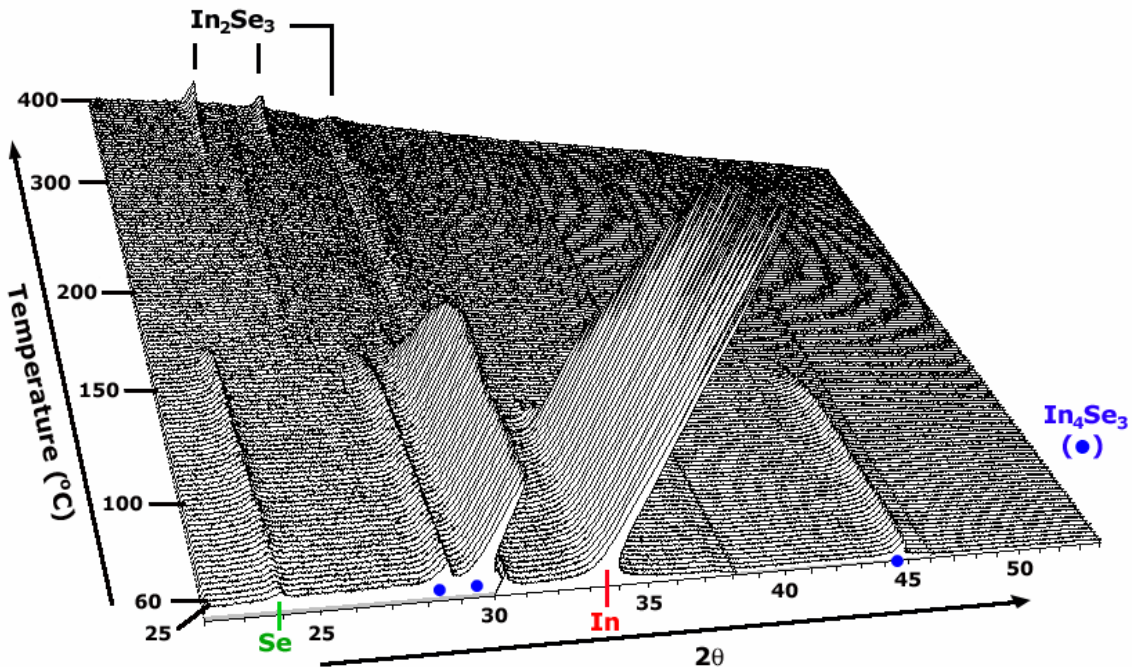
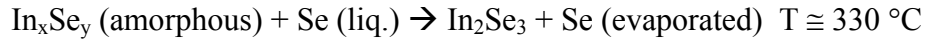


Figure 3-6. Phase evolution of glass/In/Se precursor observed by *in situ* X-ray diffraction (JCPDF) Se: 06-0362, In: 05-0642, In_4Se_3 : 83-0039, In_2Se_3 : 65-2447

According to phase diagram of the In-Se binary system shown in Figure 3-1 [Li04], there exist 4 intermediate In_xSe_y line compounds between In_4Se_3 and In_2Se_3 (InSe , In_6Se_7 , In_5Se_7 and $\text{In}_9\text{Se}_{11}$). It is reported that the crystalline phase of InSe is very difficult to

form at low temperature [Gla00]. Viswanathan *et al.* reported they could successfully deposit polycrystalline InSe on well-cleaned glass substrate at a substrate temperature of 400 °C using a vacuum coating method, while they only obtained the amorphous InSe at room temperature deposition [Vis05]. In Chapter 4, deposition of the glass/InSe/CuSe precursor [Kim05a] gave an amorphous InSe film with deposition at a substrate temperature of 250 °C using the MBE system. Finally, the crystalline In_2Se_3 , which is the most stable In-Se compound at high temperature, is obtained at around 330 °C and continues to grow until the completion of annealing (400 °C). The ICP compositional analysis (i.e., $x(\text{Se}) \sim 0.59$) on an completely annealed sample supports the single phase In_2Se_3 stoichiometry. The overall phase transformation of glass/In/Se precursor is summarized as



3.4.2 Glass/In-Se Precursor

The glass/In-Se mixed precursor was prepared to have a similar overall composition to glass/In/Se precursor, as confirmed by ICP analysis ($[\text{Se}]/[\text{In}] \sim 4.1$). Furthermore, an identical annealing procedure as used for glass/In/Se precursor was applied to glass/In-Se precursor. As shown in Figure 3-7, unlike the bi-layer precursor, no crystalline phase is detected from the as-deposited precursor. Rather a broad intensity is observed in the 2θ range 22 to 38°. Since, in general, the as-deposited pure indium has the crystalline structure as shown in glass/In/Se precursor, indium likely exists as a glassy In_xSe_y phases rather than as elemental In, and thus the selenium is partially bound in its glassy state.

Interestingly, selenium begins to crystallize at around 120 °C as evidenced by growing Se (100) peak, and then grows until temperature reaches around 200 °C, at which point the Se reflections disappear due to Se melting and/or reacting with glassy In_xSe_y . Subsequent heating leads to the formation of crystalline In_2Se_3 by further selenization of In_xSe_y , just like in the phase evolution of glass/In/Se precursor. It is interesting to note that the formation temperature of In_2Se_3 in glass/In-Se precursor is much lower than in glass/In/Se. One explanation is the shorter diffusion lengths in intimately mixed glass/In-Se precursor as compared to the bi-layer films.

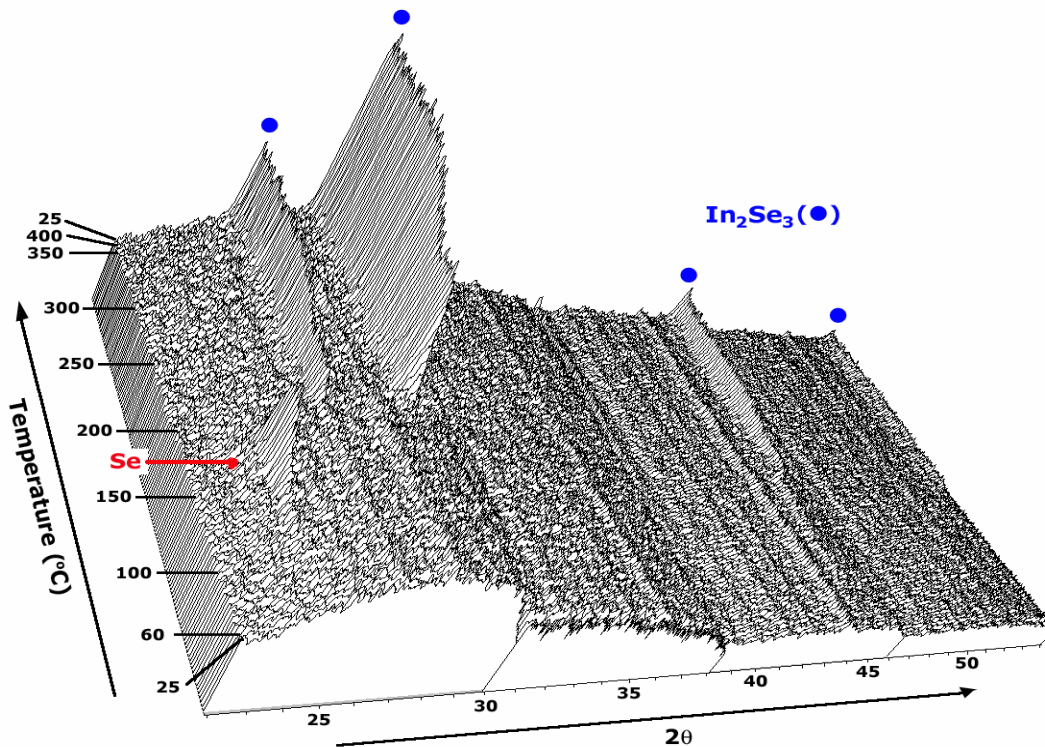
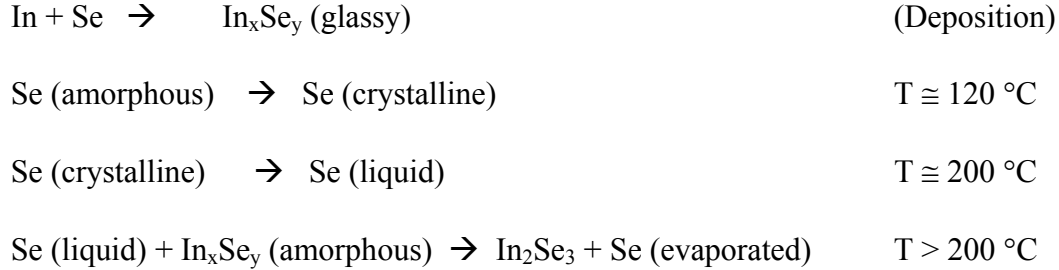


Figure 3-7. Phase evolution of glass/In-Se precursor observed by *in situ* X-ray diffraction. (JCPDF) Se: 06-0362, In_2Se_3 : 65-2447.

Again, the ICP analysis (i.e., $x(\text{Se}) \sim 0.59$) on an annealed sample strongly supports the complete transformation into In_2Se_3 without any residual phases. The overall phase evolution of glass/In-Se precursor is thus summarized as



3.5 Ga-Se Binary Formation

3.5.1 Glass/Ga/Se Precursor

The PANalytical-HTXRD system was used again for *in situ* investigation of the phase evolution of the glass/Ga/Se precursor. The same characterization scheme (i.e., temperature ramp profile and X-ray scan sequence) as used for glass/Cu/Se precursor was applied to this sample. First, the precursor was heated to 60 °C at a rate of 20 °C/min after scanned at 25 °C for 30 sec, and then the subsequent X-ray scans were executed at every 10 °C for 30 sec during heating to 500 °C, as shown in Figure 3-8.

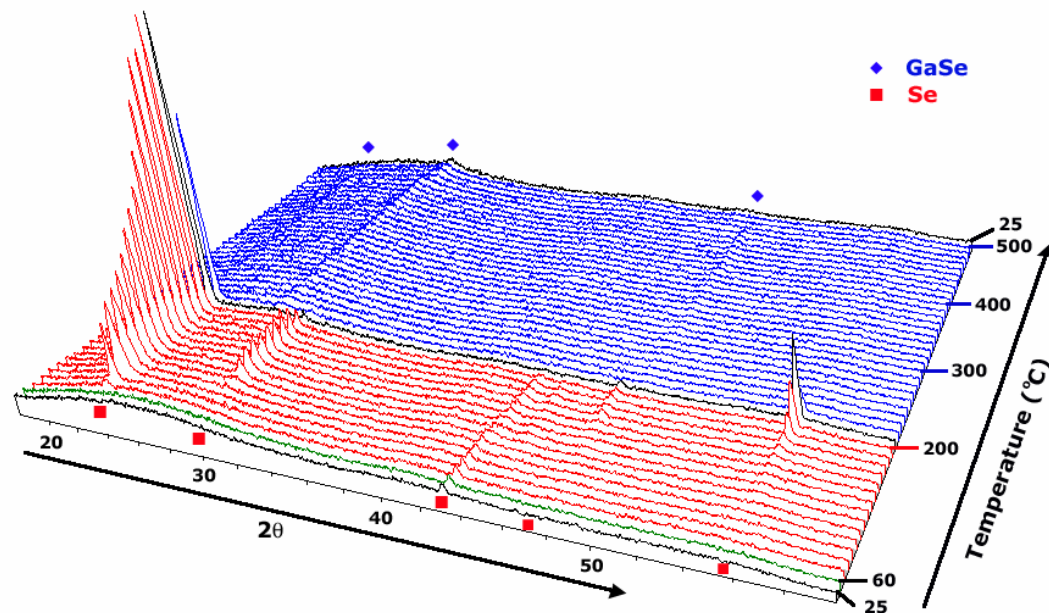
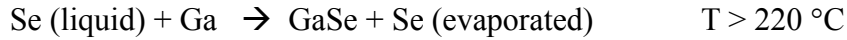
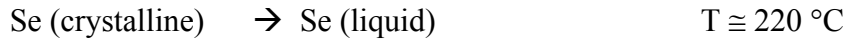
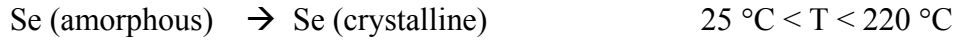


Figure 3-8. Phase evolution of glass/Ga/Se precursor observed by *in situ* X-ray diffraction (JCPDF) Se: 06-0362, GaSe: 29-0628

The room temperature X-ray diffraction on glass/Ga/Se stacked precursor with a selenium excess atomic composition of $[Se]/[Ga] \sim 3.9$ shows there is no reflection except a weak Se (102) peak. There is a broad but low intensity peak centered at $2\theta \approx 25^\circ$. As temperature increases, however, selenium begins to crystallize until temperature reaches the Se melting temperature ($\sim 221^\circ\text{C}$), at which temperature the selenium peaks abruptly disappear. Melted selenium subsequently reacts with Ga to form GaSe as evidenced by the appearance of the GaSe reflection peaks. The binary Ga-Se phase diagram shown in Figure 3-2 [Ide03] shows that Ga_2Se_3 is slightly more stable than GaSe. The excess Se used in this experiment was transformed into GaSe rather than Ga_2Se_3 as a high-temperature stable phase at 500°C , which is mainly attributed to the high vapor-pressure of Se and stacked structure of glass/Ga/Se, and thus preferable Se evaporation to reaction with Ga. Finally, the temperature-dependent phase evolution of glass/Ga/Se precursor is summarized as



3.5.2 Glass/Ga-Se Precursor

The PANalytical-HTXRD system with the same characterization procedure as used for the glass/Ga/Se sample was applied to the glass/Ga-Se mixture sample. As shown in Figure 3-9, X-ray diffraction at room temperature demonstrates no crystalline compounds are produced by the precursor deposition process. The broad reflection between 20 and 35° may be attributed to the scattering by amorphous Se or a glassy Ga-Se phase.

The crystallization of amorphous selenium is initiated at approximately 120 °C and then continues until the temperature reaches around 210 °C at which temperature all selenium reflection peaks disappear due to the melting of Se. It is worthwhile to recall the crystallization of Se at the same temperature (~120 °C) and subsequent melting at around ~200 °C, which are observed during the phase evolution of glass/In-Se precursor, as described in section 3.4. Subsequently, the melted Se reacts with Ga and/or amorphous Ga-Se compound to form the Ga_2Se_3 compound, which is the most stable Ga-Se compound. Further heating to 500 °C causes no more phase transformation. While the glass/Ga/Se precursor forms the GaSe compound at high temperature as described in the previous section, the glass/Ga-Se precursor forms the Ga_2Se_3 compound because the intermixing of Se with Ga at the molecular level during the precursor MBE deposition makes the reaction of Se with Ga preferable to the evaporation of Se.

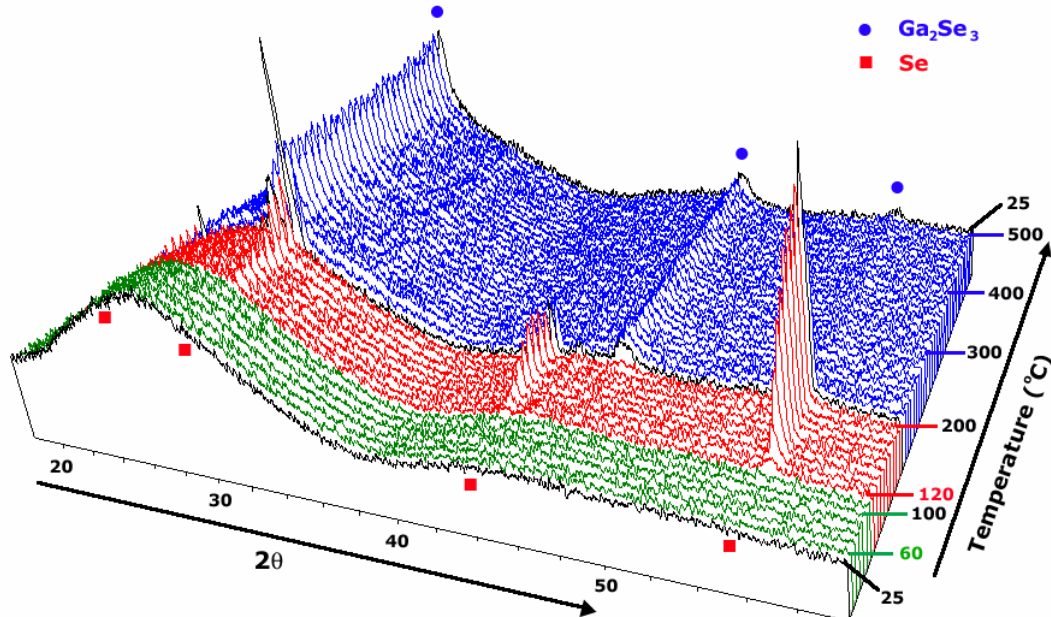
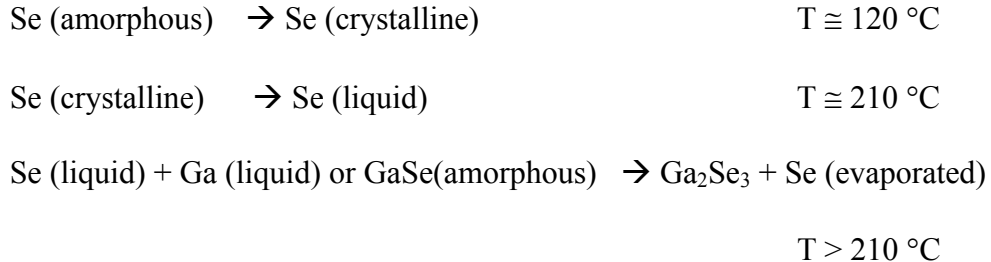


Figure 3-9. Phase evolution of glass/Ga-Se precursor observed by *in situ* X-ray diffraction. (JCPDF) Se: 06-0362, Ga_2Se_3 : 44-0931.

Therefore, the temperature-dependent phase evolution of glass/Ga-Se precursor is summarized as



3.6 Summary

The reaction pathways and phase evolution of binary Cu-Se, In-Se, and Ga-Se precursor structures were investigated using *in situ* high-temperature X-ray diffraction. The results show the overall phase transformation of binary metal (Cu, In and Ga)-Se precursors qualitatively follow the sequence predicted by the thermodynamic phase diagram. The intermediate reaction of each binary compound, however, depends on the as-deposited precursor structure and starting compounds. For instance, the intimately mixed glass/Cu-Se precursor takes the sequence of $\text{Cu}_7\text{Se}_4 \rightarrow \text{CuSe} \rightarrow \text{Cu}_2\text{Se}$ while the glass/Cu/Se bi-layer precursor beginning with the CuSe, presumably as an intermediate layer, follows the reaction path of $\text{CuSe} \rightarrow \text{CuSe}_2 \rightarrow \text{CuSe} \rightarrow \text{Cu}_{2-x}\text{Se}/\text{Cu}_2\text{Se}$. The glass/In-Se and glass/In/Se precursors have a different initial constitution, i.e., amorphous In_xSe_y and In_4Se_3 respectively, but ultimately reach the high-temperature stable In_2Se_3 . It is also found that the excess amorphous selenium in both glass/In-Se and glass/Ga-Se precursors begin to crystallize at $\sim 120 \text{ } ^\circ\text{C}$, while the crystallization of selenium is not observed in glass/Cu-Se precursor partly due to the formation of Cu_7Se_4 at $\sim 80 \text{ } ^\circ\text{C}$. In the future, the isothermal soaking experiments will be performed to give the quantitative kinetic information.

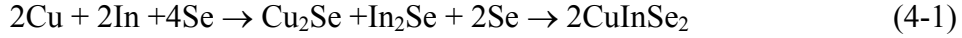
CHAPTER 4 CUINSE₂ FORMATION PATHWAYS AND KINETICS

4.1 Introduction

Chalcopyrite α -CuInSe₂ (CIS) and its alloys with Ga or S are proven absorber materials for high efficiency thin film solar cells. Interestingly, a variety of processing sequences have been demonstrated to form α -CuInSe₂ (e.g., co-deposition of elements, annealing of stacked elemental layers, direct compound formation, and selenization of metal particles). Furthermore, the processes are robust to small fluctuations in process conditions. This versatility is made possible, in part, by the complex Cu-In-Se phase diagram, which exhibits equilibria between α -CuInSe₂ and 8 different solid phases as well as a Se-rich liquid at 773 K [Göd00a-c]. Furthermore the α -CuInSe₂ phase field has a rather large range of solid solution, suggesting a point defect chemistry that includes significant compensation of electronic defects. An examination of equilibrium pathways for the formation of CIS, however, is unable to fully explain this versatility, and thus kinetic limitations are also important. While there have been several studies on the mechanism for forming CIS, the detailed reaction pathways and kinetics are not yet fully understood.

To date, most studies on the mechanism of CIS formation have been performed using *ex-situ* methods [Zwe95, Adu95], which give limited kinetic information. Recently, various *in situ* techniques have been used to investigate the reaction mechanism of CIS. Based on *in situ* high-temperature X-ray diffraction (HTXRD) analysis, Katsui

and Iwata [Kat99] suggested the following reaction pathway for CIS formation from glass/Cu/In/Se stacked elemental layers:



Wolf *et al.* [Wol00] used thin film calorimetry for the *in situ* monitoring of reaction kinetics of CIS formation from Cu/In/Se precursor. Using a Kissinger analysis, they suggested an activation energy of 160 kJ/mol with around 15% statistical error.

Brummer *et al.* [Bru03] employed *in situ* high-energy powder diffraction to investigate the phase transformation of three binary systems (Cu-Se, In-Se, Cu-In), ternary CIS and quaternary CIGS system using the stacked elemental film precursors (e.g., glass/Cu/In/Se, glass/Cu/Se, glass/In/Se and glass/Cu/In). They reported several intermediate phase transformations with temperature and the tetragonal CuInSe₂ formation temperature of 375~385 °C. The same research group identified the several CIS formation reactions during rapid thermal processing of stacked elemental layers: (1) CuSe + InSe → CuInSe₂, (2) Cu₂Se + 2InSe + Se → 2CuInSe₂, (3) Cu₂Se + In₂Se₃ → 2CuInSe₂ [Her05]. Most recently, they then reported that the kinetics of the formation of CuInSe₂ depends on the binary selenides present in the precursors and the formation of CuInSe₂ from a bilayer InSe/CuSe precursor follows the typical diffusion-controlled reaction along with an average activation energy of 128 kJ/mol [Pur06].

As part of this dissertation, a systematic study of the reaction pathways and kinetics of the formation of CIGS and its subsystems from various types of precursors was conducted using time-resolved, *in situ* high temperature X-ray diffraction technique. In a previous study [Kim05a] using the same system, the formation of CuInSe₂ from the bilayer structure InSe/CuSe showed that a non-crystalline intermediate phase, most likely

amorphous CuInSe₂, appeared during the initial stage of the isothermal heating in air in the temperature range 220 to 270 °C. Data analysis based on the Avrami and parabolic rate law models supported a one-dimensional diffusion controlled reaction mode. The combined amorphous and crystalline CuInSe₂ interfacial layer functions as a diffusion barrier as well as a nucleation barrier.

In this chapter, the results of studies on the reaction pathway and kinetics of α-CIS formation from different precursors (e.g., In₂Se₃/CuSe, CuSe/In-Se and InSe/Cu-Se) and selenization of metallic Cu-In precursor are reported.

4.2 Glass/In₂Se₃/CuSe Precursor

4.2.1 Precursor Preparation

Bilayer glass/In₂Se₃/CuSe precursor films were deposited on sodium-free thin glass substrates (Corning #7059) in the MEE reactor. The details of the deposition technique and experimental apparatus are given in chapter 1.5. Glass substrates with a thickness of 0.4 mm were employed to minimize the temperature difference and response time between the strip heater and the precursor film in the HTXRD furnace used for subsequent characterization. The samples were fabricated by first depositing a crystalline In₂Se₃ film at a substrate temperature of ~360 °C under ultra high vacuum conditions ($10^{-7} \sim 10^{-8}$ Torr). This was followed by deposition of a crystalline CuSe film on the as-grown In₂Se₃ layer at a lower substrate temperature (~150 °C) to minimize the potential reaction between the In₂Se₃ and CuSe layers. The total bilayer film thickness (~800 nm) was measured by TEM as shown in Figure 4-1, and the atomic composition of each monolayer (bottom In₂Se₃: [Se]/[In]~1.4; top CuSe: [Se]/[Cu]~0.93) and overall bilayer ([Cu]/[In]~0.94; [Se]/[Metal]~1.2) film was measured by inductively coupled plasma

optical emission spectroscopy (ICP-OES). The stable structure of both In_2Se_3 and CuSe at the growth temperature is hexagonal. XRD characterization of the precursor films revealed a highly textured (001) crystalline- In_2Se_3 /crystalline-CuSe bilayer structure as shown in Figure 4-2.

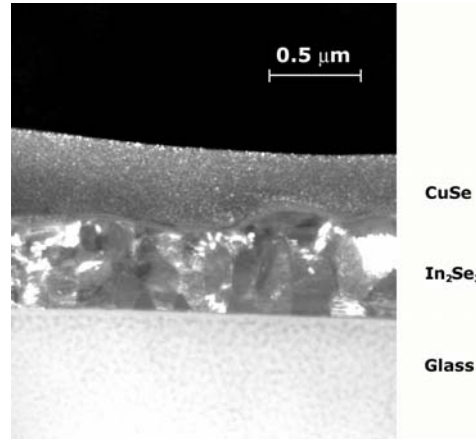


Figure 4-1. TEM micrographs of as-grown glass/ In_2Se_3 /CuSe bilayer precursor films

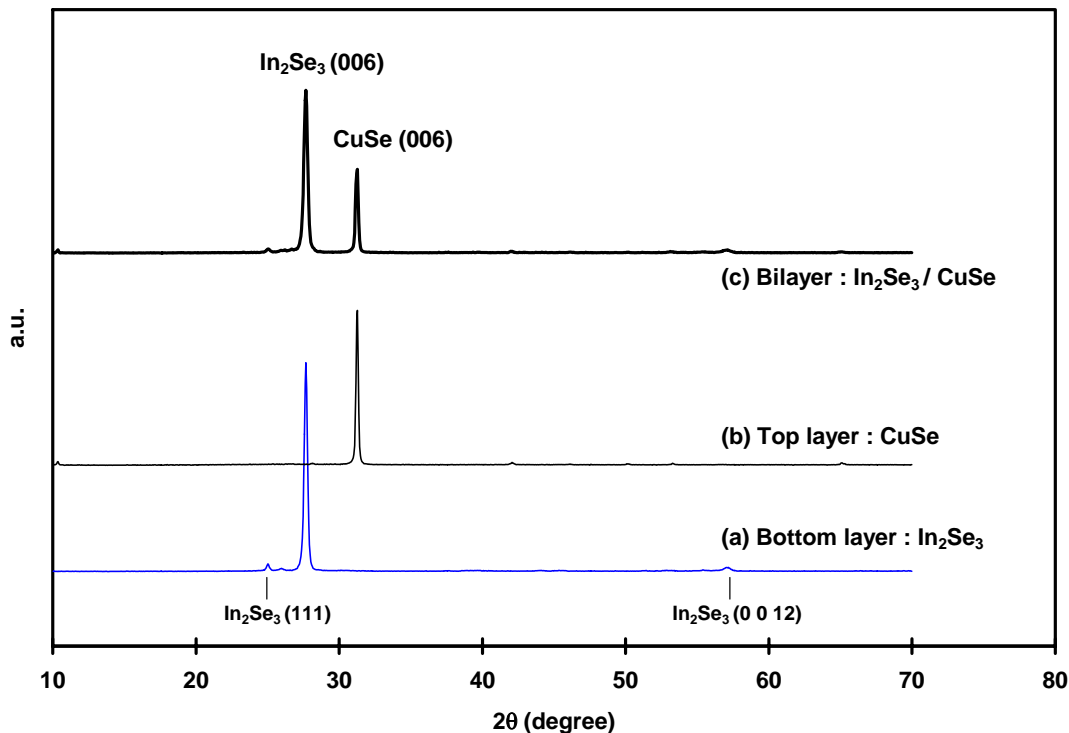


Figure 4-2. Room temperature XRD scans and TEM micrographs of as-grown precursor films: (a) glass/ In_2Se_3 monolayer, (b) glass/CuSe monolayer, (c) glass/ In_2Se_3 /CuSe bilayer

4.2.2 Temperature Ramp Annealing

Temperature ramp annealing by the Scintag-HTXRD described in chapter 3.2.2 was used to investigate the phase evolution of the samples and to establish a suitable isothermal annealing temperature range. The glass/ $\text{In}_2\text{Se}_3/\text{CuSe}$ bilayer sample was first heated to 150 °C at a rate of 10 °C/min and then X-ray diffraction data were collected during subsequent ramp heating (5 °C/min). Scans requiring ~1 min were taken at every 5 °C increment while the sample was heated from 150 to 350 °C in a flowing He atmosphere.

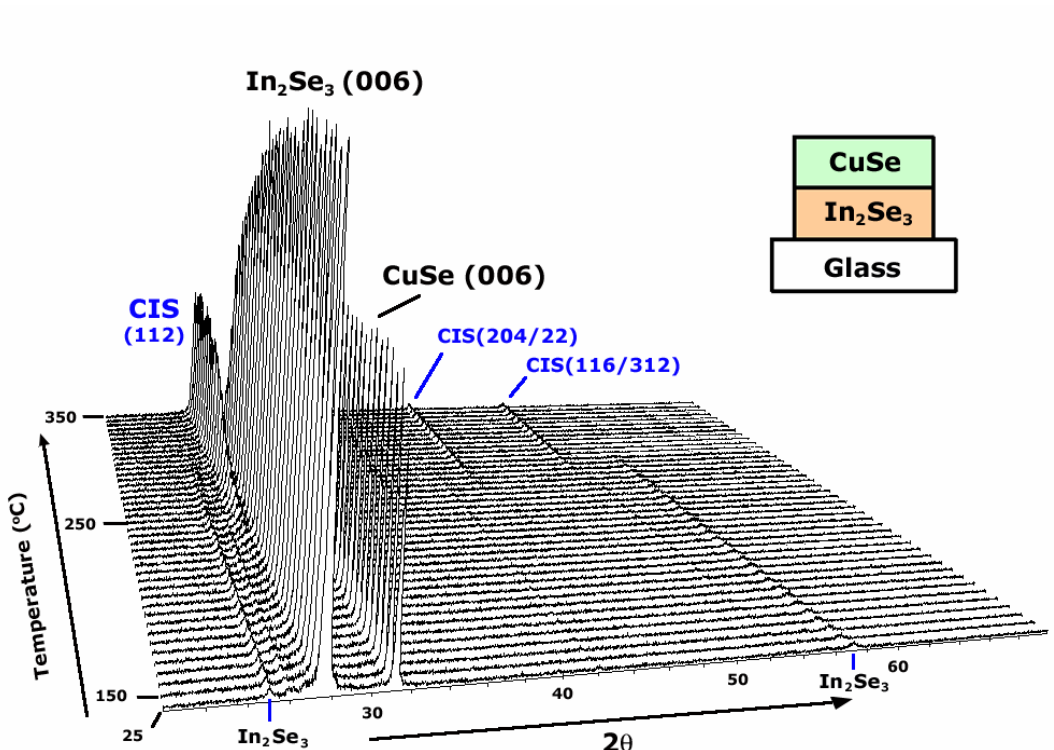
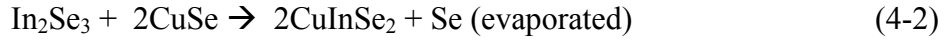


Figure 4-3. *In situ* XRD scans during temperature ramp annealing (10 °C/min) of the glass/ $\text{In}_2\text{Se}_3/\text{CuSe}$ sample

Figure 4-3 demonstrates that the initial In_2Se_3 and CuSe phases are directly transformed to $\alpha\text{-CuInSe}_2$ without any intermediate phases. CuInSe_2 begins to be detected at a temperature ~250 °C and the reaction is almost complete at 310 °C as

evidenced by the lack of detection of In_2Se_3 and CuSe . The expected interfacial reaction pathway is



4.2.3 Isothermal Annealing

Time-resolved, high temperature X-ray diffraction data were collected using a linear position sensitive detector (LPSD), while the bilayer glass/ $\text{In}_2\text{Se}_3/\text{CuSe}$ precursor films were maintained at a constant temperature in a He (flow rate ~ 100 sccm) atmosphere. The O_2 content of the outlet He gas was measured by an O_2 analyzer to be less than 0.1 ppm. In the isothermal experiment, the three step temperature ramping was used to minimize heating time without temperature overshooting. Firstly, the temperature was rapidly ramped at rate of 300 $^{\circ}\text{C}/\text{min}$ to a value of 20 $^{\circ}\text{C}$ below the set point temperature, and then at rate of 200 $^{\circ}\text{C}/\text{min}$ to a value of 10 $^{\circ}\text{C}$ below the set point temperature. Finally, the temperature was ramped to a set point at rate of 100 $^{\circ}\text{C}/\text{min}$ and then held to monitor the isothermal reaction. A set of experiments was performed with a range of set point temperature determined from the temperature ramp scan results shown in Figure 4-3. The set point temperature was set so that the total isothermal holding time was much longer (i.e., several hours) than an individual scan but sufficiently fast that an experiment could be completed in one day. Scans were taken approximately every 35 sec. It is noted that an individual scan time for the isothermal annealing experiment was much shorter (i.e., scan time of 30 to 120 sec) than for the temperature ramp annealing (i.e., scan time of 5 to 10 min) to obtain acceptable time resolution. To complete the reaction, the temperature was elevated to 350 $^{\circ}\text{C}$ and then maintained for about 12 min until only the $\alpha\text{-CuInSe}_2$ phase remained and the peak intensity remained constant (see

for example the discontinuity in peak height after 1 hr in Figure 4-4). The temperature range for the isothermal experiments was from 230 to 290 °C. The 2θ scan range (24 to 34°) for the isothermal experiments was selected to focus on the major peaks of the reactants and product, i.e., In_2Se_3 (006), CuSe (006) and $\alpha\text{-CuInSe}_2$ (112).

Figure 4-3 displays the time-resolved XRD data collected for the film isothermally reacted at 250 °C. To obtain the fractional reaction (α), the integrated areas of the In_2Se_3 (006), CuSe (006), and CuInSe_2 (112) peaks were obtained from the diffraction data using the JADE software. These values were normalized assuming that the reactants were completely transformed to crystalline CuInSe_2 after each run, and that the texture of the CuInSe_2 does not appreciably change through the entire heating process.

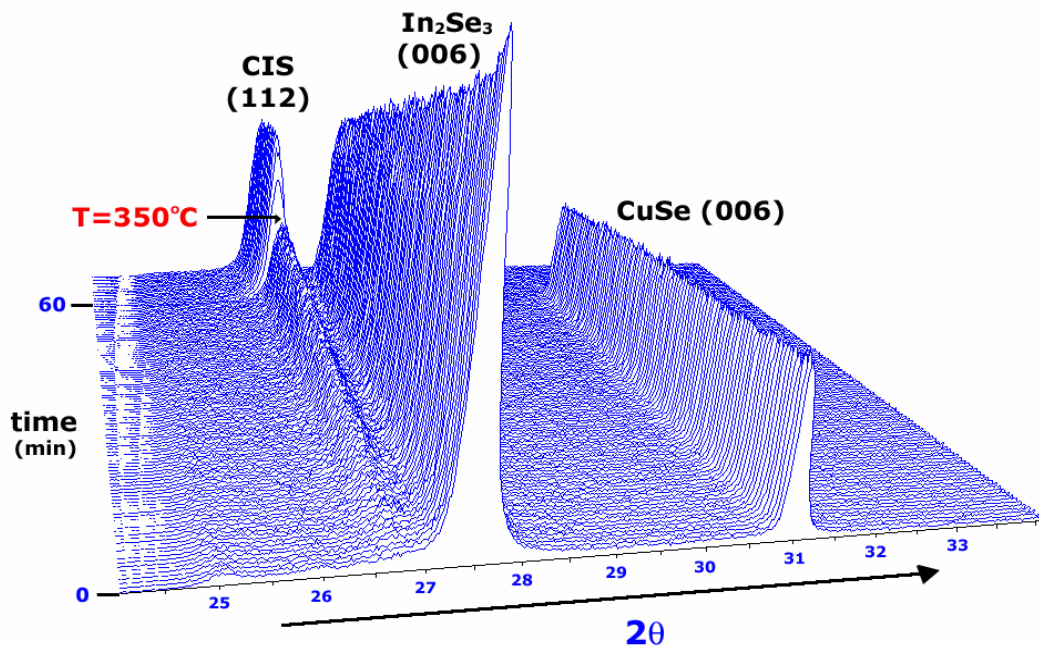


Figure 4-4. *In situ* time-resolved XRD scans during isothermal annealing of the glass/ $\text{In}_2\text{Se}_3/\text{CuSe}$ precursor structure at 250 °C

The reaction kinetics in terms of activation energy and reaction order have been investigated using two solid-state reaction models, the “Avrami” and “parabolic rate” models. Analysis of solid state reaction data using the Avrami model is commonly used for preliminary identification of the growth rate law. It has been shown that the method yields satisfactory fits to relevant experimental data [Kim05a, Bam80, Lu99]. Since this model is based on the nuclei growth and an isotropic growth is assumed, the product regions are spherical. The transformation kinetics under isothermal reaction are described by

$$\alpha = 1 - \exp[-(kt)^n] \quad (4-3)$$

or equivalently, by

$$\ln[-\ln(1-\alpha)] = n \ln t + n \ln k \quad (4-4)$$

where the fractional reaction α represents the fraction of reaction completed at time t , k is the kinetic rate constant, and n is the Avrami exponent. This analysis has been advocated by Hulbert [Hul69], who showed that the Avrami exponent can vary between 0.5 and 1.5 in the case of one-dimensional (i.e., radial direction), diffusion-controlled reactions. The value of n is close to 0.5 if the nucleation is instantaneous, and close to 1.5 if the nucleation rate is constant throughout the reaction. Figure 4-5 displays the Avrami plots for the isothermal reaction of the precursor films at different temperatures. Even though data were taken only for $0.1 < \alpha < 0.95$ to minimize experimental error, the Avrami model expressed by eq. (4-4) did not yield a satisfactory (*i.e.* linear) fit.

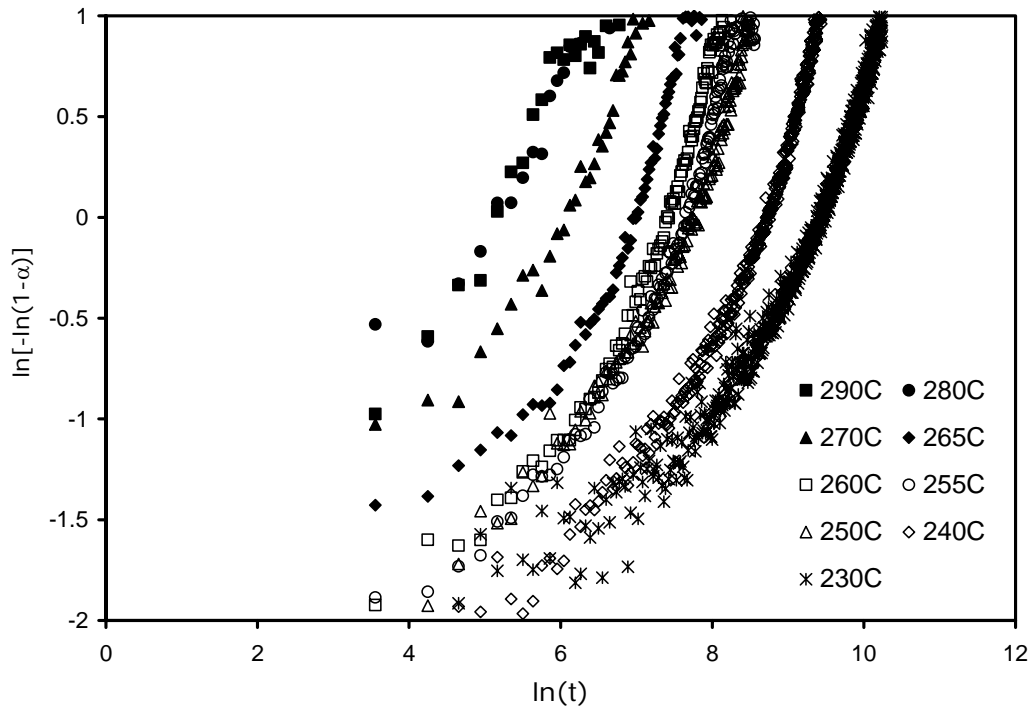


Figure 4-5. Avrami model plot for glass/In₂Se₃/CuSe precursor structure

The simple parabolic kinetic model [Hul69] was developed based on a reaction between two solid materials with planar surfaces, and identical to the In₂Se₃/CuSe precursor structure. This model is consistent with a physical process that requires a limiting reactant to diffuse across the product layer that initially formed at the interface of the two reactants. The product layer thickness increases with time to further decrease the diffusive flux of the limiting reactant. Assuming a uni-directional process, the reaction kinetics of parabolic model are described by

$$\alpha^2 = k_p t \quad (4-5)$$

where α is the fractional reaction, k_p is the parabolic rate constant including the diffusion coefficient of the migrating species, and t is the time. Figure 4-6 shows the plot of α^2 vs. t for the same data set previously analyzed by the Avrami model.

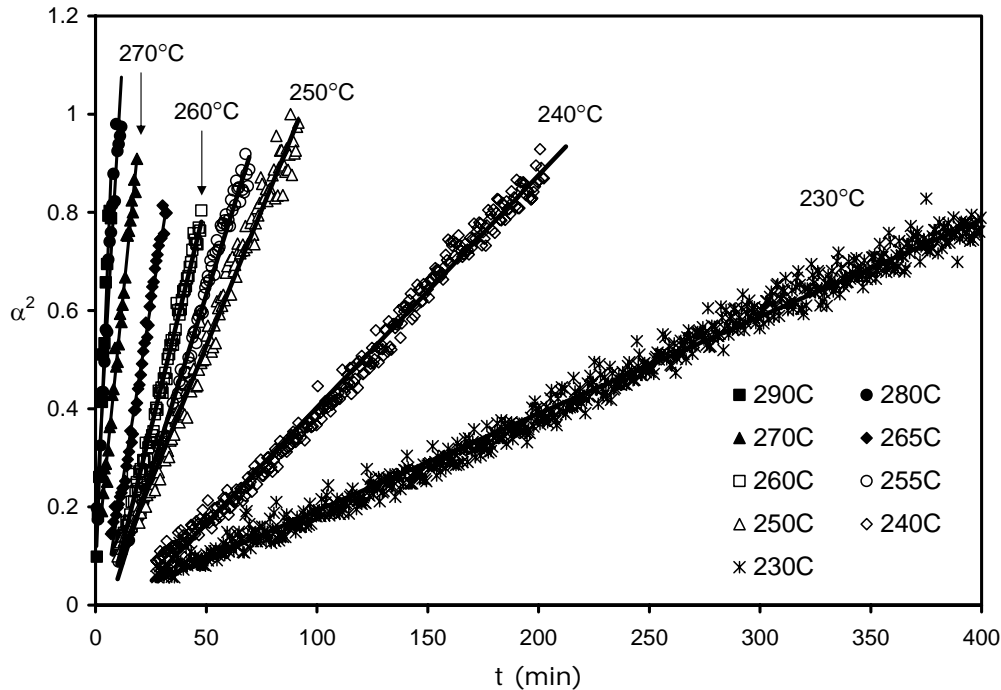


Figure 4-6. Parabolic model plot for glass/In₂Se₃/CuSe precursor structure

It is evident that the parabolic reaction model provides a much better fit to the data than the Avrami model over the entire set of isothermal temperatures (230 to 290 °C). It is thus concluded that the formation of α -CuInSe₂ in glass/In₂Se₃/CuSe bilayer precursor films is consistent with a one-dimensional diffusion controlled reaction pattern.

The Arrhenius equation

$$k_p = A \cdot \exp\left(-\frac{E_a}{RT}\right) \quad (4-6)$$

was used to estimate the apparent activation energy E_a for the α -CuInSe₂ formation process in glass/In₂Se₃/CuSe bilayer precursor films. An activation energy of 162 (± 5) kJ/mol was estimated from the Arrhenius plot shown in Figure 4-7. The estimated activation energy is very close to the value (~160 kJ/mol) suggested by Wolf *et al.*

[Wol00] for CIS formation from Cu/In/Se stacks using a Kissinger analysis for thin film calorimetry.

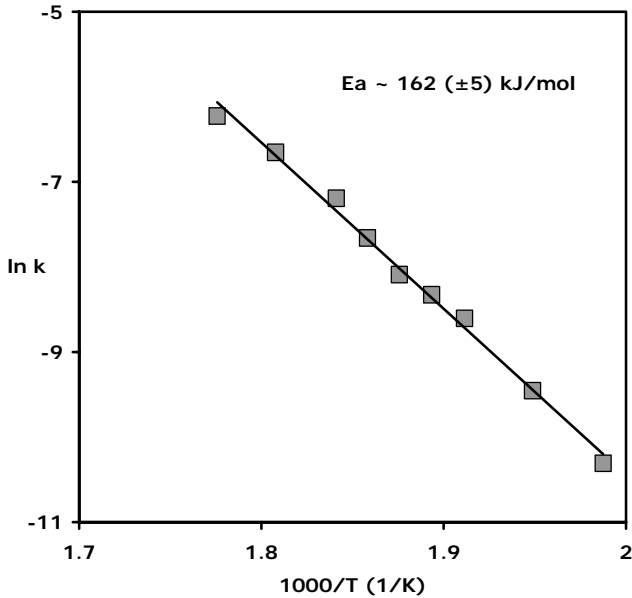


Figure 4-7. Arrhenius plot of the parabolic rate constant for glass/In₂Se₃/CuSe precursor structure

4.3 Glass/InSe/Cu-Se Precursor

4.3.1 Precursor Preparation

For the glass/InSe/Cu-Se bilayer structure, an indium selenide layer was first grown on to a thin (~0.4 mm) sodium-free glass substrate in the MEE system with a substrate temperature of approximately 250 °C. Subsequently, elemental copper and selenium were co-deposited on the as-grown InSe layer without heating the substrate to minimize potential reactions between the InSe, copper and selenium. Considering the possible loss of indium and selenium during temperature ramp annealing, extra indium and selenium were introduced, which was confirmed by inductively coupled plasma optical emission spectroscopy (ICP-OES) analysis (i.e., overall [Cu]/[In]~0.89 and [Se]/[Cu+In] ~1.67).

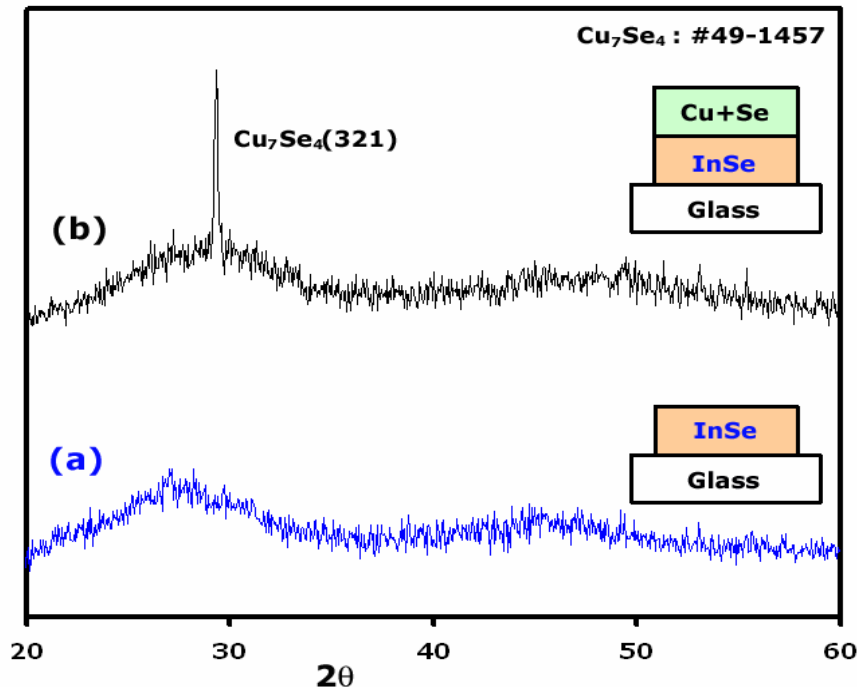


Figure 4-8. Room temperature XRD scans of as-grown precursor films: (a) glass/InSe monolayer, (b) glass/InSe/Cu-Se bilayer

The room temperature XRD data on as-deposited precursors shown in Figure 4-8 demonstrate that the as-grown InSe phase is amorphous, and that the Cu₇Se₄ phase forms during co-deposition of Cu and Se, even without heating the substrate.

4.3.2 Temperature Ramp Annealing

Temperature ramp annealing by the Scintag-HTXRD described in chapter 3.2.2 was used to investigate the phase evolution of the samples. The glass/InSe/Cu-Se bilayer sample was first heated to 50 °C at a rate of 20 °C/min and then X-ray diffraction data were collected during subsequent ramp heating (30 °C/min). Four sequential scans over a range of 20 to 54° (2θ) were taken at 10 °C increments while the sample was heated from 50 to 350 °C in a flowing He atmosphere, as shown in Figure 4-9.

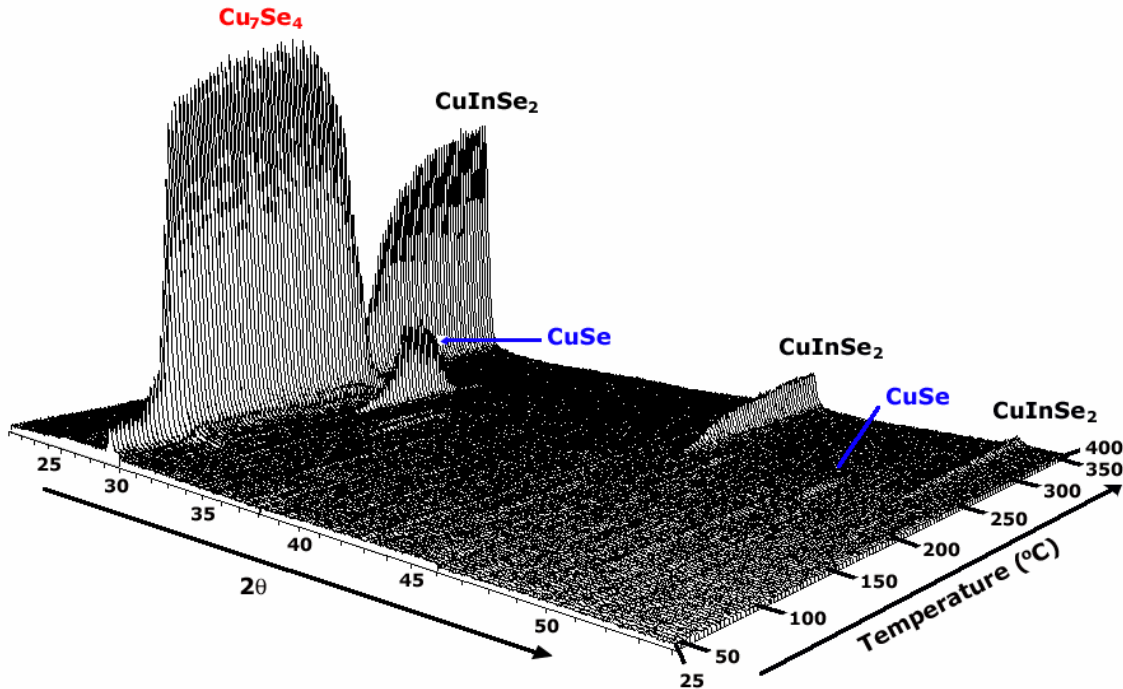


Figure 4-9. *In situ* XRD scans during temperature ramp annealing ($30\text{ }^{\circ}\text{C}/\text{min}$) of the glass/InSe/Cu-Se sample.

The results demonstrates that the initial Cu_7Se_4 phase begins to transform to CuSe by further reaction with Se at around $190\text{ }^{\circ}\text{C}$, and CuInSe_2 formation then is initiated with the decrease of CuSe peak at around $230\text{ }^{\circ}\text{C}$. No crystalline In_xSe_y compound, however, was detected, which demonstrates most of the indium is contained in amorphous In_xSe_y glass. The expected interfacial reaction pathway is



Interestingly, as shown in chapter 3.3.2, the transformation of Cu_7Se_4 into CuSe also was detected at around $170\text{ }^{\circ}\text{C}$ in the phase evolution of glass/Cu-Se precursor, just slightly lower than the temperature observed in this system.

4.4 Glass/CuSe/In-Se Precursor

4.4.1 Precursor Preparation

In the same manner as the glass/InSe/Cu-Se precursor, CuSe layer was first grown on to a thin (~0.4 mm) sodium-free glass substrate in the MEE system with a substrate temperature of approximately 150 °C. Elemental indium and selenium were then co-deposited on the as-grown CuSe layer without heating substrate. To compensate for the possible loss of indium and selenium during temperature ramp annealing, the overall atomic composition was controlled as In-rich and Se-rich, which was later confirmed by ICP results of $[Cu]/[In] \sim 0.89$ and $[Se]/[Cu+In] \sim 1.78$. The room temperature X-ray scan of as-deposited glass/CuSe/In-Se precursors, as shown in Figure 4-10, clearly shows that the crystalline CuSe forms, but no In-containing compound.

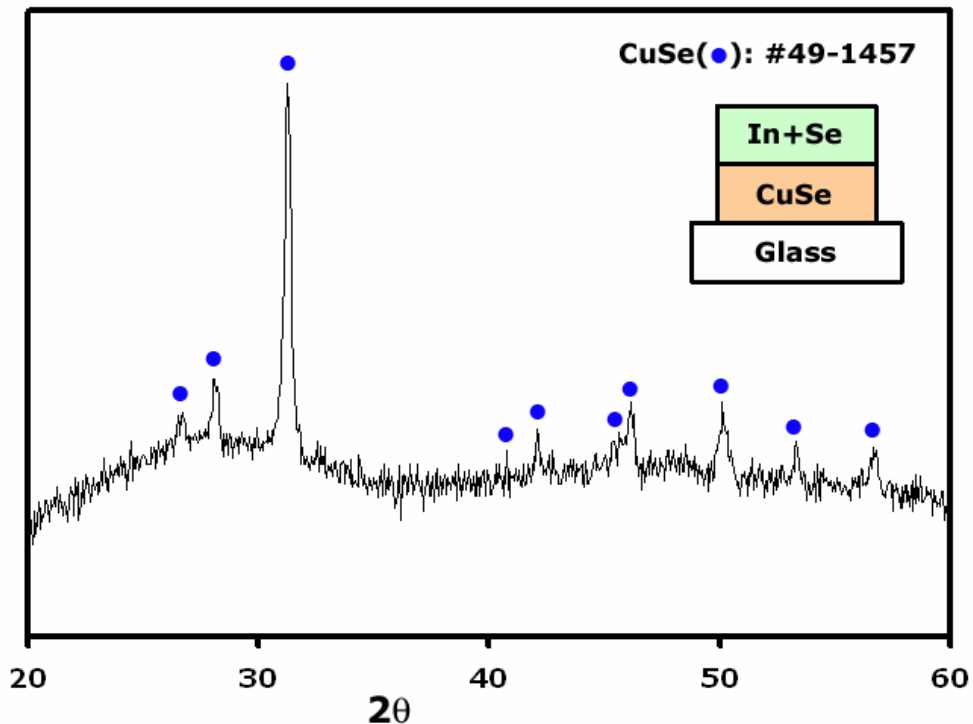


Figure 4-10. Room temperature XRD scans of as-grown glass/CuSe/In-Se precursor

4.4.2 Temperature Ramp Annealing

Temperature ramp annealing was performed using the identical procedure as used on the structure in chapter 4.3.2. The sample was first heated to 50 °C at a rate of 20 °C/min and then X-ray diffraction data were collected during subsequent ramp heating (30 °C/min) to 350 °C. Four sequential scans over a range of 20 to 54° (2θ) were taken at 10 °C increments while the sample was heated from 50 to 350 °C in a flowing He atmosphere.

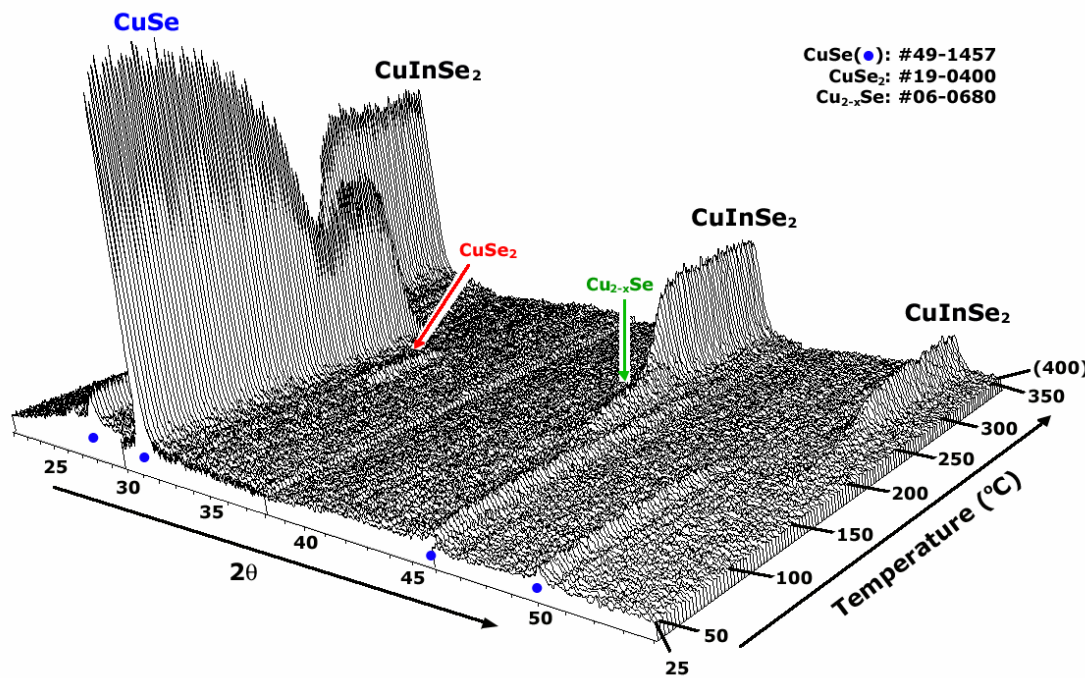
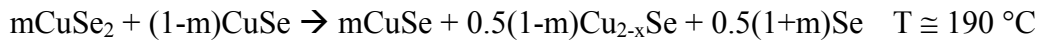


Figure 4-11. *In situ* XRD scans during temperature ramp annealing (30 °C/min) of the glass/CuSe/In-Se sample.

As shown in Figure 4-11, initial CuSe (006) peak intensity begins to decrease at around 130 °C. Part of the initial CuSe phase (not entire amount of CuSe) is first transformed to CuSe₂ at around 170 °C by reacting with selenium available in top layer. Once the CuSe₂ reaches its maximum intensity at round 190 °C, it starts to release selenium, as evidenced by the observation that the CuSe (006) peak intensity increases

again at ~ 200 °C. At the same temperature, the other portion of initial CuSe phase, which is not transformed to CuSe₂, also releases selenium and yields Cu_{2-x}Se.

Finally, the disappearance of CuSe and Cu_{2-x}Se lead to the formation of CuInSe₂. Detailed investigation of X-ray diffraction data revealed the formation of CuInSe₂ from glass/CuSe/In-Se precursor is initiated at around 220 °C, which is similar to that of CuInSe₂ formation (~ 230 °C) from glass/InSe/Cu-Se. It is noted that no crystalline In-Se phase was observed. The expected interfacial reaction pathway is



The phase evolution of CuSe phase, i.e., CuSe \rightarrow CuSe₂ \rightarrow CuSe and CuSe \rightarrow Cu_{2-x}Se, follows the general sequence of phase evolution of Cu-Se compound as predicted by Cu-Se binary phase diagram [She06] and experimentally demonstrated in chapter 3.3.

4.5 Glass/Mo/Cu-In-Se Precursor

4.5.1 Precursor Preparation

The glass/Mo/Cu-In-Se precursor was prepared by co-deposition of elemental Cu, In, and Se onto Mo-coated thin glass substrate in the MEE system without heating the substrate. The In- and Se-rich composition was intended to compensate for the possible volatilization loss of indium and selenium during temperature ramp annealing. The overall atomic composition of [Cu]/[In] ~ 0.88 and [Se]/[Cu+In] ~ 1.79 was measured by ICP. The room temperature XRD, which is not shown here, demonstrates that no crystalline phase forms during co-deposition of the precursor.

4.5.2 Temperature Ramp Annealing

During temperature ramp annealing from 25 through 350 °C, XRD data were continuously collected. Figure 4-12 demonstrates that α -CuInSe₂ formation is initiated at around 140 °C and the initial amorphous Cu-In-Se elemental mixture is directly transformed to crystalline α -CuInSe₂ phase without any intermediate phases. It is also noted that the formation reaction was not complete by the end of the experiment (350 °C).

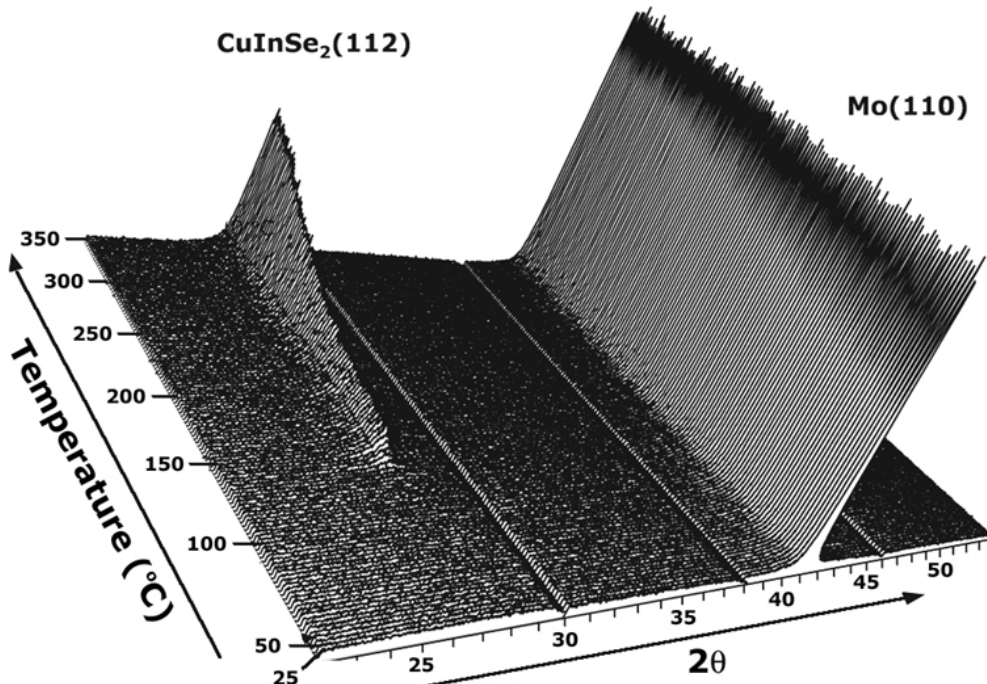


Figure 4-12. Temperature ramp annealing of glass/Mo/Cu-In-Se precursor

4.5.3 Isothermal Annealing

Based on the temperature ramp annealing results, isothermal annealing was performed over a wide range of temperature (140 to 350 °C). After isothermal annealing for an hour, the temperature was intentionally increased to 500 °C to complete the reaction, as shown in Figure 4-13.

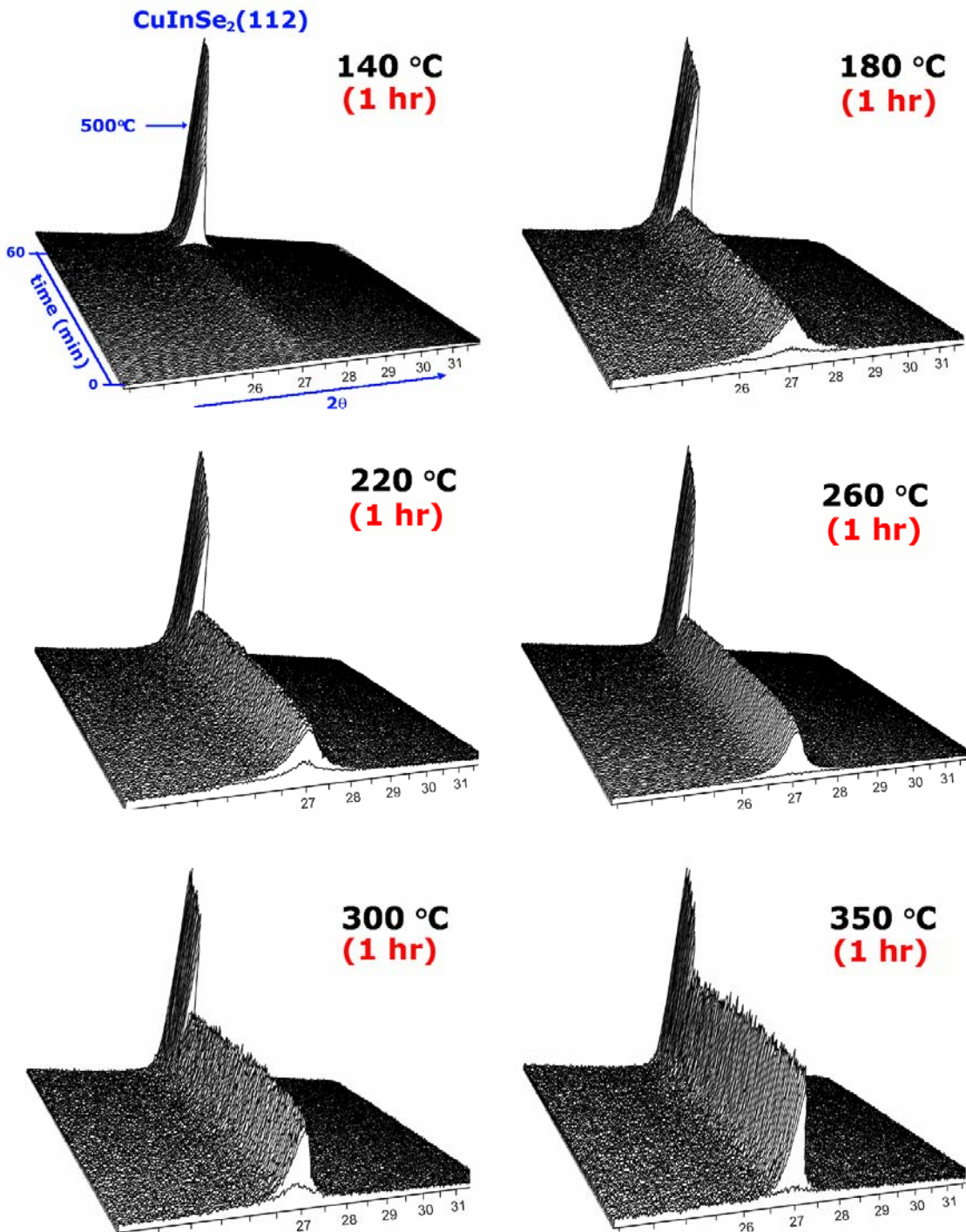


Figure 4-13. Isothermal annealing of glass/Mo/Cu-In-Se precursor at selected temperatures in the range 140 to 350 °C

The results, as shown in Figure 4-13, demonstrate that the α -CuInSe₂ formation from Cu-In-Se elemental mixture is relatively rapid at these temperatures, and thus the

time dependence is not evident in these figures. Increasing the isothermal soaking temperature causes the equilibrium fractional reaction of $\alpha\text{-CuInSe}_2$ to increase, but its FWHM (Full width at half maximum) to decrease. The total integrated areas, however, did not change. This is interpreted as the higher isothermal soaking temperature producing the larger $\alpha\text{-CuInSe}_2$ vertical grain size and thus larger and higher peaks. The estimated grain sizes with respect to isothermal temperature are compared in Figure 4-15. The grain sizes were estimated from the peak shape of the CuInSe_2 (112) shown in Figure 4-14. The average values of data calculated from 40 to 60 min were taken. However, it is noted that the crystal grain size estimated by X-ray diffraction peak is the vertical thickness of grain, but not the lateral diameter.

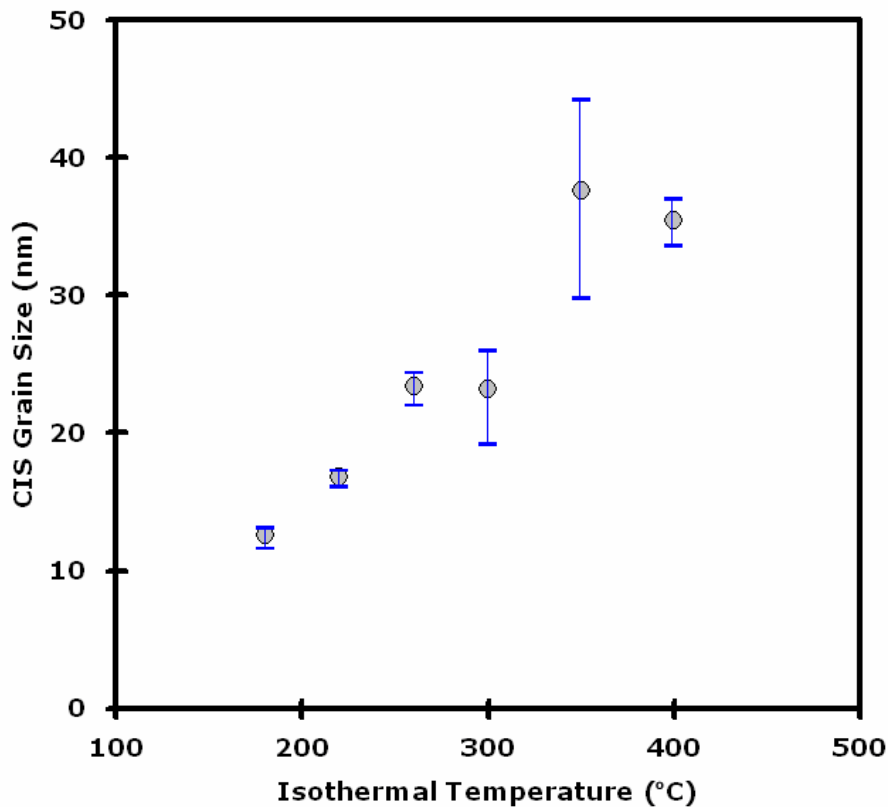


Figure 4-14. CuInSe_2 grain sizes estimated by X-ray diffraction vs. isothermal annealing temperature of glass/Mo/Cu-In-Se precursor

4.6 Selenization of Glass/Mo/Cu-In Precursor

4.6.1 Precursor Preparation

The glass/Mo/Cu-In precursor was prepared in a migration-enhanced molecular beam epitaxial (MEE) deposition system under ultra high vacuum conditions (10^{-7} to 10^{-8} Torr). Since molybdenum is widely used as a back-contact material in CIS-based solar cells, elemental Cu and In were co-deposited on the Mo-coated, sodium-free thin glass (Corning 7059: 0.4 mm thickness) without heating the substrate to minimize the reaction between Cu and In. The overall atomic composition ($[Cu]/[In] \sim 1.0$) of glass/Mo/Cu-In as-deposited precursor film was determined by inductively coupled plasma optical emission spectroscopy (ICP-OES) and its phase constitution (Cu_2In , $CuIn$, and In) was identified by both θ - 2θ and grazing incident X-ray diffraction (GIXD), as shown in Figure 4-15.

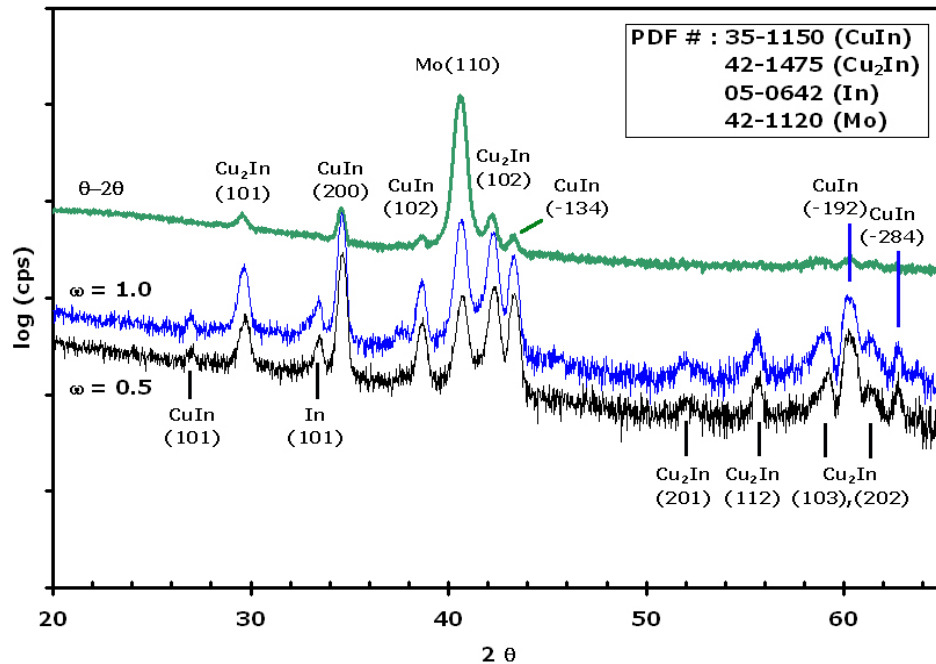


Figure 4-15. θ - 2θ and grazing incident X-ray diffraction (at $\omega = 1.0$ and 0.5°) patterns of an as-deposited glass/Mo/Cu-In precursor film

The thicknesses of the Mo layer ($\sim 0.3 \mu\text{m}$), Cu-In film ($\sim 0.6 \mu\text{m}$), and selenized CuInSe₂ film ($\sim 2 \mu\text{m}$) were measured by SEM images of cleaved samples, as shown in Figure 4-16 (b) and (d). The matrix-island structure on the surface of the as-grown precursor is apparent in the SEM surface images and the islands were identified as an indium-rich or nearly pure indium phase by GIXD and electron probe microanalysis (EPMA), as presented in Table 4-1. It is noted that the electron beam used in EPMA analysis can penetrate into the sample (at least 0.5 micron) and thus the EPMA result for island is the sum of the values for island (e.g., ~ 0.2 micron thickness) and matrix beneath (e.g., ~ 0.3 micron for the penetration depth of 0.5 micron).

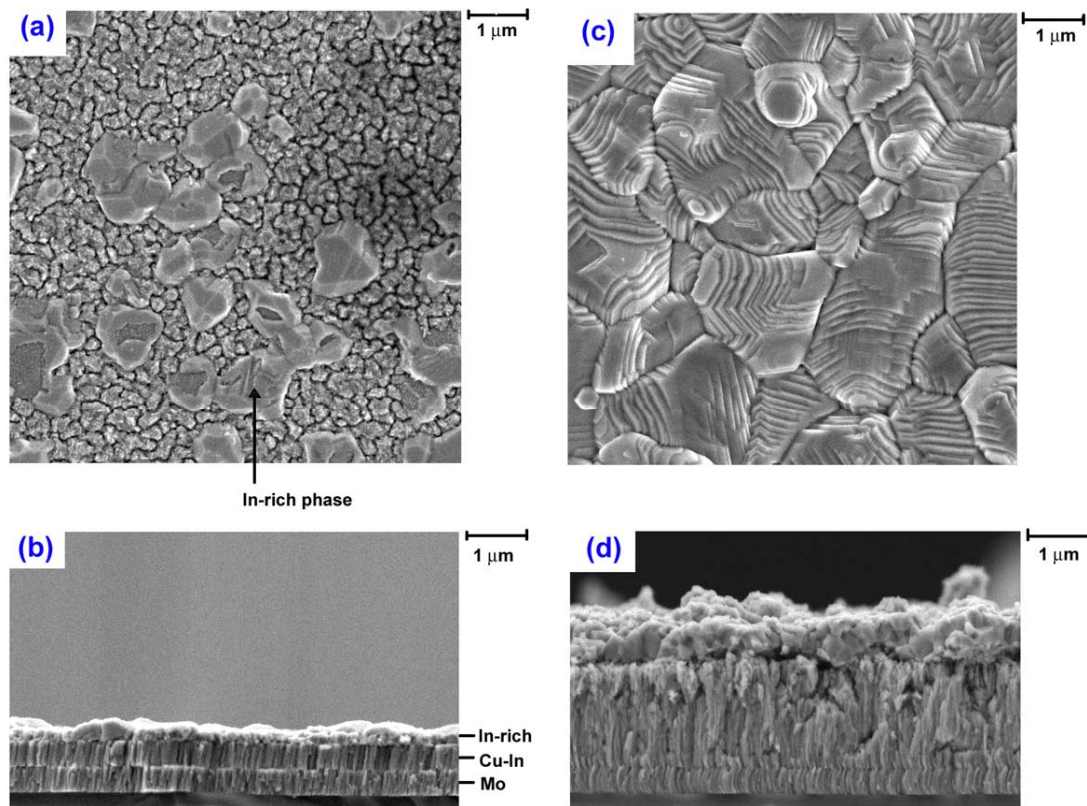


Figure 4-16. Surface and cross-sectional SEM images of an as-deposited glass/Mo/Cu-In precursor film (a: surface; b: cross-section) and selenized film (c: surface; d: cross-section)

Table 4-1. The composition of the as-deposited glass/Mo/Cu-In precursor films as determined by EPMA scans along the surface ($V_a = 6$ keV)

	Matrix	Island
Cu (at.%)	59.4 (± 1.2)	36.0 (± 1.0)
In (at.%)	40.6 (± 1.2)	64.0 (± 1.0)

4.6.2 Selenization Chamber Design

A selenization chamber was designed for use in the PANalytical X'pert system to allow *in situ* observation of CuInSe₂ formation from Cu+In elemental mixtures as shown in Figure 4-17. Selenium powder was placed on the XRD sample holder as a selenium source with the precursor sample. The sample holder containing a selenium and precursor was covered with an aluminum foil with a thickness of 18(± 2) micron and tied with a Ni wire to minimize the Se vapor loss.

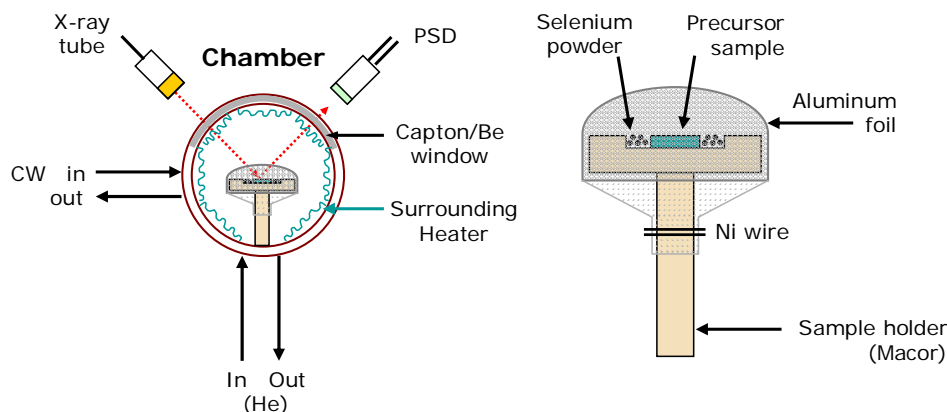


Figure 4-17. Selenium chamber design using PANalytical X'Pert system

The sample temperature was calibrated from a determination of the lattice expansion of silver powder dispersed on an identical Mo-coated glass substrate covered with an aluminum foil.

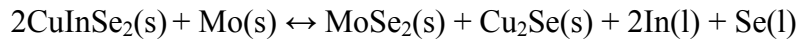
4.6.3 Temperature Ramp Selenization

During the selenization of glass/Mo/Cu-In by temperature ramp annealing ($\sim 20\text{ }^{\circ}\text{C}/\text{min}$), the formation of CuSe and its transformation to CuSe₂, and then CuSe₂ to CuInSe₂ were observed from ~ 230 to $300\text{ }^{\circ}\text{C}$ as shown in Figure 4-18(a) and (b). The formation of CuInSe₂ was initiated at a temperature between 250 and $300\text{ }^{\circ}\text{C}$. Additionally, the production of MoSe₂, accompanied by a rapid decrease of Mo (110) reflection intensity, was clearly detected at temperatures above $440\text{ }^{\circ}\text{C}$, and only after the production of CuInSe₂ was complete. In another experiment in which an insufficient amount of Se powder was placed in the well, the intensity of the CuInSe₂ reflection kept increasing without producing MoSe₂ even after $440\text{ }^{\circ}\text{C}$, which demonstrates the formation of CuInSe₂ is preferred to that of MoSe₂. These results are consistent with a simple equilibrium analysis of possible reaction pathways.

Using values for the Gibbs energy of the components [Din91, Ide03, Kna91], the Gibbs energy changes for standard reactions for Mo reduction of CuInSe₂ to produce either the elements or Cu₂Se, given below, are all positive and thus consistent with preferred formation of CuInSe₂.



$$\Delta G_f^{300\text{ }^{\circ}\text{C}} = 89.8 \text{ and, } \Delta G_f^{500\text{ }^{\circ}\text{C}} = 104 \text{ kJ/mol} \quad (4-7)$$



$$\Delta G_f^{300\text{ }^{\circ}\text{C}} = 236 \text{ and, } \Delta G_f^{500\text{ }^{\circ}\text{C}} = 249 \text{ kJ/mol} \quad (4-8)$$

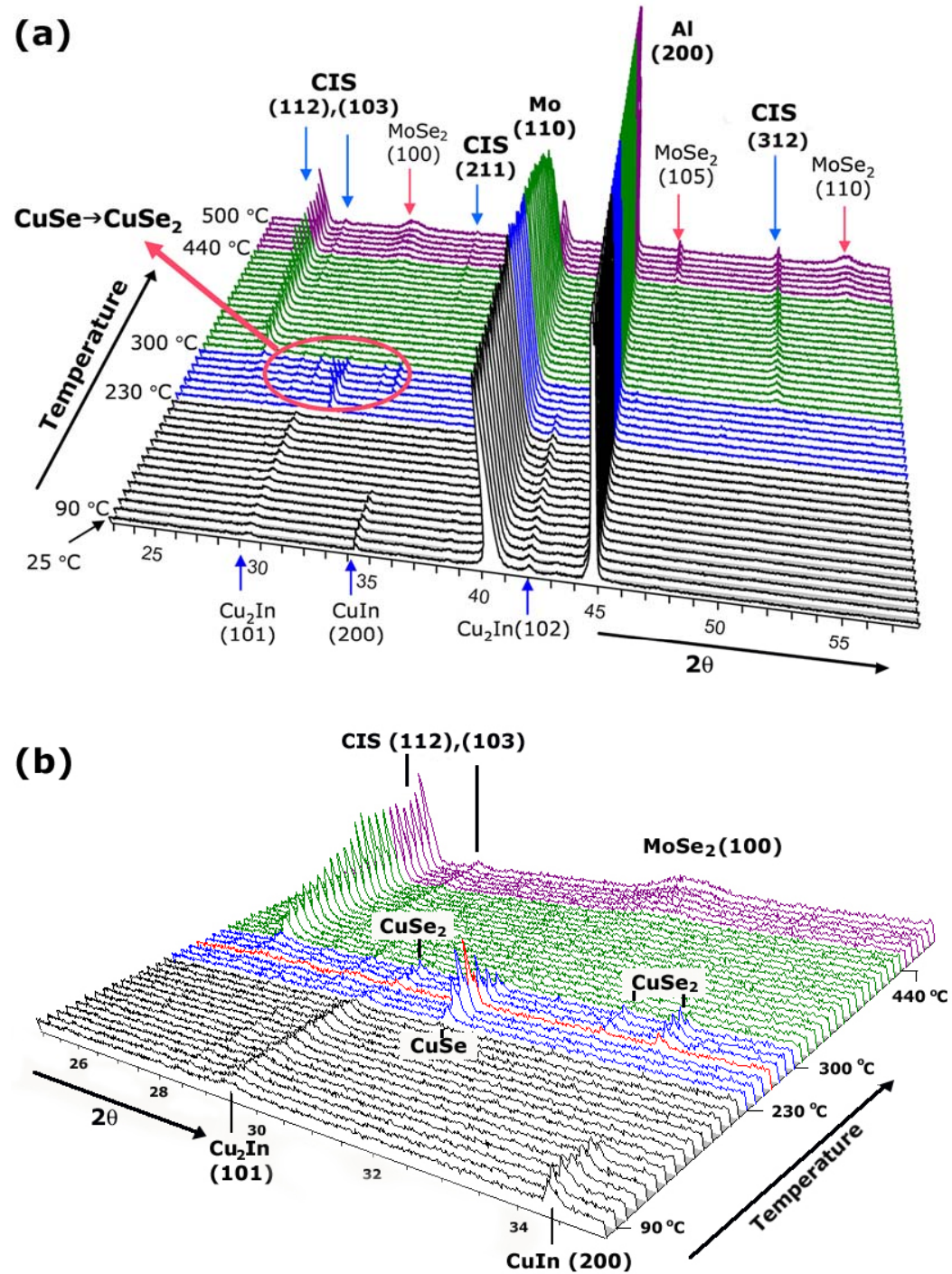


Figure 4-18. In situ X-ray diffraction pattern evolution during the selenization of a glass/Mo/Cu-In precursor films in the 2θ range (a) 23 to 58° and (b) 25 to 35°

This result suggests that monitoring the presence of MoSe₂ can be used for detecting complete formation of an absorber layer and perhaps a simple I-V characteristic

can be used. There have been a few reports about MoSe₂ formation and its contribution to the performance of CIGS solar cells. Wada *et al.* reported that the (100) and (110) reflections of MoSe₂ in Mo/CIGS absorbers deposited by a typical three stage process were detected by XRD and the Mo/CIGS hetero-contact including the MoSe₂ layer would be a favorable ohmic-type while the Mo/CIGS without MoSe₂ layer exhibits a Schottky-type contact [Wad01].

4.6.4 Isothermal Selenization

Isothermal annealing at selected temperatures between 260 and 330 °C was then performed for kinetic analysis using selected reaction models. A sample scan (scan time 1 min) is shown in Figure 4-19 for annealing at 280 °C. The 2θ scan range (20 to 30°) for the isothermal experiments was selected since the major reflection for the product CuInSe₂ (112) lies within this range.

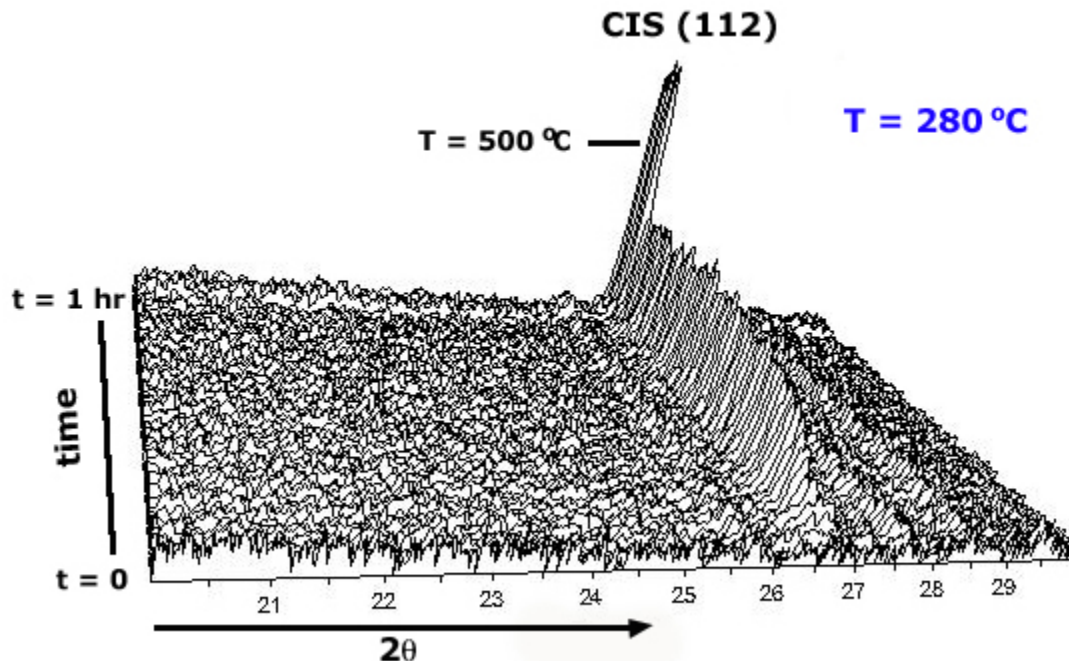


Figure 4-19. In situ X-ray diffraction pattern evolution during the isothermal selenization of a glass/Mo/Cu-In precursor film at 280 °C

To complete the reaction, the temperature was elevated to 500 °C after each run and then maintained for about 12 min until only the α -CuInSe₂ phase remained as evident by a constant peak intensity. The fractional reactions of product CuInSe₂ phase were estimated using the normalized α -CuInSe₂ (112) peak area assuming that the maximum peak area represents complete reaction. The reaction kinetics in terms of an activation energy and reaction order were estimated using two solid-state reaction models, the “Avrami” and “parabolic rate” models [Kim05a, Kim05b, Hul69], which were introduced in chapter 4.2.

In the Avrami model the transformation kinetics under isothermal reaction are described by equations (4-3) and (4-4). For experimental data of these particular samples, the n values over the entire temperature range, except at the highest temperature 330 °C (n=0.3) studied, are between 0.6 and 0.8, suggesting the Avrami model is appropriate for this reacting system below 330 °C as shown in Figure 4-20.

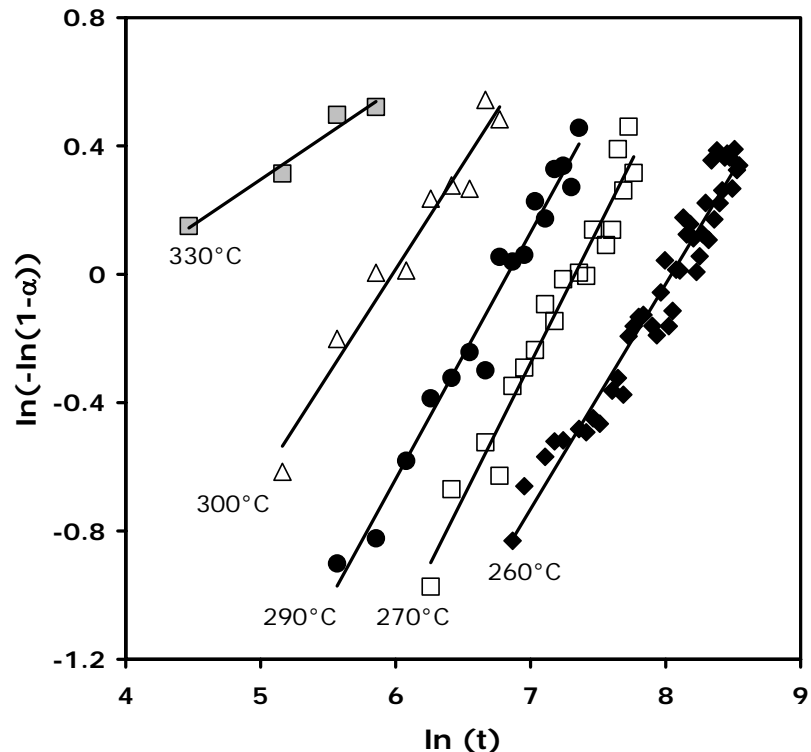


Figure 4-20. The Avrami model plot for α -CuInSe₂ formation by selenization of glass/Mo/Cu-In precursor films

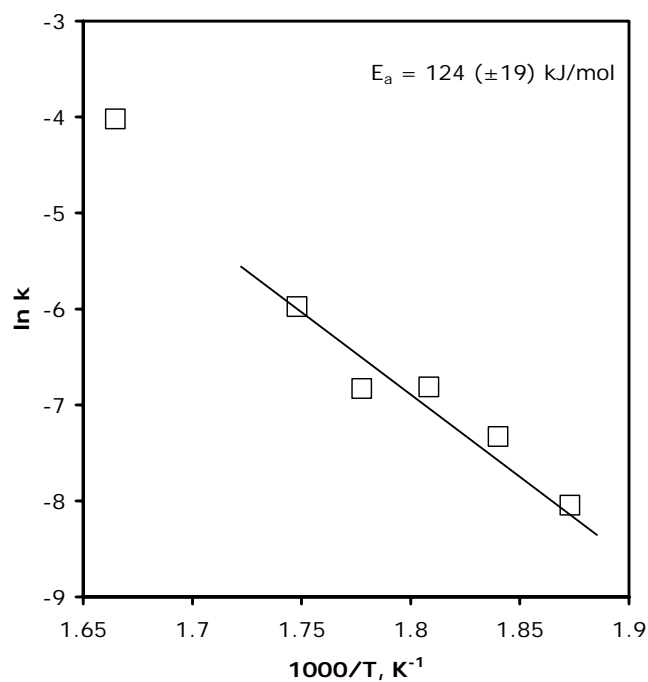


Figure 4-21. Arrhenius plot for Avrami kinetic constant for α -CuInSe₂ formation by selenization of glass/Mo/Cu-In precursor films

The low value of the estimated Avrami exponents also suggests that the nucleation of α -CuInSe₂ occurs so rapidly that the nucleation time is nearly zero. The Arrhenius equation (4-4) was used to estimate the apparent activation energy E_a for α -CuInSe₂ formation by selenization of glass/Mo/Cu-In precursor films. An activation energy of 124 (± 19) kJ/mol was estimated from the Arrhenius plot shown in Figure 4-21, where the data for 330 °C anneal was not used since it was considered as an outlier.

The simple parabolic rate model [Kim05a, Kim05b, Hul69] is another widely used one that was successfully employed for the CuInSe₂ formation from In₂Se₃/CuSe bilayer precursor in chapter 4.2. As the reaction proceeds, further reaction is limited by diffusion across the product layer to form more product layer at one of the interfaces of the two reactants. Assuming a uni-directional process (i.e., planar growth front), the reaction kinetics of the parabolic model is described by

$$\alpha^2 \sim k_p \cdot t \quad (4-12)$$

where α is the fractional reaction, k_p is the parabolic rate constant incorporating the diffusion coefficient of the migrating species, and t is time. Figure 4-22 shows the plot of α^2 vs. t for the same data set as used previously for the Avrami model analysis. The parabolic rate model also provides a good fit to the data over the entire isothermal experiment range (260 to 330 °C). An activation energy of 100 (± 14) kJ/mol estimated from the Arrhenius plot excluding the data for 330 °C is similar to the value estimated by Avrami model.

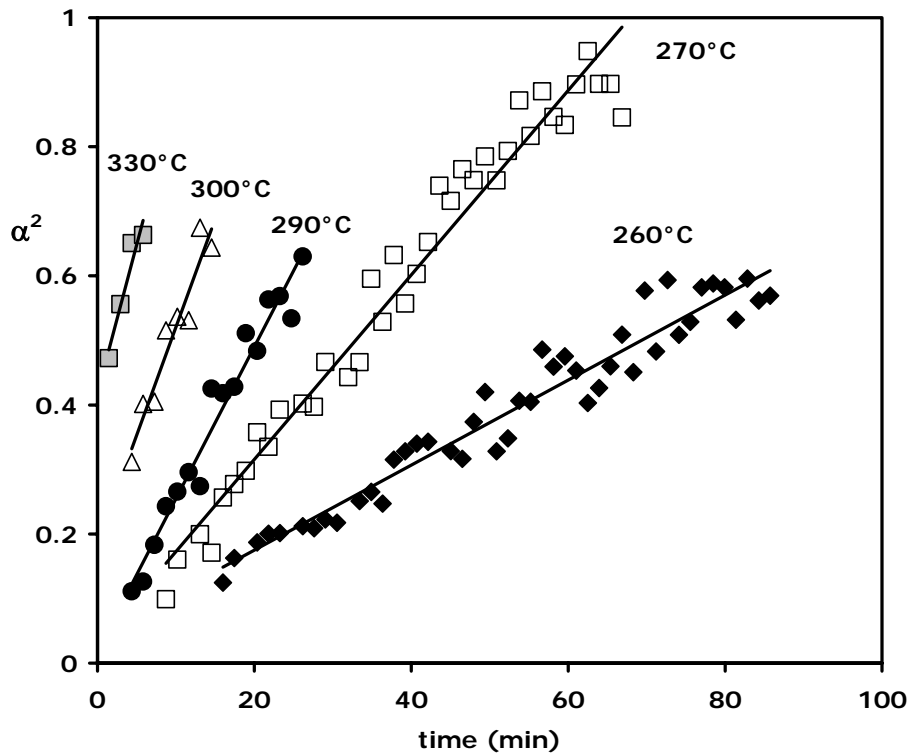


Figure 4-22. The parabolic rate model for $\alpha\text{-CuInSe}_2$ formation by selenization of glass/Mo/Cu-In precursor films

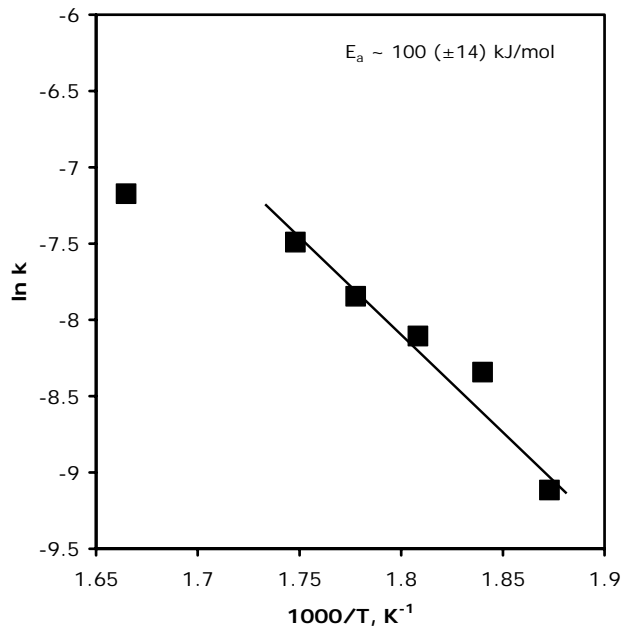


Figure 4-23. The parabolic rate model for $\alpha\text{-CuInSe}_2$ formation by selenization of glass/Mo/Cu-In precursor films

Based on the results of these two models, the formation of α -CuInSe₂ from selenization of Cu-In/Mo/glass precursor films apparently follows a one-dimensional diffusion controlled reaction with a nucleation and subsequent growth sequence. The process likely involves the rapid nucleation of CIS at the interface and formation of a thin and planar α -CuInSe₂ layer on top of the Cu-In films, which serves to limit reactant diffusion and thus formation of α -CuInSe₂.

4.7 Summary

Time-resolved, *in situ* high-temperature X-ray diffraction was successfully applied to investigate the reaction pathway and kinetics of polycrystalline α -CuInSe₂ formation from several different precursor structures, such as glass/In₂Se₃/CuSe, glass/InSe/Cu-Se, glass/CuSe/In-Se, glass/Mo/Cu-In-Se and glass/Mo/Cu-In.

The qualitative reaction pathway observation during the temperature ramp annealing of the glass/ In₂Se₃/CuSe bilayer precursor demonstrated that the stacked bilayer In₂Se₃/CuSe phases directly transform to α -CuInSe₂, as shown in Figure 4-24. Quantitative kinetic analysis of X-ray diffraction data obtained during isothermal annealing fits the parabolic rate reaction model, which suggests that α -CuInSe₂ formation in a bilayer glass/In₂Se₃/CuSe precursor follows a one-dimensional diffusion controlled reaction pattern with an activation energy of 162 (± 5) kJ/mol.

The process likely involves the formation of a thin and planar α -CuInSe₂ layer at the In₂Se₃-CuSe interface. The reaction layer forms sufficiently rapidly that no nucleation incubation time is apparent. This layer serves to limit reactant diffusion and thus the rate of further reaction. Given the rapid diffusivity of Cu in α -CuInSe₂, it seems reasonable that continued growth of α -CuInSe₂ occurs by Cu diffusion across the barrier

to the In_2Se_3 - α - CuInSe_2 interface to react with In_2Se_3 , which also requires transport of Se in the same direction. Of course it is likely that some of the excess Se is also lost on the top side due to volatilization, as evidenced by the comparison of ICP results between precursor ($[\text{Se}]/[\text{Metal}] \sim 1.2$) and annealed CuInSe_2 ($[\text{Se}]/[\text{Metal}] \sim 0.94$).

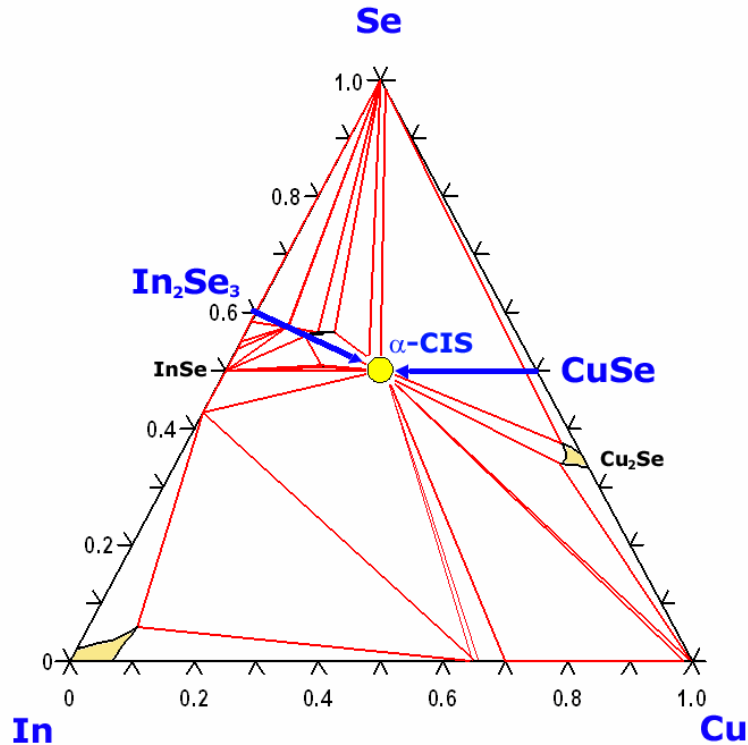


Figure 4-24. Reaction pathway of CIS formation from $\text{In}_2\text{Se}_3/\text{CuSe}$ precursor projected in ternary Cu-In-Se isothermal phase diagram at 500 °C

For glass/InSe/Cu-Se precursor, the results of temperature ramp annealing demonstrates that the initial Cu_7Se_4 phase begins to be transformed to CuSe by further reaction with Se at around 190 °C, and CuInSe_2 formation then is initiated with the decrease of CuSe peak at around 230 °C. For glass/CuSe/In-Se precursor, part of initial CuSe phase is first transformed to CuSe_2 at around 170 °C by reacting with selenium available in the top layer, then starts to release selenium at 190 °C. At the same temperature, the other portion of initial CuSe phase also releases selenium to yield the Cu_{2-x}Se . Finally, the disappearance of CuSe and Cu_{2-x}Se lead to the formation of

CuInSe_2 . On the other hand, intimately mixed glass/Mo/Cu-In-Se precursor directly forms CuInSe_2 at low temperature (200°C).

The α - CuInSe_2 formation from glass/Mo/Cu-In-Se precursor is initiated at around 140°C , and the initial amorphous Cu-In-Se elemental mixtures are directly transformed to crystalline α - CuInSe_2 phase without any intermediate phases, as illustrated in Figure 4-25. Isothermal soaking experiments at selected temperature (140 to 400°C) revealed that the α - CuInSe_2 formation occurs so rapidly (less than 1 min) at given temperature, and both the saturated fractional reaction and product grain size increase with isothermal soaking temperature.

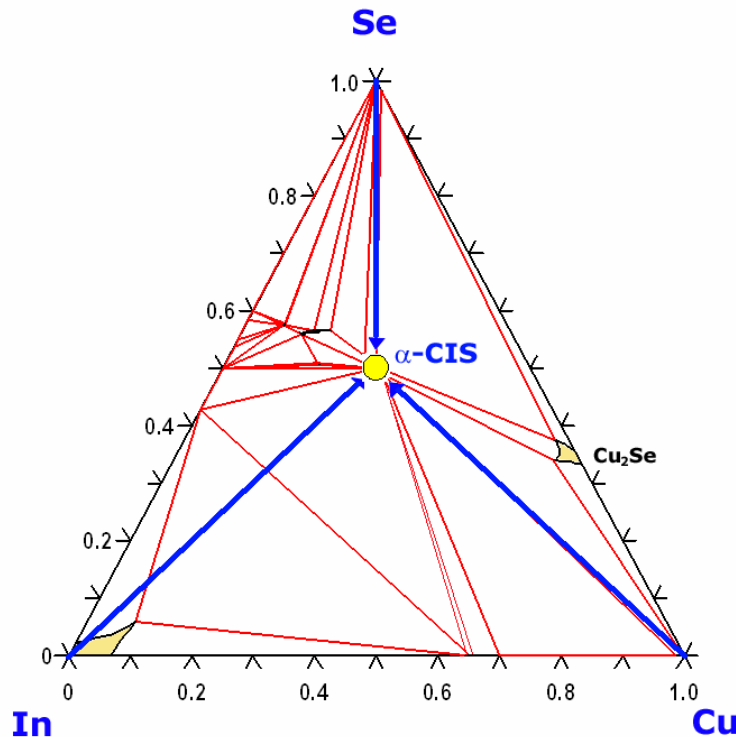


Figure 4-25. Reaction pathway of CIS formation from intimately mixed Cu-In-Se precursor projected in ternary Cu-In-Se isothermal phase diagram at 500°C

During the selenization of glass/Mo/Cu-In precursor structure by temperature ramp annealing, the formation of CuSe and its transformation to CuSe_2 , and then CuSe_2 to

CuInSe₂ were observed in the temperature range ~230 to 300 °C. The production of MoSe₂ accompanied by a rapid decrease of Mo (110) peak height, occurred at temperatures above 440 °C only after the production of CuInSe₂ was complete.

The α -CuInSe₂ formation by the selenization of glass/Mo/Cu-In precursors could be described by a one-dimensional diffusion controlled reaction process. For this reaction, the activation energies of 124 (± 19) and 100 (± 14) kJ/mol were estimated with the Avrami and parabolic rate models, respectively. Both of these values for the activation energy are between the value for CuInSe₂ formation from a glass/InSe/CuSe bilayer precursor (66 kJ/mol) and the value for CuInSe₂ formation from a glass/In₂Se₃/CuSe bilayer precursor (162 ± 5 kJ/mol) estimated from similar hot-stage XRD studies [Kim05a-b].

In summary, the reaction rates in terms of kinetic constants were compared for CIS formation from different precursor structures as shown in Figure 4-26. The kinetic analysis using both parabolic and Avrami models suggests that the CIS formation from InSe/CuSe precursor is faster than that from In₂Se₃/CuSe and Cu-In precursor structures at low temperature. Interestingly, in the plots of parabolic rate constants, the crossover between In₂Se₃/CuSe and InSe/CuSe precursors was observed at 265 °C, which concludes that In₂Se₃/CuSe precursor may lead to the CIS phase faster than InSe/CuSe precursor at the temperature higher than 265 °C.

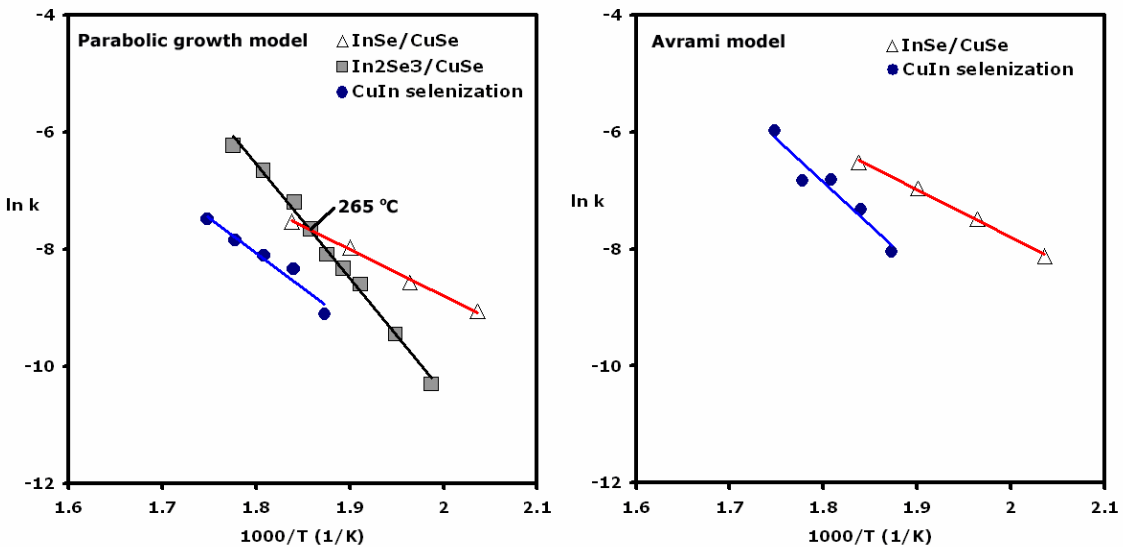


Figure 4-26. Comparison of reaction rates for CIS formation from different precursors estimated by the parabolic and Avrami model.

CHAPTER 5

CUGASE2 FORMATION PATHWAYS AND KINETICS

5.1 Introduction

One approach to obtain an even higher efficiency CIGS based-solar cell is a tandem cell structure that uses the high-efficiency In-rich CIGS device as the bottom cell and a wider band-gap absorber for the top cell. CuGaSe₂ has a band-gap energy of 1.68 eV, and thus is a promising absorber material for the top cell in a CIGS tandem solar cell structure [Sch00, Fis01, Rus04]. Recently, a record-efficiency of 10.23% for a surface-modified single junction CuGaSe₂ cell was reported by NREL [Abu05].

While there have been several studies regarding the equilibrium phase diagram [Göd00a-c] and reaction mechanism [Zwe95, Adu95, Kat99, Bru03, Wol00] of CuInSe₂, only a few fundamental investigations of the CGS system have been reported. Purwins *et al.* reported the formation of CuGaSe₂ from a stacked bilayer Ga₂Se₃/Cu₂Se followed a nucleation and growth model with an activation energy of 129 kJ/mol, which is extracted from a Kissinger analysis of differential scanning calorimetric data [Pur06].

In previous studies, *in situ* time-resolved, high-temperature X-ray diffraction was successfully employed to investigate the reaction pathway and kinetics of α -CuInSe₂ formation from different precursors (e.g., InSe/CuSe [Kim05a], In₂Se₃/CuSe [Kim05b], CuSe/In-Se, InSe/Cu-Se and Cu-In-Se) and selenization of metallic Cu-In precursor [Kim06a].

In this chapter, the reaction pathways and kinetics for CuGaSe₂ formation from thermal annealing of glass/GaSe/CuSe and glass/Mo/Cu-Ga-Se, and selenization of

glass/Mo/Cu-Ga precursor were investigated using *in situ* time-resolved, high-temperature X-ray diffraction.

5.2 Glass/GaSe/CuSe Precursor

5.2.1 Precursor Preparation

Bilayer GaSe/CuSe precursor films were deposited on extremely smooth and sodium-free (alkali level < 0.3%) thin glass substrates (Corning #7059). Glass substrates with a thickness of 0.4 (± 0.127) mm were employed to minimize the temperature difference and response time between the Pt/Rh heater strip and the precursor film in the HTXRD furnace used for subsequent characterization. The precursors were fabricated by depositing a GaSe film at a substrate temperature of ~ 250 °C, followed by deposition of a crystalline CuSe film on the as-grown GaSe layer at a lower substrate temperature of ~ 150 °C to minimize the potential reaction between the GaSe and CuSe precursor layers.

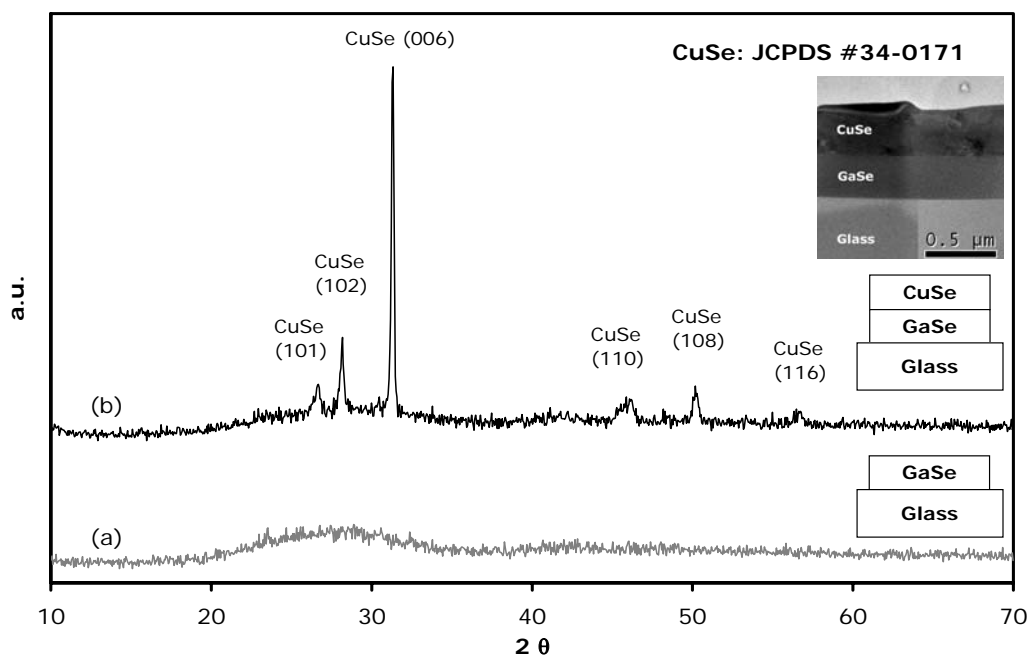
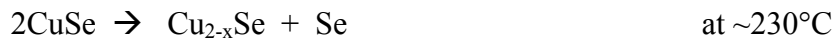


Figure 5-1. Room temperature XRD scans and TEM micrograph of as-grown precursor films: (a) glass/GaSe monolayer, (b) glass/GaSe/CuSe bilayer.

The bilayer structure and its total film thickness (~700 nm) were identified by TEM as shown in Figure 5-1, and the atomic composition was measured by inductively coupled plasma optical emission spectroscopy (ICP-OES), yielding the ratios of [Cu]/[Ga]~1.02 and [Se]/[Metal]~0.97. The XRD and TEM characterization of the precursor films revealed an amorphous-GaSe / polycrystalline-CuSe bilayer structure as shown in Figure 5-1.

5.2.2 Temperature Ramp Annealing

Temperature ramp annealing using Scintag HT-XRD system was first performed to investigate the phase evolution of the samples and to establish a suitable isothermal annealing temperature range. The glass/GaSe/CuSe bilayer sample was first heated to 150 °C at a rate of 30 °C/min and then X-ray diffraction data were collected for 1 min during subsequent ramp heating (30 °C/min). Four sequential scans over a range of 20 to 54° (2θ) were taken for 1 min at 10 °C increments while the sample was heated from 150 to 350 °C in a flowing He atmosphere. Figure 5-2 demonstrates that the initial CuSe phase begins to be transformed to β-Cu_{2-x}Se at around 230 °C, and CuGaSe₂ formation is initiated with the decrease of β-Cu_{2-x}Se peak at around 260 °C. The expected interfacial reaction pathway is



5.2.3 Isothermal Annealing

Time-resolved, high temperature X-ray diffraction data were collected using a linear position sensitive detector (LPSD), while the bilayer glass/GaSe/CuSe precursor

films were maintained at a constant temperature in a He (flow rate \sim 100 sccm) atmosphere.

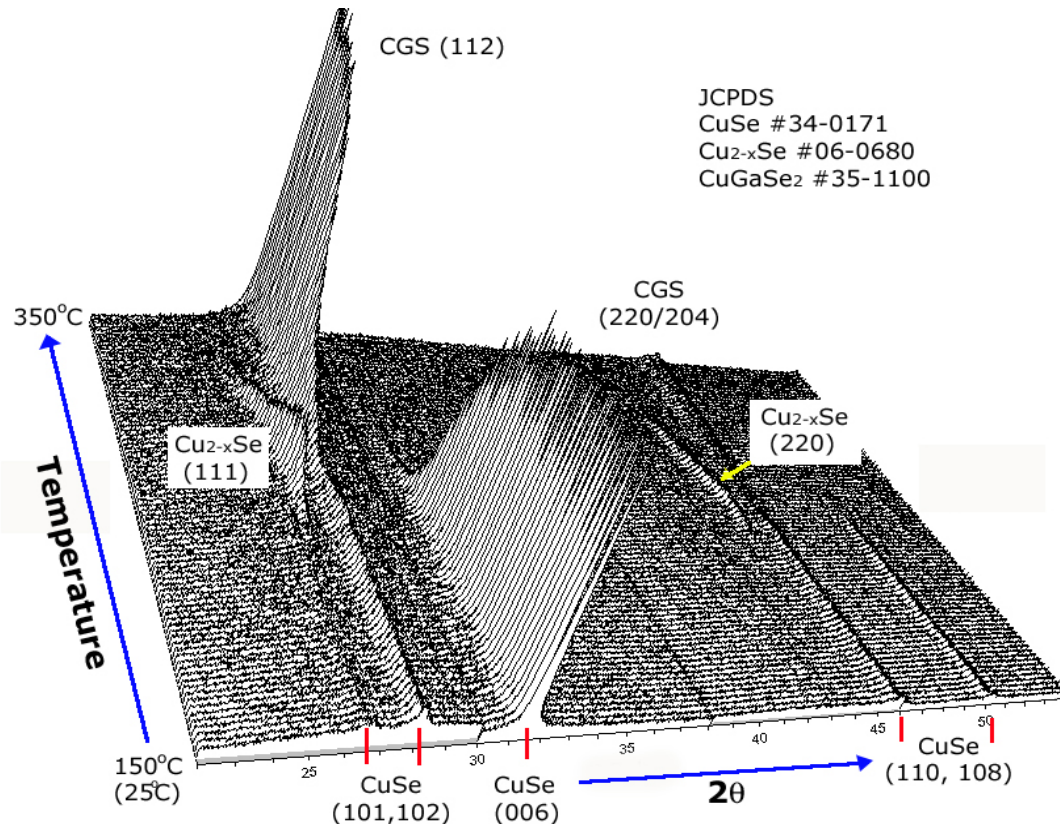


Figure 5-2. In situ XRD scans during temperature ramp annealing ($30\text{ }^{\circ}\text{C}/\text{min}$) of the glass/GaSe/CuSe sample.

A set of isothermal experiments were performed with a range of set point temperature selected from the temperature ramp scan results shown in Figure 5-2. The set point temperature was selected so that the total isothermal holding time was much longer (i.e., several hours) than an individual scan time (~ 35 sec). A three-step heating protocol was used to minimize heating time without temperature overshooting. Initially, the temperature was rapidly ramped at a rate of $300\text{ }^{\circ}\text{C}/\text{min}$ to a value $20\text{ }^{\circ}\text{C}$ below the set-point temperature, and then at a rate of $200\text{ }^{\circ}\text{C}/\text{min}$ to a value $10\text{ }^{\circ}\text{C}$ below the set-point temperature. Finally, the temperature was ramped to a set point at a rate of $100\text{ }^{\circ}\text{C}/\text{min}$, and then held at the set-point temperature to monitor the evolution of the

isothermal reaction. To complete the reaction, the temperature was elevated to 500 °C and maintained for about 12 min until only the CuGaSe₂ phase remained and the corresponding peak intensity remained constant. The temperature range for the isothermal experiments was from 280 to 370°C. The 2θ scan range (24 to 34°) for the isothermal experiments was selected to focus on the major peaks of the reactant, intermediate and product, i.e., CuSe (006), Cu_{2-x}Se (111), and CuGaSe₂ (112).

Figure 5-3 displays the time-resolved XRD data collected for the film isothermally reacted at different temperatures. The comparison between the isothermal plots at four different temperatures clearly illustrates that the reaction rate increases with temperature and follows a deceleratory reaction pattern. To obtain the fractional reaction (α), which is defined as the fraction of reaction completed at time t , the integrated intensities of the product CuGaSe₂ (112) peaks were obtained by peak fitting the diffraction data using the software package JADE, and were normalized assuming that the reactants were completely transformed to crystalline CuGaSe₂ after each run, and that the texture of the CuGaSe₂ did not appreciably change through the entire heating process. As shown in Figure 5-4, an analysis of the fractional reaction (α) with respect to time at different isothermal temperatures demonstrates that CuGaSe₂ formation follows the deceleratory reaction trend, which is consistent with diffusion-controlled reaction kinetics.

The reaction kinetics in terms of activation energy (E_a), kinetic constant (k) and reaction order (n) were investigated employing two conventional diffusion-controlled reaction models, i.e., parabolic rate and Avrami models. In chapter 4, it has been shown that these methods yield satisfactory fits to relevant experimental data such as CuInSe₂

formation from glass/InSe/CuSe and glass/In₂Se₃/CuSe bilayer precursors, and selenization of Cu-In metallic precursor.

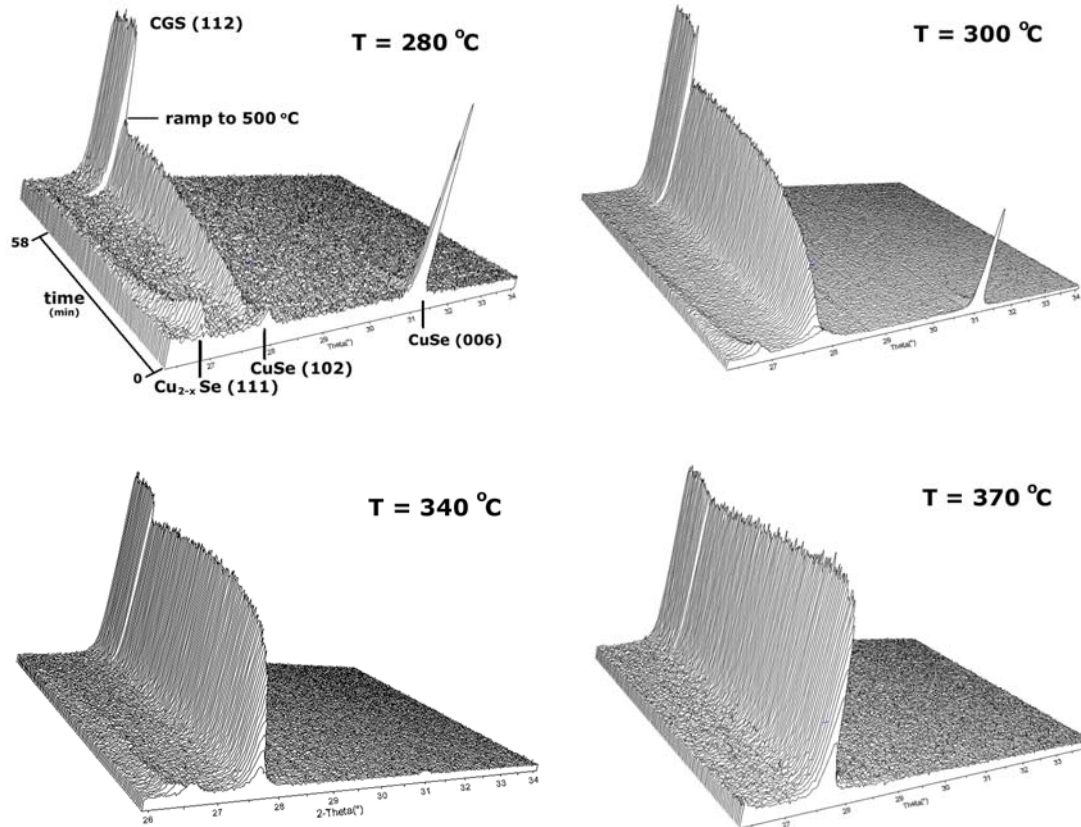


Figure 5-3. In situ time-resolved XRD scans during isothermal annealing of the glass/GaSe/CuSe precursor structure at selected temperatures (i.e., 280, 300, 330 and 370 °C)

As mentioned in chapter 4, the simple parabolic rate model [Hul69] was developed based on a reaction between two solid materials with planar surfaces, a case identical to the GaSe/CuSe precursor structure considered here. This model is consistent with a physical process that requires a limiting reactant to diffuse across the product layer that initially formed at the interface of the two reactants. The product layer thickness increases with time to further decrease the diffusive flux of the limiting reactant.

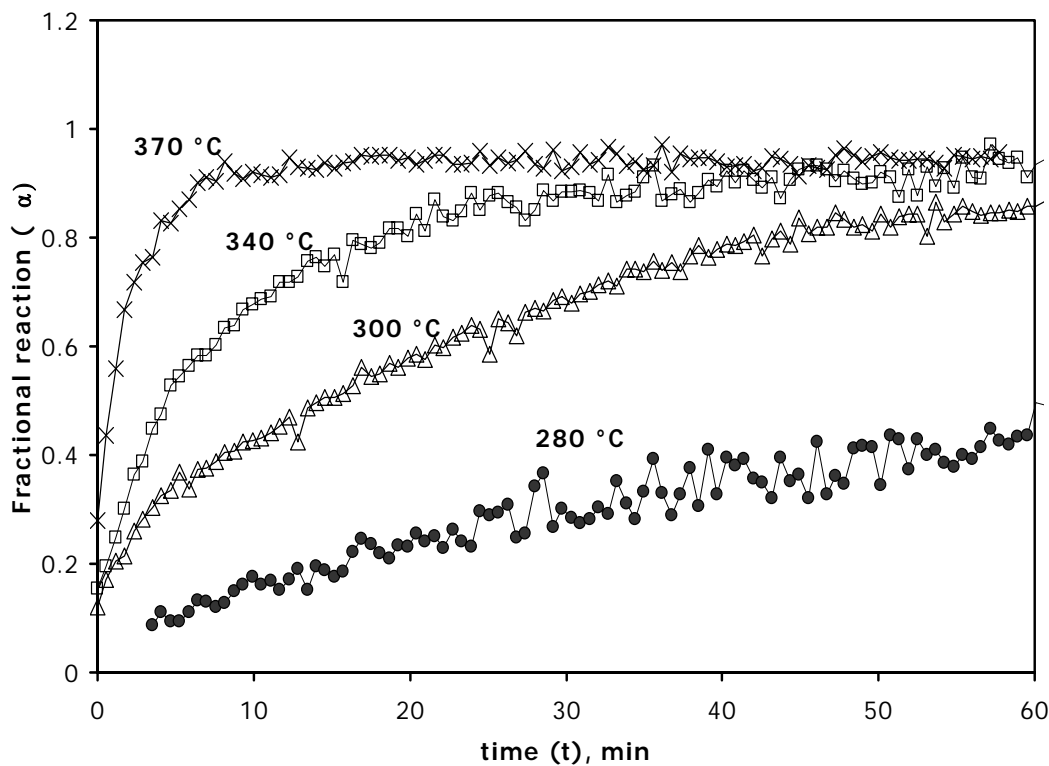


Figure 5-4. Fractional reaction (α) with respect to time (t) at selected isothermal temperatures

Assuming a uni-directional process with a boundary condition of $\alpha = 0$ at time $t = 0$, the reaction kinetics of the parabolic model are described by equation 4-4. Figure 5-5 shows the plot of α^2 vs. t for the isothermal reaction of the precursor films at different temperatures, including the corresponding Arrhenius plot as shown in Figure 5-6. It is evident that the parabolic reaction model provides a satisfactory fit to the data over the entire set of isothermal temperatures (280 to 370 °C).

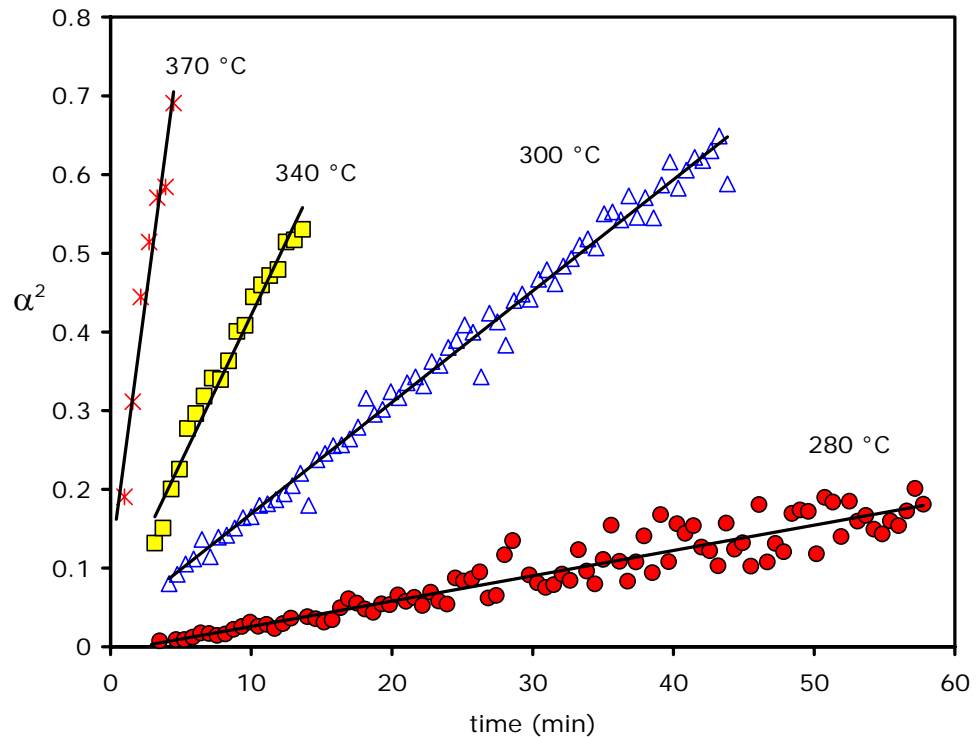


Figure 5-5. Parabolic rate model plot for glass/GaSe/CuSe precursor structure

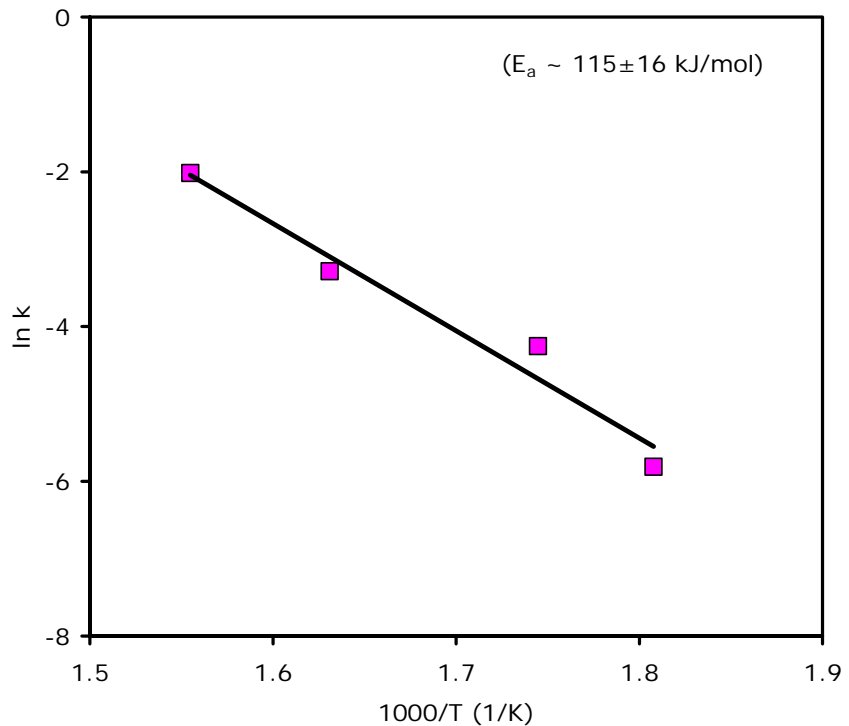


Figure 5-6. Arrhenius plot of the Parabolic rate constant for glass/GaSe/CuSe precursor structure

The extracted parabolic kinetic constants (k_p) are summarized in Table 5-1. It is concluded that the formation of CuGaSe₂ in a glass/GaSe/CuSe bilayer precursor films is consistent with a one-dimensional diffusion controlled reaction pattern. The implied process involves the formation and growth of a CuGaSe₂ layer at the GaSe-CuSe interface, which limits the reactant diffusion and thus the rate of further reaction. Finally, the data in the Arrhenius plot of Figure 5-6 along with the Arrhenius equation 4-6 is used to estimate the apparent activation energy E_a for the CuGaSe₂ formation reaction in glass/GaSe/CuSe bilayer precursor films, yielding a value of $E_a = 115 (\pm 16)$ kJ/mol.

As a more sophisticated growth model, the Avrami model was applied to the data. The Avrami model considers a reaction of the additive type between two reactants, where the product phase is growing from randomly distributed nuclei within a reactant phase. Analysis of solid-state reaction data using the Avrami model, which has more sophisticated form than parabolic rate model, is commonly used for preliminary identification of growth rate laws. Since an isotropic growth is assumed in the Avrami model, the product regions should be spherical. As a consequence, when the growth of the nuclei is diffusion-controlled, the parabolic growth law introduced in the previous section is also applicable, *i.e.*, the growth rate in any direction is proportional to $t^{0.5}$. The isothermal Avrami transformation kinetics with an initial condition of $\alpha(t=0) = 0$ are given by equation 4-3. If an induction period exists before crystallization starts, the Avrami expression can be modified as

$$\alpha = 1 - \exp(-(k(t - t_0))^n) \quad (5-1)$$

where t_0 is the time before crystallization starts [Nor69].

According to the results of our isothermal experiments shown in Figure 5-3 and 5-4, the CuGaSe₂ formation was already initiated before the temperature reached the set-point, i.e., $\alpha(t=0) \neq 0$. A model that substitutes $\alpha - \alpha_0$, where α_0 is the fractional conversion at $t=0$, was evaluated initially, but did not represent the data well. Thus a second approach was taken. Considering this initial condition, a modified Avrami expression is suggested as below, although a physical basis is not evident:

$$\alpha = 1 - \exp(-(k(t + t^*))^n) \quad (5-2)$$

or equivalently, as

$$\ln(-\ln(1-\alpha)) = n \ln(t + t^*) + n \ln k \quad (5-3)$$

where t^* is the time constant which satisfies the initial condition (i.e., $\alpha(t=0) = \alpha_0$) at given temperature. Also, this time constant represents the starting time of reaction that is extrapolated from the Avrami model plot (i.e., $\alpha(t=-t^*) = 0$). To find the kinetic parameters, n , k and t^* , the following iteration steps are employed.

- ① Guess the time constant t^*
- ② Find n and k by a linear fitting of $\ln(-\ln(1-\alpha))$ vs. $\ln(t + t^*)$
- ③ Apply the initial condition, $\alpha(t=0) = \alpha_0$ to Equation (5-3)

$$\ln(-\ln(1-\alpha_0)) - n \ln(t^*) - n \ln k = \varepsilon \quad (5-4)$$

The steps ①, ② and ③ are repeated until an acceptable error (ε) is obtained.

The resulting Avrami model plot was compared with the experimental data in Figure 5-7. The Avrami model expressed by Equation (5-3) yields a satisfactory (i.e., linear) fit with the estimated kinetic parameters summarized in Table 5-1.

Table 5-1. Estimated kinetic parameters for the CuGaSe₂ formation from glass/GaSe/CuSe bilayer precursor films (k_p and k : apparent kinetic constants n : Avrami exponents and t^* : time constant for modified Avrami model)

Temperature [°C]	Parabolic model		Modified Avrami model	
	$k_p \times 10^3$ [s ⁻¹]	n	$k \times 10^3$ [s ⁻¹]	t^* [s]
280	0.050 ($\pm 8.02 \times 10^{-4}$)	0.70 ($\pm 7.4 \times 10^{-3}$)	0.129 ($\pm 1.20 \times 10^{-4}$)	0 [#]
300	0.237 ($\pm 2.92 \times 10^{-3}$)	0.69 ($\pm 9.1 \times 10^{-3}$)	0.693 ($\pm 8.71 \times 10^{-4}$)	75.0
340	0.623 ($\pm 2.38 \times 10^{-2}$)	0.73 ($\pm 1.3 \times 10^{-2}$)	1.74 ($\pm 3.47 \times 10^{-3}$)	49.2
370	2.22 ($\pm 2.32 \times 10^{-1}$)	0.68 ($\pm 2.2 \times 10^{-2}$)	7.97 ($\pm 4.53 \times 10^{-2}$)	24.6

#: Experimentally determined since no pre-reaction was observed for this run.

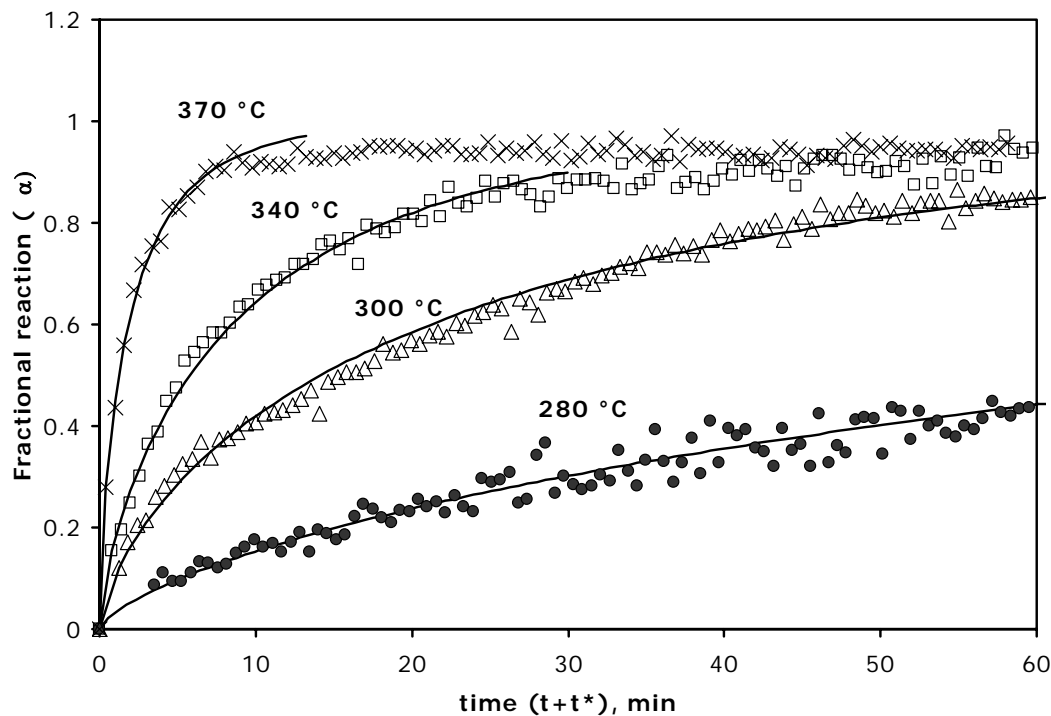


Figure 5-7. Fractional reaction (α) with respect to time ($t+t^*$) and Avrami model plot at selected isothermal temperatures (Symbols: experiments, solid line: Avrami model prediction)

In the case of one-dimensional, diffusion-controlled reactions with first-order nucleation processes, the Avrami exponent can vary between 0.5 and 1.5 depending on the nucleation frequency. The value of n is close to 0.5 if the nucleation is instantaneous, and close to 1.5 if the nucleation rate is constant throughout the reaction [Hul69]. As shown in the Table 5-1, the values of the Avrami exponents lie between 0.68 and 0.73, which are close to the lower limiting value of 0.5. Figures 5-8 and 5-9 displays the Avrami model and corresponding Arrhenius plots for the same data set previously analyzed by the parabolic rate model.

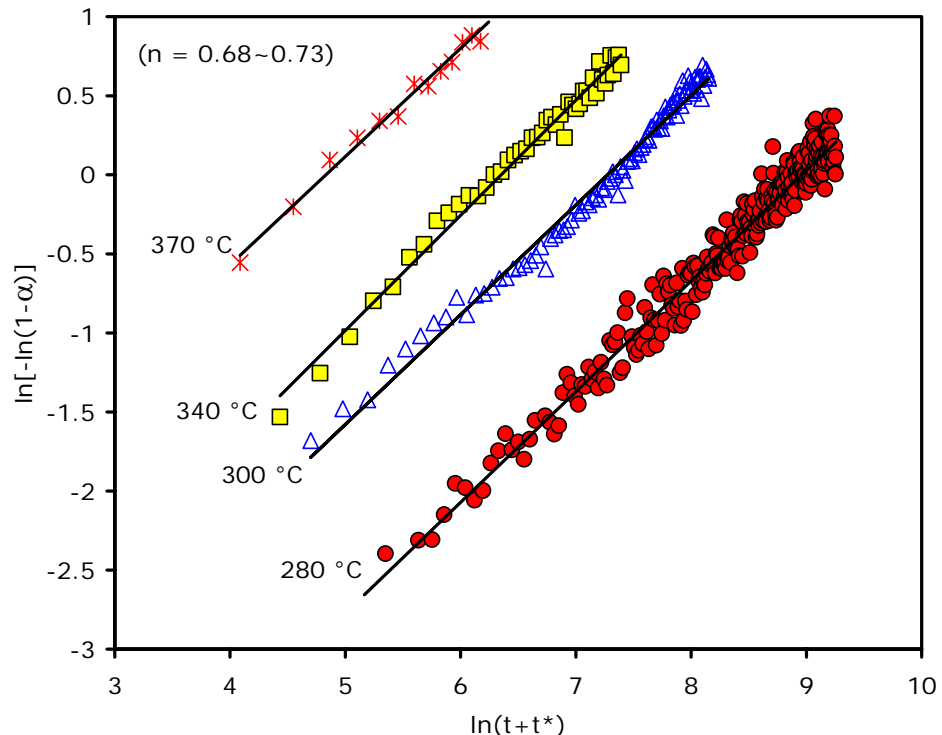


Figure 5-8. Modified Avrami model plot for glass/GaSe/CuSe precursor structure

The resulting Avrami exponents thus suggest that nucleation occurs so rapidly that the nucleation time may be neglected. This is consistent with the suggestion that nucleation and subsequent growth have occurred before the start of the isothermal experiment, i.e., $t=0$. Formation of nuclei and their growth either in the deposition

process or during the heating step is consistent with rapid nucleation as estimated by $n \approx 0.5$.

Using an Arrhenius model of the form given in Equation (5-2), it is readily established that the apparent activation energy is $124 (\pm 19)$ kJ/mol, which is in agreement with the value of $115 (\pm 16)$ kJ/mol obtained via the parabolic rate-model analysis. These activation energies for CGS formation are larger than the value of $65\sim 66$ kJ/mol [Kim05a] obtained by parabolic and Avrami model analysis for α -CIS formation from glass/InSe/CuSe stacked bilayer precursor having a structure analogous to the glass/GaSe/CuSe used in this study.

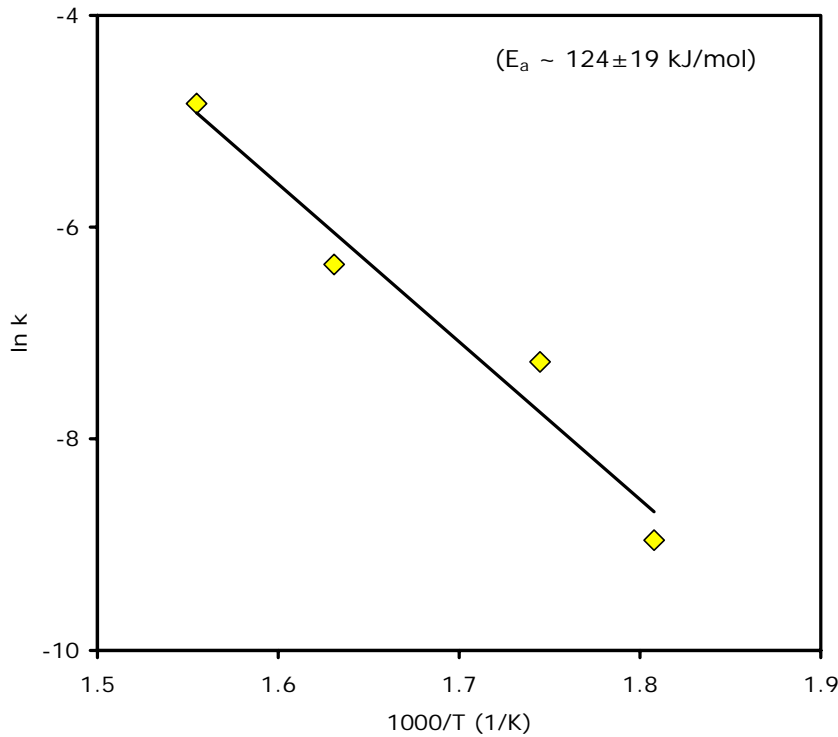


Figure 5-9. Arrhenius plot of the Avrami model rate constant for glass/GaSe/CuSe precursor structure

5.2.4 TEM-EDS Analysis

To support the high temperature X-ray diffraction results on reaction pathway and kinetics of CGS formation, a TEM-EDS (energy dispersive X-ray spectrometry) analysis was performed using a JEOL JEM 2010 F Scanning Transmission Electron Microscope. First, the glass/GaSe/CuSe precursor was isothermally soaked on the Pt/Rh strip heater of 300 °C for 30 min in a flowing He, and then quenched by turning off the heater power and increasing the He flow rate. A strip heater system directly heating the bottom of sample is much more feasible for quenching experiment than an environmental heater system heating the entire volume of ambient gas inside furnace. Both the as-grown precursor and 300 °C -annealed sample were coated by carbon to get better electrical conductivity and thus better image resolution during TEM analysis. The TEM samples were prepared using a FEI Strata DB 235 focused ion beam (FIB). It is noted that an Au-grid instead of conventional Cu-grid was used to hold TEM samples to prevent Cu-grid from interfering with the EDS analysis for Cu concentration profile.

The TEM images along with EDS line scan results were compared in Figure 5-10. A bilayer structure of as-grown glass/GaSe/CuSe precursor is clearly illustrated by the TEM image and EDS scan results in Figure 5-10(a). Interestingly, the EDS gallium concentration profile shows a small tail on the top side of the CuSe layer, which is attributed to the diffraction by gallium accumulated during the bombardment of gallium ion used by the FIB system. The TEM image and EDS line scan results of 300 °C – annealed sample shown in Figure 5-10(b) demonstrate that CuGaSe₂ forms at the interface between GaSe and CuSe layers, which explicitly supports the primary assumption of the parabolic growth model. According to the plot of fractional reactions with respect to time at 300 °C shown in Figure 5-4, the glass/GaSe/CuSe film

isothermally annealed at 300 °C for 30 min is expected to yield around 0.7 of fractional reaction, which is pictorially evidenced by TEM image in Figure 5-10(b).

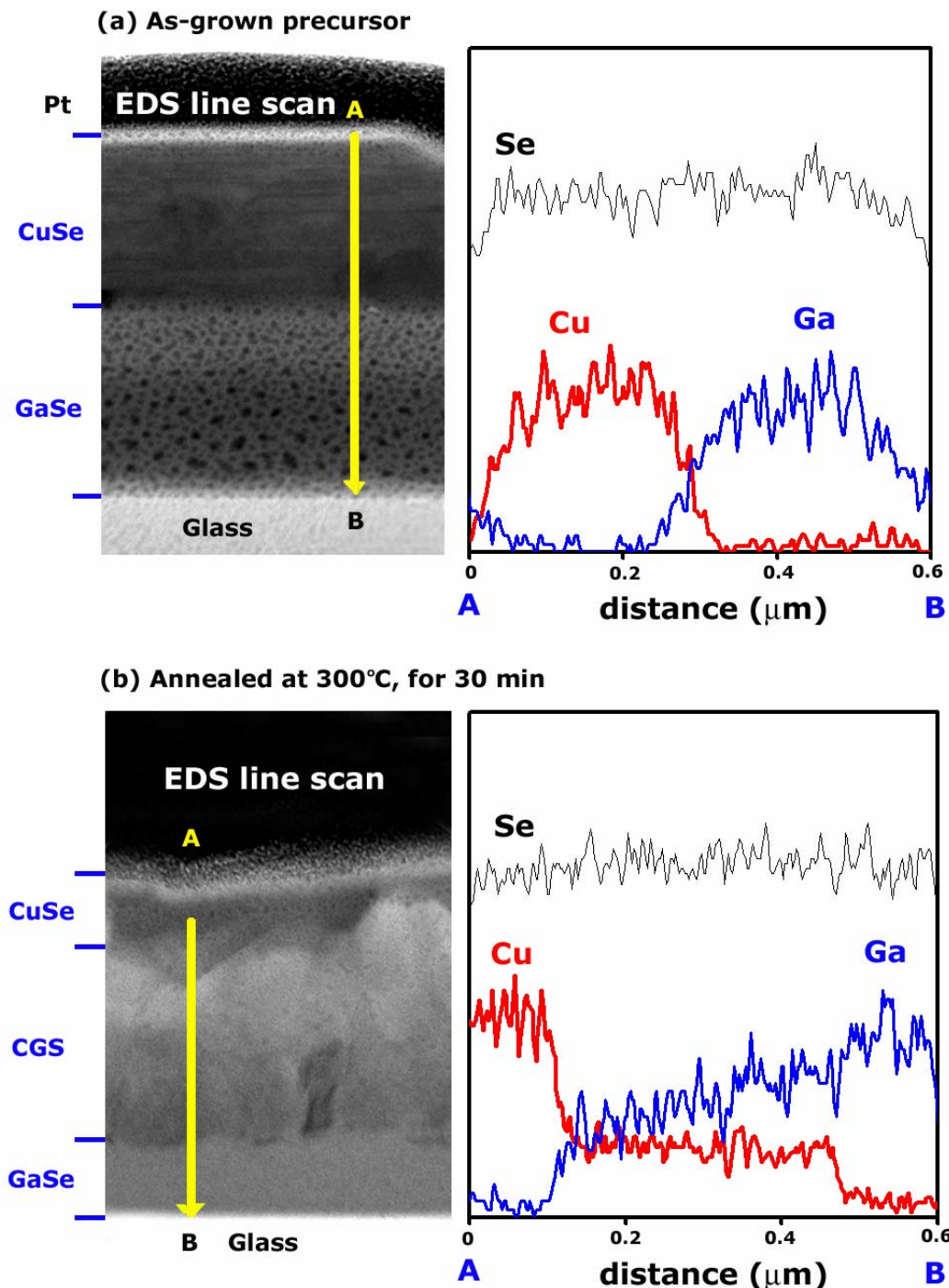


Figure 5-10. TEM-EDS analysis on (a) as-grown glass/GaSe/CuSe precursor, (b) sample annealed at 300 °C, for 30 min

There is no evidence for the Cu diffusion into GaSe and Ga diffusion into CuSe layer. There is, however, a non-uniformity in the Ga concentration within the CGS layer, while the concentration of Cu and Se is consistent over the entire CGS region. It may be qualitatively explained by a lower value of diffusivity of Ga than that of Cu into CGS that yields a Cu-rich CGS at the top part of CGS and a Ga-rich CGS at the bottom part of CGS layer.

5.3 Glass/Mo/Cu-Ga-Se Precursor

5.3.1 Precursor Preparation

The glass/Mo/Cu-Ga-Se precursors were prepared by co-deposition of elemental Cu, Ga, and Se on Mo-coated thin glass substrate in the MEE system without heating the substrate.

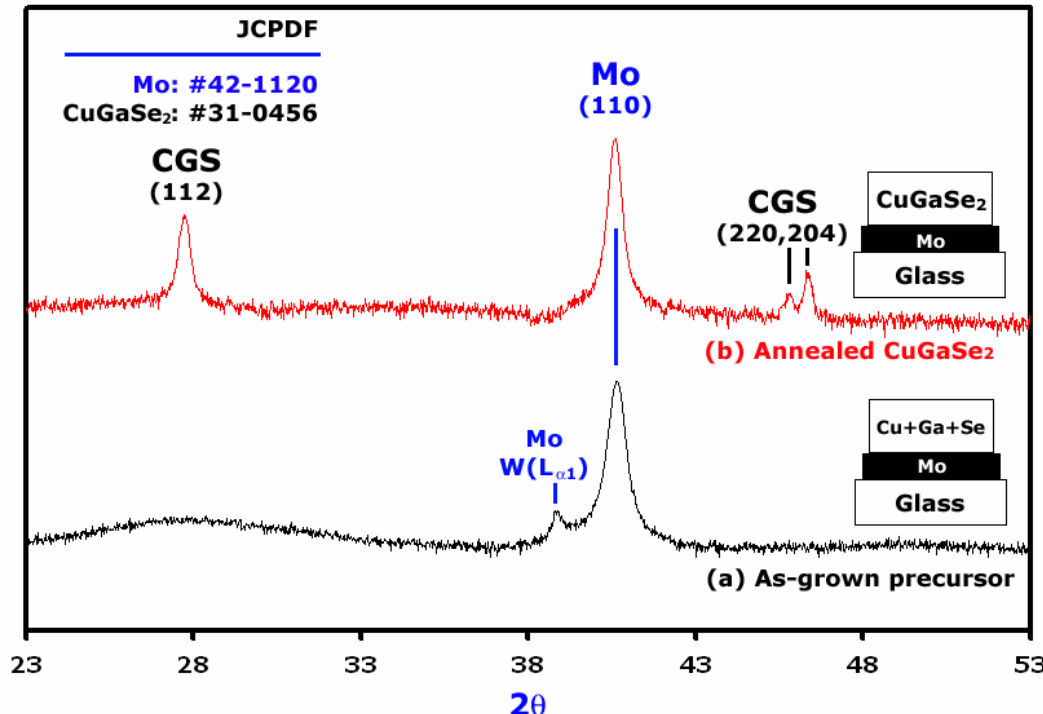


Figure 5-11. Room temperature X-ray diffraction of (a) as-grown glass/Mo/Cu-Ga-Se precursor, and (b) thermally annealed CuGaSe₂

ICP analysis revealed a Cu-rich ($[Cu]/[Ga] \sim 1.08$) and Se-rich ($[Se]/[Cu+Ga] \sim 1.73$) overall atomic composition. As shown in Figure 5-11, the room temperature XRD pattern for the as-grown precursor and completely annealed samples demonstrate that no crystalline phase forms during co-deposition of the elements (i.e., Cu, Ga, and Se), and polycrystalline $CuGaSe_2$ can be produced by thermal treatment of the Cu-Ga-Se elemental mixture.

5.3.2 Temperature Ramp Annealing

Temperature ramp annealing with Scintag HT-XRD system was used to investigate the phase evolution of the samples and to establish a suitable isothermal annealing temperature range. The glass/Mo/Cu-Ga-Se precursor was first heated to 100 °C at a rate of 30 °C/min, and then four sequential X-ray scans (scan time: 1min) over a 2θ range of 20 to 54° were taken at 10 °C increments during subsequent ramp heating up to 400 °C at a rate of 30 °C/min in a flowing He atmosphere. The O_2 content of the outlet He gas was measured by an O_2 analyzer to be less than 0.1 ppm.

The results shown in Figure 5-12 reveal that $CuSe_2$ forms at around 160 °C followed by its transformation to $CuSe$ at around 200 °C, and $CuGaSe_2$ formation then is initiated with the decrease of $CuSe$ peak at around 280 °C. No crystalline Ga_xSe_y compound, however, was detected, which suggests most of the gallium is contained in the amorphous state (Ga_xSe_y compound or liquid Ga) before participating in the $CuGaSe_2$ formation reaction. Figure 5-10(b) demonstrates the 2θ location of CGS (112) peak is relatively stable with respect to temperature while the $CuSe$ (102) peak significantly shifts to lower values of 2θ as the temperature increases, which qualitatively indicates that the thermal expansion coefficient of CGS is considerably smaller than that of $CuSe$.

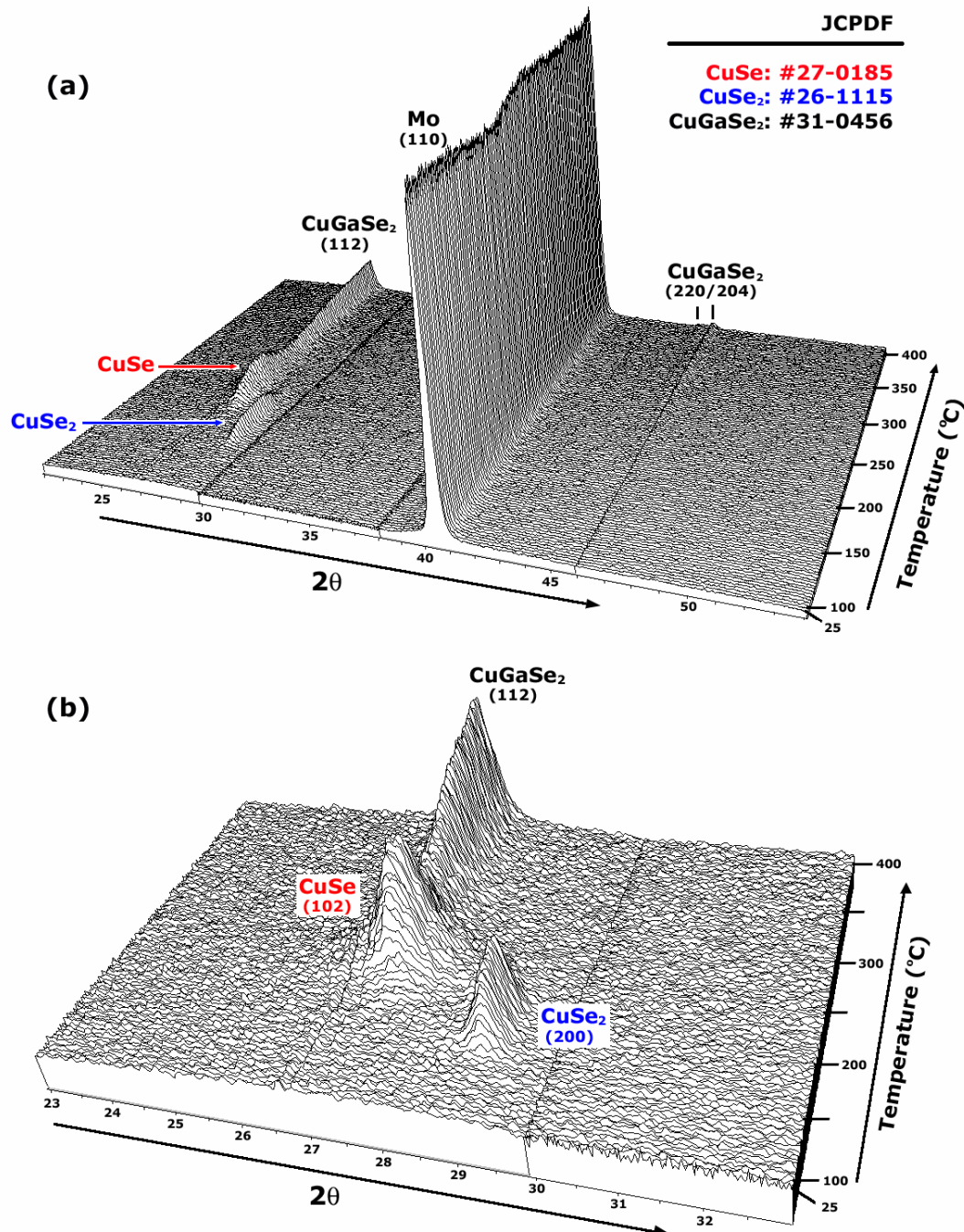


Figure 5-12. In situ XRD scans during temperature ramp annealing ($30\text{ }^{\circ}\text{C}/\text{min}$) of the glass/Mo/Cu-Ga-Se sample

5.3.3 Isothermal Annealing

Time-resolved, high temperature X-ray diffraction data were collected using a linear position sensitive detector (LPSD), while the glass/Mo/Cu-Ga-Se precursor films were maintained at a constant temperature in a He (flow rate ~100 sccm) atmosphere. In the isothermal experiment, the three-step temperature ramping protocol was used to minimize heating time without temperature overshooting, as previously mentioned at section 5.2.3. Once the temperature reached the set point value, it was held at the set-point temperature to monitor the evolution of the isothermal reaction. To complete the reaction, the temperature was elevated to 600 °C and maintained for about 12 min until only the CuGaSe₂ phase remained and the corresponding peak intensity remained constant. It is noted that, considering the formation temperature of CIS and CGS, the final elevation temperature of 500 °C instead of 600 °C was used for isothermal annealing experiments for CIS formation as described in chapter 4. The temperature range for the isothermal experiments was 300 to 400 °C and X-ray scan time was 30 sec.

Figure 5-13 displays the time-resolved XRD data collected for the glass/Mo/ Cu-Ga-Se film isothermally reacted at selected temperatures. The comparison between the isothermal plots at four different temperatures clearly illustrates that the reaction rate increases with temperature. To obtain the fractional reaction (α), which is defined as the fraction of reaction completed at time t , the peak heights of the product CuGaSe₂ (112) were obtained by peak fitting the diffraction data using JADE, and were normalized assuming that the reactants were completely transformed to crystalline CuGaSe₂ after each run, and that the texture of the CuGaSe₂ did not appreciably change through the entire heating process.

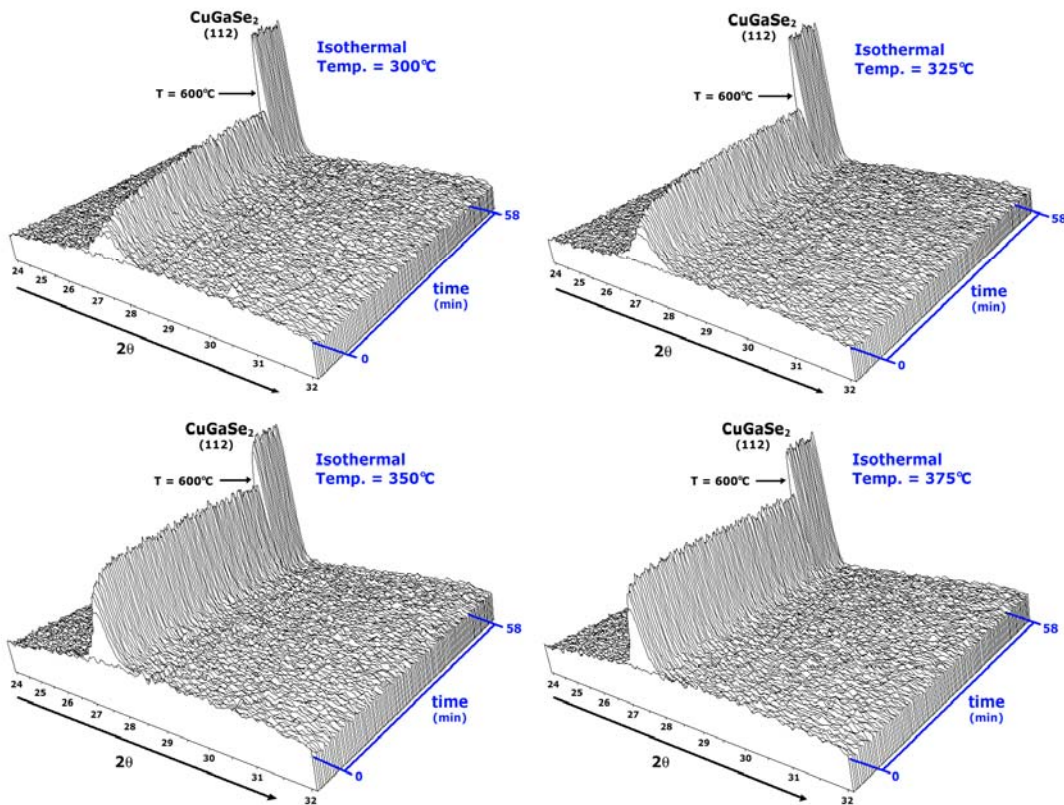


Figure 5-13. *In situ* time-resolved XRD scans during isothermal annealing of the glass/Mo/Cu-Ga-Se precursor structure at selected temperatures (i.e., 300, 325, 350 and 375 °C)

It should be pointed out that the peak height was used instead of the integrated peak intensity, because it was difficult to obtain a consistent profile of peak intensity by fitting the broad diffraction pattern, especially for the 300 and 325 °C anneals. According to the results of the previous X-ray experiments (Chapter 4 and 5) on isothermal annealing of various precursor structures, however, it is acceptable to use the peak height in place of the peak intensity within an allowable error range. Estimated fractional reaction values with respect to isothermal soaking time at different isothermal temperatures are shown in Figure 5-14.

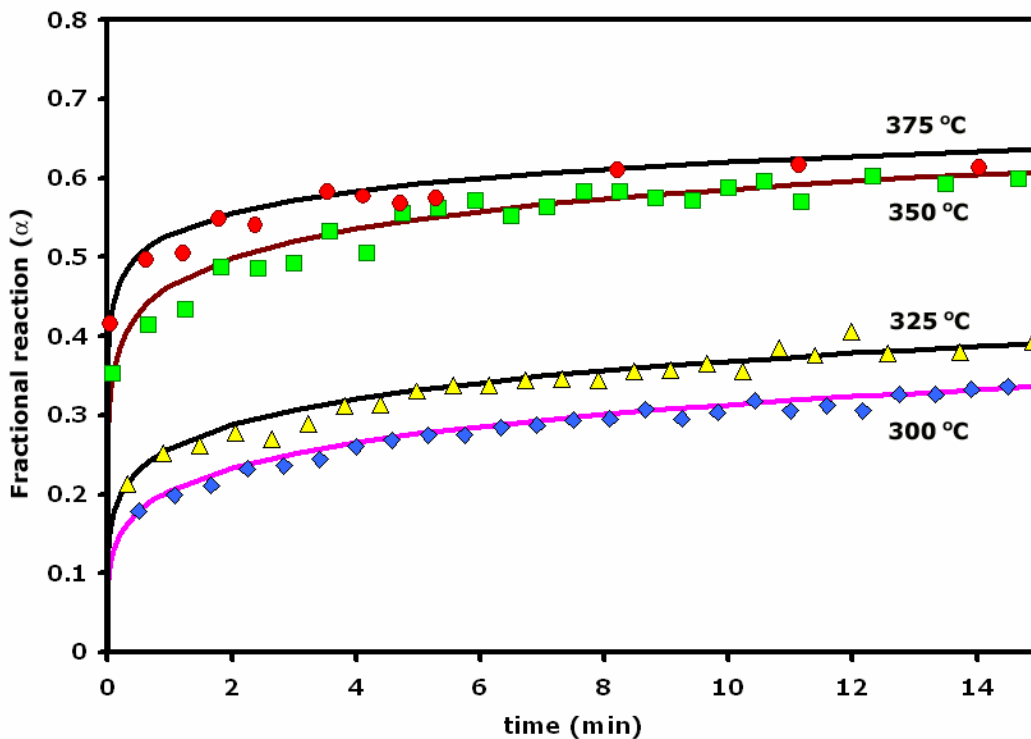


Figure 5-14. Comparison of fractional reaction for isothermal experiments and modified Avrami model prediction (Solid line: model predictions, symbol: experimental data).

The reaction kinetics in terms of activation energy (E_a), kinetic constant (k), and reaction order (n) are modeled using a modified Avrami model, which is suggested in chapter 5.2.3. According to the results of the isothermal experiments shown in Figure 5-15, part of CuGaSe_2 formation has already occurred before the sample reached the set-point temperature, i.e., $\alpha(t=0) \neq 0$. Considering this initial condition, a modified Avrami model is expressed by equation 5-3. By using the iteration procedure explained in chapter 5.2.3, Avrami exponent (n), kinetic constant (k), and time constant (t^*) are obtained, as summarized in Table 5-2.

It is seen for the results in the Table that the values of t^* are shorter for the larger isothermal soak temperature that represents more extent of pre-reaction. This is replaced by the experimental measure in absolute rate of reaction with temperature that causes

much more growth to cause and the equivalent amount of growth at time, t^* , at the higher soak temperature, will react at a higher rate.

Table 5-2. Estimated kinetic parameters for the CuGaSe₂ formation from glass/Mo/Cu-Ga-Se precursor films (k: apparent kinetic constants, n: Avrami exponents and t^* : time constant for modified Avrami model)

Temperature [°C]	Modified Avrami model		
	n	$k \times 10^3$ [s ⁻¹]	t^* [s]
300	0.22 ($\pm 5.0 \times 10^{-3}$)	0.0181 ($\pm 7.23 \times 10^{-5}$)	30.0
325	0.19 ($\pm 6.6 \times 10^{-3}$)	0.0265 ($\pm 2.40 \times 10^{-4}$)	18.8
350	0.15 ($\pm 9.6 \times 10^{-3}$)	0.722 ($\pm 1.79 \times 10^{-2}$)	5.5
375	0.11 ($\pm 1.8 \times 10^{-2}$)	1.25 ($\pm 1.76 \times 10^{-1}$)	2.8

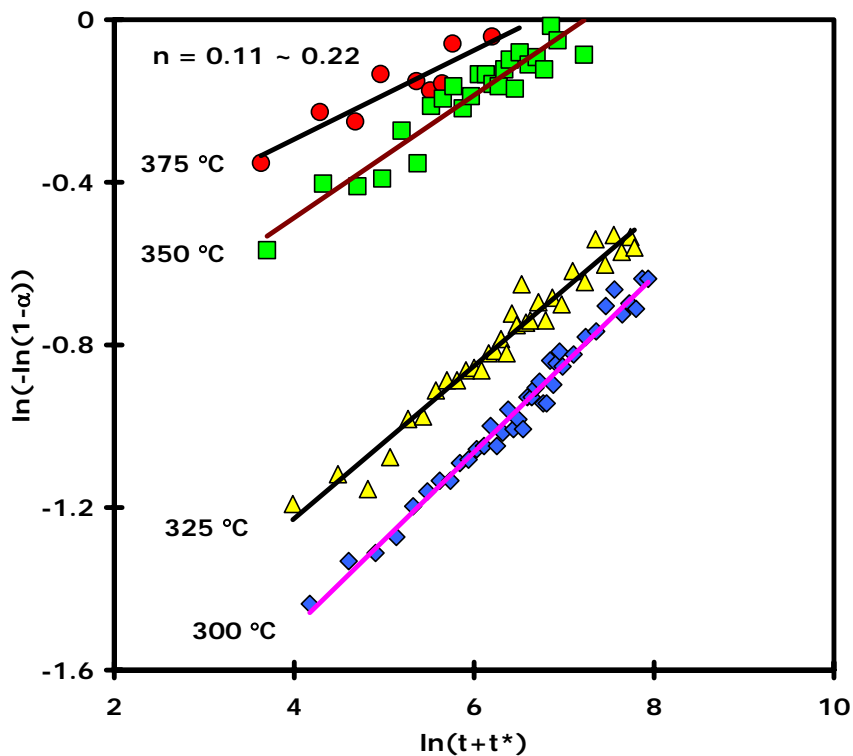


Figure 5-15. Modified Avrami model plot for glass/Mo/Cu-Ga-Se precursor structure

As shown in Figure 5-14, the fractional reactions with respect to isothermal soaking time predicted by modified Avrami model in a very good agreement with experimentally

determined values. From the Arrhenius plot for kinetic constants, as inserted in Figure 5-16, the apparent activation energy was estimated as 197 ± 50 kJ/mol.

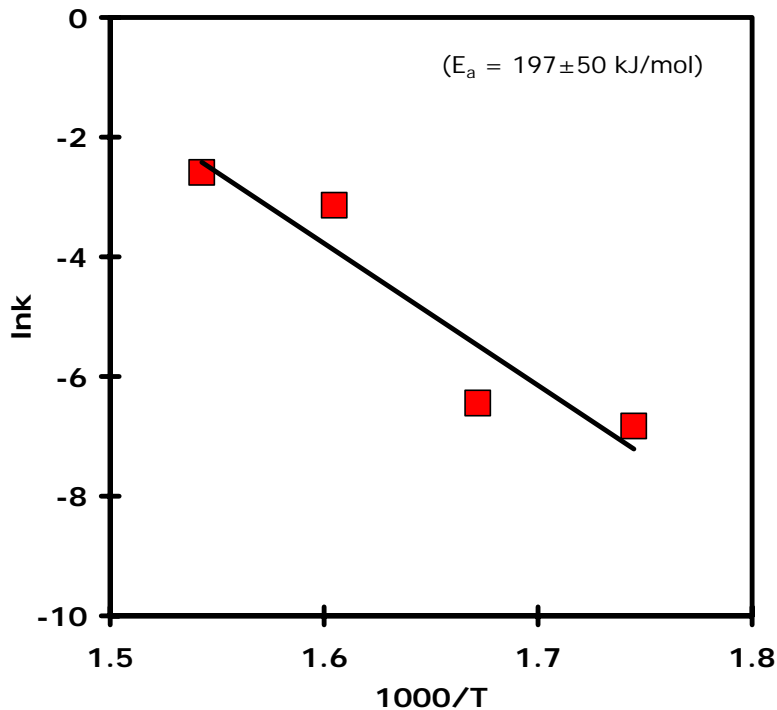


Figure 5-16. Arrhenius plot of the Avrami model rate constant for glass/Mo/Cu-Ga-Se precursor structure

It is noticeable that the time constant (t^*) decreases with temperature, which was also observed in isothermal annealing of glass/GaSe/CuSe precursor. Interestingly, the estimated values of Avrami exponents lie in the range 0.11 to 0.22, which is quite out of validity range of conventional Avrami model. Theoretically, the range of Avrami exponents should be 0.5~1.5 for one-dimensional, 1.5~2.5 for two-dimensional and 2.5~3.5 for three-dimensional diffusion controlled reaction. Although the experimental data are well fitted mathematically by a modified Avrami model, the isothermal reaction of CGS formation from glass/Mo/Cu-Ga-Se thus may not be described meaningfully by the Avrami growth model. Therefore, it is concluded that the CGS formation from intimately mixed Cu-Ga-Se precursor does not follow the diffusion controlled reaction

pattern, which is not surprising because there is no substantial diffusion barrier between intimately mixed reacting elements.

5.4 Selenization of Glass/Mo/Cu-Ga Precursor

5.4.1 Precursor Preparation

The glass/Mo/Cu-Ga precursor was prepared in a migration enhanced molecular beam epitaxial (MEE) reactor under ultra high vacuum conditions (10^{-7} to 10^{-8} Torr). Since molybdenum is a widely used back-contact material in CIGS-based solar cells, the elemental Cu and Ga were deposited on the Mo-coated, sodium-free thin glass (Corning 7059: alkali level < 0.3%, 0.4 mm thickness) without heating the substrate to minimize the unintended reaction between Cu and Ga. The overall atomic composition of the Cu-Ga film as-deposited on the Mo/glass substrate was measured as $[\text{Cu}]/[\text{Ga}] = 1.01$ by inductively coupled plasma optical emission spectroscopy (ICP-OES). The result is that the atomic ratio of the film, $[\text{Cu}]/[\text{Ga}] = 1.01$. The crystalline phases present in the as-grown precursor (mainly CuGa_2) and selenized film (mainly CuGaSe_2 and MoSe_2) were identified by room-temperature XRD (RT-XRD), as shown in Figure 5-17. The thicknesses of the Mo (~0.4 μm), Cu-Ga (~0.7 μm), and selenized CuGaSe_2 (~1.2 μm) films were measured by SEM images of cleaved samples, which are not shown here.

5.4.2 Selenization Chamber Design

The phase evolution and reaction kinetics during selenization of glass/Mo/Cu-Ga precursors were investigated using time-resolved, *in situ* high-temperature X-ray diffraction (HT-XRD), which consists of the PANalytical X’Pert Pro MPD/X-ray diffractometer equipped with an Anton Paar XRK-900 furnace and an X’Celerator solid state detector.

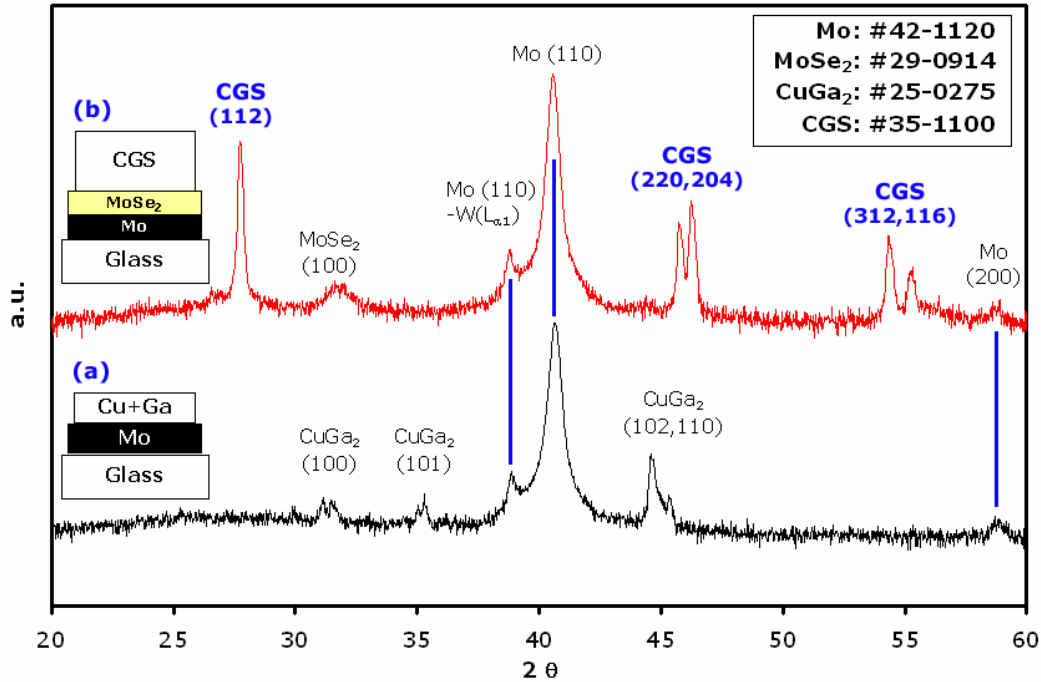


Figure 5-17. Room-temperature XRD scans of Cu-Ga as-grown precursor and selenized CuGaSe₂ film.

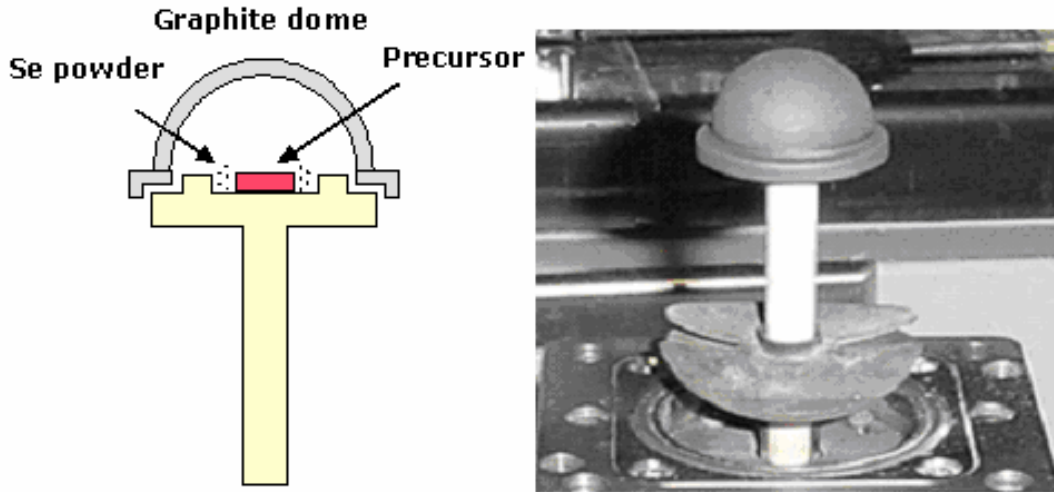


Figure 5-18. X-ray sample holder with a graphite dome for selenization of Cu-Ga precursor films.

Selenium powder was placed in wells on the HT-XRD sample holder adjacent to the precursor film. As shown in Figure 5-18, the HT-XRD sample holder containing the

precursor film and selenium powder was covered with an X-ray transparent graphite dome, which is customized to minimize Se vapor loss.

5.4.3 Temperature Ramp Selenization

The selenization reaction was thermally promoted via temperature-ramp annealing at a rate of around 20 °C/min under *in situ* XRD observation to identify the possible intermediate phases and the temperature range for formation of the CuGaSe₂. As shown in Figure 5-19, the results reveal that CuSe forms in the temperature range of approximately 260 to 370 °C, and that the onset of formation of CuGaSe₂ occurs at approximately 300 °C. A strong carbon (002) peak from the graphite dome was consistently observed at around a 2θ value of 27°. Fortunately, this peak did not overlap with any peaks of the anticipated phases. It is also noted that the peak intensities are attenuated over the entire 2θ range in the temperature range 370 and 600 °C, which is attributed to the scattering of the incoming X-ray by Se vapor within the chamber. Thus the almost full recovery of peak intensities at 600 °C demonstrates the complete consumption of Se powder at this temperature.

The formation of MoSe₂ identified in the RT-XRD scan for the selenized film, as shown in Figure 5-17(b), was not detected under *in situ* HT-XRD observation during temperature-ramp annealing, which is attributed to the relatively low resolution at the higher scan rate of HT-XRD (~8°/min) than that of RT-XRD (~1°/min). There are several reports on MoSe₂ formation at the interface of CIGS and Mo layers and its positive contribution to the efficiency of CIGS solar cells [Wad01, Sha96, Abo05].

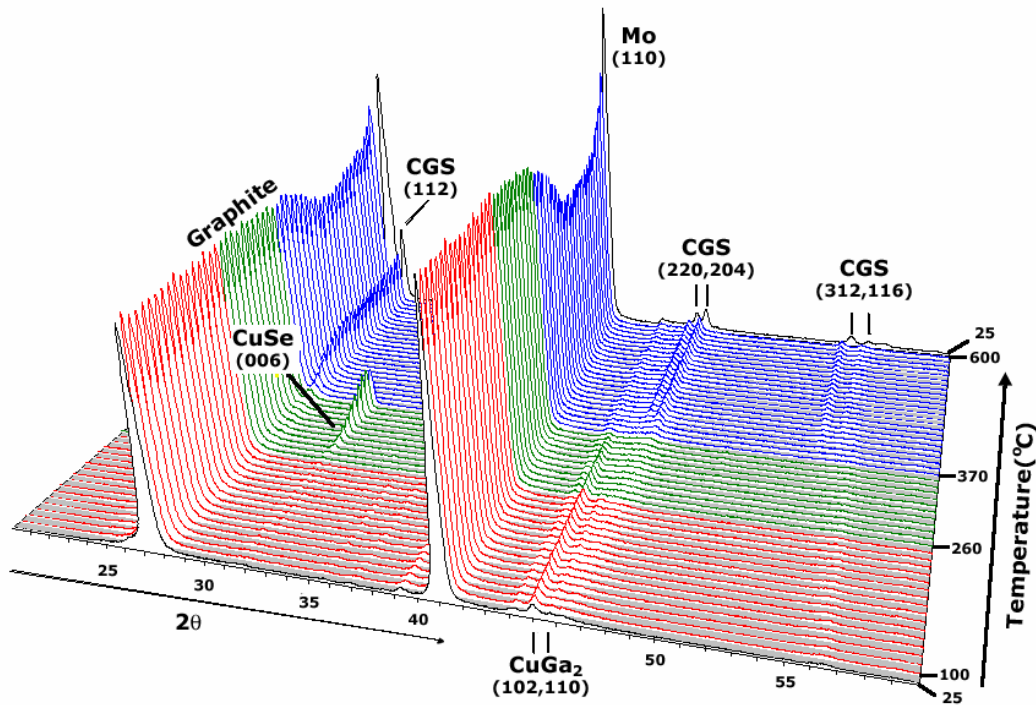


Figure 5-19. In situ XRD scans during temperature ramp selenization of Cu-Ga/Mo/glass precursor.

Wada *et al.* reported that the (100) and (110) reflections of MoSe₂ in Mo/CIGS absorbers deposited by a typical three-stage process were detected by XRD. They suggested that the Mo/CIGS hetero-contact with the MoSe₂ layer makes a favorable ohmic contact, while Mo/CIGS without a MoSe₂ layer exhibits a Schottky-type contact [Wad01]. In Chapter 3, it was shown that selenization of Cu-In/Mo/glass precursor [Kim06a] produced MoSe₂, but was only detected after complete formation of α -CuInSe₂. MoSe₂ detection was also accompanied by a rapid decrease of the Mo (110) reflection intensity, which was clearly detected at a temperature above 440 °C. The greater thermodynamic stability of CIS over MoSe₂ is consistent with this observation. Since MoSe₂ was not detected during thermal anneal because of the low sensitivity of the detection in this specific set of experiments, it is not clear if MoSe₂ only forms after complete CGS formation.

5.4.4 Isothermal Selenization

Isothermal annealing at selected temperatures between 330 and 400 °C was then performed for estimating kinetic parameters using an appropriate reaction model. The 2θ scan range (22 to 30°) for the isothermal experiments was selected since the major reflection for the product CuGaSe₂ (112) lies within this range. To complete the reaction, the temperature was elevated to 550 °C after each run and then maintained at this temperature for about 12 min or until only the CuGaSe₂ phase remained as evidenced by constant peak intensity. Figure 5-20 displays the time-resolved XRD data collected for the film isothermally annealed at different temperatures. The comparison between the isothermal plots at four different temperatures clearly illustrates that the reaction rate increases with temperature.

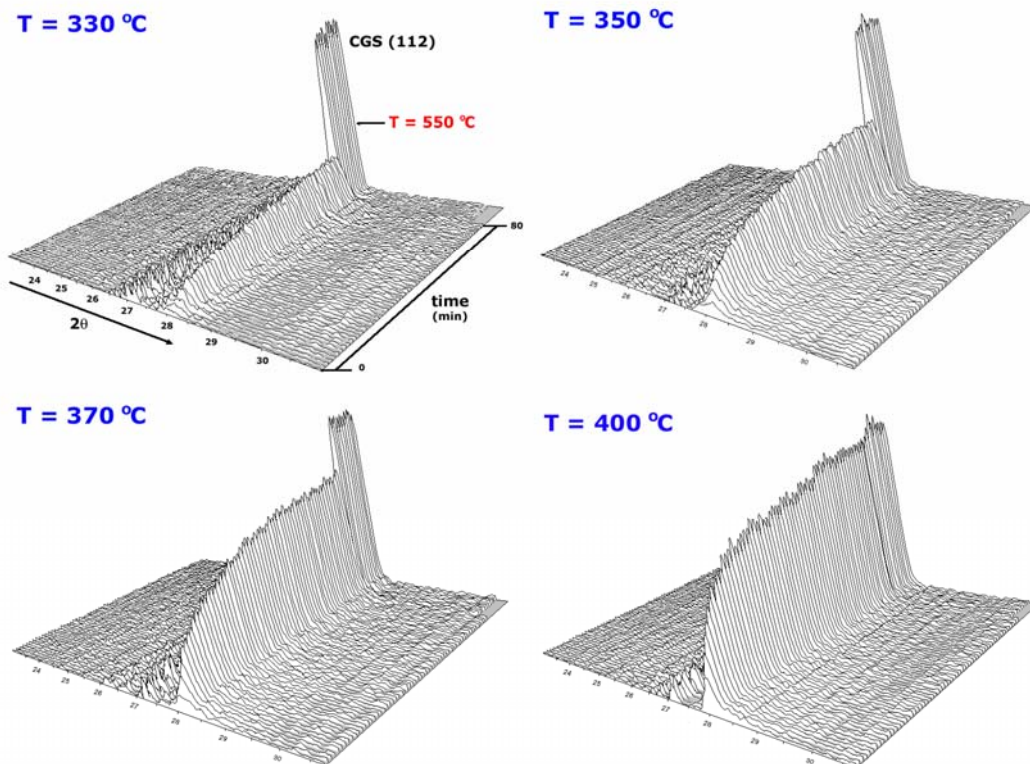


Figure 5-20. In situ XRD scans during isothermal selenization of Cu-Ga/Mo/glass precursor at four different temperatures.

To obtain the fractional reaction (α), which is defined as the fraction of reaction completed at time t , the integrated intensities of the product CuGaSe₂ (112) peaks were obtained by fitting the diffraction data. The integrated intensities were then normalized assuming that the Cu-Ga precursors were completely selenized to crystalline CuGaSe₂ after the high temperature anneal at the end of the run, and that the texture of the CuGaSe₂ did not appreciably change through the entire heating process. According to the results of the isothermal experiments shown in Figure 5-20, nucleation and partial growth of the CuGaSe₂ phase occurred during the heating period before the sample temperature reached the set-point value, *i.e.*, $\alpha(t=0) \neq 0$. The reaction kinetics in terms of an activation energy and reaction order was investigated using the modified Avrami model which is suggested in the previous chapter 5.2. Detailed procedure to find kinetic parameters using the modified Avrami model was described in the previous chapter 5.2.3. For these experimental data, the estimated Avrami exponents (n), kinetic constants (k), and time constants (t^*), are summarized in Table 5-3.

Table 5-3. Estimated kinetic parameters for the CuGaSe₂ formation from selenization of glass/Mo/Cu-Ga precursor films. (k : apparent kinetic constants, n : Avrami exponent and t^* : time constant of the modified Avrami model)

Temperature [°C]	Modified Avrami Model Parameters		
	n	$k \times 10^3$ [s ⁻¹]	t^* [s]
330	0.57 ($\pm 1.5 \times 10^{-2}$)	0.302 ($\pm 1.63 \times 10^{-3}$)	0 [#]
350	0.55 ($\pm 1.1 \times 10^{-2}$)	0.703 ($\pm 2.27 \times 10^{-3}$)	38.6
370	0.61 ($\pm 1.7 \times 10^{-2}$)	1.38 ($\pm 7.71 \times 10^{-3}$)	62.0
400	0.61 ($\pm 2.8 \times 10^{-2}$)	2.92 ($\pm 4.26 \times 10^{-2}$)	54.3

#: Experimentally determined since no pre-reaction was observed for this run.

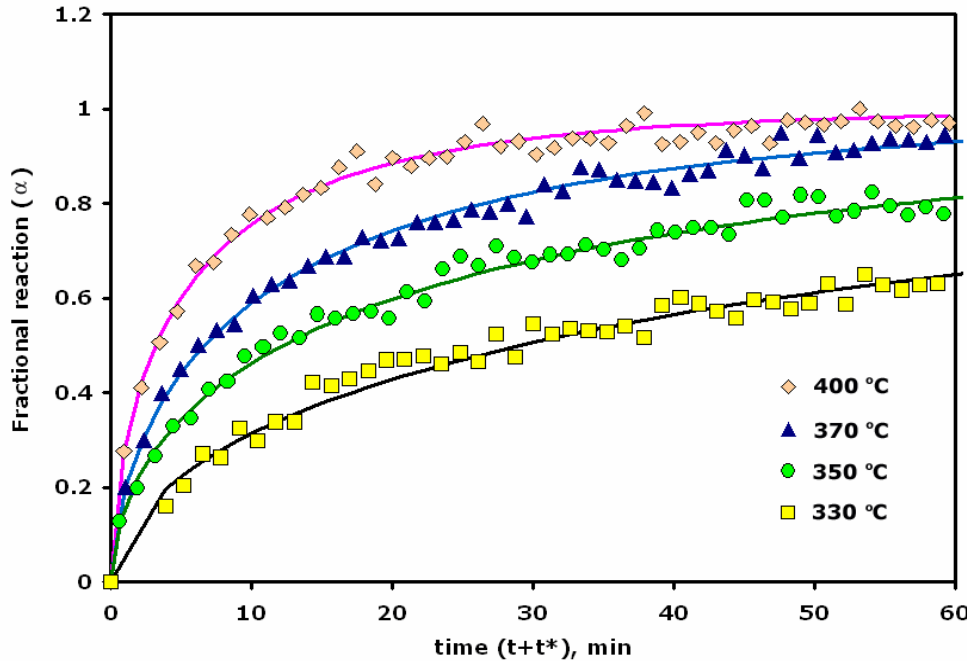


Figure 5-21. Comparison of fractional reaction for isothermal experiments and modified Avrami model prediction (Solid line: model predictions, symbol: experimental data)

As shown in Figure 5-21, the comparison between the fractional reaction by experiments and the prediction by a modified Avrami model demonstrates that a modified Avrami model fits the experimental data set very well. The n values over the entire temperature range (330 to 400 °C) lie in the relatively narrow range 0.55 and 0.61. These values are close to the lower limiting value of 0.5 thus suggesting rapid nucleation. The low value of the estimated Avrami exponents suggests that the nucleation of CuGaSe₂ occurs so rapidly (e.g., during the ramping time) that the nucleation time is nearly negligible. The Arrhenius equation was used to estimate the apparent activation energy, E_a , for CuGaSe₂ formation by selenization of glass/Mo/Cu-Ga precursor films. An activation energy of 109 (± 7) kJ/mol was estimated from the Arrhenius plot shown in Figure 5-23.

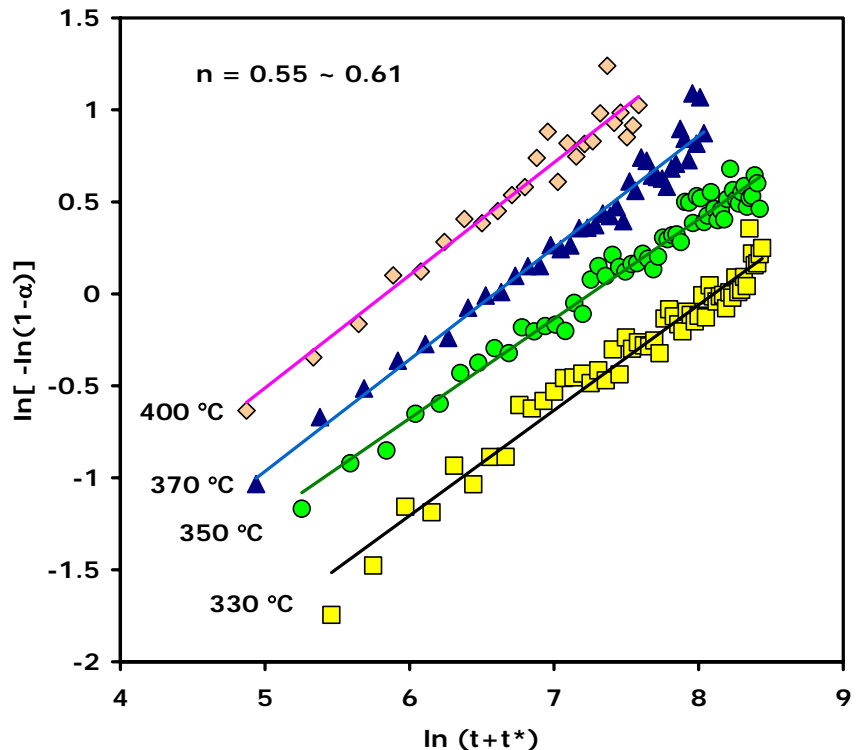


Figure 5-22. Modified Avrami model for the CuGaSe_2 formation by selenization of glass/Mo/Cu-Ga precursor

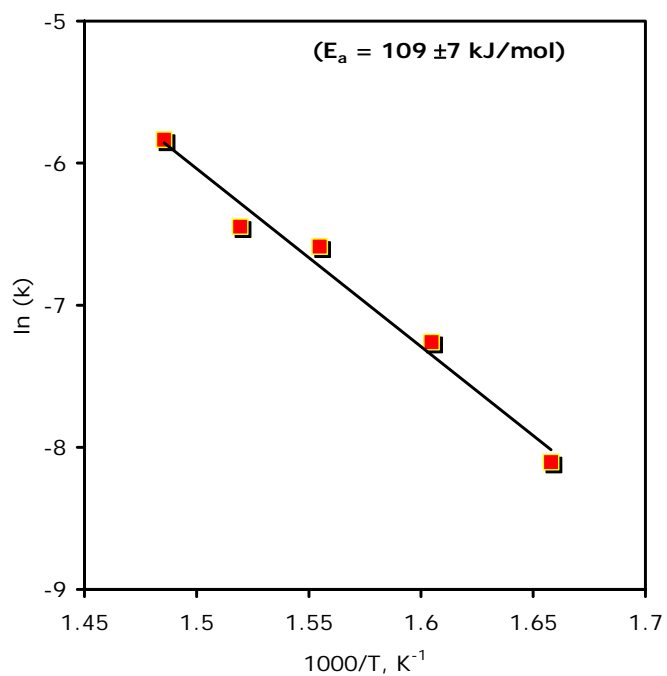


Figure 5-23. Arrhenius plot of the Avrami model rate constant for the CuGaSe_2 formation by selenization of glass/Mo/Cu-Ga precursor

The value of 109 (± 7) kJ/mol is similar to the activation energy of 124 (± 19) kJ/mol estimated for selenization of glass/Mo/Cu-In precursor using the Avrami model and Arrhenius plot [Kim06a]. Also, this value is reasonably close to the activation energies of 124 (± 19) kJ/mol estimated for CGS formation from bilayer glass/GaSe/CuSe in chapter 5.2 and 129 kJ/mol estimated for CGS formation from the stacked bilayer $\text{Ga}_2\text{Se}_3/\text{Cu}_2\text{Se}$ by Purwins *et al.* [Pur06]. It is interesting to compare the results for formation of CGS to those for CuInSe_2 . Similar experiments using a Cu-In precursor showed a different reaction sequence (CuSe formation followed by CuSe_2 and then CuInSe_2). Analysis of the rate data by both the Avrami and parabolic rate models provided estimated activation energies of 124 (± 19) and 100 (± 14) kJ/mol, respectively, which are similar to the values determined here for CGS, suggesting the CuSe diffusion-controlled formation step may be rate limiting.

It is also noted that from comparison of the standard errors of activation energies for CuGaSe_2 and CuInSe_2 formation by selenization of metallic precursors, it is concluded that the graphite dome used for selenization of Cu-Ga provides more reliable experimental results than the aluminum foil cover used for selenization of Cu-In. The experimental reliability of a graphite dome could be attributed to its superior X-ray transparency and operability to an aluminum foil. The X-ray transparency of the graphite dome is clearly evidenced by the negligible loss in reflection intensity, while employing an aluminum foil cover sacrifices the reflection intensity and thus the accuracy of experiments. Based on the results of the Avrami model analysis, the formation of CuGaSe_2 from selenization of glass/Mo/Cu-Ga precursor films apparently

follows a one-dimensional diffusion controlled reaction with a nucleation and subsequent growth sequence.

5.5 Summary

Time-resolved, *in situ* high-temperature X-ray diffraction was successfully applied to investigate the reaction pathway and kinetics of polycrystalline CuGaSe₂ formation from thermal annealing of glass/GaSe/CuSe bilayer and glass/Mo/Cu-Ga-Se elementally mixed precursor, and selenization of glass/Mo/Cu-Ga metallic precursors.

The qualitative reaction pathway observation during the temperature ramp annealing of glass/GaSe/CuSe bilayer precursor demonstrated that the initial CuSe phase begins to be transformed to β -Cu_{2-x}Se at approximately 230 °C, followed by CuGaSe₂ formation initiated at around 260 °C, which may be described as the reaction Cu_{2-x}Se + 2GaSe + Se → 2CuGaSe₂. Quantitative kinetic analysis of X-ray diffraction data obtained during isothermal annealing fits both the parabolic rate and Avrami growth models, which suggests that CuGaSe₂ formation in a bilayer glass/GaSe/CuSe precursor follows a one-dimensional diffusion controlled reaction pattern. The activation energy of this reaction, 115 (± 16) kJ/mol (parabolic rate model) or 124 (± 19) kJ/mol (Avrami model), is much higher than that found for α -CIS obtained by the same type of experiments, i.e., glass/InSe/CuSe [Kim05a]. The TEM-EDS analysis on 300 °C – annealed sample demonstrates that CuGaSe₂ forms at the interface between GaSe and CuSe layers, which explicitly supports the primary assumption of parabolic growth model.

The results of temperature ramp annealing of glass/Mo/Cu-Ga-Se precursor revealed that the CuSe₂ forms at around 160 °C followed by its transformation to CuSe at

around 200 °C, and CuGaSe₂ formation then is initiated with the decrease of CuSe peak at around 280 °C. The kinetic analysis using a modified Avrami model for isothermal soaking experiments suggest that this reaction should not follow the diffusion controlled reaction pattern since there is no substantial diffusion barrier between intimately mixed reactants.

The reaction pathways and chemical kinetics of CuGaSe₂ formation from glass/Mo/Cu-Ga precursor structures were investigated using time-resolved *in situ* high-temperature X-ray diffraction equipped with a graphite dome. The results show that the selenization process of Cu-Ga films produces a CuSe phase at temperatures ranging from 260 to 370 °C, and that CuGaSe₂ phase first starts to appear at approximately 300 °C. The kinetic analysis on the selenization of Cu-Ga films shows that a modified Avrami model for chemical reaction fits the experimental data set well, yielding an activation energy of $E_a = 109 (\pm 7)$ kJ/mol. This value of activation energy is very close to that estimated for the CuGaSe₂ formation from glass/GaSe/CuSe bilayer (i.e., 124 ± 19 kJ/mol estimated with the modified Avrami model) and from selenization of Cu-In/Mo/glass precursor (i.e., 124 ± 19 kJ/mol estimated with the Avrami model). It is concluded that the Cu-Ga selenization also follows a pathway along a one-dimensional diffusion-controlled reaction that takes place in concert with a nucleation and growth mechanism.

As summary, the reaction rates of CIS and CGS formation are compared using kinetic constants for different precursor structures displayed in Figures 5-24 and 5-25. The kinetic analysis using both parabolic and Avrami models suggests that the CGS formation from GaSe/CuSe precursor or from selenization of Cu-Ga precursor is much slower than that CIS formation from similar precursor structures. Furthermore, the CGS

formation using a GaSe/CuSe precursor is even faster than using the selenization of Cu-Ga precursor. In the near future, the CGS fabrication using the rapid thermal processing of a GaSe/CuSe precursor structure will be performed in our research group.

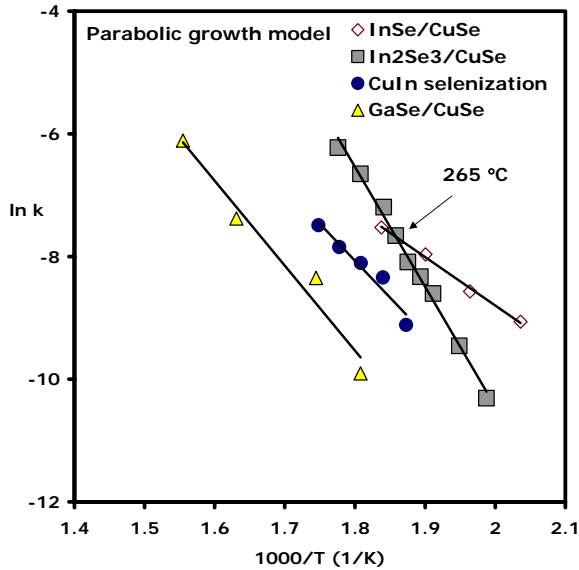


Figure 5-24. Comparison of reaction rates for CIS and CGS formation from different precursors estimated by the parabolic model.

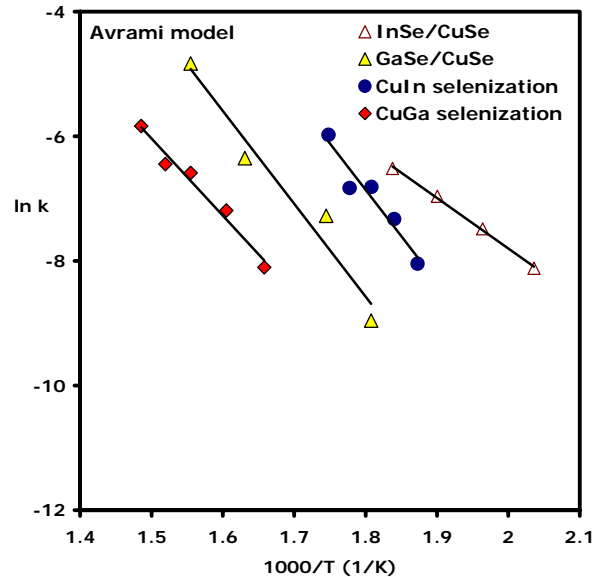


Figure 5-25. Comparison of reaction rates for CIS and CGS formation from different precursors estimated by the Avrami model

CHAPTER 6

CU(IN,GA)SE₂ FORMATION FROM SELENIZATION OF METALLIC CU-GA-IN

6.1 Introduction

Recent advances in the development of high efficiency (19.5 % AM1.5G [Con05]) polycrystalline thin film Cu(In_xGa_{1-x})Se₂ (CIGS) solar cells are extremely promising. In addition to its high cell efficiency, CIGS thin-film solar cells exhibit outstanding long-term outdoor stability, excellent radiation hardness, and the potential for use in a CIGS/CGS tandem arrangement. The route used to synthesize the CIGS absorber material is critical to achieving high cell efficiency as well as high processing throughput. Interestingly, a variety of processing sequences lead to the formation of CIGS, for instance, co-deposition of elements, rapid thermal processing of stacked elemental layer, and selenization of metallic precursor. This flexibility is partly due to an inherent stability of α -CIGS and a rich phase diagram (α -CuInSe₂ is in equilibrium with 8 different solid phases and a Se-rich liquid) [Göd00a-c]. The complex chemistry of the 4-component CIGS system, however, has forced absorber synthesis optimization to primarily traverse an empirical path and discouraged exploration of substantially different approaches. In particular, very little is known about the fundamental thermochemistry and reaction pathways in the system. In chapters 4 and 5, the reaction pathways and kinetics of α -CIS formation from different precursors (e.g., InSe/CuSe [Kim05a], In₂Se₃/CuSe [Kim05b], Cu-In-Se) and selenization of metallic Cu-In precursor [Kim06a], and CGS formation from thermal annealing of GaSe/CuSe and selenization of Cu-Ga

precursor [Kim06b] were investigated. In this chapter, the reaction kinetics for CIGS formation by the selenization of co-deposited metallic Cu-Ga-In precursors is reported.

6.2 Experimental

The glass/Mo/Cu-Ga-In precursors were grown using Migration Enhanced Epitaxy (MEE) deposition system under ultra high vacuum conditions ($10^{-7} \sim 10^{-8}$ Torr). Since molybdenum is widely used as a back-contact material in CIGS-based solar cells, elemental Cu, Ga, and In were co-deposited on the Mo-coated, sodium-free thin glass (Corning 7059: alkali level < 0.3%, 0.4 mm thickness) without heating the substrate to minimize the reaction between elements. The overall atomic composition of the as-deposited precursor film is determined by inductively coupled plasma optical emission spectroscopy (ICP-OES). Further description of MEE reactor and deposition technique was given in chapter 1.5.

The phase evolution and reaction kinetics during selenization of glass/Mo/Cu-Ga-In precursors were investigated using time-resolved, *in situ* high-temperature X-ray diffraction (HT-XRD), which consists of a PANalytical X’Pert Pro MPD/X-ray diffractometer equipped with an Anton Paar XRK-900 furnace and an X’Celerator solid state detector. Selenium powder was placed in wells on the HT-XRD sample holder adjacent to the precursor film. The HT-XRD sample holder containing the precursor film and selenium pellet was then covered with an X-ray transparent graphite dome to minimize Se vapor loss, as used for the selenization of glass/Mo/Cu-Ga precursor described in chapter 5.

6.3 Results and Discussion

6.3.1 Precursor Characterization

The overall composition of as-deposited glass/Mo/Cu-Ga-In precursor film was close to that known to produce high efficiency CIGS cells, *i.e.*, Cu-rich ($\text{Cu}/\text{Ga}+\text{In} \sim 1.3$) and $\text{Ga}/\text{Ga}+\text{In} \sim 0.3$. The room-temperature XRD pattern shown in Figure 6-1 suggests that $\text{Cu}_{11}\text{In}_9$, CuIn, and pure In formed during deposition of the precursor layer.

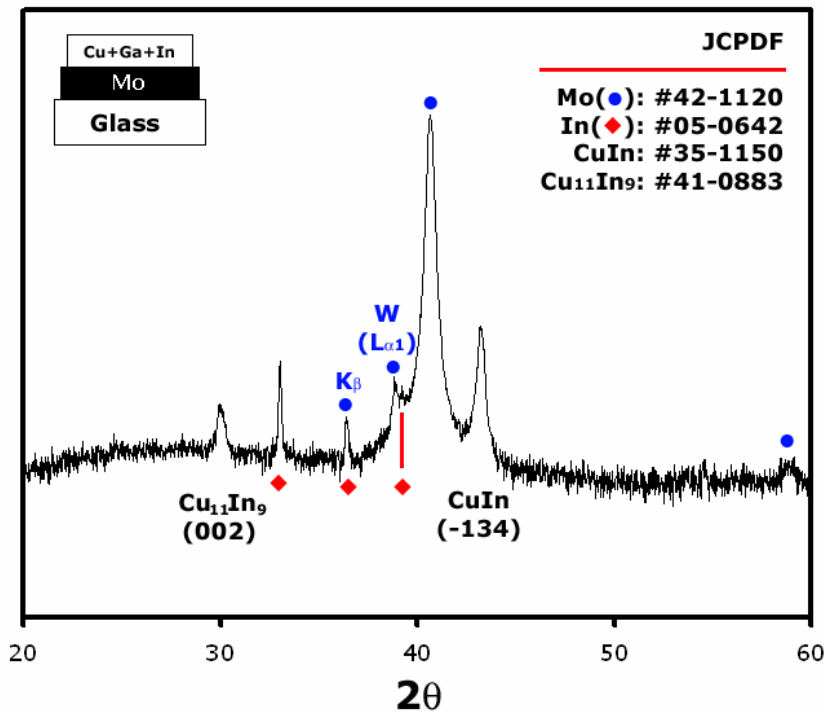


Figure 6-1. Room-temperature XRD scans of glass/Mo/Cu-Ga-In as-grown precursor

In the Cu-In binary phase diagram (Figure 2-16) suggested by Liu [Liu02], however, the compound CuIn is not considered to be stable while the compound $\text{Cu}_{11}\text{In}_9$ is well known to be stable. There are many reports concerning the observation of the apparently meta-stable CuIn phase during Cu-In or Cu-Ga-In film preparation [Che96, Mat97, Pis03, Son03]. In particular, Song *et al.* [Son03] reported that the CuIn phase was identified along with $\text{Cu}_{11}\text{In}_9$ in the multilayer Cu-Ga-In precursor film deposited on

glass by DC magnetron sputtering. It is also noted that no phase containing Ga was detected, which suggests Ga present in an amorphous state perhaps as a glass or slightly super-cooled liquid (Ga melting temperature is 29.78 °C). The thicknesses of Mo (~0.4 μm), Cu-Ga-In film (~0.6 μm), and selenized CIGS film (~1.1 μm) were measured by SEM images of cleaved samples, as shown in Figure 6-2.

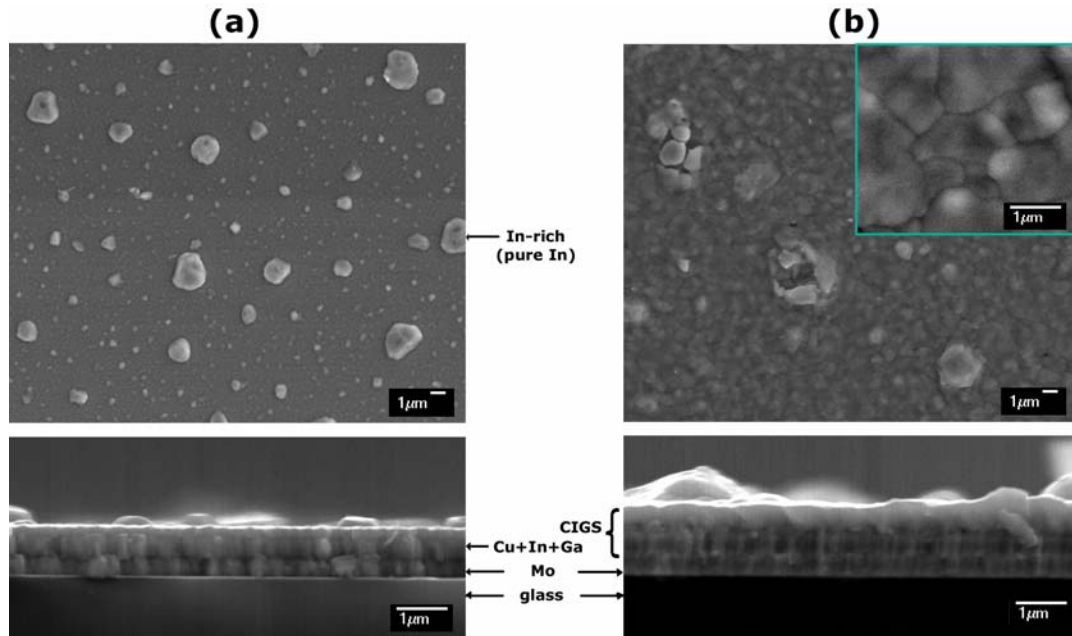


Figure 6-2. Surface (top) and cross-sectional (bottom) SEM images of (a) an as-deposited glass/Mo/Cu-Ga-In precursor film and (b) selenized film.

The matrix-island structure on the surface of the as-grown precursor is apparent in the SEM surface images of Figure 6-2(a). The islands were identified as an indium-rich or nearly pure indium phase by SEM-EDS (energy dispersive x-ray spectrometer). It is interesting that the same matrix-island structure containing In-rich islands was observed on the surface of the glass/Mo/Cu-In precursor films as shown in Chapter 4.5.

6.3.2 Temperature Ramp Annealing

As a preliminary experiment, a background scan was taken using a bare glass substrate covered by the graphite dome under a flowing He. The temperature ramp rate

and X-ray scan conditions matched those used in the runs with the Mo and metal precursors in place during selenization. As shown in Figure 6-3, a strong carbon (002) peak from the graphite dome was detected at $2\theta \sim 27^\circ$, which is very close to the position of the preferred CIGS (112) peak ($2\theta = 26.9^\circ$). Thus the height of sample inside the XRD chamber was intentionally shifted away from the normal to cause the sample reflection peaks to shift sufficiently to separate the CIGS (112) peak from the carbon (002) peak with only a slight decrease in the sample reflection intensities.

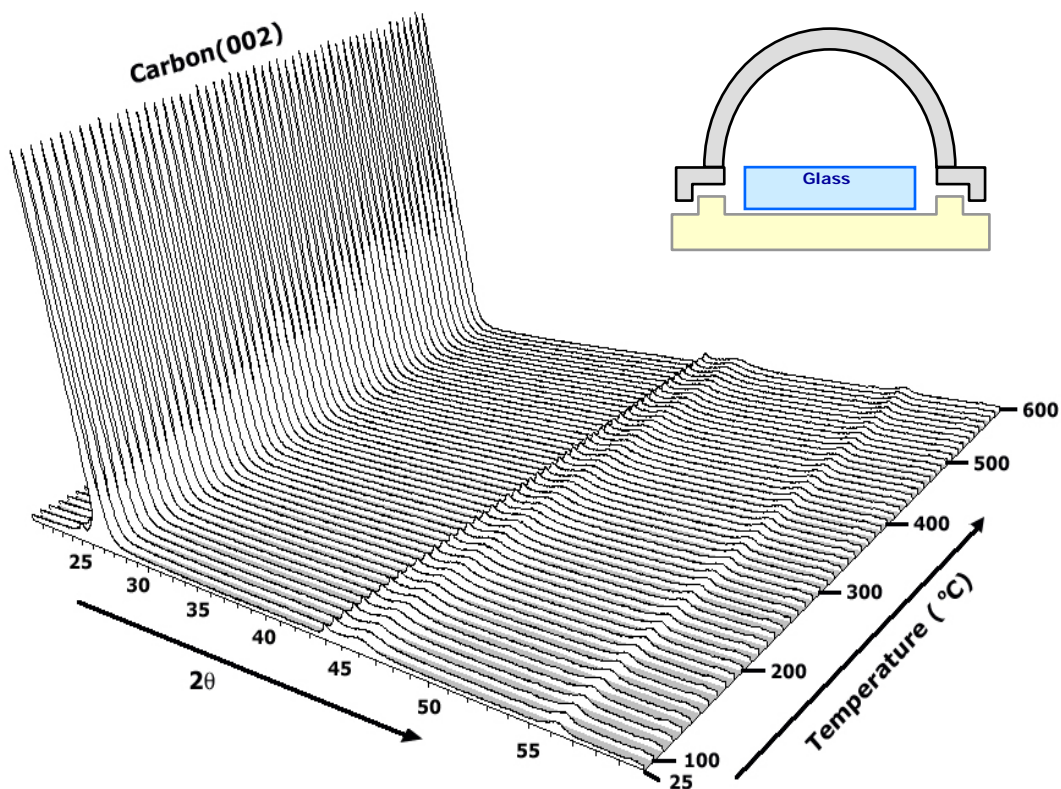


Figure 6-3. Temperature ramp HT-XRD scans with a bare glass substrate.

The selenization reactions were followed during temperature-ramp annealing under *in situ* XRD observation to identify the temperature range for formation of CIGS, as well as any intermediate and by-product phases. The precursor was first scanned at 25 °C and then heated to 100 °C at a rate of 20 °C/min. The X-ray diffraction data were collected at

every 10 °C interval during subsequent ramp heating to 600 °C. A 2θ scan in the range 20 to 60° could be taken in 5 min. Finally, the selenized sample was scanned again at room temperature.

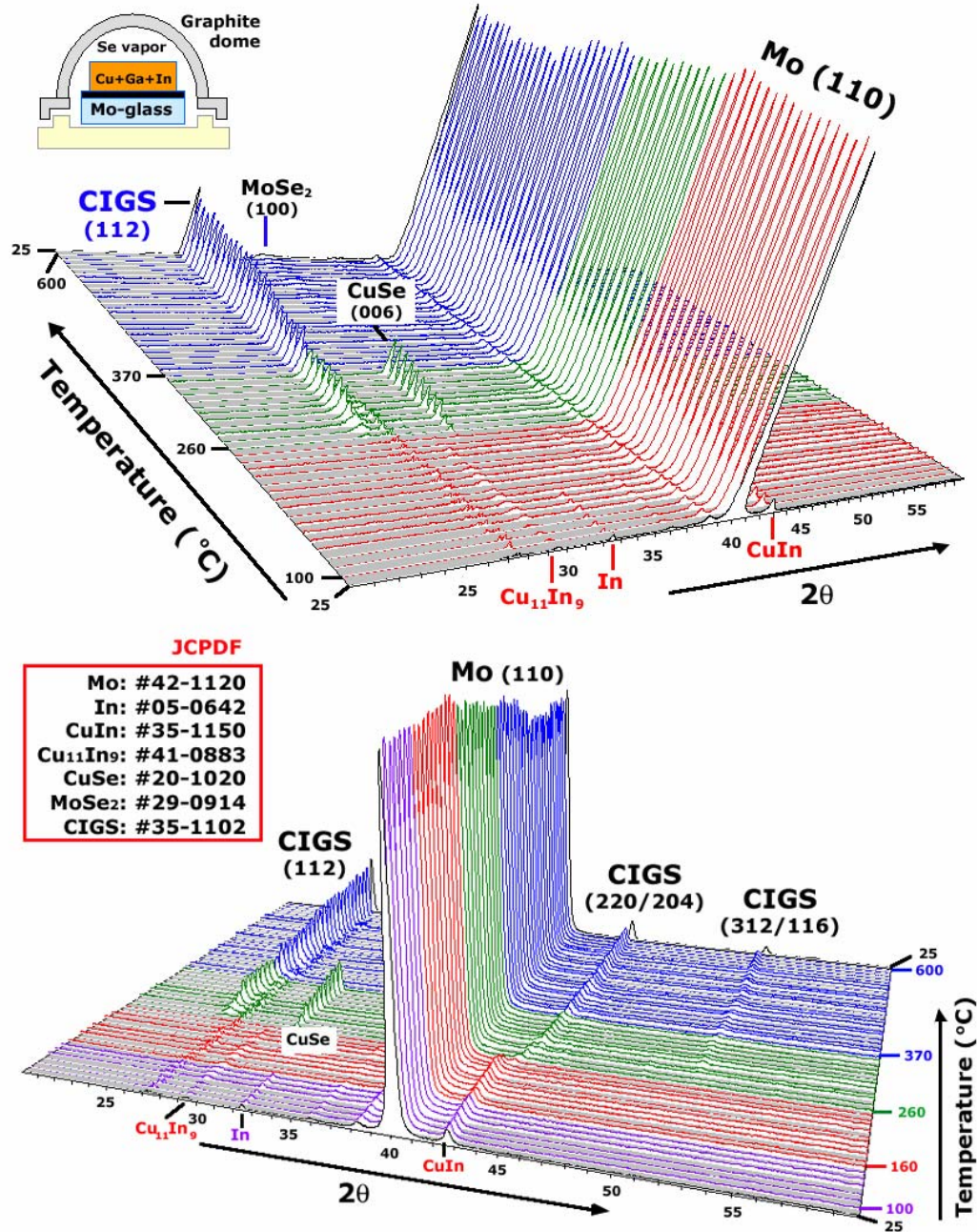


Figure 6-4. In situ XRD scans during temperature ramp selenization of Cu-Ga-In/Mo/glass precursor.

The background scan data shown in Figure 6-3 were carefully subtracted from the original scans using the JADE software to make the resultant sample peaks more visible, as shown in Figure 6-4.

The results revealed that the In (110) peak disappears above its melting temperature (~151 °C), followed by the melting of Cu₁₁In₉ at around 250 °C, which is slightly lower than the Cu₁₁In₉ equilibrium melting temperature of ~307 °C [Liu02]. The disappearance of the CuIn ($\bar{1}34$) peak along with the subsequent appearance of CIGS (220/204) peak is consistent with the formation of CIGS by reaction of Cu-In with amorphous Ga containing material (e.g., Cu-Ga solid solutions) and Se at around 260 °C. The CuSe begin to form approximately 260 °C but disappeared at 370 °C. The onset of formation of CIGS also occurred at approximately 260 °C. Additionally, the production of MoSe₂, accompanied by a decrease of Mo (110) reflection intensity, was explicitly detected at temperature above approximately 400 °C. The MoSe₂ formation is known not only to improve the adhesion but also to produce a good quality ohmic-type contact at the CIGS/Mo interface, which improves the efficiency of CIGS cells [Wad01, Sha96, Abo05].

The Ga composition in the resulting CIGS was estimated by the unit cell refinement method using X-ray diffraction data, as shown in Figure 6-5. The tetragonal I-42d (122) Cu(In_{0.7}Ga_{0.3})Se₂ structure was used as an initial cell for the refinement, and the 6 peaks of CIGS (i.e., 112, 103, 211, 220, 312 and 400) evident in the XRD pattern of selenized CIGS were taken into account, calibrating their 2θ location internally by the strong Mo (110) peak.

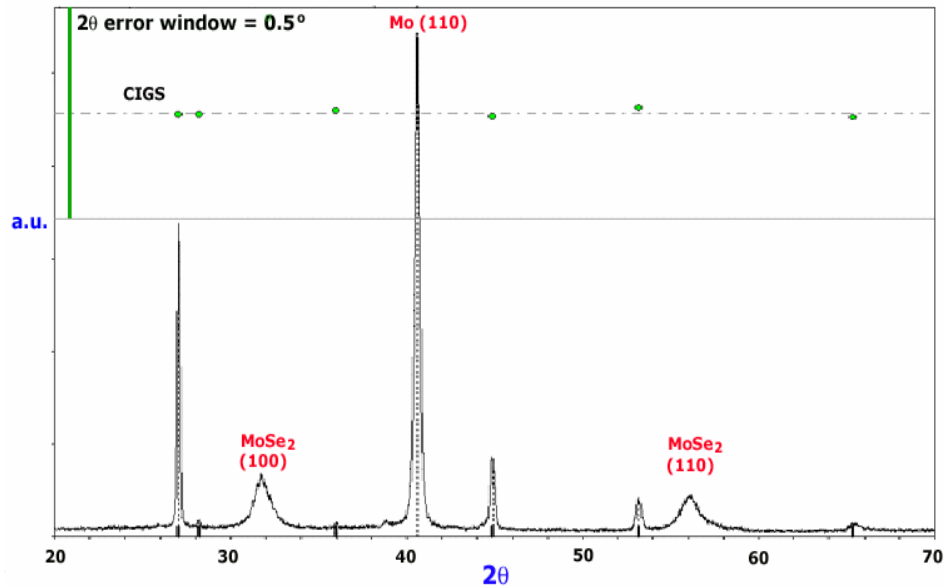


Figure 6-5. Cell refinement for room temperature X-ray diffraction data of a selenized CIGS sample using the tetragonal, I-42d (122) cell type

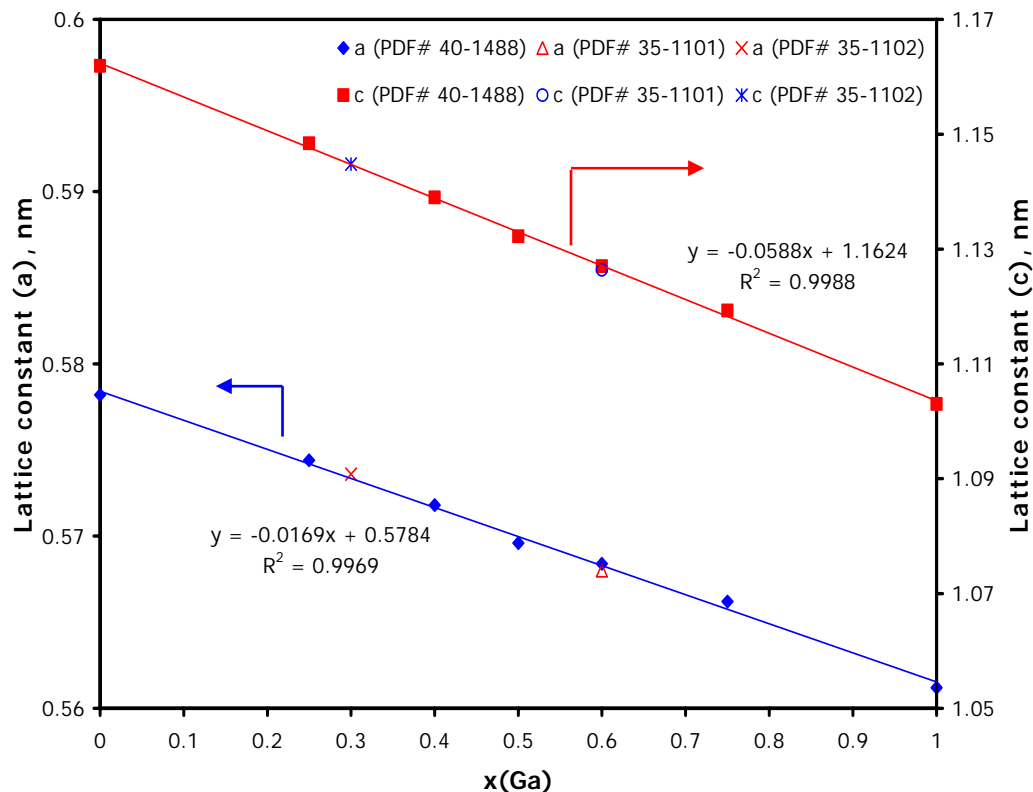


Figure 6-6. Lattice constants (a, c) vs. Ga composition of CIGS

Using the refined CIGS cell lattice constants $a \sim 0.571 (\pm 1.08 \times 10^{-4})$ and $c \sim 1.14 (\pm 9.08 \times 10^{-4})$ nm along with the relationship between composition and lattice constants for Cu(In,Ga)Se₂ shown in Figure 6-6, the Ga composition was estimated as $x(\text{Ga}) = 0.35$ to 0.39. This result suggests partial evaporation of indium occurred during the temperature ramp annealing. This is not surprising since the vapor pressure of In is relatively high (1.0×10^{-10} Torr at 400 °C)

6.3.3 Isothermal Annealing

Isothermal annealing at selected temperatures between 250 and 320 °C was then performed for kinetic analysis using a selected reaction model. The 2θ scan range (22 to 30°) for the isothermal experiments was used since the major reflection for the product CIGS (112) lays within this range. To complete the reaction, the temperature was elevated to 550 °C after each run and then maintained at this temperature for about 12 min or until the peak intensity of CIGS phase remained constant.

Figure 6-7 displays the time-resolved XRD data collected for the film isothermally soaked at selected different temperatures. The background scan data (Figure 6-3) corresponding with isothermal soak temperatures were subtracted from isothermal X-ray pattern. The comparison between the isothermal transformations at four different temperatures explicitly illustrates that the reaction rate increases with temperature.

To obtain the fractional reaction (α), which is defined as the fraction of reaction completed at time t , the intensities of the product CIGS (112) peaks were integrated by precisely fitting the diffraction data using JADE program. The integrated intensities then were normalized assuming that the Cu-Ga-In precursors were completely selenized to crystalline CIGS (i.e., $\alpha = 1$) after the high temperature (550 °C) anneal at the end of the

run, and that the texture of the CIGS did not appreciably change through the entire heating process.

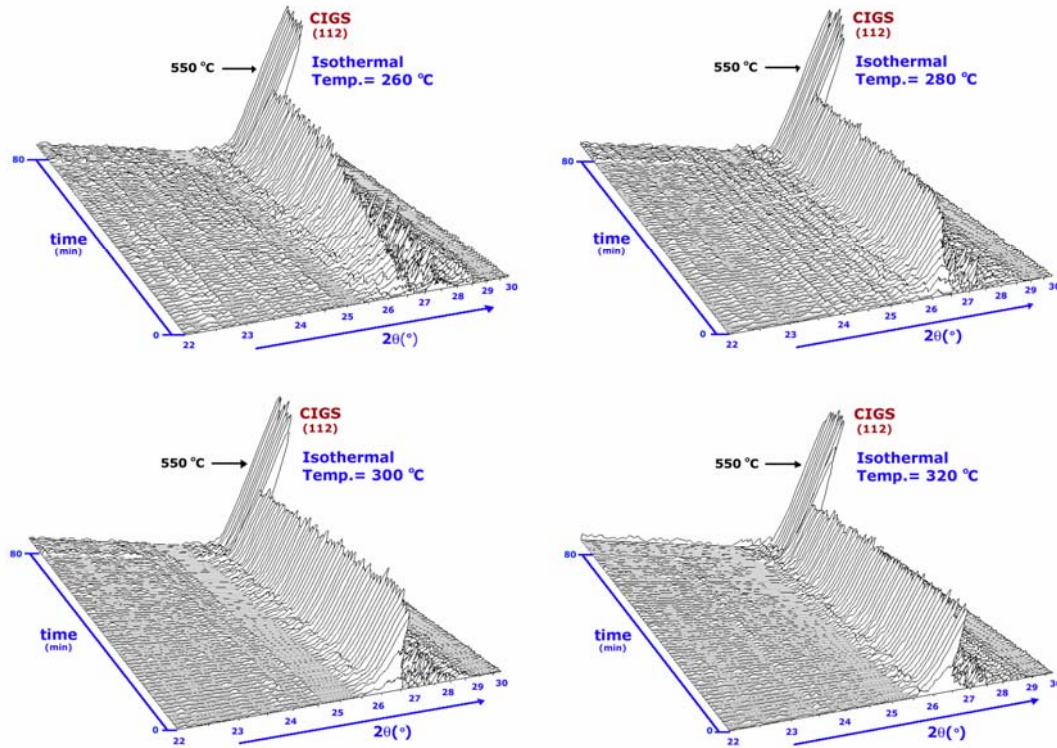


Figure 6-7. In situ XRD scans during isothermal selenization of glass/Mo/Cu-Ga-In precursor at four different temperatures

The reaction kinetics in terms of a rate constant, reaction order, and activation energy were quantitatively investigated using the Avrami model [Kim05a, Kim06a-b, Hul69], which is commonly used in Chapters 4 and 5. For our experimental data, the kinetic constants (k) and Avrami exponents (n) were estimated by linear regression using equation (4-4) as shown in Figure 6-8, and the resulting kinetic parameters were summarized in Table 6-1. The comparison between the fractional reaction by experiments and the prediction by an Avrami model demonstrates that an Avrami model fits the experimental data set very well, as shown in Figure 6-9.

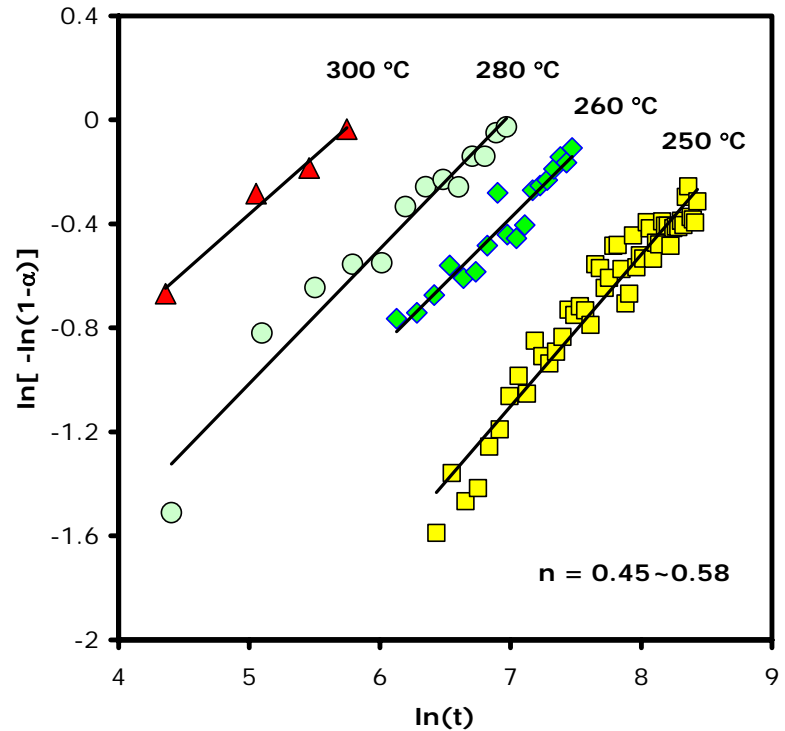


Figure 6-8. Avrami model and corresponding Arrhenius plot (inset) for CIGS formation by selenization of glass/Mo/Cu-Ga-In precursor.

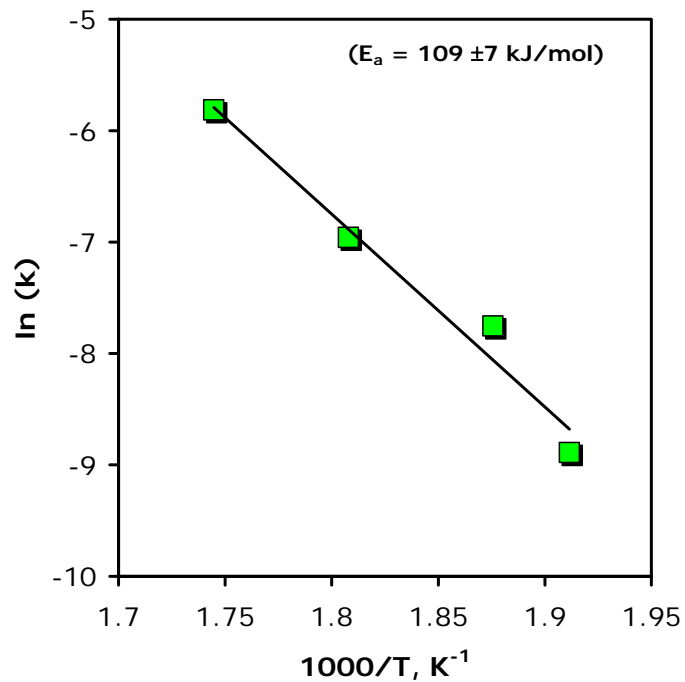


Figure 6-9. Arrhenius plot for Avrami rate constant for CIGS formation by selenization of glass/Mo/Cu-Ga-In precursor

The n values over the entire temperature range (250 to 300 °C) lie in between 0.45 and 0.58, which are close to the lower limiting value of 0.5 for one-dimensional, diffusion-controlled reactions. The low value of the estimated Avrami exponents suggests that the CIGS formation by selenization of glass/Mo/Cu-Ga-In precursor films follows one-dimensional, diffusion-controlled reaction pattern, where the nucleation of CIGS occurs so rapidly that the nucleation time is nearly negligible.

Table 6-1. Estimated kinetic parameters for the CIGS formation from selenization of glass/Mo/Cu-Ga-In precursor films (k : apparent kinetic constants and n : Avrami exponents)

Temperature [°C]	n	$k \times 10^3$ [s ⁻¹]
250	0.58 (± 0.022)	0.138 ($\pm 1.50 \times 10^{-3}$)
260	0.50 (± 0.036)	0.430 ($\pm 1.54 \times 10^{-2}$)
280	0.52 (± 0.034)	0.951 ($\pm 2.61 \times 10^{-2}$)
300	0.45 (± 0.044)	2.99 ($\pm 1.55 \times 10^{-1}$)

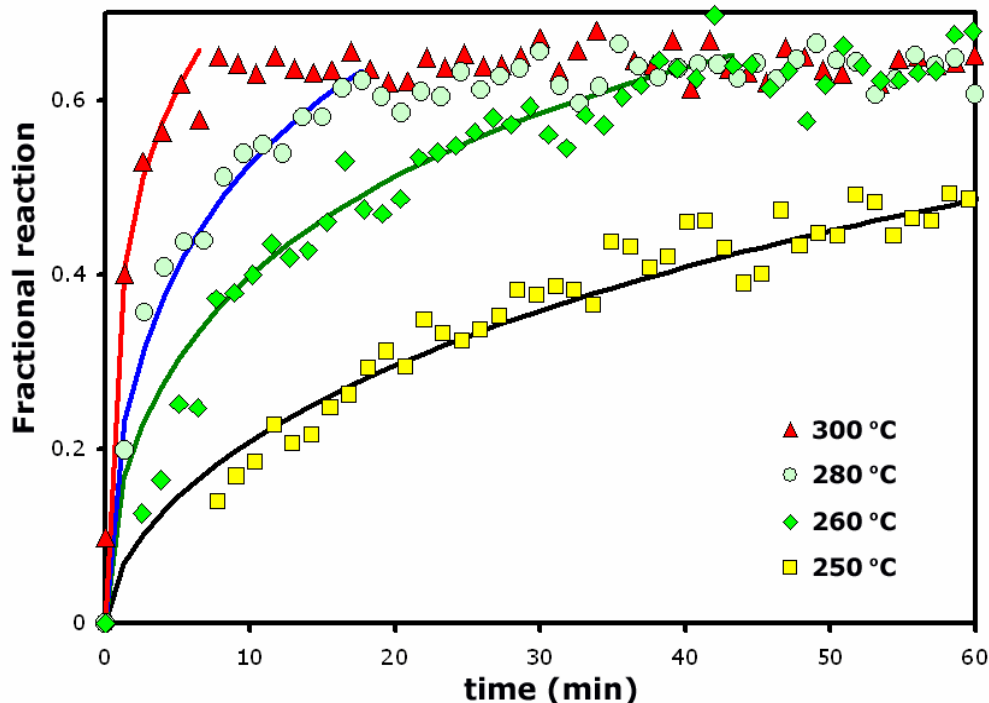


Figure 6-10. Comparison of fractional reaction for isothermal experiments and Avrami model prediction (Solid lines: model predictions, symbols: experiments).

The Arrhenius equation (4-6) was used to estimate the apparent activation energy E_a for CIGS formation by selenization of glass/Mo/Cu-Ga-In precursor films. The Arrhenius plot inserted in Figure 6-10 yields an activation energy of 144 (± 17) kJ/mol.

6.3.4 Comparison Between CIS, CGS, and CIGS Formation

It is interesting to compare the formation of CIGS from selenization of Cu-Ga-In precursor with that of CIS [Kim06a] and CGS [Kim06b] from selenization of Cu-In and Cu-Ga precursors, respectively. Their experimental results are summarized in Table 6-2.

Table 6-2. Comparison of reaction pathways and kinetics for CIS, CGS and CIGS formation from selenization of metallic precursors.

Precursors (glass/Mo/ Metal)	Selenization pathways	CIGS Fo rm ati on	Avrami model analysis			Ref.
			n	E_a (kJ/mol)	Temp.	
Cu-In	\rightarrow CuSe \rightarrow CuSe ₂ \rightarrow CIS	~ 250 °C	0.61~0.84	124 (± 19)		Kim06a
Cu- (Ga _{0.3} In _{0.7})	\rightarrow CuSe \rightarrow CIGS	~ 260 °C	0.45~0.58	144 (± 17)		This w o r k
Cu-Ga	\rightarrow CuSe \rightarrow CGS	~ 300 °C	0.55~0.61	109 (± 7)		Kim06b

Each precursor film (i.e., Cu-In, Cu-Ga and Cu-Ga_{0.3}-In_{0.7}) was prepared on a Mo-coated thin glass substrate by co-deposition of elements without heating the substrate. During the selenization of Cu-Ga and Cu-Ga-In precursors, the formation of CuSe followed by CGS and CIGS formation was detected, while the selenization of Cu-In precursor showed a different reaction sequence, *i.e.*, CuSe formation followed by CuSe₂ and then CuInSe₂. Additionally, the production of MoSe₂, accompanied by a decrease of Mo (110)

reflection intensity, was observed in experimental results with three precursors. The formation temperature of CGS (~ 300 °C), as estimated by temperature ramp anneal at a rate of 20 °C/min, was relatively higher than that of CIS (~ 250 °C) and CIGS (~ 260 °C). The Avrami model analysis suggested the formation of CIS, CGS and CIGS from selenization of their metallic precursors follows one-dimensional, diffusion-controlled reaction pattern along with an activation energy range of 110 to 140 kJ/mol. The formation of CGS, which has the highest formation temperature (~ 300 °C), showed the lowest apparent activation energy of 109 (± 7) kJ/mol. The reaction rates for selenization of Cu-In, Cu-Ga, and Cu-Ga-In metallic precursors were compared using Avrami kinetic constants, as shown in Figure 6-11. The comparison revealed that the selenization rates of Cu-In and Cu-Ga-In ([Ga]:[In]~30:70) are similar to each other, but considerably higher than that of Cu-Ga precursor.

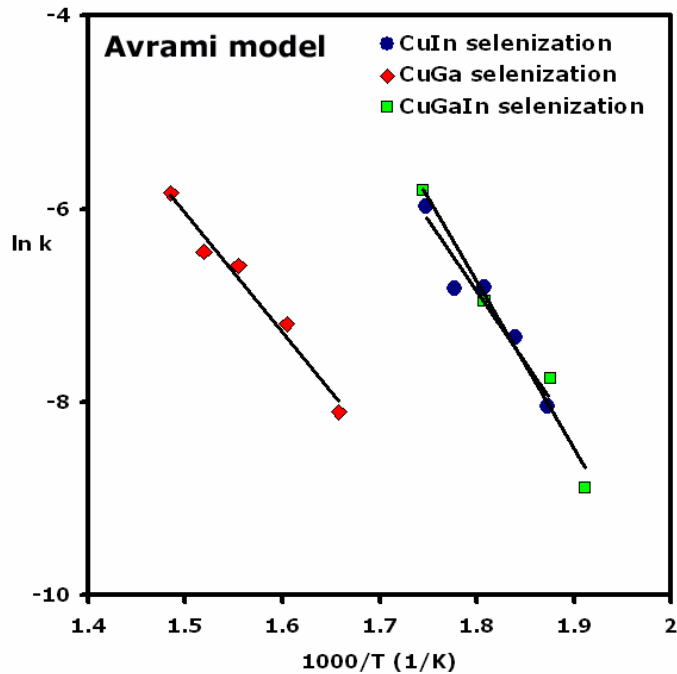


Figure 6-11. Comparison of reaction rates for selenization of different metallic precursors estimated by the Avrami model.

6.4 Summary

The reaction pathways and chemical kinetics of Cu(In,Ga)Se₂ formation from glass/Mo/Cu-Ga-In precursor were investigated using time-resolved, *in situ* high-temperature X-ray diffraction equipped with a graphite dome. The results show that the selenization of glass/Mo/Cu-Ga-In produces an intermediate CuSe phase in the temperature range 260 to 370 °C. The formation of CIGS is initiated at approximately 260 °C, which is close to the temperature of the initial appearance of CuSe. The MoSe₂ formation was detected at a temperature above approximately 400 °C. The estimated Ga composition of the CIGS suggested the partial loss of indium during temperature ramp selenization. The Avrami model analysis suggested that the Cu(In,Ga)Se₂ formation by the selenization of glass/Mo/Cu-Ga-In precursors could be described by a one-dimensional diffusion controlled reaction process yielding an apparent activation energy of 144 (± 17) kJ/mol. This value of activation energy is higher than that (i.e., 109 ± 7 kJ/mol) estimated for the CuGaSe₂ formation from selenization of glass/Mo/Cu-Ga precursor. It is concluded that the Cu-Ga-In selenization follows a pathway along a one-dimensional diffusion-controlled reaction that takes place in concert with a nucleation and growth mechanism.

CHAPTER 7

DIFFUSION MODELING OF CU-IN SELENIZATION

7.1 Introduction

In the previous Chapters 4 through 6, it was experimentally demonstrated that the Cu(In,Ga)Se₂ formation by annealing bilayer binary precursors (i.e., InSe/CuSe [Kim05a], In₂Se₃/CuSe [Kim05b] and GaSe/CuSe) and selenizing metallic precursors (i.e., Cu-In [Kim06a], Cu-Ga [Kim06b] and Cu-In-Ga [Kim06c]) follow a one-dimensional diffusion controlled reaction pattern. To simulate these diffusion-controlled transformations, both thermodynamic and kinetic descriptions are essential. Thus the results of simulations and their accuracy critically depend on the quality of these descriptions. A complete thermodynamic description consists of Gibbs energy expressions for every phase in the system and kinetic descriptions provide expressions for the mobility of every species in each phase and the rate constants for chemical reaction of all phases and species. The software ThermoCalc and DICTRA (DIffusion-Controlled TRAnsformation) [Bor00] considers the thermodynamic and diffusion information, and execute two main functions. One is to evaluate the model parameters of the thermodynamic and kinetic parameters. The other is to perform simulation of the thermodynamic and kinetic behavior of a system.

The Main features of ThermoCalc and DICTRA are (1) capability to predict thermodynamic and kinetic behavior of a higher order system based on the information of its sub-systems, (2) capability to predict thermodynamic and kinetic behavior of a system

under conditions where no experimental data are available, and (3) reduction of storage of data.

Our research group has been working on establishing the thermodynamic database of subternary (i.e., Cu-In-Se [She06]), pseudo-binaries (i.e., Cu₂Se-In₂Se₃ and Cu₂Se-Ga₂Se₃) and sub-binaries (e.g., Cu-Se, In-Se, Ga-Se [Ide03]) of the quaternary Cu-In-Ga-Se system using ThermoCalc program and EMF measurements.

The DICTRA package is a flexible system for simulation of diffusion-controlled transformations in multi-component alloys and has been employed successfully to simulate complex systems, e.g., heat treatments of multi-component alloys [Hög97]. The DICTRA program, however, can only handle simple geometries such as planar, cylindrical and spherical, of which all can be reduced into one space variable. Also, unfortunately the mobility or diffusivity information on Cu-In-Ga-Se and its subsystems is not well established. In this work, an attempt was made to estimate mobility in the Cu-In-Se system by analysis of the *in situ* HT-XRD measurements using the DICTRA program.

7.2 Multi-component Diffusion Theory

In the presence of a concentration gradient, a net flux of the corresponding species follows Fick's first law, which, in the isothermal and isobaric one-phase binary alloy with diffusion of species k in only the z direction, is expressed as

$$J_k = -D_k \frac{\partial c_k}{\partial z} \quad (7-1)$$

where J_k is the interdiffusion flux defined with respect to the fixed-volume, c_k is the concentration of k , and D_k is the diffusivity or the interdiffusion coefficient of species k [Bor00].

Fick's first law is not very useful by itself, but its combination with the continuity equation leads to the fundamental diffusion equation, which is usually called Fick's second law.

$$\frac{\partial c_k}{\partial t} = \frac{\partial}{\partial z} (-J_k) \quad (7-2)$$

$$\frac{\partial c_k}{\partial t} = \frac{\partial}{\partial z} \left(D_k \frac{\partial c_k}{\partial z} \right) \quad (7-3)$$

In multi-component systems, it is noted that the diffusivity (D_k) in equation (7-1) not only depend on concentration but also on the concentration gradients. The multi-component extension to Fick's first law was first expressed by Onsager [Ons31a, b], who postulated that each thermodynamic flux was linearly related to every thermodynamic force. Thus, in the same case of equation (7-1), we have

$$J_k = - \sum_{i=1}^n L'_{ki} \frac{\partial \mu_i}{\partial z} \quad (7-4)$$

where μ_i is the chemical potential for each species which may be assumed to be a unique function of the composition, i.e., $\mu_i = f(c_1, c_2, \dots, c_n)$ and L'_{ki} can be considered as a proportional factor which depends on the mobility of the individual species. The flux, J_k , is defined as

$$\sum_{i=1}^n V_k J_k = 0 \quad (7-5)$$

where V_k is the volume of each species. Generally, however, it is much more convenient to express the fluxes as functions of gradient in concentration rather than gradient in chemical potential, which can be obtained by applying the chain rule for derivation, i.e.,

$$J_k = - \sum_{i=1}^n L_{ki} \sum_{j=1}^n \frac{\partial \mu_i}{\partial c_j} \frac{\partial c_j}{\partial z} \quad (7-6)$$

or equivalently,

$$J_k = - \sum_{j=1}^n D_{kj} \frac{\partial c_j}{\partial z} \quad (7-7)$$

$$\text{and } D_{kj} = - \sum_{i=1}^n L_{ki} \frac{\partial \mu_i}{\partial c_j} \quad (7-8)$$

where $\partial \mu_i / \partial c_j$ values are purely thermodynamic quantities, sometimes referred to as thermodynamic factors. It is thus evident that the diffusivities can be composed of two separate terms, purely thermodynamic part and kinetic part, which will be described later.

The n concentration gradients in equation (7-7) are not independent and, for practical calculations, one usually eliminates one of them. The reduced diffusivities in a fixed volume frame of reference, where it is assumed that all the substitutional species have the same partial molar volumes and furthermore only the substitutional species contributes to the volume, are expressed as

$$D_{kj}^n = D_{kj} - D_{kn} \quad (\text{when } j \text{ is substitutional}) \quad (7-9)$$

$$D_{kj}^n = D_{kj} \quad (\text{when } j \text{ is interstitial}) \quad (7-10)$$

where the concentration gradient of n has been eliminated. By applying this simplification, equation (7-7) becomes

$$J_k = - \sum_{j=1}^{n-1} D_{kj}^n \frac{\partial c_j}{\partial z} \quad (7-11)$$

This equation suggests the possibility that the concentration gradient of one species may cause another species to diffuse, which was proposed [Dar42] and experimentally verified [Dar49] by Darken. In his experiment, two Fe-Si-C steels with similar carbon

content, but with different silicon content, were welded together and annealed. It was observed that carbon diffused from low carbon concentration to high concentrations, so-called up-hill diffusion.

By combining equation (7-11) with equation (7-2), the coupled partial differential equations (PDE's), which are suitable for practical calculations in multi-component system, are obtained. If all D_{kj}^n are constant, it is possible to obtain analytical solutions [Gup71], but generally numerical methods must be used as in DICTRA.

7.3 Thermodynamic and Kinetic Basis for DICTRA

As described in the previous section, it is evident that the simulation using the DICTRA program requires both thermodynamic and kinetic information. The calculation of phase diagram (CALPHAD) method, established by the pioneering work of Kaufman and Bernstein [Kau70], is one of most powerful techniques to calculate phase diagrams using thermodynamic data. In the CALPHAD method, the Gibbs energy of an individual phase is modeled as a function of temperature, composition, and sometimes pressure. The equilibrium at given conditions is simply calculated by a Gibbs energy minimization procedure. The thermodynamic parameters in the Gibbs energy models are evaluated from the available thermodynamic information by an optimization program, e.g., PARROT [Jan84] in ThermoCalc.

Inspired by the CALPHAD method, Andersson and Ågren [And92] suggested a similar method to calculate kinetic data, which represents the atomic mobility of the individual species in a multi-component phase as a function of temperature, pressure, and composition. From absolute-reaction rate theory arguments, they expressed the mobility

coefficient for element B (M_B) in terms of a frequency factor (M_B^0) and an activation enthalpy (Q_B) such as

$$M_B = \frac{M_B^0}{RT} \exp\left(\frac{-Q_B}{RT}\right) \quad (7-12)$$

where R is the ideal gas constant and T is the absolute temperature. In general, both M_B^0 and Q_B depend on temperature, pressure and composition. In the same manner as the CALPHAD approach, they represented the composition dependency of M_B^0 and Q_B as a linear combination of the values at each end-point of the composition space and a Redlich-Kister expansion, i.e.,

$$\Phi_B = \sum_i x_i \Phi_B^i + \sum_i \sum_{j>1} x_i x_j \left[\sum {}^r \Phi_B^{i,j} (x_i - x_j)^r \right] \quad (7-13)$$

where Φ_B represents $\ln(M_B^0)$ or Q_B . The Φ_B^i and ${}^r \Phi_B^{i,j}$ terms are the Φ_B values for pure i element and the binary interaction parameter between i and j elements, respectively. The x_i and x_j are the mole fractions for i and j elements. Each individual model parameter (i.e., Φ_B^i and ${}^r \Phi_B^{i,j}$) is stored in the DICTRA database and may be expressed as a polynomial in temperature and pressure, if necessary. In the CALPHAD method, the model parameters (i.e., Φ_B^i and ${}^r \Phi_B^{i,j}$) are determined by an optimization procedure using experimental information. The reason to store the individual mobilities in the DICTRA database instead of the interdiffusion coefficients is to reduce the data storage requirement. The interdiffusion coefficients can be calculated from the element mobilities and thermodynamic factors using equation (7-8). Further information on DICTRA is available in the DICTRA manual and review paper [Bor00].

7.4 Diffusion Modeling of Selenization of Cu-In Precursor

7.4.1 Kinetic Experiments

Reaction kinetics of α -CuInSe₂ (CIS) formation from Cu-In/Mo/glass precursor during selenization was investigated using *in situ* high-temperature X-ray diffraction [Kim06a], as described in chapter 3. Since the kinetic data obtained from XRD analysis were well fitted with the parabolic rate model, it was concluded that the reaction follows one-dimensional diffusion controlled reaction pattern. By assuming that the total film thickness is 2 micron and the fractional reaction of CIS is directly proportional to the thickness of CIS layer via one-dimensional growth model, the CIS thickness profile is obtained with respect to time, as shown in Figure 7-1. This kinetic result was used as input data for DICTRA modeling.

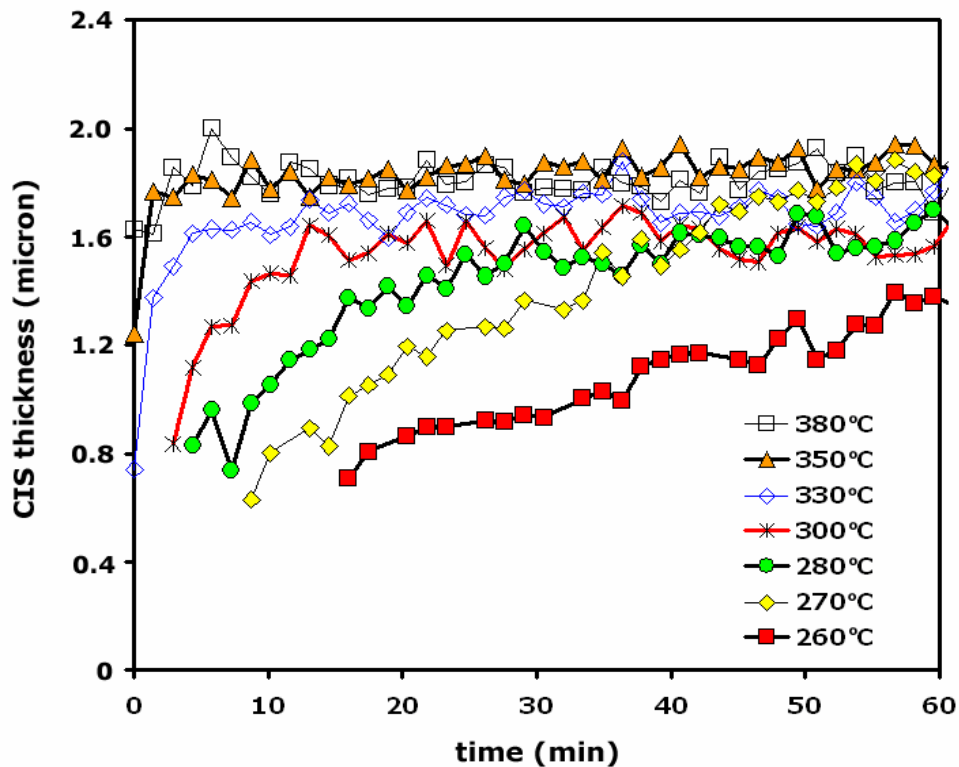


Figure 7-1. The CIS thickness vs. time obtained from kinetic experiment.

In the kinetics experiment, the overall atomic composition ($[Cu]/[In] = 1.0$) of the as-deposited Cu-In/Mo/glass precursor film was determined by inductively coupled plasma optical emission spectroscopy (ICP-OES) and its phase constitution (Cu_2In , $CuIn$ and In) was identified by both θ - 2θ and grazing incident X-ray diffraction (GIXD).

Therefore, the overall selenization of Cu-In precursor to yield α - $CuInSe_2$ is expressed as



Unfortunately, the current version of DICTRA program can not handle external boundary conditions in conjunction with stoichiometric phases and this problem becomes more evident in ternary or higher order system. Although the system of interest is non-stoichiometric, it will be simplified as a stoichiometric one. Thus reacting system is a pseudo-binary system by considering the Cu-In precursor as a single element. Since the atomic composition of Cu-In precursor was determined as $[Cu]/[In] \sim 1.0$, the stoichiometric Cu_1In_1 compound was assumed as a single reacting element. Therefore, the simplified pseudo-binary reaction is expressed as



and schematically shown in Figure 7-2.

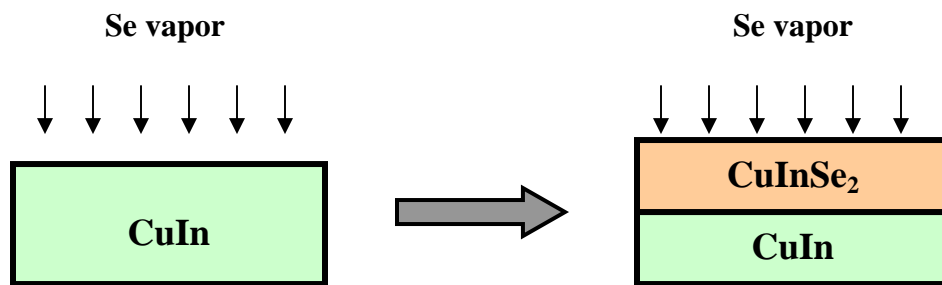


Figure 7-2. The schematic diagram of the simplified reaction of $CuInSe_2$ formation from selenization of Cu-In precursor.

7.4.2 Diffusion Modeling Using DICTRA

As mentioned in section 7.3, the diffusion coefficient of each element is calculated by the product of a thermodynamic factor and a kinetic factor. Thermodynamic database of Cu-In-Se ternary system was recently established by the assessment of experimental phase diagrams [Göd00a, Göd00b, Göd00a], EMF measurement of ternary compounds [Ide03] and thermodynamic models of sub-binaries (i.e., Cu-Se, In-Se and Cu-In), as described in chapter 3. Therefore, the thermodynamic information for the ternary α -CuInSe₂ and elemental Se is available. The thermodynamic information of CuIn compound, however, is not obvious because the CuIn compound is not included in the assessed Cu-In binary phase diagram [Liu02], and thus in the Cu-In-Se ternary phase diagram either. The identification of the CuIn compound was reported in several papers [Pis03, Son03, Mat97]. Pisarkiewicz *et al.* observed the CuIn phase along with Cu₂In, Cu₁₁In₉ and CuIn₂ in the multilayer metallic Cu/In precursor film fabricated by magnetron sputtering [Pis03]. Similarly, Song *et al.* reported that the CuIn phase was identified in the multilayer Cu-Ga-In precursor film deposited on glass by DC magnetron sputtering [Son03]. Thus, it is evident that the CuIn compound forms, but is likely to be a metastable phase. In this work, the metastable CuIn phase was intentionally added to the Cu-In thermodynamic database by optimizing thermodynamic parameters while retaining the existing Cu-In phase diagram and equilibrium phase relationships, as shown in Figure 7-3. Thus, the thermodynamic information for the CuIn phase can be calculated.

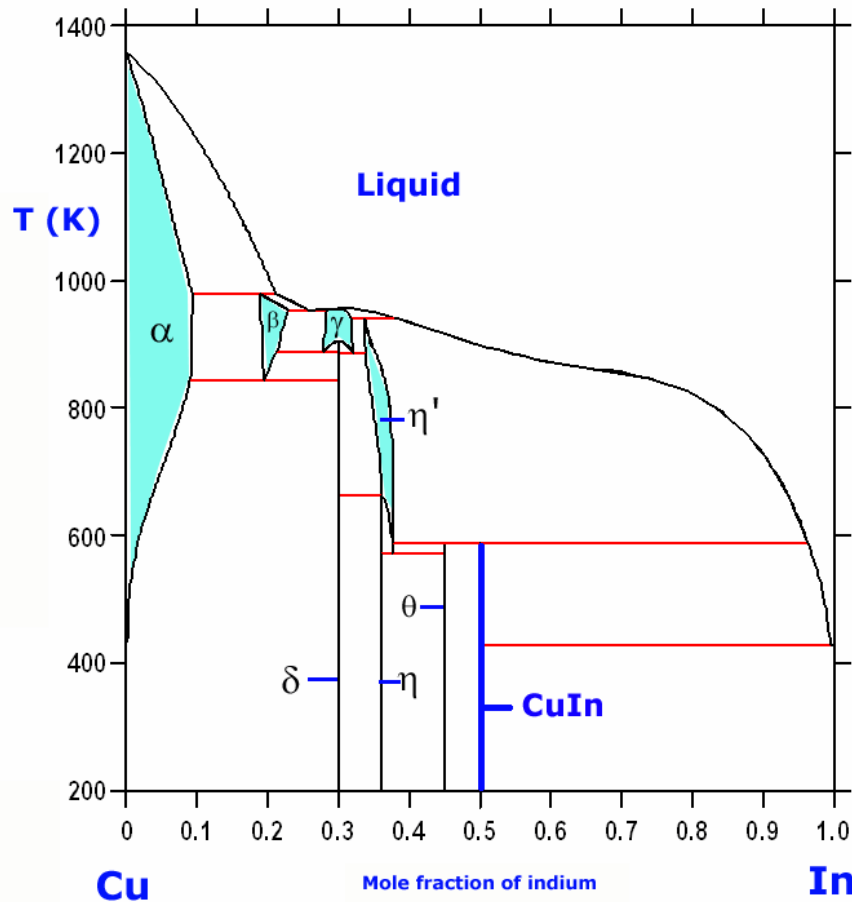


Figure 7-3. The modified Cu-In phase diagram including metastable CuIn phase

In the current DICTRA simulation, only three phases (i.e., α -CuInSe₂ (CIS), CuIn and Se) are considered, as shown in Figure 7-2. It is also assumed that Se diffuses through CIS layer to reach the interface of CIS-CuIn and then reacts with CuIn to form additional CIS. Therefore, the driving force for the growth of α -CuInSe₂ would be the difference of Se chemical potential between the top (i.e., Se-CIS interface) and bottom (i.e., CIS-CuIn interface) part of CIS layer. The mobility parameters of Se in CIS phase are evaluated by DICTRA optimization to fit the kinetic experimental data. In DICTRA database, the mobility parameter, MQ, is expressed as a function of temperature such as

$$MQ = -Q_B + RT \ln(M_B^0) \quad (7-13)$$

where the M_B^0 is a frequency factor and the Q_B is an activation enthalpy as described in equation (7-12). The numerical optimization using the given experimental data yielded these mobility parameters as

$$MQ = -Q_B + RT \ln(M_B^0) = -136,725 + RT \ln(0.01406) \text{ [J/mol]} \quad (7-14)$$

and thus,

$$Q_B = 136,725 \text{ [J/mol]} \quad (7-15)$$

$$M_B^0 = 0.01406 \quad (7-16)$$

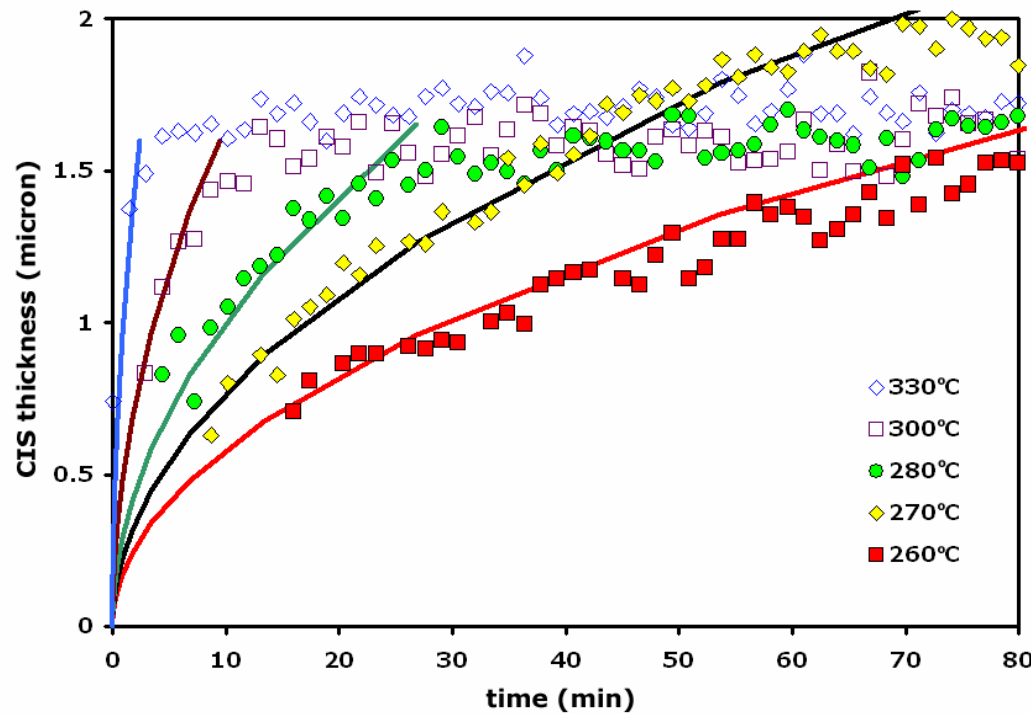


Figure 7-4. The comparison of CIS growth rates between the DICTRA prediction (solid lines) and experiments (symbols).

It is interesting to note that the value of resultant activation enthalpy ($Q_B \sim 137$ kJ/mol) is close to the activation energy ($E_a = 100 \pm 14$ kJ/mol) estimated by parabolic growth model using experimental data [Kim06a]. The growth rates of CIS layer

predicted by DICTRA simulation agree well with the experimental results as shown in Figure 7-4.

7.5 Summary

Based on the kinetic data obtained by *in situ* time-resolved, high-temperature X-ray diffraction, the DICTRA simulation on the CIS formation by selenization of Cu-In precursor was performed. Due to the limitation of current version of DICTRA program, the target reaction system was simplified as $\text{CuIn} + 2\text{Se} \rightarrow \text{CuInSe}_2$. For this simple reaction, the reliable mobility parameters of Se were obtained by the optimization using experimental data. Accordingly, it is evident that the predicted growth rates of CIS agree very well with the experimental results. Interestingly, the calculated activation enthalpy ($Q_B \sim 137 \text{ kJ/mol}$) is similar to the activation energy ($E_a = 100 \pm 14 \text{ kJ/mol}$) estimated by parabolic growth model using experimental data.

CHAPTER 8
DEFECT CHARACTERIZATION BY DEEP LEVEL TRANSIENT SPECTROSCOPY
(DLTS) TECHNIQUE

8.1 Introduction

The large composition homogeneity range and the deviation from stoichiometry in compound semiconductors such as Cu(In,Ga)Se₂ (CIGS) are attributed to defects in material such as anti-site defects, vacancies, interstitials, and defect clusters. It is well known that CIGS films can be produced in both p- and n-type conductivities by introducing native defects with or without extrinsic impurities. The doping mechanism and point defect chemistry of CIGS, however, are not well understood at the fundamental level. Deep-level defects are known to play an important role in determining the recombination mechanisms, which directly control minority carrier lifetimes and thus cell efficiency in p-n junction solar cells. Therefore, it is extremely important to understand defect properties to further improve the cell efficiency of solar cells.

The deep level transient spectroscopy (DLTS) technique is a powerful tool for determining the defect energy level, capture cross-section, and trap density [Lan74]. Several DLTS results on CIGS-based solar cells have been reported by Igalsen [Iga00, Iga01, Iga02, Iga03]. They have employed conventional DLTS, reverse-bias DLTS, and Laplace transform analysis of capacitance transients to investigate the defect spectra in the bulk and at the interface of standard ZnO/CdS/ Cu(In,Ga)Se₂ devices. They also used a modified DLTS that combines junction spectroscopy with illumination in a double pulse approach to identify the minority carrier traps acting as recombination centers in

the CIGS absorber layer. Bhattacharya et al. at NREL reported DLTS results for CdS/CIGS-based cells prepared from solution-based electroplated and auto-plated precursors, and by physical vapor deposition [Bha01]. In a previous study that included this author, DLTS analysis was performed on CIS and CIGS-based solar cells produced by NREL, EPV and UF [Ker04]. In this chapter, the experimental setup and operation procedures for the DLTS system are described, and DLTS measurements were conducted on several CIS- and CIGS- solar cells.

8.2 Operation Principle of DLTS Technique

The DLTS technique is based on the transient capacitance change associated with the thermal emission of charge carriers from a trap level to thermal equilibrium after an initial non-equilibrium condition in the space-charge region of a Schottky barrier or a p-n junction diode. The polarity of the DLTS peak depends on the capacitance change after trapping the minority or majority carriers. In general, a minority carrier trap produces a positive DLTS peak, while a majority carrier trap yields a negative DLTS peak.

If an abrupt junction with $N_t \ll N_d$ is assumed in a p-n junction diode, the change of transient capacitance can be simplified to

$$\Delta C(t) \approx \Delta C(0) \cdot e^{-t/\tau}, \quad (8-1)$$

where N_t is the trap density, N_d is the background doping density, and τ is the reciprocal emission time constant. The DLTS scan along the temperature axis is obtained by taking the difference of equation (8-1) at preset t_1 and t_2 rate windows, as expressed by

$$S(\tau) = \Delta C(t_1) - \Delta C(t_2) = \Delta C(0) \left(e^{-t_1/\tau} - e^{-t_2/\tau} \right) \quad (8-2)$$

The maximum emission rate, $1/\tau_{\max}$, can be obtained by setting $dS(\tau)/d\tau=0$, which yields

$$\tau_{\max} = \frac{t_1 - t_2}{\ln(t_1 / t_2)} \quad (8-3)$$

It is noted that the DLTS signal, $S(\tau)$, reaches its maximum at τ_{\max} corresponding to the characteristic temperature, T_m . In the DLTS operation, τ_{\max} is controlled by a manipulated variable called “delay time”, and a set of characteristic temperatures (T_m) are obtained at different delay time variables ($\sim \tau_{\max}$)

For an electron trap in a p-n junction diode, the electron emission rate (e_n) can be expressed by

$$e_n = \frac{1}{\tau} = \sigma_n \langle v_{th} \rangle N_c \frac{1}{g} \exp\left(-\Delta E/kT\right), \quad (8-4)$$

where σ_n is the electron capture cross-section, $\langle v_{th} \rangle$ is the average thermal velocity, N_c is the effective density of conduction band states, g is the degeneracy factor, and ΔE is the activation energy of the electron trap. Since N_c and $\langle v_{th} \rangle$ are varied with temperature to $T^{1.5}$ and $T^{0.5}$ respectively, equation (8-4) can be expressed as

$$\frac{e_n}{T^2} = \frac{1}{\tau T^2} = A \sigma_n \exp\left(-\Delta E/kT\right), \quad (8-5)$$

where A is a proportionality constant. The DLTS thermal scans provide information about characteristic temperatures (T_m) corresponding to the maximum DLTS signal at the pre-set delay time ($\sim \tau_{\max}$). Therefore, the capture cross-section (σ_n) and trap activation energy (ΔE) can be estimated from the Arrhenius plot as expressed by

$$\ln\left(\frac{e_n}{T_m^2}\right) = \ln\left(\frac{1}{\tau_{\max} T_m^2}\right) = \ln(A \sigma_n) - \frac{\Delta E}{k} \left(\frac{1}{T_m}\right) \quad (8-6)$$

Finally, assuming that the trap density is much smaller than the doping concentration, *i.e.*, $N_t \ll N_d$ (or N_a), the trap density (N_t) can be estimated by

$$N_t \cong \left(\frac{2\Delta C(0)}{C_0} \right) N_d, \quad (8-7)$$

where $\Delta C(0) = C_0 - C(0)$ is the net capacitance change due to thermal emission of electrons from the trap level, $C_0 = C(V_R)$ is the junction capacitance measured at a quiescent reverse bias voltage (V_R), $C(0)$ is the capacitance measured at $t=0$ and N_d is the background doping density. Further detailed description about the principles of DLTS can be found in other references [Li93]. The standard procedure to perform DLTS scan and data analysis to obtain the trap information is described in section 8.4.

8.3 Equipment Description of UF-DLTS System

The UF Deep Level Transient Spectroscopy (DLTS) system, which was commercially developed by Sula Technologies, consists of a deep level spectrometer, a Lake Shore 331S temperature controller, a roughing pump, and a liquid nitrogen cryostat, which allows the temperature as low as 77K by combination with a variable speed circulation pump, is shown in Figures 8-1 and 8-2. The control unit of the deep level spectrometer is composed of five functional groups as shown in Figure 8-1. A pulse generator applies repetitive bias pulses to sample, and also provides 1 MHz test signal for capacitance measurements. The capacitance meter consists of an innovative self-balancing bridge circuit that detects small, rapid change in capacitance following junction bias pulse. It can also be used for static capacitance-voltage (C-V) measurements. The correlator automatically removes DC background from capacitance meter output and amplifies the resultant signal change. The transient is then analyzed using the rate window algorithm reported by Lang [Lan74]. Correlation is based on a modified double boxcar signal averaging technique.

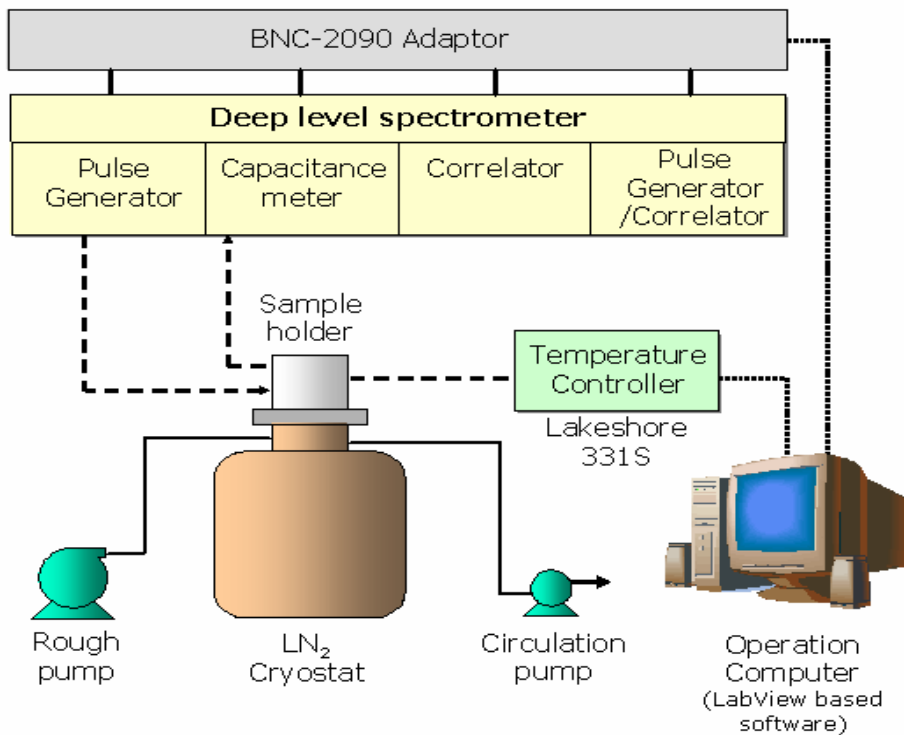


Figure 8-1. Schematic diagram of UF-DLTS system.

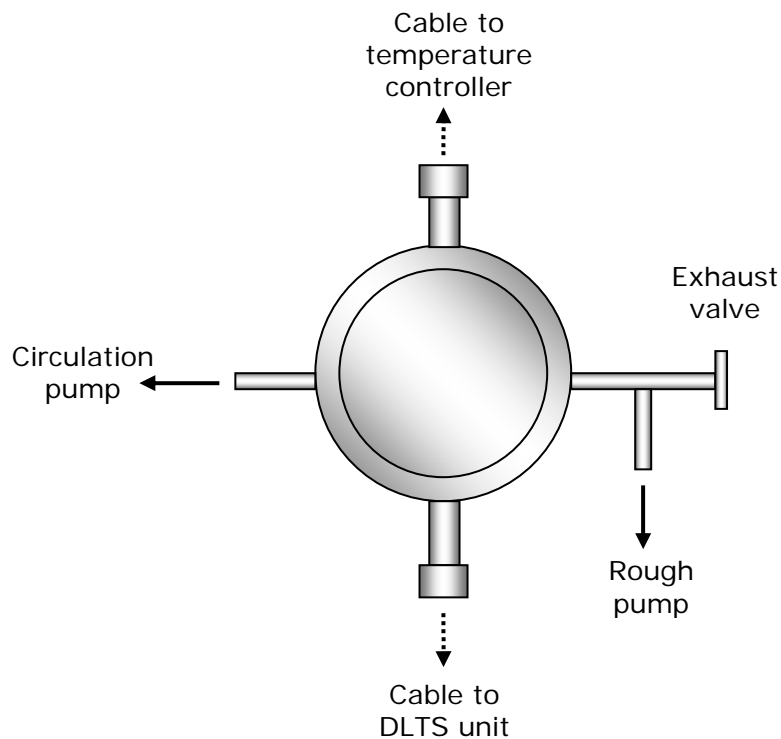


Figure 8-2. Schematic top view of LN₂ cryostat in the DLTS system.

Finally, an additional pulse generator and a correlator are used for spatial profiling of deep levels using Double Correlation Deep Level Spectroscopy (DDLTS). The second correlator can also be used to record simultaneously two DLTS spectra at different rate windows. The temperature controller is operated directly by computer and the control unit of the deep level spectrometer is connected to the computer via a BNC adaptor and NI-DAQ card.

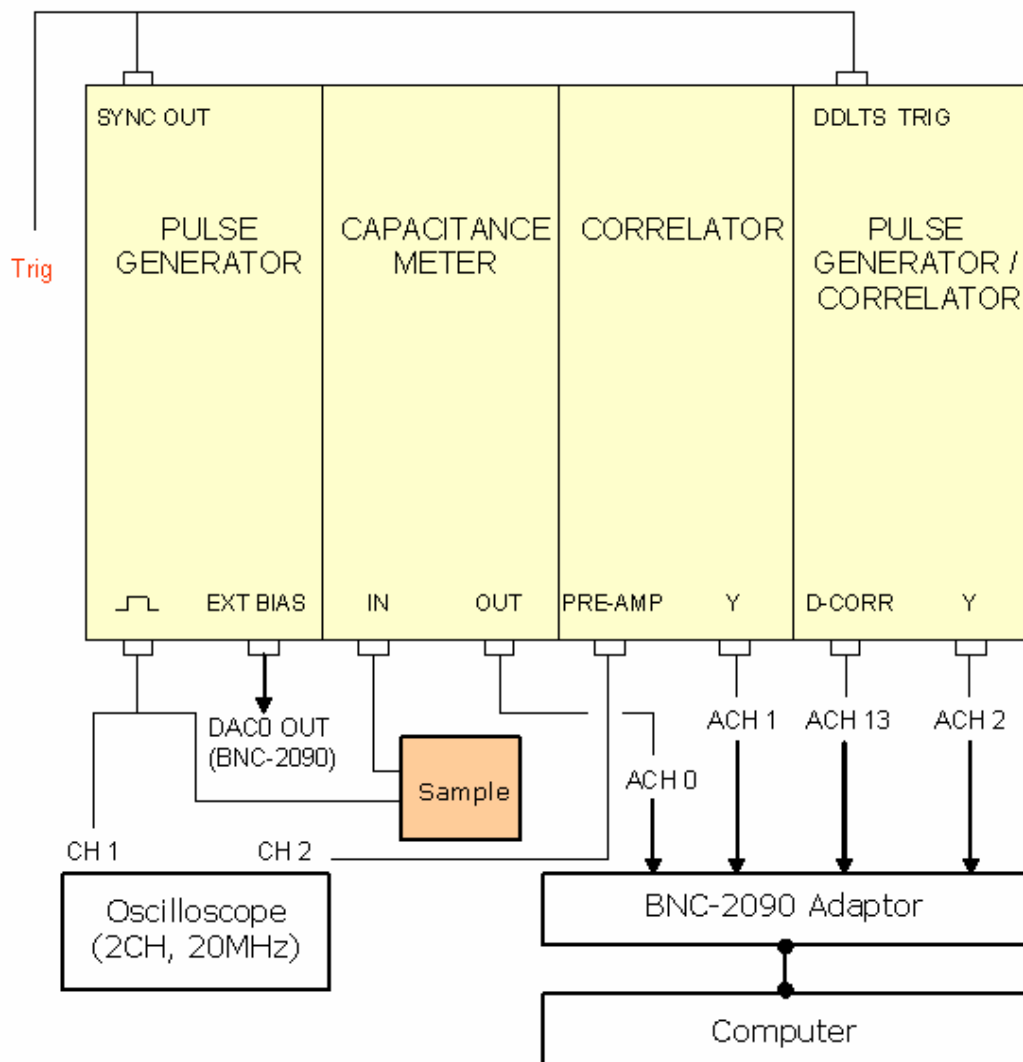


Figure 8-3. Simplified wiring diagram of UF-DLTS system.

The Sula Technologies operating software developed using National Instruments LabVIEW (ver.5.1) is available both as a source code and as an executable program. Currently, a stand-alone executable program is installed in the DLTS system. The simplified wiring diagram is shown in Figure 8-3. The DLTS system was originally purchased from Sula Technologies in 1990, and recently (in 2003) some components were upgraded including operation software and temperature controller. The actual picture of upgraded UF-DLTS system is shown in Figure 8-4, and equipment specifications are summarized in Table 8-1.

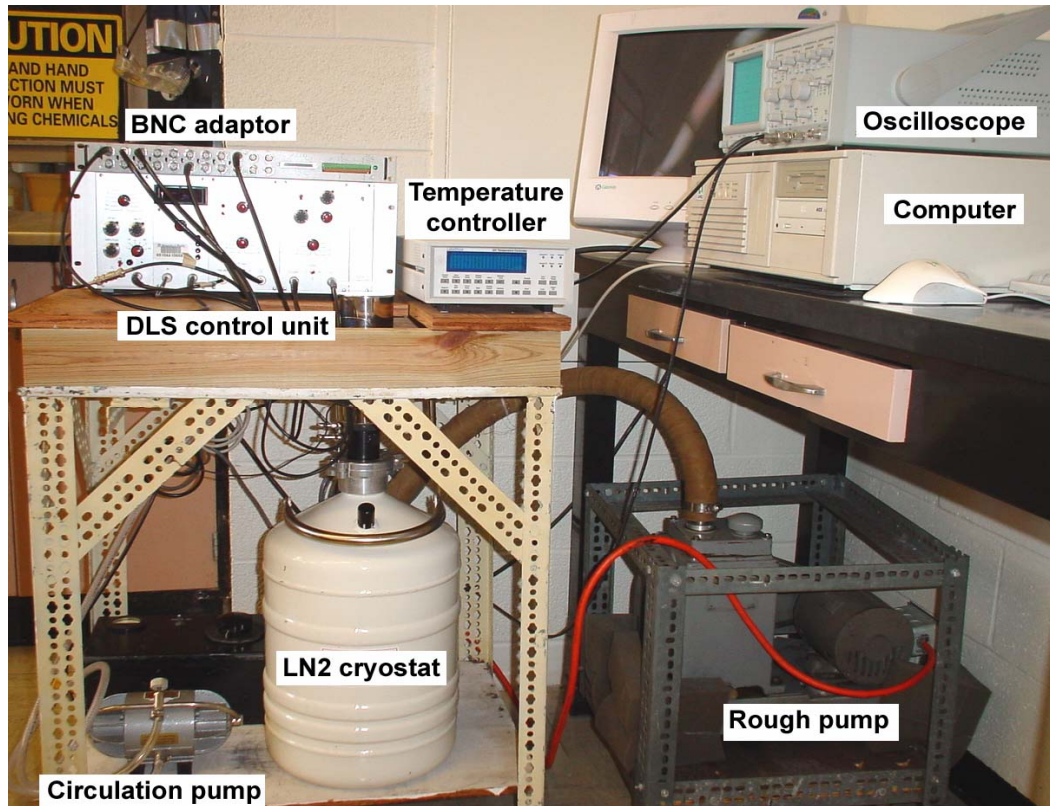


Figure 8-4. UF-DLTS system (Picture taken in 2004).

Table 8-1. Equipment specification of UF-DLTS system.

No.	Components	Vendor (Model)
1	DLS (Deep Level Spectrometer)	Sula technologies
2	Operation software (executable version)	Sula technologies
3	Temperature controller	Lakeshore (331S)
4	LN2 cryostat	Sula technologies
5	2-channel Oscilloscope (20MHz)	Tequipment.net (Leader LS8022)
6	BNC adapter module	National Instruments (BNC 2090)
7	Probe tips for electrodes	Micromanipulator Co. (7B-100)
8	Circulation pump	Walchem 406G

8.4 DLTS Measurement of CIGS Cells

In this section, the detailed procedures to perform the DLTS scans, analyze the scan data, and then obtain the defect information (defect activation energy, defect density and capture cross-section) are described using the DLTS results of CIGS solar cells provided by Energy Photovoltaic (EPV) Inc.

8.4.1 DLTS Scan

First, a series of DLTS scans was taken at selected operation conditions with the different rate windows (τ). For the EPV-CIGS cells, a reverse bias (V_R) of 0.4 V, a trap-filling pulse of 0.8 V, and a saturation pulse width of 10 ms were employed. During the DLTS thermal scans, the temperature ramping rate was limited at 0.1 K/sec or less for the precise temperature control.

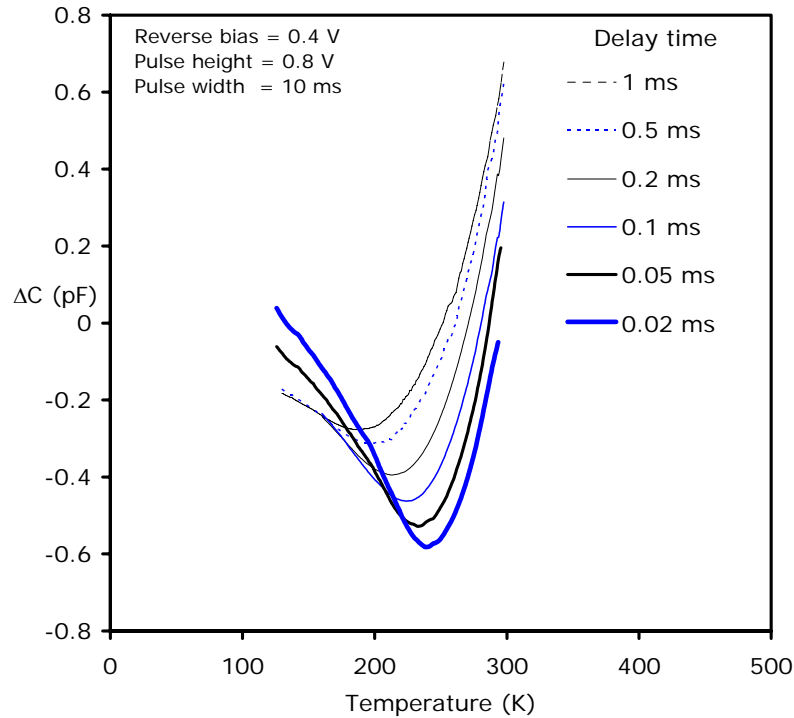


Figure 8-5. DLTS scans for the EPV-CIGS cell at different delay times (0.02 to 1.0 ms).

Since the sensitivity of the DLTS signal is generally proportional to $\Delta C/C_0$, a smaller junction capacitance (C_0) would provide a better sensitivity. It is also known that the junction capacitance is directly proportional to the junction area for a given device. Therefore, the CIGS cell with a small area of $1 \text{ mm} \times 0.8 \text{ mm}$ was used to maximize the sensitivity of the DLTS signal. As shown in Figure 8-5, a majority carrier (i.e., hole) trap was observed from the DLTS scans. Based on Figure 8-5, characteristic temperatures (T_m) were obtained at different rate windows (τ), as summarized in Table 8-2. In the UF DLTS system, a rate window (τ) is calculated by multiplying the preset delay time by a proportional factor (=4.3), e.g., $\tau = 4.3 \times \text{delay time}$. It is also noted that the characteristic temperatures (T_m) can be estimated from both the heating and cooling cycles of the DLTS scans for given delay times. For the reasonably low temperature

ramp rate, both heating and cooling scans are expected to provide similar results. As shown in Table 8-2, the T_m values obtained by heating scans are much higher than those by cooling scans for delay time ≤ 0.05 ms, while both results are almost identical for delay time ≥ 0.1 ms. Therefore, the average values of T_m were used for the subsequent analysis.

Table 8-2. DLTS scan results of EPV-CIGS cells at a reverse bias (V_R) of 0.4 V, a trap-filling pulse of 0.8 V, and a saturation pulse width of 10 ms.

Delay time (ms)	Rate window, τ (sec)	T_m by cooling (K)	T_m by heating (K)	Ave. T_m (K)
0.02	0.000086	238.5	257.5	248.0
0.05	0.000215	232.5	241.5	237.0
0.1	0.00043	224.7	224.5	224.6
0.2	0.00086	213.7	214.5	214.1
0.5	0.00215	198.5	198.5	198.5
1.0	0.0043	187.4	187.5	187.5

8.4.2 Estimation of Trap Activation Energy and Capture Cross-section

To estimate the trap activation energy and capture cross-section, Arrhenius plot is used as expressed by

$$\ln\left(\frac{e_n}{T_m^2}\right) = \ln\left(\frac{1}{\tau_{\max} T_m^2}\right) = \ln(A\sigma_n) - \frac{\Delta E}{k}\left(\frac{1}{T_m}\right), \quad (8-6)$$

and is graphically shown in Figure 8-6. The results represent the hole trap activation energy ($\Delta E = E_t - E_v$) of 0.20 ± 0.0076 eV which is similar to that of V_{ln} (0.17 eV) calculated by Zhang [Zha98], and capture cross-section (σ_p) of 3.1×10^{-24} cm². In these DLTS measurements, it was assumed that the capture cross-section (σ_p) is independent of temperature. However, more generally, the capture cross-section (σ_p) can be expressed by

$$\sigma_p = \sigma_0 \cdot e^{-\Delta E_b / kT}, \quad (8-8)$$

where σ_0 is the capture cross-section when temperature approaches infinity, and ΔE_b is the activation energy of capture cross-section.

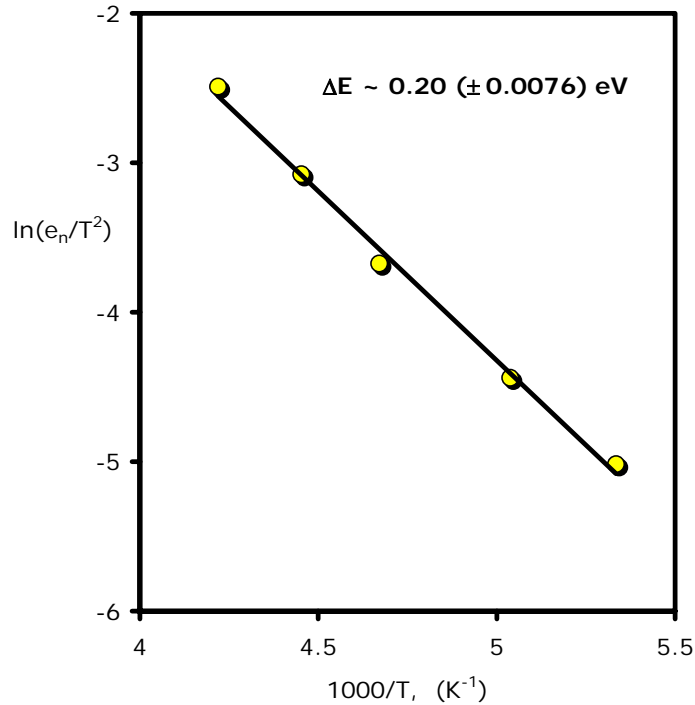


Figure 8-6. Arrhenius plot of DLTS scans for EPV-CIGS cells.

8.4.3 Estimation of Trap Density

In DLTS analysis, a trap density is calculated approximately by

$$N_t \approx \left(\frac{2\Delta C(0)}{C_0} \right) N_a \quad (8-9)$$

The variables in equation (8-9), however, have different values depending on characteristic temperatures (T_m) listed in Table 8-2. First, in the DLTS system, $\Delta C(0)$ is obtained directly from DLTS signal corresponding to the characteristic temperature at different delay time. The C_0 is the junction capacitance measured at a quiescent reverse bias voltage (V_R), which also depends on temperature.

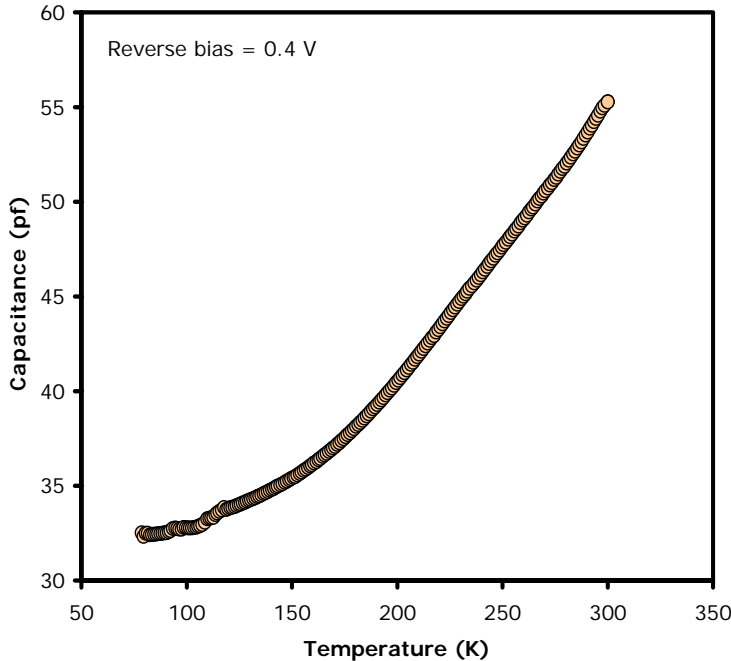


Figure 8-7. Capacitance-temperature scan for a EPV-CIGS cell at a reverse bias of 0.4 V.

To get $C_0(T, V_R)$, an additional capacitance-temperature (C-T) scan should be performed at given reverse bias, e.g., $V_R = 0.4$ V in this case, as shown in Figure 8-7. Finally, the background doping density, N_a , can be estimated by capacitance-voltage (C-V) measurements at different temperature. For an asymmetrically doped abrupt junction, junction capacitance is simplified to

$$\frac{1}{C^2} = \frac{2}{qN_a\epsilon_s\epsilon_0 A^2} (V_{bi} - V_a) \quad (8-10)$$

where C is the junction capacitance, q is the electronic charge ($\sim 1.6 \times 10^{-19}$ C), ϵ_s is the dielectric constant, ϵ_0 is the permittivity of free space ($\sim 8.85 \times 10^{-12}$ F/m), A is the area of diode, V_{bi} is the built-in voltage of device and V_a is the applied voltage. Equation (8-10) shows that N_a can be extracted from the slope for a linear plot of $1/C^2$ vs. V_a , and V_{bi} is estimated from the intercept of plot..

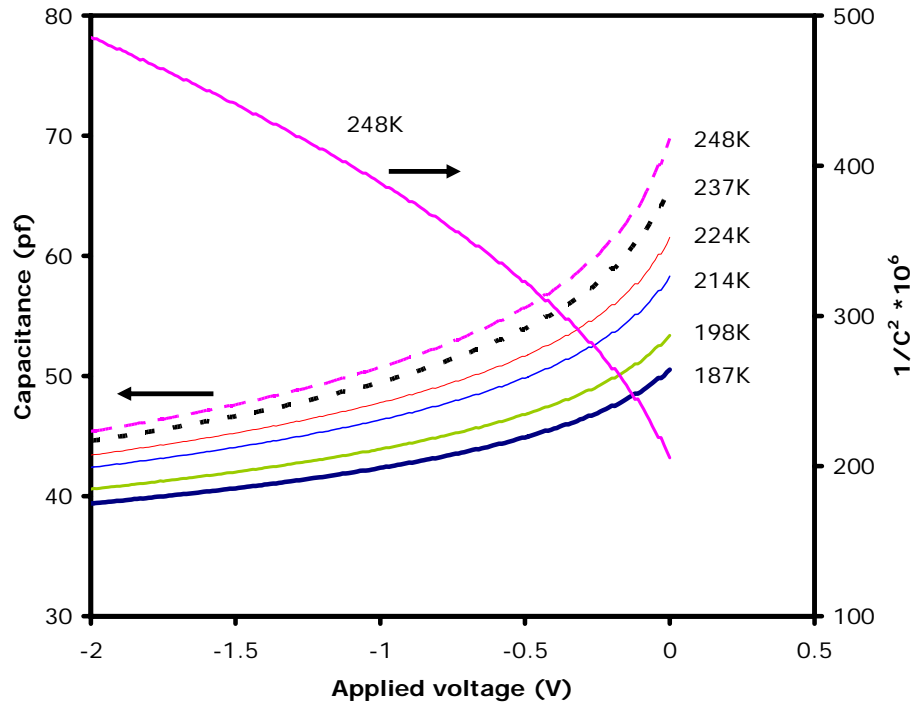


Figure 8-8. Capacitance-voltage (C-V) measurement for EPV-CIGS at different temperatures.

For different temperatures, capacitance-voltage (C-V) measurement results are shown in Figure 8-8. As shown in Figure 8-8, the $1/C^2$ vs. V_a plot for CIGS cell does not show a straight line, which suggests a non-uniformity of doping concentration. Therefore, average doping density is used to estimate a trap density. Finally, the calculated trap densities are summarized in Table 8-3.

Table 8-3. Trap density calculation from DLTS analysis of EPV-CIGS cell.

Delay time (ms)	Ave. T_m (K)	$\Delta C(0)$ (pF)	C_0 (pF)	N_a (cm^{-3})	N_T (cm^{-3})
0.05	237.0	0.5296	45.80	1.31×10^{15}	3.03×10^{13}
0.1	224.6	0.4628	44.00	1.34×10^{15}	2.82×10^{13}
0.2	214.1	0.3949	42.54	1.35×10^{15}	2.51×10^{13}
0.5	198.5	0.3128	40.31	1.38×10^{15}	2.14×10^{13}
1.0	187.5	0.2772	38.94	1.40×10^{15}	1.99×10^{13}

The DLTS analysis for the NREL-CIGS cell was also performed by following the same procedure. The results revealed a minority carrier trap with an activation energy of $\Delta E = 0.069$ eV. Interestingly, this value is identical to our previous result ($\Delta E = 0.07$ eV) [Ker04] estimated for another NREL-CIGS cell by using the NREL DLTS system, which clearly demonstrates the reliability of our DLTS system. The DLTS results of both EPV-CIGS and NREL-CIGS cell are summarized in Table 8-4 and 8-5, respectively.

8.5 Summary

The UF-DLTS system was successfully upgraded and its parameters were reasonably optimized. The detailed system description including an equipment specification was summarized, and the standard operation procedure (SOP) was illustrated using the DLTS results of EPV-CIGS cell. A comparison of the trap activation energy estimated by our DLTS system with that by NREL DLTS system demonstrates a good reliability of our system.

Table 8-4. Summary of DLTS analysis for EPV-CIGS cell.

DLTS Analysis - EPV (V_R /Pulse = 0.4/0.8)

Delay time	τ (sec)	Tm (K) - Cooling	Tm (K) - Heating	Tm(H)-Tm(C)	Ave. Tm	1000/T	Ln(T2/En)
0.02	0.000086	238.5	257.5	19	248	4.0323	-1.6657
0.05	0.000215	232.5	241.5	9	237	4.2194	-2.4912
0.1	0.00043	224.7	224.5	-0.2	224.6	4.4524	-3.0769
0.2	0.00086	213.7	214.5	0.8	214.1	4.6707	-3.6743
0.5	0.00215	198.5	198.5	0	198.5	5.0378	-4.4393
1	0.0043	187.4	187.5	0.1	187.45	5.3348	-5.0179

slope	-2264.45	
Y-intercept	7.000	
k_B	8.62E-05	eV/K

ΔE	-0.195	eV
σ	3.12E-24	cm ²

Reverse bias = 0.4 V
Pulse height = 0.8 V
Pulse width = 10 ms

Delay time

- 1 ms
- 0.5 ms
- 0.2 ms
- 0.1 ms
- 0.05 ms
- 0.02 ms

ΔC (pF)

Temperature (K)

$\ln(e_n/T^2)$

$1000/T, (K^{-1})$

$\Delta E \sim 0.20 (\pm 0.0076) \text{ eV}$

Delay time	Ave. T _m	$\Delta C(0)$	C ₀ (T _m)	N _a (T _m)	N _T
0.05	237	0.5296	45.8	1.31E+15	3.03E+13
0.1	224.6	0.4628	44	1.34E+15	2.82E+13
0.2	214.1	0.3949	42.54	1.35E+15	2.51E+13
0.5	198.5	0.3128	40.31	1.38E+15	2.14E+13
1	187.45	0.2772	38.94	1.40E+15	1.99E+13

Table 8-5. Summary of DLTS analysis for EPV-CIGS cell.

DLTS Analysis - NREL-CIGS (V_R /Pulse = 0.5/0.7)

Delay time	τ (sec)	Tm (K) - Cooling	Tm (K) - Heating	Tm(H)-Tm(C)	Ave. Tm	1000/T	Ln(T ₂ /E _n)
0.02	0.000086						
0.05	0.000215	120			120	8.333333	-1.13011
0.1	0.00043	112			112	8.928571	-1.68527
0.2	0.00086	104			104	9.615385	-2.23020
0.5	0.00215	97			97	10.30928	-3.00713
1	0.0043	88			88	11.36364	-3.50553

slope	-805.00	
Y-intercept	5.505	
k_B	8.62E-05	eV/K

ΔE	-0.069	eV
σ	1.39E-23	cm ²

Reverse bias = 0.5 V
Pulse height = 0.7 V
Pulse width = 10 ms

Legend:

- 0.05 ms
- 0.1 ms
- 0.2 ms
- 0.5 ms
- - - 1 ms

Inset Plot: $\ln(e_n/T^2)$ vs $1000/T, K^{-1}$

CHAPTER 9 CONCLUSIONS AND FUTURE WORK

A thermodynamic description for the Cu-Se binary system was successfully established using the abundant experimental data, recent evaluation by Glazov [Gla00], and previous optimization work by Chang [Cha99]. Sub-lattice models with various constitutions were reasonably applied to describe the Gibbs energy of different phases of the system. Furthermore, these Cu-Se optimization results were utilized to obtain a reliable set of expressions for Gibbs energy for solution in the ternary Cu-In-Se system. The EMF experimental results, defect formation energy by *ab initio* calculation, and phase equilibrium data were integrated to obtain a reliable set of expressions of Gibbs energy for ternary solution in the Cu-In-Se system. The Cu-Ga-In ternary phase diagram was predicted by a Maggianu's equation based on the sub-binary phase diagrams. Subsequently, the predicted ternary phase diagrams were modified using recent experimental data. Since the assessment of the Cu-In-Se and Cu-Ga-In ternary systems was performed by now, it is proposed to continue the research on Cu-Ga-Se and Ga-In-Se phase diagrams to predict the complete thermochemistry of the quaternary Cu-In-Ga-Se system.

In situ high-temperature X-ray diffraction technique was successfully employed to investigate the reaction pathways and phase evolution of binary Cu-Se, In-Se and Ga-Se compounds. It is concluded that the overall phase transformation of binary metal (Cu, In and Ga)-Se compounds qualitatively follows the sequence predicted by the thermodynamic phase diagram, but the detailed reaction path of each binary compound

depends on the as-deposited precursor structure and starting compounds. As future work, the isothermal soaking experiments characterized by TEM-EDS as well as HTXRD are suggested to estimate the kinetic parameters (e.g., rate constants and activation energies) and species diffusivities, which are essential to the development of robust process model.

Reaction pathways and kinetics of polycrystalline α -CIS, CGS, and CIGS formation were systematically investigated using thermal annealing of stacked bilayer and intimately mixed monolayer precursor, and selenization of elementally mixed metal precursors. Generally, annealing of precursors having different structures follows different reaction routes and thus yields slightly different initiation temperature of $\text{Cu}(\text{In}_x\text{Ga}_{1-x})\text{Se}_2$ formation. The selenization chamber using selenium powders (or small pellets) was successfully employed, and the MoSe_2 formation was always clearly observed during selenization. The results of reaction kinetics using Avrami and parabolic growth models are summarized in Table 9-1.

Table 9-1. Summary of reaction kinetics of $\text{Cu}(\text{In}_x\text{Ga}_{1-x})\text{Se}_2$ formation from different precursor structures

Precursor	Ambient	Product	T_f (product) [°C]*	Avrami model		Parabolic
				n	E_a (kJ/mol)	E_a (kJ/mol)
**InSe/CuSe	Air	CIS	220	0.6-0.8	66	65
$\text{In}_2\text{Se}_3/\text{CuSe}$	He	CIS	250	N/A	N/A	162 ± 5
InSe/Cu-Se	He	CIS	230	-	-	-
CuSe/In-Se	He	CIS	220	-	-	-
Cu-In-Se	He	CIS	140	N/A	N/A	N/A
Cu-In	He/Se	CIS	270	0.6-0.8	124 ± 19	100 ± 14
GaSe/CuSe	He	CGS	260	0.7	124 ± 19	115 ± 16
Cu-Ga-Se	He	CGS	280	0.1-0.2	197 ± 50	N/A
Cu-Ga	He/Se	CGS	300	0.6	109 ± 7	N/A
Cu-Ga-In	He/Se	CIGS	260	0.5-0.6	144 ± 17	N/A

* T_f (product): Temperature of product formation

** InSe/CuSe: Data cited from our previous publication [Kim05a].

The results summarized in the Table 9-1 lead to the following conclusions:

1. Formation temperatures of CGS (i.e., 260 to 300 °C) are relatively higher than those of CIS (i.e., 140 to 250 °C) and CIGS (i.e., 260 °C).
2. The Cu(In_xGa_{1-x})Se₂ formation from thermal annealing of binary bilayer precursors and selenization of metallic precursors follows one-dimensional diffusion controlled reaction, while Cu(In_xGa_{1-x})Se₂ formation from intimately mixed precursors (e.g, Cu-In-Se and Cu-Ga-Se) does not.
3. The lowest temperature to form CIS is identified as ~140 °C, which is achieved by thermal annealing of intimately mixed Cu-In-Se precursor.
4. The Cu(In_xGa_{1-x})Se₂ formation by thermal annealing of binary bilayer precursors follows both a simple parabolic rate and Avrami growth model, except for crystalline/crystalline bilayer precursor (e.g., In₂Se₃/CuSe), which is only explained by a parabolic rate model.
5. The Cu(In_xGa_{1-x})Se₂ formation by selenization of elemental metal mixtures (e.g, Cu-In, Cu-Ga, Cu-In-Ga) follows a one-dimensional diffusion controlled reaction with a nucleation and growth sequence.

DICTRA simulation of CIS formation by selenization of a Cu-In precursor was performed using the kinetic results obtained by time-resolved, *in situ* HTXRD along with thermodynamic descriptions achieved in chapter 2 and already available in literature.

Due to the limitation of current version of DICTRA program, however, the target reaction system was simplified as a pseudo-binary reaction, CuIn + 2Se → CuInSe₂, for which the reliable mobility parameters of Se were obtained.

APPENDIX A EXPLORATION OF MEDICI SIMULATION OF CIGS SOLAR CELLS

A.1 Overview of Medici

Medici is a commercial device simulation program that can be used to simulate the behavior of semiconductor devices such as MOS and bipolar transistors [Med]. It models the two-dimensional distributions of potential and carrier concentrations in a device, and predicts electrical characteristics for arbitrary bias conditions. The program solves Poisson's equation and both the electron and hole current-continuity equations to analyze devices such as diodes and bipolar transistors as well as effects in which the current flow involves both carriers, such as CMOS and latch-up. It simulates the behavior of deep submicron devices by providing the ability to solve the electron and hole energy balance equations self-consistently with other device equations. Basically, Medici uses a non-uniform triangular simulation grid, and can model arbitrary device geometries with both planar and non-planar surface topographies. The simulation grid can also be refined automatically during the solution process. This flexibility makes modeling of complicated devices and structures possible. A number of physical models are incorporated into this program for accurate simulations, including models for recombination, photo-generation, impact ionization, band-gap narrowing, band-to-band tunneling, and carrier mobility and lifetime. Medici also incorporates the Boltzmann and Fermi-Dirac statistics, including the incomplete ionization of impurities.

Due to the high cost and complexity, however, Medici has not been used for solar cell simulation as often as AMPS-1D (Analysis of Microelectronic and Photonic

Structures) and SCAPS-1D (Solar cell CAPacitance Simulator in 1 Dimension). In a previous study, the effects of grain boundaries in the CIS absorber layer on the device performance of ZnO/CdS/CIS/Mo-glass solar cells were successfully modeled using Medici [Yoo05].

A.2 Non-uniformity of Doping Concentration

In chapter 8.4.3, the results of capacitance-voltage (C-V) measurements on CIGS cell showed the non-linear plot of $1/C^2$ vs. V, which suggests a non-uniformity of doping concentration. A possible cause of the variation in doping concentration is Ga- grading within CIGS layer, which is generated unintentionally during the CIGS deposition process (e.g., 3 stage process) or intentionally by controlling the composition of CIGS absorber. Unintentional process-related Ga grading is known to be a consequence of the Cu depleted absorber surface in high-efficiency CIGS cell [Dul01]. Dullweber et al. [Dul01] reported that the graded band gap reduces recombination in solar cell, and hence improve the open-circuit voltage. Furthermore, appropriate band gap grading increases the short-circuit current by increasing light absorption and carrier collection, and thus the cell efficiencies. Song et al. [Son04] studied a variety of graded band-gap structures including space charge region (SCR) grading, back surface region grading, and double grading of the CIGS absorber layer using AMPS-1D simulation program. They reported that an optimal band-gap profile, adopting a double grading consisting of the front space-charge region (SCR) grading and back surface grading, improves significantly the cell efficiency up to 19.83% (AM1.5G) while the uniform band gap cell shows 15.42% efficiency. In this chapter, the simulation of C-V profile for band gap graded CIGS cell was carried out using Medici (Avant!) software with a band gap profile as input parameters.

A.3 Medici Simulation of C-V Profile

To verify the feasibility of Medici simulation for non-linear $1/C^2$ vs. V, two simplified CIS/CdS/ZnO solar cell structures were used. One structure (e.g., CIS-uniform) has a uniform band-gap and doping concentration while the other (e.g., CIS-grading) has a grading band gap and doping concentration profile. The front and back contact electrodes, i.e., ZnO and Mo, were assumed to be Ohmic type. Most of the physical and electrical parameters of each layer for both structures were cited in the previous Medici [Yoo05] and AMPS-1D [Son04] simulations, as shown in Table A-1 and Figure A-1. A band gap grading and doping profile for CIS-grading cell was used for this preliminary simulation.

Table A-1. Design parameters of solar cell for Medici simulation.

Layers	Thickness (nm)	Band gap Eg (eV)	Electron affinity χ (eV)	Doping (cm ⁻³)	Dielectric constant, ϵ
CIS-uniform					
ZnO	50	3.3	4.00	5×10^{17}	9
CdS	100	2.4	3.75	6×10^{16}	10
CIS	2000	1.04	3.80	8×10^{16}	13.6
CIS-grading					
ZnO	50	3.3	4.0	5×10^{17}	9
CdS	100	2.4	3.75	6×10^{16}	10
CIS-1	400	1.04	3.80	1×10^{15}	13.6
CIS-2	400	1.1	3.78	5×10^{15}	13.6
CIS-3	400	1.2	3.73	1×10^{16}	13.6
CIS-4	400	1.3	3.69	5×10^{16}	13.6
CIS-5	400	1.4	3.65	1×10^{17}	13.6

The variation of Ga composition in CIGS films is expected to change the physical and electrical properties of the CIS films such as band gaps, hole concentrations [Sch99], bulk defect densities [Han01], absorption coefficients and electron affinities. It is reported that the addition of Ga to CIS films increases the band gap by mainly lowering

the position of the conduction-band minimum [Wei95], but makes a negligible change in mobility at room temperature [Sch99].

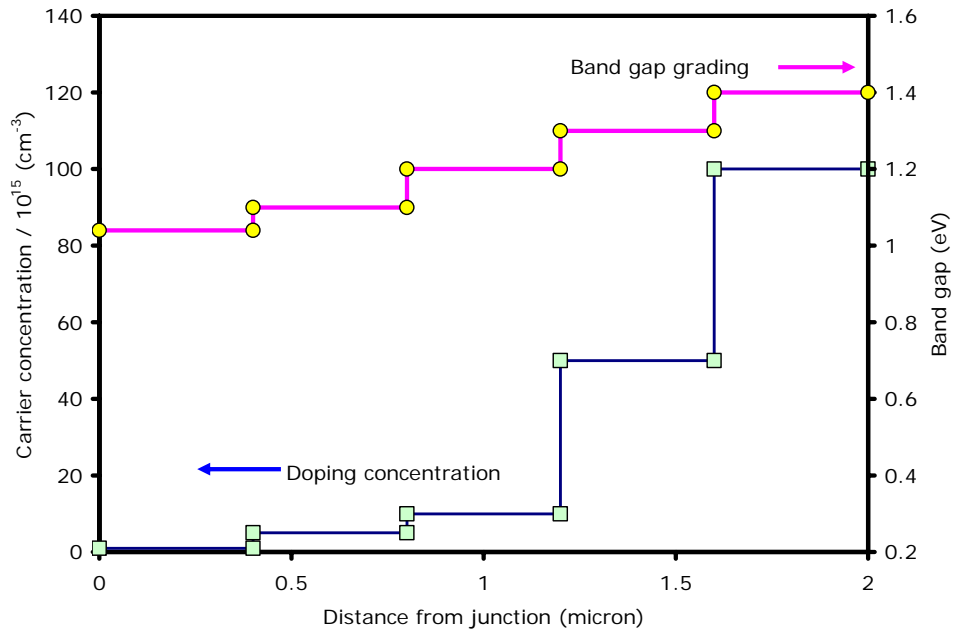


Figure A-1. A band-gap and doping profile for CIS-graded solar cell.

As shown in Table A-1, different parameters (e.g., electron affinities and doping density) for the band gap graded CIS layers were applied in this Medici simulation. The light absorption coefficient profiles for the CIS layers with different band gaps and other layers were summarized in Figure A-2. In this preliminary simulation, defect densities were not considered. To obtain the C-V profile, an AC small signal analysis with a 1MHz frequency was performed for the applied reverse bias range of -2 to 0V. The C-V simulation results for CIS-uniform and CIS-grading cells are shown in Figure A-3. As revealed in Figure 8-11, a uniform band gap CIS cell shows a linear $1/C^2$ vs. V relationship which is a conventional behavior for a one-side abrupt p-n junction diode, while a band gap graded CIS cell follows a non-linear $1/C^2$ vs. V relationship which is similar to the behavior of a traditional CIGS cell measured in Figure 8-8.

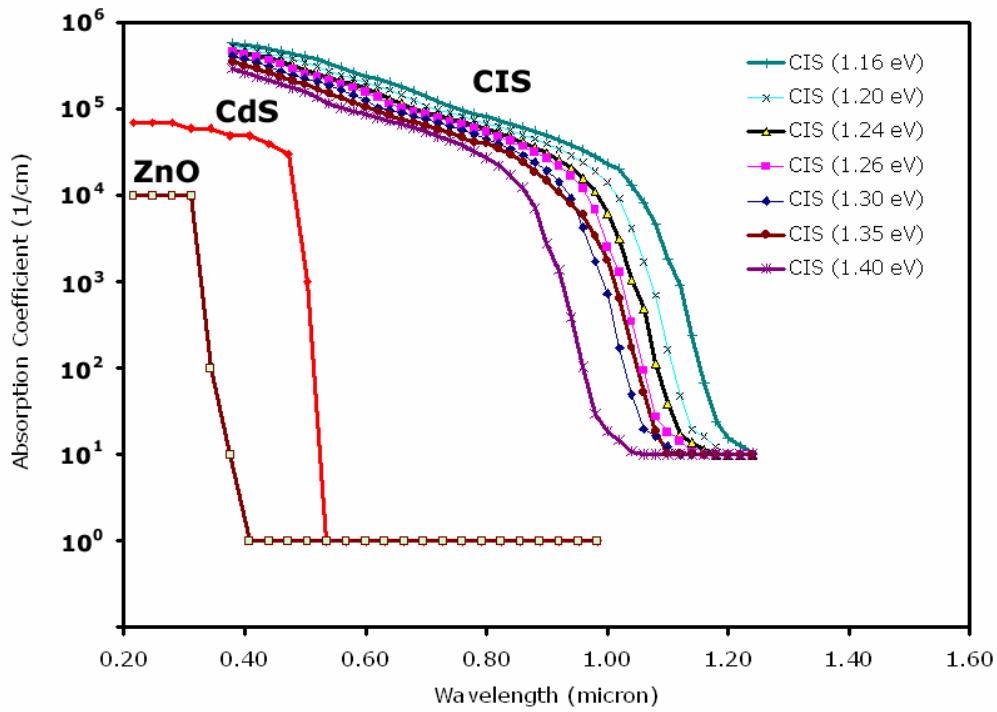


Figure A-2. Absorption coefficient profiles for the materials used in Medici simulation.

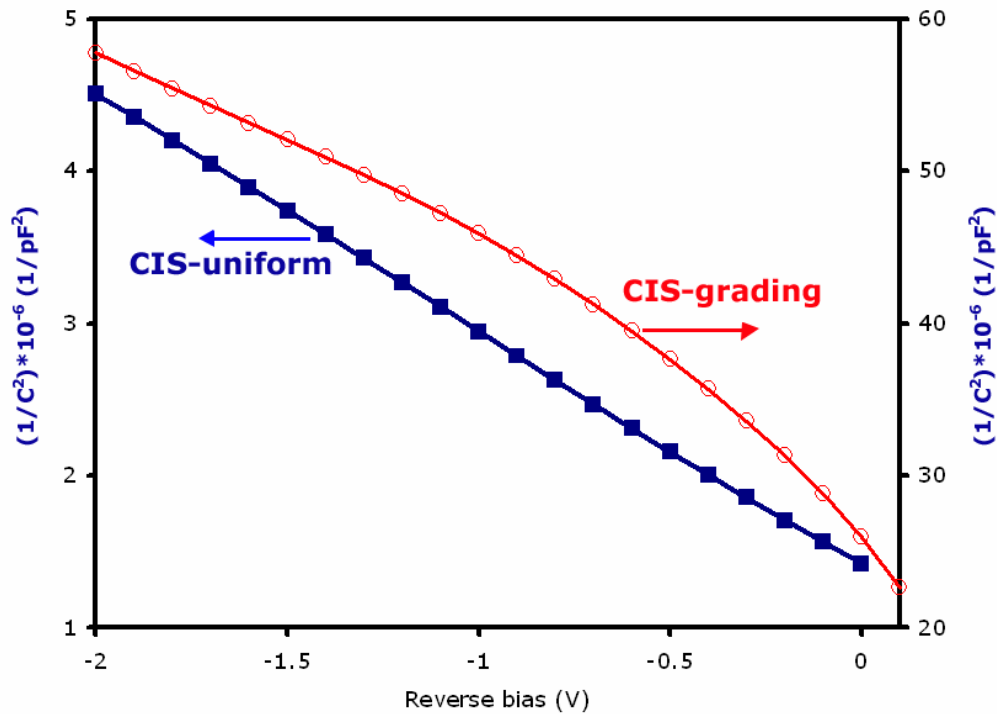


Figure A-3. Medici simulation results on C-V profile for the uniform doping and graded doping CIS cells.

A.4 Medici Simulation on Grading Band Gap CIGS Cell

Based on the preliminary results, more detailed CIGS cells with a graded band gap were designed for the performance simulation. Basic design parameters of each layer were determined with reference to our AMPS-1D simulation work [Son04] on the CIGS cells with various band gap profiles. It is noted that, in this simulation, two layers with a high recombination interface layer (HRL in Table A-2) and an inverted surface layer (OVC in Table A-2) were added to the model with an effective recombination center. An inverted surface layer, which is referred to as an ordered vacancy compound (OVC), is considered as a thin In-rich n-type layer (e.g., CuIn₂Se_{3.5} or CuIn₃Se₅) [Sch93] or a general surface defect layer [Her99, Gui98]. This layer can improve the cell performance since the electrical junction is shifted away from the high-recombination interface between the CdS and CIGS layers, and thus the recombination rate decreases [Son04].

Table A-2. Basic design parameters of solar cell for Medici simulation

Layers	Thickness (nm)	Band gap E_g (eV)	Affinity χ (eV)	Doping (cm ⁻³)	Remark
CIGS-uni					
n-ZnO	50	3.3	4.00	5×10^{17}	
n-CdS	30	2.4	3.75	6×10^{16}	
n-HRL	5	1.5	3.8	5×10^{14}	
n-OVC	30	1.3	3.95	3×10^{12}	
p-CIGS	1965	1.2	3.85	8×10^{16}	$E_a=40, 90$ meV $E_d=70$ meV
CIGS-grade					
n-ZnO	50	3.3	4.0	5×10^{17}	
n-CdS	100	2.4	3.75	6×10^{16}	
n-HRL	5	1.5	3.8	5×10^{14}	
n-OVC	30	1.3	3.95	3×10^{12}	
p-CIGS-1	865	1.16	3.87	8×10^{16}	
p-CIGS-2	220	1.2	3.85	8×10^{16}	
p-CIGS-3	220	1.24	3.83	8×10^{16}	$E_a=40, 90$ meV
p-CIGS-4	220	1.3	3.80	8×10^{16}	$E_d=70$ meV
p-CIGS-5	220	1.35	3.77	8×10^{16}	
p-CIGS-6	220	1.4	3.75	8×10^{16}	

As summarized in Table A-2 and A-3, it is assumed that the doping concentration, deep-level defect density and carrier life times (τ_n or τ_p) are constant in the CIGS layers. Deep-level defect parameters of each layer are summarized in Table A-3. In this simulation, an AM1.5 spectrum [ASTM G173] which is used as a standard spectrum for solar cell application was adopted to improve the reliability of simulation results.

Table A-3. Deep defect parameters of solar cells for Medici simulation

Layers	Donor defects				Acceptor defects			
	E_d (eV)	N_d (cm $^{-3}$)	τ_n (sec)	τ_p (sec)	E_a (eV)	N_a (cm $^{-3}$)	τ_n (sec)	τ_p (sec)
CIGS-uni								
n-ZnO	1.7	1.5×10^{17}	3.3×10^{-9}	3.3×10^{-8}	1.7	1.5×10^{17}	3.3×10^{-8}	3.3×10^{-9}
n-CdS	1.2	1.0×10^{16}	1.0×10^{-8}	1.0×10^{-7}	1.2	1.0×10^{16}	1.0×10^{-7}	1.0×10^{-8}
n-HRL	0.8	1.0×10^{17}	5.0×10^{-9}	5.0×10^{-8}	0.8	1.0×10^{17}	1.7×10^{-7}	1.7×10^{-8}
n-OVC	0.7	8.0×10^{15}	1.1×10^{-7}	1.1×10^{-6}	0.7	8.0×10^{15}	1.1×10^{-6}	1.1×10^{-7}
p-CIGS	1.07	1.0×10^{15}	9.1×10^{-7}	9.1×10^{-6}	0.87	1.0×10^{15}	9.1×10^{-6}	9.1×10^{-7}
CIGS-grade								
n-ZnO	1.7	1.5×10^{17}	3.3×10^{-9}	3.3×10^{-8}	1.7	1.5×10^{17}	3.3×10^{-8}	3.3×10^{-9}
n-CdS	1.2	1.0×10^{16}	1.0×10^{-8}	1.0×10^{-7}	1.2	1.0×10^{16}	1.0×10^{-7}	1.0×10^{-8}
n-HRL	0.8	1.0×10^{17}	5.0×10^{-9}	5.0×10^{-8}	0.8	1.0×10^{17}	1.7×10^{-7}	1.7×10^{-8}
n-OVC	0.7	8.0×10^{15}	1.1×10^{-7}	1.1×10^{-6}	0.7	8.0×10^{15}	1.1×10^{-6}	1.1×10^{-7}
p-CIGS-1	1.07	1.0×10^{15}	9.1×10^{-7}	9.1×10^{-6}	0.87	1.0×10^{15}	9.1×10^{-6}	9.1×10^{-7}
p-CIGS-2	1.07	1.0×10^{15}	9.1×10^{-7}	9.1×10^{-6}	0.87	1.0×10^{15}	9.1×10^{-6}	9.1×10^{-7}
p-CIGS-3	1.07	1.0×10^{15}	9.1×10^{-7}	9.1×10^{-6}	0.87	1.0×10^{15}	9.1×10^{-6}	9.1×10^{-7}
p-CIGS-4	1.07	1.0×10^{15}	9.1×10^{-7}	9.1×10^{-6}	0.87	1.0×10^{15}	9.1×10^{-6}	9.1×10^{-7}
p-CIGS-5	1.07	1.0×10^{15}	9.1×10^{-7}	9.1×10^{-6}	0.87	1.0×10^{15}	9.1×10^{-6}	9.1×10^{-7}
p-CIGS-6	1.07	1.0×10^{15}	9.1×10^{-7}	9.1×10^{-6}	0.87	1.0×10^{15}	9.1×10^{-6}	9.1×10^{-7}

The current density-voltage (J-V) plots of uniform band gap and grading band gap CIGS cells predicted by Medici simulation are shown in Figure A-4. The performance parameters (e.g., J_{sc} , V_{oc} , FF and η) obtained by Medici simulation were compared with the results of AMPS-1D simulation [Son04] for the CIGS cells with the similar structure and device parameters in Table A-4. The comparison between the Medici and AMPS-1D

simulations demonstrates that the simulation results by Medici are acceptable even though further optimization of device parameters is necessary to achieve better reliability.

Table A-4. Comparison of performance parameters of CIGS cells simulated by Medici

	Cell	Jsc (mA/cm ²)	Voc (mV)	FF (%)	η (%)
Medici	CIGS-uni	28.4	710	79.3	16.0
	CIGS-grade	30.1	700	80.7	17.0
AMPS-1D [Son04]	CIGS-uni	32.3	655	74.6	15.7
	CIGS-grade	34.3	675	79.4	18.4

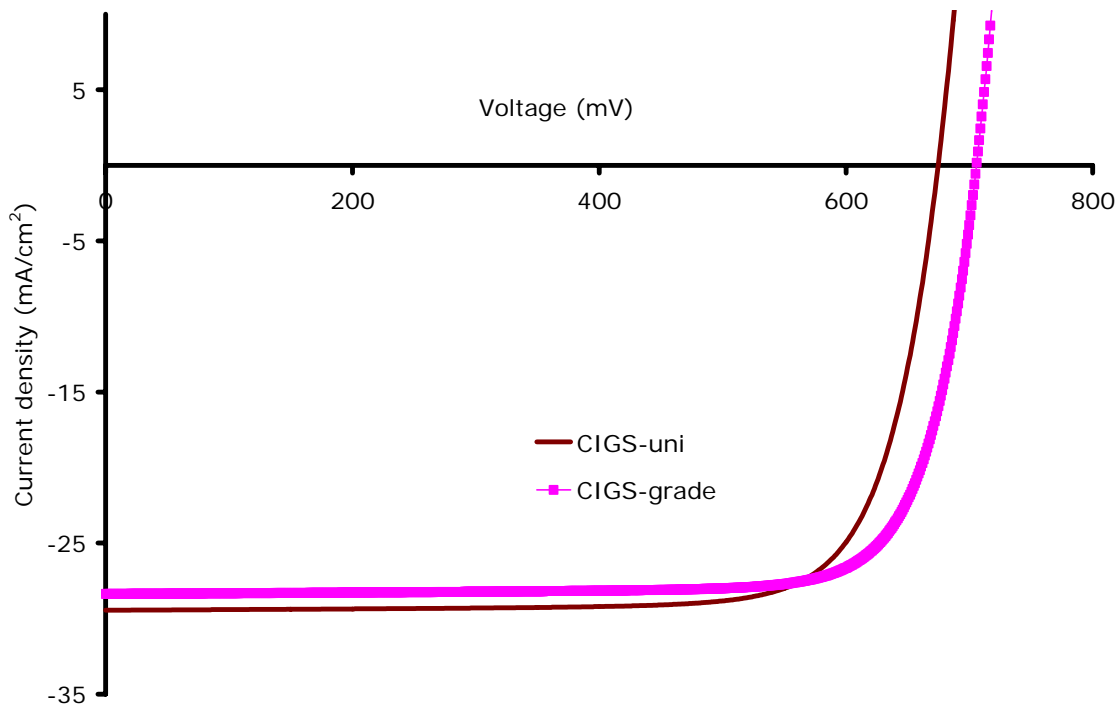


Figure A-4. Current- Voltage (C-V) plots for CIGS cells predicted by Medici simulation.

LIST OF REFERENCES

- Abo05 D. Abou-Ras, G. Kostorz, D. Bremaud, M. Kalin, F. V. Kurdesau, A. N. Tiwari and M. Dobeli, *Thin Solid Films*, 480-481 (2005) 433.
- Abr84 N. Kh. Abrikosov, V. F. Bankina, M. A. Korzhuev, G. K. Demeskii and O. A. Teplov, *Sov. Phys. Solid State*, 25 (1984) 1678.
- Abu05 J. A. Abushama, S. Johnston, D. Young and R. Noufi, *MRS Spring Meeting*, CA, (2005).
- Adu95 F. O. Adurodija, M. J. Carter and R. Hill, *Sol. Energ. Mat. Sol. C.*, 37 (1995) 203.
- Adu99 F. O. Adurodija, J. Song, S. D. Kim, S. H. Kwon, S. K. Kim, K. H. Yoon and B. T. Ahn, *Thin Solid Films*, 338 (1999) 13.
- And91 T. J. Anderson, I. Ansara, *J. Phase Equilib.*, 12 (1991) 64.
- And92 J. -O. Andersson and J. Ågren, *J. Appl. Phys.*, 72 (1992) 1350.
- And02 J. Andersson, T. Helander, L. Hoglund, P. F. Shi and B. Sundman, *CALPHAD*, 26 (2002) 273.
- Ans78 I. Ansara, C. Bernard, L. Kaufman and P. Spencer, *CALPHAD*, 2 (1978) 1.
- Ask76 K. A. Askerova, N. A. Alieva, T. Kh. Azizov, A. S. Abbasov and F. M. Mustafayev, *Izv.An. Azerb. SSR*. 6 (1976) 137.
- Aza76 T. Azakami and A. Yazawa, *Can. Metall. Quart.*, 15 (1976) 111.
- Bab75 A. A. Babitsyna, T. A. Emelyanova, M. A. Chernitsyna, V. T. Kalinnikov and J. Russ., *Inorg. Chem.*, 20 (1975) 1711.
- Bac88 Bachmann, K.J., Goslawsky, H., Fiechter, S. J. *Cryst. Growth*, 89 (1988) 160.
- Bah99 Z. Bahari, E. Dichi and B. Legendre, *Z. Metallkd.*, 90 (1999) 55.
- Bah03 Z. Bahari, E. Dichi, B. Legendre and Jérôme Dugué, *Thermochimica Acta* (2003) 131.

- Bam80 C.H. Bamford, and C.F.H. Tipper, Reactions in the Solid State, Elsevier Scientific Publishing Company, Amsterdam, New York, (1980).
- Bec39 A.E. Becquerel, Comt. Rend. Acad. Sci., 9 (1839) 561.
- Bek01 J. Bekker, V. Albers and M. J. Witcomb, Thin Solid Films, 387 (2001) 40.
- Ber68 J. Berkowitz and W. A. Chupka, J. Chem. Phys., 48 (1968) 5743.
- Ber72 G. P. Bernardini, F. Corsini and R. Trosti, Period. Miner., 41 (1972) 565.
- Ber73 Berger, L.I., Bondar, S.A., Lebedev, V.V., Molodyk, A.D., and Strel'chenko, S.S., Nauka I Tekhnika, 2 (1973) 48.
- Bha00 R. N. Bhattacharya, W. Batchelor, K. Ramanathan, M. A. Contreras, T. Moriarty, Sol. Energy Mater. Sol. Cells, 63 (2000) 367.
- Bha01 R. N. Bhattacharya, A. Balcioglu and K. Ramanathan, Thin Solid Films, 384 (2001) 65.
- Bha98 R. N. Bhattacharya, W. Batchelor, J. E. Granata, F. Hasoon, H. Wiesner, K. Ramanathan, J. Keane, R. N. Noufi, Sol. Energy Mater. Sol. Cells, 55 (1998) 83.
- Bin03 K. Bindu, C. Sudha Kartha, K.P. Vijayakumar, T. Abe and Y. Kashiwaba: Sol. Energy Mater. Sol. Cells, 79 (2003) 67.
- Bla78a R. Blachnik and G. Bolte, J. Less-Common Metals, 57 (1978) 21.
- Bla78b R. Blachnik and P-G. Gunia, Z. Naturforsch. A: Phys. Sci., 33 (1978) 190.
- Boe87 Boehnke, U.-C., Kuehn, G. J. Mater. Sci., 22 (1987) 1635.
- Bol93 A. Bolcavage, S. W. Chen, C. R. Kao, Y. A. Chang, and A. D. Romig, Jr., J. Phase Equilib., 14 (1993) 14.
- Bor00 A. Borgenstam, A. Engström, L. Höglund and J. Ågren, J. Phase Equilib., 21 (2000) 269.
- Bru03 A. Brummer, V. Honkimaki, P. Berwian, V. Probst, J. Palm and R. Hock, Thin Solid Films, 437 (2003) 297.
- Bur74 B. P. Burylev, N. N. Fedorova and L. Sh. Tsemekhman, Russ. J. Inorg. Chem., 19 (1974) 1249.
- Cab05 R. Caballero and C. Guillén, Sol. Energ. Mat. Sol. C., 86 (2005) 1.
- Cal98 M. E. Calixto, R. N. Bhattacharya, P. J. Sebastian, A. M. Fernandez, S. A. Gamboa, R. N. Noufi, Sol. Energy Mater. Sol. Cells, 55 (1998) 23.

- Cha81 D. J. Chakrabarti and D. E. Laughlin, Bull. Alloy Phase Diag., 2 (1981) 305.
- Cha99 C. H. Chang, Ph.D. Dissertation, University of Florida, Gainesville, FL (1999).
- Che96 Y.-C. Chen and C.C. Lee, Thin Solid Films, 283 (1996) 243.
- Con05 M.A. Contreras, K. Ramanathan, J. AbuShama, F. Hasoon, D.L. Young, B. Egaas and R. Noufi, Prog. Photovolt: Res. Appl., 13 (2005) 209.
- Dar42 L.S. Darken, Tran AIME, 150 (1942) 157.
- Dar49 L.S. Darken, Tran AIME, 180 (1949) 430.
- Dic00 E. Dichi and B. Legendre, Z. Metallkd., 91 (2000) 47.
- Die82 J. Dieleman, F. H. M. Sanders, and J. H. J. Van Dommelen, Philips J. Res., 37 (1982) 204.
- Din91 A.T. Dinsdale, CALPHAD, 15 (1991) 317.
- Dul01 T. Dullweber, G. Hanna, U. Rau and H.W. Schock, Sol. Energ. Mat. Sol. C., 67 (2001) 145.
- Fea86 M.L. Fearheiley, Sol. Cells, 16 (1986) 91.
- Fis01 D. Fischer, N. Meyer, M. Kuczmicik, M. Beck, A. Jäger-Waldau and M. Ch. Lux-Steiner, Sol. Energ. Mat. Sol. C., 67 (2001) 105.
- Gan06 M. Ganchev, J. Kois, M. Kaelin, S. Bereznev, E. Tzvetkova, O. Volobujeva, N. Stratieva and A. Tiwari, Thin Solid Films, 511-512 (2006) 325.
- Gat56 G. Gattow and A. Schneidener, Z. Anorg. Allg. Chem., 286 (1956) 296.
- Gla00 V. M. Glazov, A. S. Pashinkin and V. A. Fedorov, Inorg. Mater., 36 (2000) 775.
- Gla79 Glazov, V. M., Lebedev, V. V., Molkyn, A. D., and Pashinkin, A. S., Inorganic Materials, 15 (1979) 1865.
- Gla91 V. M. Glazov and S. G. Kim, Inorg. Mater., 26 (1991) 2141.
- Göd00a T. Gödecke, T. Haalboom and F. Ernst, Z. Metallkd., 91 (2000) 622.
- Göd00b T. Gödecke, T. Haalboom and F. Ernst, Z. Metallkd., 91 (2000) 635.
- Göd00c T. Gödecke, T. Haalboom and F. Ernst, Z. Metallkd., 91 (2000) 651.

- Goe03 A. Goetzberger, C. Hebling and H.-W. Schock, Mat. Sci. Eng. R., 40 (2003) 1.
- Gom84 Gombia, E., Leccabue, F., and Pelosi, C., Mater. Lett., 2 (1984) 429.
- Gui98 J. Guillemoles, T. Haalboom, T. Gödecke, F. Ernst and D. Cahen, Mat. Res. Soc. Symp. Proc., 485 (1998) 127.
- Gui03 D. Guimard *et al.* MRS Proceedings, Spring (2003) B6.9.
- Gup71 P.K. Gupta and A.R. Cooper, Physica, 54 (1971) 39.
- Haa98 Haalboom, T., Goedecke, T., Ernst, F., Ruehle, M., Herberholz, R., Schock, H.W., Beilharz, C., Benz, K.W. Ternary and Multinary Compounds, 152 (1998) 249.
- Han58 M. Hansen and K. Anderko, Constitution of Binary Alloys, McGraw-Hill, New York (1958) 582.
- Han01 G. Hanna, A. Jasenek, U. Rau, H.W. Schock, Thin Solid Films, 387 (2001) 71.
- Her99 R. Herberhoz *et al.*, Euro. Phys. J. Appl. Phys. 6 (1999) 131.
- Her05 F. Hergert, R. Hock, A. Weber, M. Purwins, J. Palm and V. Prost, J. Phys. Chem. Solids., 66 (2005) 1903.
- Hey66 R. D. Heyding, Can. J. Chem., 44 (1966) 1233.
- Hil80 M. Hillert, CALPHAD, 4 (1980) 1.
- Hög97 L. Höglund: Internal Report, Trita-Mac-0605, Division of Physical Metallurgy, Royal Institute of Technology, Stockholm, (1997).
- Hua03 C-H Huang, Ph.D. dissertation, University of Florida (2003).
- Hul69 F. Hulbert, J. Br. Ceram. Soc., 6 (1969) 11.
- Ide03 M. Ider, Ph.D. Dissertation, University of Florida, Gainesville, FL (2003).
- Iga00 M. Igelson and P. Zabierowski, Thin Solid Films, 361-362 (2000) 371.
- Iga01 M. Igelson, A. Kubiaczyk, P. Zabierowski, M. Bodegard and K. Granath, Thin Solid Films, 387 (2001) 225.
- Iga02 M. Igelson, M. Wimbor and J. Wennerberg, Thin Solid Films, 403-404 (2002) 320.

- Iga03 M. Igelson, M. Bodegard and L. Stolt, Journal of Physical and Chemistry of Solids, 64 (2003) 2041.
- Jan84 B. Jansson, Internal Report, Trita-Mac-234, Division of Physical Metallurgy, Royal Institute of Technology, Stockholm, (1984).
- Kae04 M. Kaelin, D. Rudmann, A. N. Tiwari, Solar Energy 77 (2004) 749.
- Kao93 C. R. Kao, A. Bolcavage, S.-L. Chen, S. W. Chen, Y. A. Chang, and A. D. Romig, Jr., J. Phase Equilib., 14 (1993) 22.
- Kap01 V. K. Kapur, M. Fisher and R. Roe, Mat. Res. Soc. Proc. 668 (2001) H2.6.1.
- Kap03 V. K. Kapur, A. Bansal, P. Le, and O. Asensio, Thin Solid Films, 431-432 (2003) 53.
- Kat99 A. Katsui and T. Iwata, Thin Solid Films, 347 (1999) 151.
- Kau70 L. Kaufman and H. Bernstein, Computer Calculations of Phase Diagrams, Academic Press, New York, NY (1970).
- Ker04 L. L. Kerr, S. S. Li, S. W. Johnston, T. J. Anderson, O. D. Crisalle, W. K. Kim, J. Abushama and R.N. Noufi, Solid State Electronics, 48 (2004) 1579.
- Kim05a S. Kim, W.K. Kim, E.A. Payzant, R.M. Kaczynski, R.D. Acher, S. Yoon, T. J. Anderson, O.D. Crisalle, and S.S. Li, J. Vac. Sci. Technol. A, 23 (2005) 310.
- Kim05b W.K. Kim, S. Kim, E.A. Payzant, S.A. Speakman, S. Yoon, R.M. Kaczynski, R.D. Acher, T.J. Anderson, O.D. Crisalle, S.S. Li and V. Craciun, J. Phys. Chem. Solids. 66 (2005) 1915.
- Kim06a W.K. Kim, E.A. Payzant, S. Yoon and T.J. Anderson, J. Crystal. Growth. (in press).
- Kim06b W.K. Kim, E.A. Payzant, and T.J. Anderson, Thin Solid Films (in press).
- Kim06c W.K. Kim, E.A. Payzant, S.S. Li, O.D. Crisalle and T.J. Anderson, Proceedings of World Conference on Photovoltaic Energy Conversion (WCPEC-4), Waikoloa, HI (2006).
- Kin02 S. Kincaid, Ph.D. Dissertation, University of Florida, Gainesville, FL (2002).
- Kit64 J. E. Kittl and T. B. Massalski, J. Inst. Metals, 93 (1964-65) 182.
- Kna91 O. Knacke, O. Kubaschewski and K. Hesselmann, Thermochemical Properties of Inorganic Substances, Springer, Berlin (1991).

- Koh00 Kohara, N., Nishiawaki, S., Negami, T., Wada, T. *Jpn. J. Appl. Phys.*, 39 (2000) 6316.
- Kon82 Koneshova, T.I., Babitsyna, A.A., Kalinnikov, V.I. *Inorg. Mater.*, 15 (1982) 1267.
- Kub73 P. Kubaschewski and N. Nšlting, *Ber. Busen. Phys. Chem.*, 77 (1973) 70.
- Kun99 S. N. Kundu, D. Bhattacharyya, S. Chaudhuri and A. K. Pal, *Mater. Chem. Phys.*, 57 (1999) 207.
- Kur04 F. Kurdesau, M. Kaelin, V. B. Zalesski and V.I. Kovalewsky, *J. Alloy Compd.*, 378 (2004) 298.
- Lak96 S. T. Lakshmikumar and A.C. Rastogi, *J. Appl. Phys.*, 79 (1996) 3585.
- Lan74 D. V. Lang, *J. Appl. Phys.*, 45 (1974) 3014.
- Li93 S. S. Li, *Semiconductor Physical Electronics*, Plenum Press, New York (1993).
- Li04 J. –B. Li, M. –C. Record and J. –C. Tedenac, *Z. Metallkd.* 94 (2004) 381.
- Liu02 H. S. Liu, X. J. Liu, Y. Cui, C. P. Wang, I. Ohnuma, R. Kainuma, Z. P. Jin and K. Ishida, *J. Phase Equilib.*, 23 (2002) 409.
- Lu99 K. Lu, M. L. Sui, J. H. Perepezko and B. Lanning, *J. Mater. Res.*, 14 (1999) 771
- Mat97 H. Matsushita and T. Takizawa, *J. Cryst. Growth*, 179 (1997) 503.
- Med User's manual of Medici version 2001.4.
- Mer00 Merino, J.M., Mahanty, S., Leon, M., Diaz, R., Rueda, F., de Vidales, J.L.M. *Thin Solid Films*, 70-73 (2000) 361.
- Mil74 K. C. Mills, *Thermodynamic Data for Inorganic Sulphides, Selenides and Tellurides*, Butterworth, London (1974).
- Möл93 H. J. Möller, *Semiconductors for Solar Cells*, Artech House, Boston (1993)
- Moo99 J. B. Mooney, and R. H. Lamoreaux, *Solar Cells*, 16 (1999) 211.
- Mos89 S. N. Mostafa, S. R. Selim, S. A. Soliman and F. A. El-lakwah, *Ber. Busen. Phys. Chem.*, 93 (1989) 123.
- Mur75 R. M. Murray and R. D. Heyding, *Can. J. Chem.*, 53 (1975) 878.

- Nor69 P. Norby, A. Nørlund Christensen and J. C. Hanson, Inorg. Chem., 38 (1999) 1216.
- Nre06 NREL, Learning about renewable energy & energy efficiency, http://www.nrel.gov/learning/re_photovoltaics.html (2006).
- Ogo69 Z. Ogorelec and B. Celustka, J. Phys. Chem. Solids, 30 (1969) 149.
- Ogo72 Z. Ogorelec, B. Mestnik and D. Devcic, J. Mater. Sci., 7 (1972) 967.
- Ons31a L. Onsager, Phys. Rev., 37 (1931) 405.
- Ons31b L. Onsager, Phys. Rev., 38 (1931) 2265.
- Pal03 J. Palm *et al.*, Thin Solid Films, 431-432 (2003) 514.
- Pal04 J. Palm, V. Probst and F. H. Karg, Sol. Energy, 77 (2004) 757.
- Pie96 R. F. Pierret, Semiconductor Device Fundamentals, Addison-Wesley, New York (1996)
- Pis03 T. Pisarkiewicz and H. Jankowski, Vacuum, 70 (2003) 435.
- Pro96 P. P. Prosini, M. L. Addonizio, A. Antonaia, S. Loreti, Thin Solid Films 288 (1996) 90.
- Pur06a M. Purwins, A. Weber, P. Berwian, G. Müller, F. Hergert, S. Jost and R. Hock, J. Crystal Growth, 287 (2006) 408.
- Pur06b M. Purwins, R. Enderle, M. Schmid, P. Berwian, G. Müller, F. Hergert, S. Jost and R. Hock, Thin Solid Films, (2006) in press.
- Ram05 K. Ramanathan, G. Teeter, J.C. Keane and R. Noufi, Thin Solid Films, 480-481 (2005) 499.
- Rau70 H. Rau and A. Rabenau, J. Solid State Chem., 1 (1970) 515.
- Red48 O. Redlich, and A. Kister, Ind. Eng. Chem., 40 (1948) 345.
- Rus04 M. Rusu *et al.*, Thin Solid Films, 451-452 (2004) 556.
- Sau98 N. Saunders and A. P. Miodownik, Calculation of Phase Diagrams (CALPHAD), Oxford, New York, Pergamon (1998).
- Sch00 O. Schenker, M. Klenk, and E. Bucher, Thin Solid Films, 361-362 (2000) 454.
- Sch93 D. Schmid, M. Ruckh, F. Grunwald, H.W. Schock, Journal of Applied Physics, 73 (1993) 2902.

- Sch98 D.L. Schulz *et al.* J. Electron. Mater., 27 (1998) 433.
- Sch99 D.J. Schroeder, J.L. Hernandez, A.A. Rockett, Proceedings of 11th International Conference on Ternary and Multinary Compound, (1999) 749.
- Sha96 W. N. Shafarman and J. E. Phillips, Proceeding of 25th IEEE Photovoltaic Specialists Conference, Washington D.C., USA, May 13-17 (1996) 917.
- She06 J.Y. Shen, W.K. Kim, S.L. Shang, M.Y. Chu, C.S. Cao and T.J. Anderson, "Thermodynamic Description of the ternary compounds in Cu-In-Se System," Rare Metals (in press).
- Sma46 J. S. Smart and A. A. Smith, Trans. AIME, 166 (1946) 144.
- Son03 H. K. Song, S. G. Kim, H. J. Kim, S. K. Kim, K. W. Kang, J. C. Lee and K. H. Yoon, Solar Energy Materials & Solar Cells, 75 (2003) 145.
- Son04 J. Song, S.S. Li, C.H. Huang, O.D. Crisalle and T.J. Anderson, Solid State Electronics, 48 (2004) 73.
- Sta02 B. J. Stanbery, S. Kincaid, S. Kim, C. H. Chang, S. P. Ahrenkiel, G. Lippold, H. Nuemann, T. J. Anderson, and O. D. Crisalle, J. Appl. Phys., 91 (2002) 3598.
- Sto96 S. Stolen, H. Fjelvag, F. Grenvold, T. Sipowska, F. Edgar and J. Westrum, J. Chem. Thermodyn., 28 (1996) 753.
- Sub88 P. R. Subramanian, T. B. Massalski and D. E. Laughlin, Acta metall., 36 (1988) 937.
- Tau05 S. Taunier *et al.*, Thin Solid Films 480-481 (2005) 526.
- Tay76 P. L. Taylor, D. L. Wagoner and C. H. Pitt, Met. Trans., 7B (1976) 103.
- Tou77 Y. S. Touloukian, R. K. Kirby, R. E. Taylor, and P. D. Desai, Thermophysical Properties of Matter, 12 (1977) 298.
- Val68 N. Valverde, Z. Phys. Chem Neue Fol, 61 (1968) 92.
- Vis05 C. Viswanathan, V. Senthilkumar, R. Sriranjini, D. Mangalaraj, Sa. K. Narayandass, and J. Yi, Cryst. Res. Technol., 40 (2005) 658.
- Wad01 T. Wada, N. Kohara, S. Nishiwaki and T. Negami, Thin Solid Films, 387 (2001) 118.
- Wei95 S.H. Wei, A. Zunger, Journal of Applied Physics, 78 (1995) 3846.
- Wei99 S-H Wei, S.B. Zhang and A. Zunger, Journal of Applied Physics, 85 (1999) 7214.

- Wol00 D. Wolf and G. Müller, *Thin Solid Films*, 361-362 (2000) 155.
- Yoo05 S. Yoon, Ph.D. Dissertation, University of Florida, Gainesville, FL (2005).
- Zha98 S. B. Zhang, S. -H. Wei, A. Zunger, H. Katayama-Yoshita, *Phys. Rev. B*, 57 (1998) 9642.
- Zwe95 S. Zweigart, D. Schmid, J. Kessler, H. Dittrich and H. W. Schock, *J. Crystal Growth*, 146 (1995) 233.
- Zwe99 K. Zweibel, *Sol. Energy Mater. Sol. Cells*, 59 (1999) 1.
- Zwe05 K. Zweibel, Solar Program Review Meeting, Denver, Colorado (2005).

BIOGRAPHICAL SKETCH

Woo Kyoung Kim was born at a small town, DongHae in South Korea, on 24 December 1971. He entered Sung Kyun Kwan University in 1990, where he studied chemical engineering and graduated at the top of engineering college. Then he joined the polymer and colloid engineering laboratory at chemical engineering department of Seoul National University for his master's research in 1994. His master's research covered the thermally induced phase separation in Nylon-PEG blends. After receiving his master's degree in 1994, he started his industrial research at Samsung General Chemicals, Co., in South Korea, where he mainly has worked on the process development and scale-up of polyethylene and polypropylene polymerization process. During the industrial experience at petrochemical company for more five years, he was encouraged to study the environmentally friendly future energy. Finally, he joined the electronic material processing group at chemical engineering department in University of Florida, where he stepped into new field, thin film solar cells.